

Storage conditions and degassing processes of low-K
and high-Al tholeiitic island-arc magmas: Experimental
constraints and natural observations for Mutnovsky
volcano, Kamchatka

Von der Naturwissenschaftlichen Fakultät
der Gottfried Wilhelm Leibniz Universität Hannover
zur Erlangung des Grades
Doktorin der Naturwissenschaften
Dr. rer. nat.

genehmigte Dissertation

von
Tatiana Shishkina,
Magistr geologii
geboren am 12.03.1983 in Kursk (Russland)

2012

Referent: Prof. Dr. François Holtz
Korreferent: Prof. Dr. Max Wilke
Tag der Promotion: 28. Juni 2012

Erklärung zur Dissertation

gemäß §6(1) der Promotionsordnung der Naturwissenschaftlichen Fakultät der
Gottfried Wilhelm Leibniz Universität Hannover

für die Promotion zum Dr. rer. nat

Hierdurch erkläre ich, dass die Dissertation mit dem Titel

**“Storage conditions and degassing processes of low-K and high-Al tholeiitic
island-arc magmas: Experimental constraints and natural observations for
Mutnovsky volcano, Kamchatka“**

selbstständig verfasst und alle benutzten Hilfsmittel und Quellen sowie gegebenenfalls
die zu Hilfeleistung herangezogene Institutionen vollständig angegeben wurden.

Die Dissertation wurde nicht schon als Masterarbeit, Diplomarbeit oder andere
Prüfungsarbeit verwendet.

Hannover, den 29. März 2011

Tatiana Shishkina

Acknowledgements

A carrying out, realization and accomplishment of this PhD-work was possible only with a help of many people whom I would like to thank here.

First of all I would like to express my sincere gratitude to the best team of the supervisors – Prof. Dr. François Holtz, Dr. Roman Botcharnikov and Dr. Renat Almeev who have introduced to me the World of the Experimental Petrology and patiently taught me how to operate with the experimental and analytical devices, and what is more importantly - how to understand and interpret the experimental and natural observations. Many-many thanks for all your kindness, wisdom, understanding, sense of humour and help during these four years!

A special thank to Maxim Portnyagin for guiding us to the world of Kamchatka, melt inclusions and other interesting areas and also for the useful discussions of my work.

I would like to thank all the people of the Institute of Mineralogy in Hannover which became my second home for the last four years due to a great friendly atmosphere created by the people working here. Many big thanks to Otto Diedrich without your thin-sections and other types of samples preparation my work would be almost impossible! Thanks to the Workshop team - Ullrich Kroll, Marcus Köhler and Fabian for the technical support of the life in the Experimental Labs. Thanks to Prof. Dr. Harald Behrens for teaching me how to work on KFT, FTIR and Raman and for a good mood and energy that you distribute around. Thanks to the Microprobe group – Prof. Dr. Jürgen Koepke, Wanja Dziony and Eric Wolff for a help with performing the analytical sessions on Electron Microprobe. Thanks to our Secretaries - Sabine Kropp, Kristin Kortland and Merle for the help in a dealing with the bureaucratic things.

Many students and PhD students were helping me on the different stages of the project by performing the experiments and various analytical procedures or giving the useful advises, fruitful discussions and simply being the very good Friends: Sarah Cichy, Wanja Dziony, Annette Quetscher, Sara Fanara, Tapas Debnath, Anna Simonyan, Andre Stechern, Alex Bartels, Adrian Fiege, Anna-Maria Welsch, Eric Wolff, Parveen Fuchs, Anika Husen, Chao Zhang, Jaayke Knipping, Ute Bauer, Marcel Dietrich, Martin Erdmann, Anna W., Dawid M., Christoph O., Lars C., Franziska A., Tobias W., Peter N. and many others.

Many big thanks and wishes of all the best to my Russian community in Hannover who became my second Family – Roman, Anna, Liza, Dasha, Renat, Anna and Timur.

Looking back I can not miss a chance to give many thanks to the staff and students of my Alma Mater - the Geological Faculty of the Lomonosov Moscow State University. This place and people have given me a fundamental knowledge in Geology and Petrology and general philosophical view which has helped me to reach the Doctor degree and go further on the way of Science. A special thank to my former supervisor Prof. Dr. Pavel Pletchov who first has introduced me the World of Volcanoes, melt inclusions and Kamchatka.

And of course I would like to thank my big Family in Russia – parents, sisters, brother, aunts and uncles, cousins and nephews who have strongly supported and encouraged me though being on a big distance. I was always feeling a positive fluids coming from my Family and Friends in Russia and all over the World.

Abstract

The main result of this study is a determination of magma storage and pre-eruptive conditions of Mutnovsky volcano (Kamchatka, Russia) using a complex of petrological method: phase relation experiments, volatiles solubility experiments, study of petrography, mineralogy and melt inclusions in natural samples. An important part of this work is systematically experimentally determined solubility of mixed H₂O-CO₂-bearing fluids in a wide compositional range of mafic melts at pressures between 50 and 900 MPa.

Phase relation experiments were performed with primitive basalt from Mutnovsky (50 wt.% SiO₂, 7 wt.% MgO) at 100 and 300 MPa and in the temperature range from 950 to 1200°C and various aH₂O (fO₂) conditions. Experiments at both pressures have reproduced natural mineral associations of Mutnovsky basalts: plagioclase+olivine+clinopyroxene+Ti-magnetite as well as compositions of coexisting minerals and have shown that fractional crystallization of basaltic magma may lead to the formation of Mutnovsky volcanic series. The best conditions for simultaneous crystallization of a Plag+Ol+CPx assemblage with mineral compositions close to natural phenocrysts (An 85-94, Fo 72-84, Mg#CPx 74-81) were found in experiments at 300 MPa pressure within a temperature interval of 1025-1075°C. Melts might have contained 2 to 5 wt.% H₂O, which correspond to water activity between 0.3 and 0.9 and oxygen fugacity at the level of QFM+2.2 to QFM +2.7.

The presence of a relatively shallow magma storage reservoir located about 1.5 – 3 km below Mutnovsky volcano, filled with partially degassed and crystallized magma containing 1.5-2.5 wt.% H₂O is suggested. Crystallization of this magma produces association of high-Ca-plagioclase and olivine crystals at temperatures of 1050-1075°C. The heat and fluids produced by this shallow magma body may be the reason of intensive hydrothermal activity in the crater of Mutnovsky.

Solubility of H₂O-CO₂-bearing fluids was systematically studied in a wide pressure range (100 – 500 MPa) at temperatures above liquidus (1200-1250°C) in island-arc tholeiite, MORB, ferrobasalt, alkali basalts, basanites and nephilinite. The results show a strong non-linear effect of melt composition on solubility of CO₂. For example, at 500 MPa tholeiite dissolves about 3300 ppm CO₂, whereas nephilinite can dissolve almost 4 times more, about 13000 ppm CO₂. A compositional parameter $\Pi^* = (\text{Ca}^{2+} + 0.8\text{K}^{+} + 0.7\text{Na}^{+} + 0.4\text{Mg}^{2+} + 0.4\text{Fe}^{2+}) / (\text{Si}^{4+} + \text{Al}^{3+})$ which can be used to predict the solubility of CO₂ in different mafic melts is presented. The effect of composition on the solubility of H₂O is negligible at low pressures (50 - 100 MPa) but increases at higher pressure. It may be described as linear dependence on SiO₂ or alkali contents in the melt.

Systematic study of solubility of mixed H₂O-CO₂-bearing fluids in island-arc tholeiitic basalt (sample from Mutnovsky volcano) in the pressure range of 50 – 900 MPa has provided a systematic quantitative database which can be used for determination of volatile saturation pressures in natural basaltic melts (e.g. melt inclusions in phenocrysts). It is shown that the solubility of mixed fluids can be described as almost ideal (Henrian) at low pressures, whereas non-ideality strongly increases with pressure showing the most pronounced effect at pressures above 500 MPa.

The presented dataset of volatile solubility determinations allows improving of numerical solubility models for H₂O and CO₂ in mafic melts with quantification of effects of melt composition and pressure.

Keywords: *island arc tholeiites, crystallization, volatile solubility*

Zusammenfassung

Die Festlegung der Bedingungen innerhalb der Magmakammer sowie der präeruptiven Bedingungen des Mutnovsky Vulkans (Kamtschatka, Russland) sind das Kernergebnis dieser experimentellen Studie. Hierzu wurden vielfältige petrologische Methoden eingesetzt. Diese umfassen Experimente zur Bestimmung der Phasenbeziehungen und der Gaskomponentenlöslichkeit, petrografische und mineralogische Untersuchungen sowie die Untersuchung von Schmelzeinschlüssen in den natürlichen Proben. Ein wichtiger Bestandteil dieser Arbeit sind die experimentell bestimmten Löslichkeiten von H₂O-CO₂-Gemischen in mafischen Schmelzen unterschiedlichster Zusammensetzung bei Drücken zwischen 50 und 900 MPa.

Experimente zur Bestimmung der Phasenbeziehungen wurden mit einem primitiven Basalt des Mutnovsky Vulkans (50 Gew.-% SiO₂, 7 Gew.-% MgO) bei 100 und 300 MPa im Temperaturbereich zwischen 950°C und 1200°C und verschiedenen *a*H₂O (*f*O₂) durchgeführt. Bei beiden Drücken konnten die Mineralparagenese des Mutnovsky Basalts (Olivin + Plagioklas + Ca-Pyroxen + Titanomagnetit) sowie die Zusammensetzungen der koexistierenden Minerale experimentell reproduziert werden. Außerdem haben diese Experimente gezeigt, dass die fraktionierte Kristallisation des basaltischen Magmas zur Bildung der vulkanischen Serie des Mutnovsky führen kann. Die besten Bedingungen für eine gleichzeitige Kristallisation von Plag + Ol + CPx mit Zusammensetzungen nahe an denen der natürlichen Phänokristen (An 85-94, Fo 72-84, Mg# CPx 74-81) wurden bei Experimenten bei 300 MPa im Temperaturbereich von 1025 - 1075°C gefunden. Die Schmelze muss 2 bis 5 Gew.-% H₂O enthalten, welches einer Wasseraktivität von 0,3 bis 0,9 oder einer Sauerstoffugazität entsprechend QFM + 2,2 bis QFM + 2,7 entspricht.

Die Resultate dieser Arbeit deuten auf die Existenz einer relativ oberflächennah unter dem Mutnovsky Vulkan gelegenen Magmakammer in einer Tiefe von 1,5 – 3 km hin, deren Magma partiell entgast ist und einen Wassergehalt von 1,5 - 2,5 Gew.-% aufweist. Die Kristallisation dieses Magmas bei Temperaturen von 1050 – 1075°C führt zur Bildung von Ca-reichem Plagioklas und Olivin. Die Wärme sowie die Fluide, die von diesem oberflächennahen Magmakörper produziert werden, könnten die Ursache für die starke hydrothermale Aktivität im Krater des Mutnovsky Vulkans sein.

Die Löslichkeit von H₂O- und CO₂-haltigen Fluiden in Inselbogen-Tholeiiten, MORB, Ferrobasalt, Alkalibasalten, Basaniten und Nephelinit wurde systematisch über einen weiten Druckbereich (100 - 500 MPa) bei Temperaturen oberhalb der Liquidustemperatur (1200 – 1250°C) untersucht.

Die Ergebnisse zeigen einen starken, nicht-linearen Einfluss der Schmelzzusammensetzung auf die Löslichkeit von CO₂. Bei 500 MPa beispielsweise lösen sich in einem Tholeiit ca. 3300 ppm CO₂, während es in einem Nephelinit fast viermal so viel ist, ca. 13000 ppm CO₂. Es wird der Parameter $\Pi^* = (\text{Ca}^{2+} + 0.8\text{K}^+ + 0.7\text{Na}^+ + 0.4\text{Mg}^{2+} + 0.4\text{Fe}^{2+}) / (\text{Si}^{4+} + \text{Al}^{3+})$ eingeführt, der zur Vorhersage der CO₂-Löslichkeit in verschiedenen mafischen Schmelzen benutzt werden kann. Der Einfluss der Zusammensetzung auf die H₂O-Löslichkeit ist bei niedrigen Drücken (50 – 100 MPa) vernachlässigbar, nimmt aber mit steigendem Druck zu und könnte als eine lineare Abhängigkeit vom SiO₂- oder Alkaligehalt der Schmelze beschrieben werden.

Die systematische Untersuchung der Löslichkeit von gemischt H₂O- und CO₂-haltigen Fluiden in Inselbogen-Tholeiitbasalt (Probe vom Mutnovsky Vulkan) im Druckbereich von 50 – 900 MPa hat die Erstellung eines H₂O-CO₂-Löslichkeitsdiagramms mit Isobaren und Isoplethen ermöglicht. Dieses kann zur Bestimmung der Gaskomponentensättigungsdrücke in natürlichen Basaltschmelzen (z.B. für Schmelzeinschlüsse in Phänokristen) genutzt werden. Es wird gezeigt, dass sich bei niedrigen Drücken die Löslichkeit von Mischfluiden als nahezu ideal (Henrysches Gesetz) beschreiben lässt, die Nichtidealität jedoch mit steigendem Druck stark zunimmt, und über 500 MPa ein Maximum der Löslichkeitskurve erreicht wird. Die ermittelten Daten zur Bestimmung der Gaslöslichkeit erlauben Verbesserungen der numerischen Löslichkeitsmodelle für H₂O und CO₂ in mafischen Schmelzen inklusive der Quantifizierung des Einflusses der Schmelzzusammensetzung und des Druckes.

Stichworte: *Inselbogen-Tholeiite, Kristallisation, Löslichkeit von Volatilen*

TABLE OF CONTENTS

INTRODUCTION.....	1
CHAPTER I.	
MAGMA STORAGE CONDITIONS OF MUTNOVSKY VOLCANO: NATURAL OBSERVATIONS AND EXPERIMENTAL CONSTRAINTS.....	17
1. GEOLOGICAL OVERVIEW.....	18
1.1. A summary of previous investigations: geology, eruptive history, petrology and geothermal fields of Mutnovsky volcano.....	18
1.2 Mutnovsky Scientific Drilling Project (MSDP).....	25
2. METHODS OF INVESTIGATION.....	27
2.1. Studied natural samples.....	27
2.2. Methods applied for melt inclusions.....	28
2.3. Phase relations experiments.....	29
2.4. Analytical methods.....	33
3. RESULTS.....	39
3.1. Study of natural samples.....	39
3.1.1 Petrography and mineralogy of Mutnovsky natural samples.....	39
3.1.2 Mineral associations (paragenesis) in Mutnovsky natural rocks.....	48
3.1.3. Melt inclusions in olivine phenocrysts.....	50
3.1.4. Natural LLDs (bulk rocks, melt inclusions, residual glasses).....	54
3.2. Phase relations experiments at 100 and 300 MPa.....	60
3.2.1 Phase assemblages in experimental products.....	60
3.2.2 Phase proportions (as a function of T, aH ₂ O).....	63
3.2.3 Phase compositions in experimental products.....	64
4. DISCUSSION.....	77
4.1. Comparison of natural and experimental phase associations.....	77
4.2. Comparison of natural and experimental mineral compositions.....	80
4.3. Compositions of coexisting minerals in natural rocks and experimental products.....	82
4.4. Comparison of natural and experimental LLDs + inclusions.....	85
4.5. Redox state of Mutnovsky magmas.....	89
4.6. Volatiles saturation pressures.....	89
4.7. Magma storage conditions of Mutnovsky volcano.....	90
5. CONCLUSIONS.....	92
References.....	94
CHAPTER II.	
SOLUBILITY OF H₂O- AND CO₂-BEARING FLUIDS IN THOLEIITIC BASALTS AT PRESSURES UP TO 500 MPA.....	101
1. INTRODUCTION.....	103
2. EXPERIMENTAL AND ANALYTICAL METHODS.....	104
2.1 Starting materials and capsule preparation for solubility experiments.....	104
2.2 Experimental technique.....	105
2.3 Determination of fluid composition after experiment.....	109
2.4 Water determination by Karl-Fischer Titration.....	109
2.5 Determination of total dissolved carbon in reference glasses.....	110
2.6 Fourier-transform infrared spectroscopy (FTIR).....	110

2.7 Electron microprobe.....	111
2.8 Wet-chemical colorimetric method for determination of redox state of Fe.....	112
3. RESULTS.....	112
3.1 Experimental products and glass composition.....	112
3.2 Determination of IR absorption coefficients.....	113
3.3 Concentrations of water and CO ₂ in coexisting fluids and glasses.....	118
4. DISCUSSION.....	121
4.1 Solubility curves in basaltic melts and composition of coexisting fluids.....	121
4.2 Comparison with numerical models.....	122
4.3. Implications for natural systems.....	126
5. CONCLUSION.....	128
References.....	129

CHAPTER III.

COMPOSITIONAL AND PRESSURE EFFECTS ON THE SOLUBILITY OF H₂O AND CO₂ IN MAFIC MELTS.....	135
1. INTRODUCTION.....	138
2. EXPERIMENTAL AND ANALYTICAL METHODS.....	139
2.1 Preparation of starting materials and capsules for solubility experiments.....	139
2.1.1 Starting compositions.....	139
2.1.2 Capsule preparation.....	142
2.2 Experimental technique.....	142
2.3 Analytical methods.....	147
2.3.1 Major element glass composition.....	147
2.3.2 Fluid composition after the experiments.....	147
2.3.3 Determination of bulk concentrations of volatiles in glasses.....	147
2.3.4 Determination of H ₂ O and CO ₂ concentrations in glasses by Fourier-transform infrared spectroscopy (FTIR).....	148
3. RESULTS.....	149
3.1 Experimental products and glass composition.....	149
3.2 Infrared spectroscopy and determination of IR absorption coefficients.....	150
3.3 Concentrations of H₂O and CO₂ in coexisting fluids and glasses.....	155
3.3.1 H ₂ O and CO ₂ concentrations in mafic melts at 100 and 500 MPa.....	155
3.3.2 Solubility of mixed H ₂ O-CO ₂ fluids in mafic melts at 100 and 500 MPa.....	157
3.3.3 Volatile solubility in tholeiite at 700 and 900 MPa.....	158
4. DISCUSSION.....	160
4.1 Pressure effect on the solubility of mixed CO ₂ -H ₂ O-bearing fluids in basaltic melts..	160
4.2 Compositional effect on the solubility of H ₂ O in basaltic melts.....	161
4.3 Compositional effect on CO ₂ solubility in basaltic melts.....	165
5. CONCLUDING REMARKS.....	173
References.....	174

APPENDIX.....	183
----------------------	------------

CV.....	214
----------------	------------

INTRODUCTION

Island arc volcanism

Island arc volcanoes, located above convergent boundaries of lithospheric plates, are important "windows" into the interiors of the Earth providing important information on the origin and evolution of subduction zone magmas. Subduction zones have been creating over 20% of the current terrestrial magmatic products and have formed $7.35 \cdot 10^9$ km³ of andesitic crust throughout Earth's history (e.g., Taylor & McLennan 1995; Tatsumi et al., 2008b). Over 80% of arc volcanoes erupt andesitic lavas (Gill 1981) and built up the continental crust ("subduction factory" Tatsumi and Kogiso 2003). However, melts generated in the mantle at subduction zones, as in other tectonic settings, are mostly basaltic. The origin of differentiated andesitic crust thus provides a clue to understanding the evolution of the solid Earth. In addition, island arc volcanoes are important contributors of large amounts of volatiles (e.g. H₂O, CO₂, SO₂, H₂S, HCl etc.) to the planet's surface, thus affecting Earth atmosphere and climate (e.g., Stoiber and Jepsen, 1973; Gerlach, 1991; Williams et al., 1992). Hazardous explosive eruptions of island-arc volcanoes have strong effect on humans' life and social and economic activity. Therefore, understanding the processes of magma generation, magma differentiation and magma degassing in active island-arc volcanic systems is a long-standing problem in igneous petrology.

It has been found in the beginning of the last century that distinct types of magmatic series may form in island-arcs volcanoes (as well as in other geological settings) (Bowen, 1928; Fenner, 1929). Two main trends of magma evolution have been distinguished for volcanic rocks of low and normal alkalinity: *tholeiitic* (TH) and *calc-alkaline* (CA) (Fig. 1) (Wager and Deer, 1939; Kuno, 1959, 1968 a, b; Nockolds and Allen, 1953, 1954, 1956). Tholeiitic trend (Fenner-type) is characterized by strong FeO- and FeO/MgO enrichment and nearly constant behavior of SiO₂ during initial stages of magma evolution with subsequent slowing-down of FeO- and FeO/MgO increase and with prominent enrichment of SiO₂. In contrast, calc-alkaline series (Bowen-type) follow strong silica enrichment trend with nearly constant FeO/MgO and Fe-depletion with progression of crystallization (Wager & Deer 1939; Miyashiro, 1974).

The TH volcanic series are typified eruptive products of divergent margins (mid-ocean ridges, MOR) and volcanic fronts of oceanic island arcs, whereas CA-series are predominate products of mature continental arcs (e.g. Miyashiro, 1974), although they also occur in island arcs. Sometimes lavas of both volcanic series may occur within one magmatic system indicating the importance of evolution of magma storage conditions with

time (e.g. Zao volcano, NE Japan, Tatsumi et al., 2008b; Myoko-Kuroshime in Central Japan, Sakuyama, 1981; Mt Shasta, USA, Baker et al., 1994).

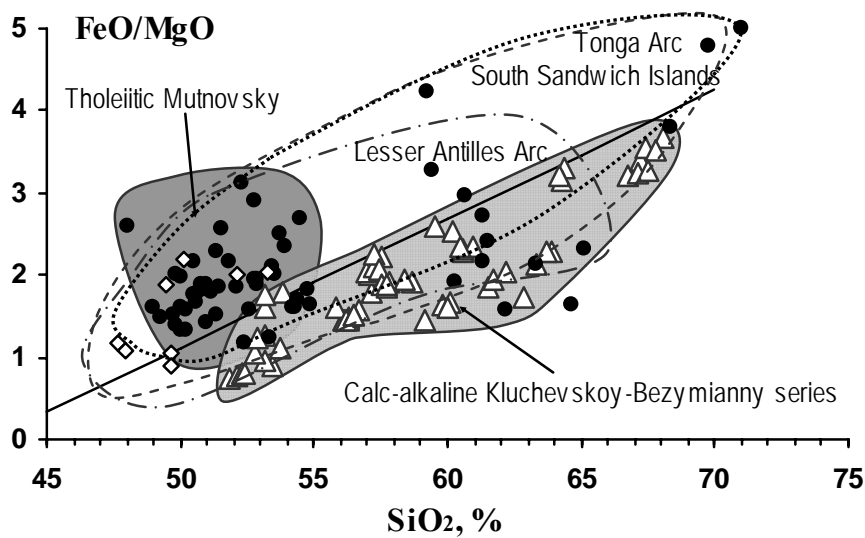


Fig. 1. SiO₂ versus FeO/MgO classification diagram of Mutnovsky tholeiitic basalts. Solid circles represent Mutnovsky rocks, open diamonds - glass inclusion compositions provided by M. Portnyagin (unpublished data). Solid line dividing tholeiitic and calc-alkaline magmatic series is after Miyashiro (1974). Fields of other typical island arc tholeiitic lavas from Tonga Arc, Northern Lesser Antilles and South Sandwich islands (source of data: GEOROC petrological database, <http://georoc.mpch-mainz.gwdg.de/georoc/>) and calc-alkaline series of Klyuchevskoy-Bezymianny volcanoes (Almeev, 2005) are shown for comparison. Glass inclusion compositions provided by M. Portnyagin (unpublished data).

Magma differentiation trends

In petrography textbooks and scientific literature there are a number of hypothesis explaining formation mechanisms of these two trends of magma differentiation. “Disequilibrium” features, petrographically observed in any volcanic rock (both in MORB tholeiites and essentially in calc-alkaline andesites), are usually invoked to demonstrate that the processes of assimilation and/or mixing with silicic low-Fe melts (Sakuyama, 1981; Grove and Baker, 1984; McBirney et al., 1987; George et al., 2004) as well as mantle-melt and/or crust-melt reactions (Kelemen, 1990) can play a crucial role in magma genesis. On the other hand, a large number of experimental studies conducted from the beginning of 1980th also demonstrated the importance of phase equilibrium control on the evolution of the residual melts and *general* differentiation of the magmas as a result of cooling, crystallization and phase separation. For example, it has been recognized that oxygen fugacity (fO_2) and water activity (aH_2O) are two dominant factors which control the path of magma crystallization leading the melt evolution along TH or CA magma differentiation trend:

- 1) TH-evolutionary trend was reproduced as a result of crystallization of primitive basaltic melts at anhydrous (very low aH_2O , $H_2O < 0.5$ wt%, Sobolev and

Chaussidon, 1996) and relatively reduced ($fO_2 \sim \text{QFM}$, Quartz-Fayalite-Magnetite oxygen buffer) conditions (e.g., Osborn, 1959; Grove and Baker 1984; Tormey et al., 1987; Kinzler and Grove, 1992; Toplis and Carroll, 1995; Yang et al., 1996; Berndt et al., 2005; Botcharnikov et al., 2008). During basalt crystallization at low to moderate pressures ($< 800 \text{ MPa}$), due to low $a_{\text{H}_2\text{O}}$, plagioclase is prevailing in solid assemblage resulting in strong FeO enrichment of residual melts. Relatively reduced conditions prevent earlier appearance of Fe-Ti oxides (magnetite), which significantly affects FeO (depletion) and SiO_2 (enrichment) concentrations in the residual melts.

- 2) CA-evolutionary trend can be only realized at oxidized ($fO_2 > \text{QFM}+1$) and hydrous conditions (middle to high $a_{\text{H}_2\text{O}}$, $\text{H}_2\text{O} > 2 \text{ wt.}\%$). Due to high $a_{\text{H}_2\text{O}}$, plagioclase crystallization is significantly suppressed (e.g., Osborn, 1959; Grove and Kinzler 1986; Baker and Egger, 1987; Sisson & Grove, 1993a; Kawamoto, 1996; Grove et al., 2003; Berndt et al., 2005; Pichavant & MacDonald, 2007; Hamada & Fuji, 2008; Tatsumi & Suzuki, 2009). This leads to the strong FeO-depletion and Al_2O_3 enrichment of residual melts. In addition, oxidized conditions and high $a_{\text{H}_2\text{O}}$ favor earlier stabilization of magnetite (simultaneous crystallization with anhydrous silicates) and also promote crystallization of hornblende at late stages. The presence of both magnetite and hornblende in solid assemblage results in strong SiO_2 enrichment, FeO depletion and a weak increase of FeO/MgO ratio in coexisting residual melts.

Island arc tholeiitic series

Low-K and high-Al *tholeiitic* series are typical for many volcanoes of frontal parts of island-arcs (e.g. Kurile-Kamchatka, Japan, Northern Lesser Antilles, Tonga, South Sandwich Islands) (Fig. 1,2). Despite the general similarity of island-arc tholeiites (IAT) with MOR tholeiites (MORB - mid-ocean ridge basalts), there is also a prominent difference between them. "Dry" MORBs are characterized by strong FeO and TiO_2 enrichment along a whole differentiation trend (8.5-4 wt.% MgO). In contrast, in IAT there is a weak TiO_2 and FeO enrichment at early stages of differentiation with further decrease in the concentrations of these oxides, which indicates the crucial role of Fe-Ti-bearing minerals at middle to later stages of magma evolution. (Fig. 2). Behavior of Al_2O_3 is also contrasting between MORBs and IAT: in IAT there is a lack or prominent delay of Al_2O_3 depletion which would be expected for crystallization of dry basalt along Ol+Pl+Cpx cotectics (MORB, Fig. 2). These compositional features point to the important role of water and more oxidized conditions prevailing in magma chambers of tholeiitic island arc

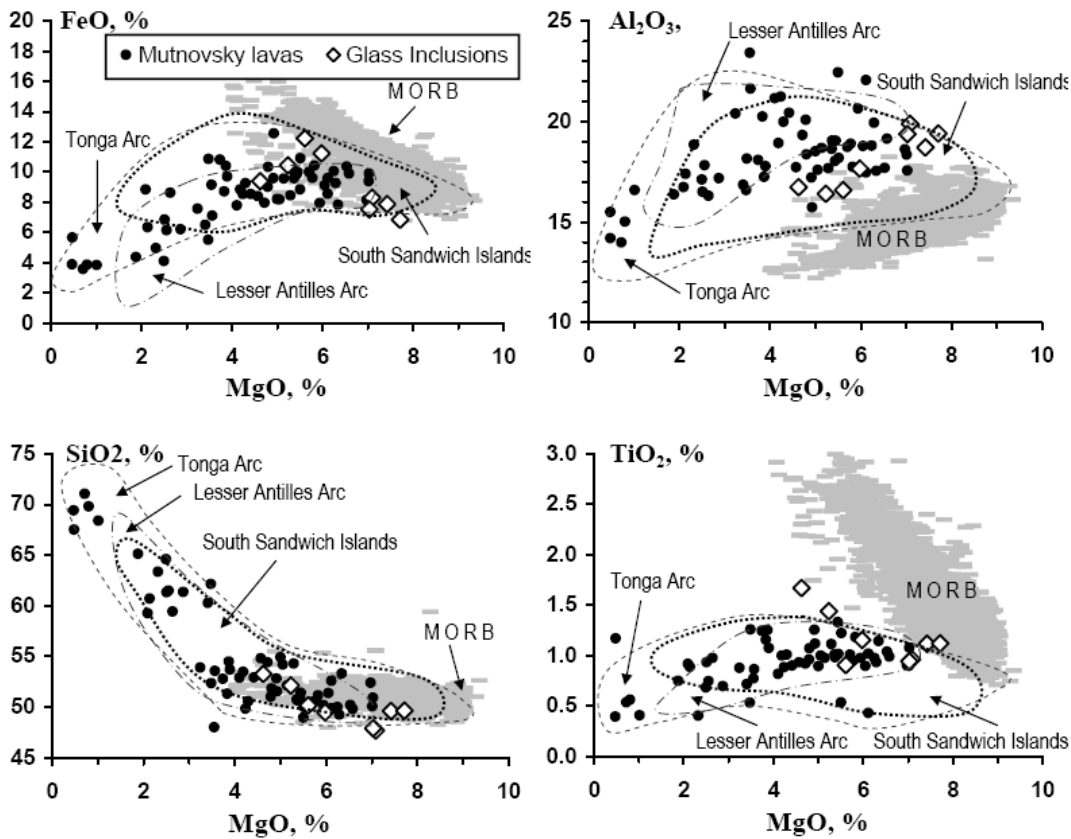


Fig. 2. Chemical compositions of the Mutnovsky volcano lavas (open circles) and glass inclusion (diamonds). Fields of typical MORBs and island arc tholeiitic lavas from Tonga Arc, Northern Lesser Antilles and South Sandwich islands are shown for comparison. Source of data: GEOROC petrological database (<http://georoc.mpch-mainz.gwdg.de/georoc/>). Glass inclusion compositions provided by M. Portnyagin (unpublished data).

volcanoes in contrast to that of MOR tholeiites. This is supported by recent studies of melt inclusions in island-arc tholeiitic basalts (Izu, Kurile-Kamchatka, Mariana, Lesser Antilles arcs) which show that IAT magmas may contain up to 5 wt.% H₂O (e.g.: Saito et al., 2005; Hamada and Fujii, 2007; Straub and Layne, 2003; Saito et al., 2010, Plechov et al., 2008; Newman and Stolper, 2000; Schaw et al., 2008; Bouvier et al., 2008; Portnyagin et al., 2007). **Such elevated H₂O contents in typical IAT volcanoes put a question: if Island Arc tholeiitic trend might be also derived by fractionation of H₂O-rich magma, what is the maximum H₂O content which still governs magma evolution along the TH-trend, and what is the minimum H₂O content required to the realization of calc-alkaline tendency of residual melt evolution?**

Although several experimental studies were focused on determination of magma storage conditions beneath typical IAT volcanoes, the *systematic quantitative* information on the relative role of ($P, a_{\text{H}_2\text{O}}, f_{\text{O}_2}$) in the genesis of tholeiitic island arc magmas is scarce (Fig. 3). Experimental studies performed at H₂O-saturated conditions ($a_{\text{H}_2\text{O}}=1$) and low pressures (below 200 MPa) produced only few Ol+Pl+Cpx±Mt-saturated glasses (Sisson and Grove, 1993b) compositionally similar to IAT (Fig. 3), whereas most of them revealed

typical CA-trend of magma evolution (e.g. (Sisson and Grove, 1993b; Gaetani et al., 1994; Wagner et al., 1995; Grove et al., 1997; Moore and Carmichael, 1998; Koepke et al., 2004; Berndt et al., 2005). Experimental studies performed at dry conditions between 1.0 and 1.5 GPa also produced IAT-like glasses (slightly less calcic than IAT). These melts, however, at high pressures were also saturated with orthopyroxene (in addition to Ol+Pl+Cpx, Draper and Johnston, 1992; Meen, 1990). However, in many IAT basalts Opx rarely coexists with Ol usually originating as a result of peritectic reaction between melt and olivine in more differentiated basalts. Recently, Hamada & Fuji (2008) presented results of their melting experiments with high-Mg arc basalt (MgO #=60) at fO_2 at NNO+1 and NNO-1 at pressures 200, 400 and 700 MPa, and reproduced TH trend in the experimental melts at low-P runs in the presence of 2 wt% H₂O in parental magma. At higher pressures they also observed Opx mostly due to high normative orthopyroxene (relatively low CaO) in their studied basalt. Due to this difference in composition, this study can not be directly applied to other island arc tholeiites. It should be noted that in most hydrous experiments available in the literature there is a lack of direct and accurate determinations of water contents in experimental melts. Thus, there is a crucial need of new experimental studies with accurate determination and control of thermodynamic parameters of crystallization (P , a_{H_2O} , fO_2) in island arc tholeiitic systems.

Mutnovsky volcano, Kamchatka

One of the typical examples of island-arc volcano with magmas belonging to low-to medium-K, high-Al tholeiitic island arc series is Mutnovsky volcano located in southern part of Kamchatka peninsula (Russia) within the frontal part of Eastern Volcanic Front (Fig. 1-1; Active volcanoes..., 1991; Chashchin et al., 2011). Compositions and evolutionary trends of eruptive products of Mutnovsky are very similar to other IAT-volcanoes e.g. Tonga Arc, Northern Lesser Antilles and South Sandwich islands (Fig. 1, 2) and therefore the data obtained for this volcano can be applied for other island-arc tholeiitic systems in the world. Another important peculiarity of Mutnovsky volcano that makes it an attractive object for investigation is a large and very active hydrothermal system within the crater of volcano and in adjacent areas providing geothermal energy used in geothermal power plants. This system is supplied and maintained by an interaction with a magmatic chamber beneath Mutnovsky. The evaluation of the input of magmatic system in the production of fluids and heat for the hydrothermal system is needed for the understanding of interaction between magmatic and hydrothermal systems.

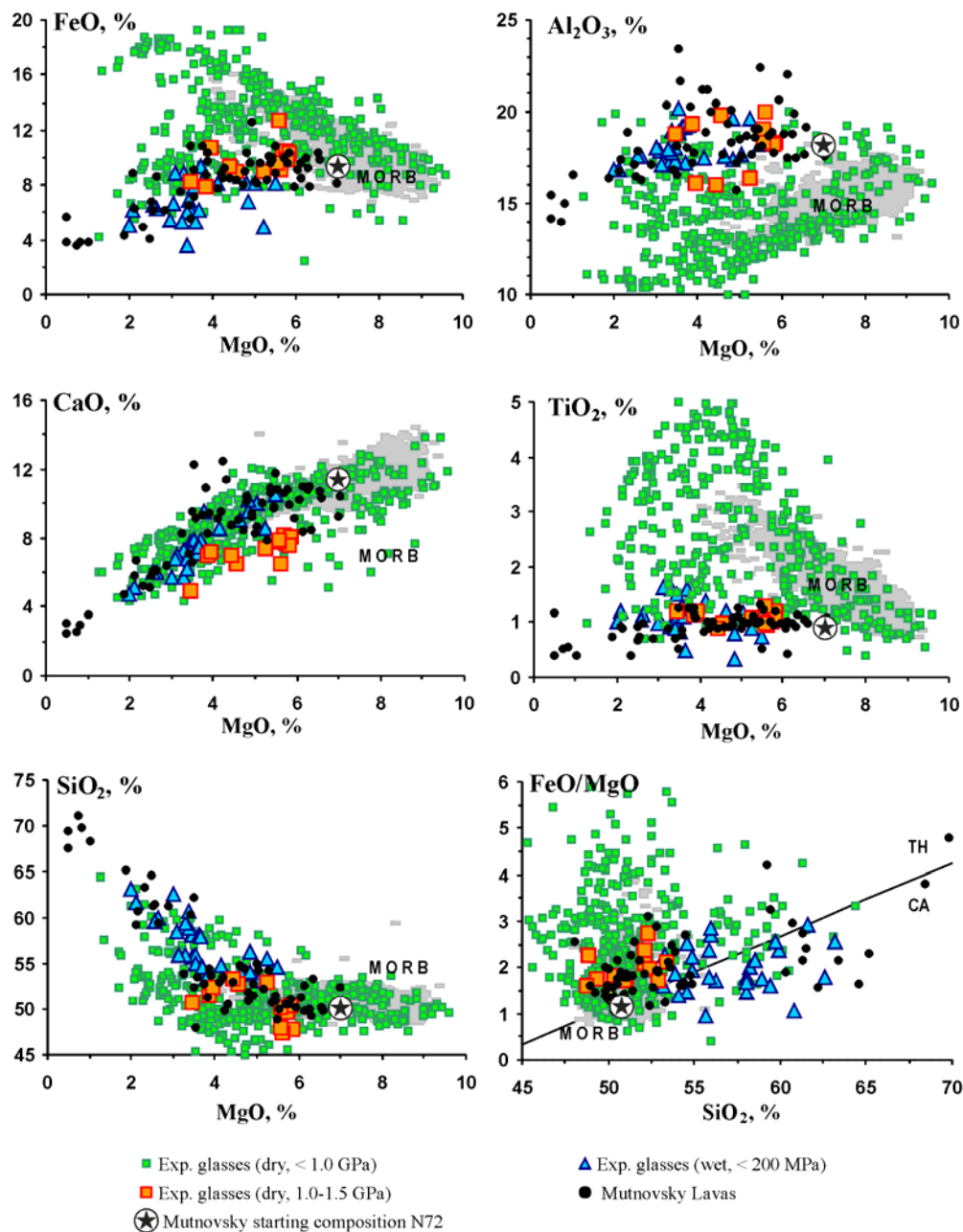


Figure 3. Major element compositions of natural island arc tholeiitic series (black dots, Mutnovsky volcano) and ocean tholeiites (MORBs, grey field, GEOROC database) in comparison to compositions of experimental glasses equilibrated with Ol+Pl+Cpx (\pm Opx \pm Mt) solid assemblage at different conditions: low pressure (< 1 GPa) anhydrous (green squares), high pressure (1-1.5 GPa) dry (orange squares), low pressure (< 200 MPa) hydrous (mostly H₂O-saturated, all blue triangles). Using the INFOREX database (Ariskin *et al.*, 1996) we selected only experimental basaltic to andesitic glasses which are in equilibrium with Ol+Pl+Cpx (\pm Opx \pm Mt), the mineral assemblage representative of the typical set of phenocrysts in Mutnovsky basalts (Martynov & Chashchin, 1989). The total number of Ol+Pl+Cpx (\pm Opx \pm Mt) bearing glasses includes 383 compositions, synthesized at dry to H₂O-saturated conditions from 1 atm to 1.5 GPa. It is worth to note that only H₂O-bearing (n=5) or H₂O-saturated (n=37) experimental glasses (blue triangles) produced at low pressures from 60 to 200 MPa are in agreement with natural compositions (all these glasses are Opx-free). Majority of dry Ol+Pl+Cpx bearing basaltic liquids produced at pressures < 1 GPa are noticeably displaced towards natural MORB compositions. Some high pressure (1-1.5 GPa) experimental glasses (blue squares, n=14) are within the natural trend of Mutnovsky compositions. However, all these high-pressure glasses are characterized by the presence of Opx in addition to Ol+Pl+Cpx. Mutnovsky basalt N72 experimentally studied in this work is shown by star in open circle. All other experiments are from Sisson and Grove, 1993b; Gaetani *et al.*, 1994; Wagner *et al.*, 1995; Grove *et al.*, 1997; Moore and Carmichael, 1998; Koepke *et al.*, 2004; Berndt *et al.*, 2005; Draper and Johnston, 1992; Meen, 1990.

This requires quantitative knowledge on the magma storage conditions, crystallization and magma degassing processes.

In 2006, Mutnovsky volcano was proposed as a possible object for scientific deep drilling (MSDP) in the frame of ICDP program. It was aimed to study the interaction between the magma and hydrothermal systems of the volcano (Eichelberger et al., 2009). It was planned to drill a borehole within the transition zone between the active craters Mutnovsky and the geothermal production field located about 8 km north-east from the volcano and to sample rock cores and fluids (Eichelberger et al., 2009). Main scientific objectives were stated as: (1) understanding of relationship of hydrothermal activity and active volcanism, (2) study of ore-deposition processes in volcanic systems, (3) new constraints on the volatile budget of arc volcanoes (e.g. SO₂) which can be used as a monitoring and eruption-predictive tool, (4) study of deep structure and feeding system of arc volcano (Eichelberger et al., 2009).

Understanding and evaluation of input of magmatic process into hydrothermal activity of the volcano requires estimation of parameters in magmatic system of Mutnovsky such as location of magma bodies as well as pressures, temperatures, regime of volatiles and composition of eruptive products. Previous geophysical (e.g. Grib, 1989; Active volcanoes..., 1991; Fedotov et al., 2005, rus), geochemical (e.g. Bortnikova et al., 2007; Zelensky and Taran, 2011) and some petrological studies (Chashchin et al., 2011) allowed authors to predict the presence of a shallow (1-10 km) hot magma body beneath Mutnovsky volcano, which acts as a source of heat and fluids for adjacent hydrothermal system. However, until now these preliminary estimates have not been supported by experimental studies.

In this study, crystallization conditions of typical IAT-basalts from *Mutnovsky volcano*, Kuril-Kamchatka island arc (Fig. 1,2,3) have been determined based on results of crystallization experiments at 100 and 300 MPa and conducted in a wide range of a_{H_2O} and f_{O_2} (Chapter 2 of this thesis). **Results obtained in the course of our experimental work and a complementary study of melt inclusions provide important information to constrain the magma storage conditions and to trace the magma evolution trend of the typical island arc tholeiitic volcano.**

Behavior of H₂O and CO₂: constraints on magma degassing

Important information on processes occurring in volcanic conduits may be derived from the studies of volatiles dissolved in magmas (e.g. H₂O and CO₂). A widely-used method for evaluation of saturation pressures in magmatic systems is the analyses of

volatile contents in melt inclusions, hosted by main phenocrysts in volcanic rocks (e.g. reviews by Moore, 2008; Metrich and Wallace, 2008). However, quantitative estimations of pressures can be only possible if the solubility data for volatiles are determined experimentally. At the time of starting of this project only few works on solubility of mixed H₂O-CO₂-bearing fluids in basaltic melts at crustal pressures were available: Dixon et al. (1995) (MORB, pressures below 100 MPa), Botcharnikov et al. (2005) (alkali basalt, 200 MPa) and Behrens et al., 2009 (phonotephrite, 200 and 500 MPa).

A systematic experimental study on the solubility of mixed H₂O-CO₂ fluids in low-K high-Al tholeiitic basalt from Mutnovsky volcano (same sample that was used for phase relation experiments) has been conducted at pressures between 50 to 900 MPa (Shishkina et al., 2010). The high-P experiments at 700 and 900 MPa allowed demonstration that non-ideality of mixed fluids increases significantly with pressure. The solubility behavior of mixed volatiles at pressures above 200 MPa can not be governed by ideally mixed fluids (Henrian law) indicating that the existing numerical models (Newman and Lowenstern, 2002; Papale et al., 2006) must be used with caution (Chapter 3 of this thesis). **The new experimental dataset provides quantitative information on the solubility of H₂O-CO₂-bearing fluids in basaltic melts in a wide range of pressures and fluid compositions** (Chapter 3 of this thesis). Combined with the data on volatile concentrations in melt inclusions, this allowed an evaluation of volatile saturation pressures and estimation of fluid composition in natural tholeiitic basalts of Mutnovsky volcano.

It should be noted that in addition to pressure, melt composition is another important parameter, which significantly affects solubility of volatiles. It is well known, that solubility of H₂O increases in the sequence: basalts – andesites – rhyolites (e.g. Holtz et al., 1995; Moore et al., 1998). Effect of melt composition on the solubility of CO₂ is more dramatic, though it is not very well described. The speciation of dissolved CO₂ depends on melt composition: it dissolves in the form of carbonate ion (CO₃²⁻) in mafic melts (basalts) (e.g. Dixon et al., 1995; Botcharnikov et al., 2005; Behrens et al., 2009), in the form of molecular species (CO₂-mol) in rhyolitic melts (e.g. Fogel and Rutherford, 1990; Tamic et al., 2001), whereas both species are present in melts (glasses) of intermediate compositions (andesites, e.g. King and Holloway, 2002; Botcharnikov et al., 2006).

In addition to concentration of SiO₂, the alkalis play also a crucial role on CO₂ solubility. In mafic melts with relatively similar SiO₂, CO₂ solubility may differ by a factor of 3 to 4 depending on their alkalis contents. For example at 500 MPa about 9000 ppm CO₂

can be dissolved in high-K-phonotephrite dissolves (Behrens et al., 2009), whereas only 3300 ppm are dissolving in tholeiitic melts (Shishkina et al., 2010, Chapter 2).

Thus, with the purpose of better understanding of the effect of melt composition (alkalis) on CO₂ and H₂O solubilities the systematic experimental study has been conducted at pressures between 100 and 500 MPa, using wide range of mafic compositions (where CO₂ dissolves only as CO₃²⁻) which include typical MORB, IAT, alkali basalts, ferrobasalt, basanite and nephelinite (Chapter 3 of this thesis). Our new dataset provides quantitative parameterization on the effect of melt composition on volatiles solubility.

The main aims of the presented PhD-Thesis are as follows:

- Experimental investigation of the effects of H₂O, fO_2 and pressure on magma evolution trends for island-arc tholeiites (Chapter 1);
- Determination of magma storage conditions for Mutnovsky volcano using a combination of experimental methods and investigation of natural samples (e.g. mineralogy, melt inclusions in phenocrysts and bulk rock compositions) (Chapter 1);
- Experimental study of solubility of mixed H₂O-CO₂-bearing fluids in tholeiitic melts in a range of pressures between 50 and 900 MPa (Chapters 2 and 3);
- Systematical experimental study of the effect of melt composition and pressure on solubilities of CO₂ and H₂O in mafic melts (Chapter 3).

References

Ariskin, A.A., Barmina, G.S., Meshalkin, S.S., Nikolaev, G.S., and Almeev, R.R. (1996) INFOREX-3.0: A database on experimental studies of phase equilibria in igneous rocks and synthetic systems: II. Data description and petrological applications. *Computers and Geosciences*, 22(10), 1073-1082.

Baker, D. R. and Eggler, D. H. (1987). Compositions of anhydrous and hydrous melts coexisting with plagioclase, augite, and olivine or low-Ca pyroxene from 1atm to 8 kbar3Application to the Aleutian volcanic center of Atka. *American Mineralogist* 72, 12-28.

Baker, M. B., Grove, T. L. and Price, R. (1994). Primitive basalts and andesites from the Mt. Shasta region, N. California: products of varying melt fraction and water content. *Contributions to Mineralogy and Petrology* 118, 111-215

Behrens, H., Misiti V., Freda C., Vetere F., Botcharnikov, R.E., Scarlato, P., 2009. Solubility of H₂O and CO₂ in ultrapotassic melts at 1200 and 1250°C and pressure from 50 to 500 MPa. *American Mineralogist* 94, 105-120.

Berndt, J., Koepke, J., and Holtz, F. (2005) An experimental investigation of the influence of water and oxygen fugacity on differentiation of MORB at 200 MPa. *Journal of Petrology*, 46(1), 135-167.

Bortnikova, S.B., Sharapov, V.N., and Bessanova, E.P., 2007. Hydro-geochemical composition of springs at the Donnoe Fumarole Field, Mutnovsky Volcano (Southern Kamchatka) and problems of their relation with supercritical magmatic fluids. *Dokl Earth Sci.*, 413A(3):410–414, doi:10.1134/S1028334X07030208.

Botcharnikov, R. E., Behrens, H. and Holtz, F. (2006a). Solubility and speciation of C-O-H fluids in andesitic melt at T = 1100-1300 °C and P = 200 and 500 MPa. *Chemical Geology* 229, 125-143.

Botcharnikov, R., Freise, M., Holtz, F. and Behrens, H. (2005a). Solubility of C-O-H mixtures in natural melts: new experimental data and application range of recent models. *Annals of Geophysics* 48, 633-646.

Botcharnikov, R.E., Almeev, R.R., Koepke, J. and Holtz, F. (2008) Phase relations and liquid lines of descent in hydrous ferrobasalt - Implications for the Skaergaard Intrusion and Columbia River flood basalts. *Journal of Petrology*, 49(9), 1687-1727.

Bouvier AS, Metrich N, Deloule E (2008) Slab-derived fluids in magma sources of St Vincent (Lesser Antilles Arc): volatiles and light elements imprints. *J Petrol* 49:1427-1448

Bowen, N. L. (1928). *The Evolution of the Igneous Rocks*. Princeton, NJ: Princeton University Press.

Chashchin A.A., Martynov Yu.A. (2011) Petrology of Gorely and Mutnovsky volcanoes rocks (Southern Kamchatka). Vladivostok. Dalnauka. 270 p. (in Russian)

Dixon, E. J., Stolper, E. M. and Holloway, J. R. (1995). An experimental study of water and carbon dioxide solubilities in mid-ocean ridge basaltic liquids. Part 1: Calibration and solubility models. *Journal of Petrology* 36, 1607-1631.

Draper, D.S., and Johnston, A.D. (1992) Anhydrous PT phase relations of an Aleutian high-MgO basalt: an investigation of the role of olivine-liquid reaction in the generation of arc high-alumina basalts. *Contributions to Mineralogy and Petrology*, 112(4), 501-519.

Eichelberger, J., Kiryukhin, A. and Simon, A. (2009) The magma-hydrothermal system at Mutnovsky volcano, Kamchatka peninsula, Russia. *Scientific Drilling*, 7, p. 54-59.

- Fedotov S.A., 2005, Magmatic Feeding Systems and Mechanizm of Volcanoes Eruptions. Moscow. Nauka Publ., 300 p. (in Russian)
- Fenner, C.N. (1929). The crystallization of basalts. *Amer. J. Science*. V. 18, p. 225-253.
- Fogel, R.A., Rutherford, M.J., 1990. The solubility of carbon dioxide in rhyolitic melts: a quantitative FTIR study. *Am. Mineral*. 75, 1311–1326.
- Gaetani, G.A., Grove, T.L., and Bryan, W.B. (1994) Experimental phase relations of basaltic andesite from hole 839B under hydrous and anhydrous conditions. *Proceedings of the Ocean Drilling Program, Scientific Results*, 135, 557-565.
- George, R., Turner, S., Hawkesworth, C., Bacon, C. R., Nye, C., Stelling, P. and Dreher, S. (2004). Chemical versus temporal controls on the evolution of tholeiitic and calc-alkaline magmas at two volcanoes in the Alaska-Aleutian arc. *Journal of Petrology* 45, 203-219.
- Gerlach, T.M., (1991) Present-day CO₂ emissions from volcanoes, *EOS* 72, (1991) 249–255.
- Gill, J.B. (1981) *Orogenic andesite and plate tectonics*. 385 p. Springer-Verlag, Berlin, Heidelberg, New York.
- Grib, E.N. (1989) Composition and parameters of crystallization of lavas of volcanic structures of Severno-Mutnovsky volcanic zone. *Volcanology and Seysmology*, V. 4, p. 29-43 (in Russian)
- Grove, T. L., Elkins-Tanton, L. T., Parman, S. W., Chatterjee, N., Mu«ntener, O. and Gaetani, G. A. (2003). Fractional crystallization and mantle-melting controls on calc-alkaline differentiation trends. *Contributions to Mineralogy and Petrology* 145, 515-533.
- Grove, T.L., and Baker, M.B. (1984) Phase equilibrium controls on the tholeiitic versus calc-alkaline differentiation trends. *J. Geophysical Research*, 89(B5), 3253-3274.
- Grove, T.L., and Kinzler, R.J. (1986) Petrogenesis of andesites. In G.W. Wetherill, Ed. *Annual review of earth and planetary sciences*, V. 14, p. 417-454, Palo Alto, California.
- Grove, T.L., Donnelly-Nolan, J.M., and Housh, T. (1997) Magmatic processes that generated the rhyolite of Glass Mountain, Medicine Lake volcano, N. California. *Contributions to Mineralogy and Petrology*, 127(3), 205-223.
- Hamada, M. and Fujii, T. (2008). Experimental constraints on the effects of pressure and H₂O on the fractional crystallization of high-Mg island arc basalt. *Contributions to Mineralogy and Petrology* 155, 767-790.

Hamada, M., Fujii, T., 2007. H₂O-rich island arc low-K tholeiite magma inferred from Ca-rich plagioclase-melt inclusion equilibria. *Geochem. J.* 41, 437–461.

Holtz, F., Behrens, H., Dingwell, D.B., Johannes, W., 1995. Water solubility in haplogranitic melts. Compositional, pressure and temperature dependence. *American Mineralogist* 80, 94-108.

Kawamoto, T. (1996). Experimental constraints on differentiation and H₂O abundance of calc-alkaline magmas. *Earth and Planetary Science Letters* 144, 577-589.

Kelemen, P. B. (1990). Reaction between ultramafic rock and fractionating basaltic magma. 1. Phase-relations, the origin of calcalkaline magma series, and the formation of discordant dunite. *Journal of Petrology* 31, 51-98.

King, P. L. and Holloway, J. R. (2002). CO₂ solubility and speciation in intermediate (andesitic) melts: the role of H₂O and composition. *GCA*, v.66, p.1627-1640.

Kinzler, R. J. and Grove, T. L. (1992). Primary magmas of midocean ridge basalts. 2. Applications. *Journal of Geophysical Research* 97, 6907-6926.

Koepke, J., Feig, S.T., Snow, J., and Freise, M. (2004) Petrogenesis of oceanic plagiogranites by partial melting of gabbros: an experimental study. *Contributions to Mineralogy and Petrology*, 146, 414-432.

Kuno, H. (1959) Origin of Cenozoic petrographic provinces of Japan and surrounding area. *Bull. Vulcanol.* V. 20, p. 37-76.

Kuno, H. (1968a) Differentiation of basalt magmas. In: Hess, H. H. and Poldervaart, A. (eds) *Basalts - The Poldervaart Treatise on Rocks of Basaltic Composition*, 2. New York: Interscience, pp. 623-688.

Kuno, H. (1968b) Origin of andesite and its bearing on the island arc structure. *Bull. Vulcanol.* v. 32, p. 141-176.

McBirney, A. R., Taylor, H. P. and Armstrong, R. L. (1987) Paricutin re-examined - a classic example of crustal assimilation in calcalkaline magma. *Contributions to Mineralogy and Petrology* 95, 4-20.

Meen, J. (1990) Evaluation of potassium content of basaltic magma by fractional crystallization: the effect of pressure. *Contributions to Mineralogy and Petrology*, 104(3), 309-331.

Metrich, N. and Wallace, P.J. (2008): Volatile abundances in basaltic magmas and their degassing paths tracked by melt inclusions. In “Minerals, Inclusions and Volcanic Processes”, K.D. Putirka and F.J. Tepley, III, eds., *Rev. Mineral. Geochem.*, Mineralogical Society of America, 69, 363–402.

Miyashiro, A. (1974). Volcanic rock series in island arcs and active continental margins. *American Journal of Science* 274, 321-355.

Moore, G., 2008. Interpreting H₂O and CO₂ Contents in Melt Inclusions: Constraints from Solubility Experiments and Modeling Reviews in *Mineralogy and Geochemistry* 69, 333-362.

Moore, G., and Carmichael, I.S.E. (1998) The hydrous phase equilibria (to 3 kbar) of an andesite and basaltic andesite from western Mexico: constraints on water content and conditions of phenocryst growth. *Contributions to Mineralogy and Petrology*, 130, 304-319.

Moore, G., Vennemann, T., Carmichael, I.S.E. (1998) An empirical model for the solubility of H₂O in magmas to 3 kilobars. *American Mineralogist*, 83, 36–42.

Newman S., Stolper E., and Stern R.J. (2000) H₂O and CO₂ in magmas from the Mariana arc and back arc system. *Geochem. Geophys. Geosys.*, 1999GC0 00027.

Nockdols, S.R. and Allen., R. (1953) Average chemical compositions of some igneous rocks-I. *Geochim. et Cosmochim. Acta.* v. 4, p. 105-142.

Nockdols, S.R. and Allen., R. (1954) Average chemical compositions of some igneous rocks-II. *Geochim. et Cosmochim. Acta.* v. 5, p. 245-285.

Nockdols, S.R. and Allen., R. (1956) Average chemical compositions of some igneous rocks-III. *Geochim. et Cosmochim. Acta.* v. 9, p. 34-77.

Osborn, E. F. (1959) Role of oxygen pressure in the crystallization and differentiation of basaltic magmas. *Australian Journal of Earth Sciences* 257(9): 609-647.

Papale, P., Moretti, R. and Barbato, D. (2006). The compositional dependence of the saturation surface of H₂O + CO₂ fluids in silicate melts. *Chemical Geology* 229, 78-95.

Pichavant, M., Macdonald, R. (2007) Crystallization of primitive basaltic magmas at crustal pressures and genesis of the calc-alkaline igneous suite: experimental evidence from St Vincent, Lesser Antilles arc. *Contrib Mineral Petrol* 154:535–558

Plechov, P.Yu., Shishkina, T.A., Ermakov, V.A., and Portnyagin, M.V., Formation Conditions of Allivalites, Olivine–Anorthite Crystal Inclusions, in *Volcanics of the Kuril–Kamchatka Arc*, *Petrologiya*, 2008, vol. 16, no. 3, pp. 1–30.

Portnyagin M, Hoernle K, Plechov P, Mironov N, Khununaya S (2007) Constraints on mantle melting and composition and nature of slab components in volcanic arcs from volatiles (H₂O, S, Cl, F) and trace elements in melt inclusions from the Kamchatka Arc. *Earth Planet Sci Lett* 255:53-69

Saito, G., Uto, K., Kazahaya, K., Shinohara, H., Kawanabe, Y., Satoh, H., 2005. Petrological characteristics and volatile content of magma from the 2000 eruption of Miyakejima Volcano, Japan. *Bull. Volcanol.* 67, 268–280.

Saito, G., Y. Morishita, and H. Shinohara (2010), Magma plumbing system of the 2000 eruption of Miyakejima volcano, Japan, deduced from volatile and major component contents of olivine-hosted melt inclusions, *J. Geophys. Res.*, 115, B11202.

Sakuyama, M. (1981). Petrological study of the Myoko and Kurohime volcanoes, Japan: crystallization sequence and evidence for magma mixing. *Journal of Petrology* 22, 553-583.

Shaw A.M., Hauri, E.H., Fischer, T.P., Hilton, D.R., Kelley, K.A., 2008. Hydrogen isotopes in Mariana arc melt inclusions: implications for subduction dehydration and the deep-Earth water cycle. *Earth Planetary Science Letters* 275, 138-145.

Shishkina, T.A., Botcharnikov, R.E., Holtz, F., Almeev, R.R., Portnyagin, M.V. (2010) Solubility of H₂O- and CO₂-bearing fluids in tholeiitic basalts at pressures up to 500 MPa. *Chemical Geology*, 277, 115–125.

Sisson, T.W., and Grove, T.L. (1993a) Experimental investigations of the role of H₂O in calc-alkaline differentiation and subduction zone magmatism. *Contributions to Mineralogy and Petrology*, 113(2), 143-166.

Sisson, T.W., and Grove, T.L. (1993b) Temperatures and H₂O contents of low-MgO high-alumina basalts. *Contributions to Mineralogy and Petrology*, 113(2), 167-184.

Sobolev, A.V., Chaussidon, M., 1996. H₂O concentrations in primary melts from island arcs and mid-ocean ridges: implications for H₂O storage and recycling in the mantle. *Earth Planet. Sci. Lett.* 137, 45–55.

Stoiber R.E., A. Jepsen, A. (1973), Sulfur dioxide contributions to the atmosphere by volcanoes, *Science* 182, 577–578.

Straub, S.M., Layne, G.D., 2003. The systematics of chlorine, fluorine, and water in Izu arc front volcanic rocks: implications for volatile recycling in subduction zones. *Geochim. Cosmochim. Acta* 67, 4179–4203.

Tamic, N., Behrens, H. and Holtz, F. (2001). The solubility of H₂O and CO₂ in rhyolitic melts in equilibrium with a mixed CO₂-H₂O fluid phase. *Chemical Geology* 174, 333-347.

Tatsumi, Y. and Suzuki, T. (2009) Tholeiitic vs Calc-alkalic Differentiation and Evolution of Arc Crust: Constraints from Melting Experiments on a Basalt from the Izu-Bonin-Mariana Arc. *Journal of Petrology*. V. 50, N. 8, p. 1575-1603.

Tatsumi, Y., and Kogiso, T. (2003) The subduction factory: its role in the evolution of Earth's crust and mantle. In R.D. Larter, and P.T. Leat, Eds. *Intra-Oceanic Subduction Systems: Tectonic and Magmatic Processes*, 219, p. 55-80. Geological Society of London, London.

Tatsumi, Y., Takahashi, T., Hirahara, Y., Chang, Q., Miyazaki, T., Kimura, J.-I., Ban, M. and Sakayori, A. (2008b). New insights into andesite genesis: the role of mantle-derived calc-alkalic and crust derived tholeiitic melts in magma differentiation beneath Zao volcano, NE Japan. *Journal of Petrology*, v. 49, N11, p. 1971-2008.

Taylor, S. R. and McLennan, S. M. (1985). *The Continental Crust: its Composition and Evolution*. Oxford: Blackwell, 312 p.

Toplis, M. J. and Carroll, M. R. (1995). An experimental study of the influence of oxygen fugacity on Fe–Ti oxide stability, phase relations, and mineral–melt equilibria in ferro-basaltic systems. *Journal of Petrology* 36, 1137–1170.

Tormey, D.R., Grove, T.L., and Bryan, W.B. (1987) Experimental petrology of normal MORB near the Kane Fracture Zone: 22o-25oN, mid-Atlantic ridge. *Contributions to Mineralogy and Petrology*, 96(1), 121-139.

Wager L.R. Deer W.A. (1939). "Geological investigations in East Greenland, Part III. The petrology of the Skaergaard intrusion, Kangerdlugssuaq, East Greenland." *Meddelelser om Gronland* 105: 1-352.

Wagner, T.P., Donnelly-Nolan, J.M., and Grove, T.L. (1995) Evidence of hydrous differentiation and crystal accumulation in the low-MgO, high-Al₂O₃ Lake Basalt from Medicine Lake volcano, California. *Contributions to Mineralogy and Petrology*, 121(2), 201-216.

Williams S.N., Schaefer S.J., Calvache M.L., Lopez D. (1992), Global carbon dioxide emission to the atmosphere by volcanoes, *Geochim. Cosmochim. Acta* 56, 1765–1770.

Yang, H.J., Kinzler, R.J., and Grove, T.L. (1996) Experiments and models of anhydrous, basaltic olivine-plagioclase-augite saturated melts from 0.001 to 10 kbar. *Contributions to Mineralogy and Petrology*, 124(1), 1963-1973.

Zelenski M, Taran Y (2011) Geochemistry of volcanic and hydrothermal gases of Mutnovsky volcano, Kamchatka: evidence for mantle, slab and atmosphere contributions to fluids of a typical arc volcano. In: Inguaggiato S, Shinohara H, and Fischer T (eds) *Geochemistry of volcanic fluids: a special issue in honor of Yuri A. Taran*. *Bull Volcanol* 73(4): 373–394

Chapter I.

Magma storage conditions of
Mutnovsky volcano: Natural
observations and experimental
constraints

CHAPTER I. MAGMA STORAGE CONDITIONS OF MUTNOVSKY VOLCANO: NATURAL OBSERVATIONS AND EXPERIMENTAL CONSTRAINTS

1. GEOLOGICAL OVERVIEW

1.1. A summary of previous investigations: geology, eruptive history, petrology and geothermal fields of Mutnovsky volcano

The Kuril-Kamchatkan island arc is one of the most active volcanic zones on Earth. Two main volcanic zones can be distinguished (Fig. 1-1): The Sredinny Range (SR) and the Eastern volcanic front (EVF) located south of the Bering- Alpha Fault Zone. The EVF can be subdivided into a northern, central and southern segment. The former is hosting Central Kamchatkan Depression (CKD) with famous active volcanoes of the Klyuchevskoy group. The other two are separated by the Petropavlovsk Fault zone. The southern part of the EVF continues into the northern Kurile arc situated due south of the Kamchatkan peninsula. Most of the active Kamchatkan volcanoes are found in the EVF that is formed largely parallel to the Kurile-Kamchatkan trench where the Pacific plate is subducted with ~ 7.8 cm/y (Gorbatov et al., 1997, 1999). Along the volcanic front of southern Kamchatka the volcanic centers are situated ~ 90 – 110 km above the Wadati-Benioff Zone, whereas the rear-arc volcanoes are located above slab surface depths ranging from ~ 100 – 220 km (Fig. 1-1).

The Holocene Mutnovsky stratovolcano is located in the southern part of the Kamchatka peninsula within the Eastern Volcanic Front (elevation 2323 m; coordinates $52^{\circ} 27' 10.8''$ N, $158^{\circ} 11' 42''$ E). It is situated approximately ~ 100 km above the surface of the subducting slab (Gorbatov et al., 1997; Duggen et al., 2007) in a frontal arc setting in contrast to adjacent (~ 15 km westward) rear-arc Gorely volcanic center (~ 120 km above the slab). (Fig. 1-1, 2).

The formation of Mutnovsky started in the middle-late Pleistocene on the basement composed of Paleogene – Middle Pleistocene volcanogenic-sedimentary strata (Active volcanoes..., 1991). Mutnovsky has a complex volcanic structure consisting of four main stratocones (Mutnovsky I - IV) which form a ridge in north-western direction (Fig. 1-3). Each new stratocone was formed continuously after the attenuation of the previous one following the main sequence: growth of the cone – formation of the summit caldera – growth of the intracaldera structure – attenuation of the volcanic activity with subsequent shifting of a discharge channel and repeating of the scheme (Selyangin, 1993).

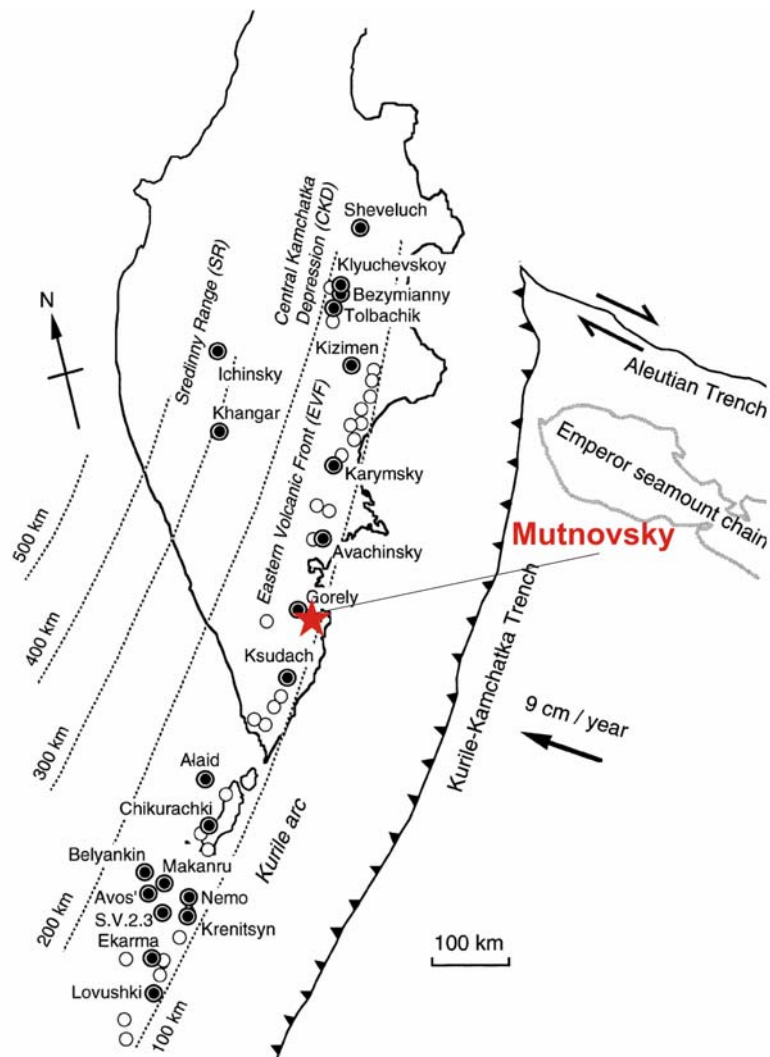


Fig. 1-1. Tectonic structure of the Kurile–Kamchatka arc (after Ishikawa et al., 2001) with location of Mutnovsky volcano. Dot-lines show isobaths for the top of the deep seismic zone (Wadati-Benioff zone) taken from Tatsumi et al. (1994).

The volcanic products of Mutnovsky are presented by a wide spectrum of volcanic rocks ranging from basalts to rhyodacites with the strong predominance of basaltic lavas (Selyangin, 1993; Martynov et al., 1995; Chashchin et al., 2011). The oldest Mutnovsky-I (Q_3^2) is composed of basalts and basaltic andesites with a small amount of andesites and dacites. Mutnovsky-II (Q_3^3) mostly composed of basalts with rare andesites and rhyodacites. Mutnovsky-III (Q_3^4) is composed of rocks ranging from basalts to andesitic dacites with prevailing basalts. The youngest, fourth stage of volcanic activity Mutnovsky-IV ($Q_3^4 - Q_4$) has started in the early Holocene and is characterized by eruptions of exclusively mafic lavas (basalts and basaltic andesites) (Selyangin, 1993).



Fig. 1-2. A general view of the north-western slope of Mutnovsky volcano (foto of M. Zelensky) and the crater of Mutnovsky volcano with emissions of hydrothermal fluids

Basalts and basaltic andesites are the most abundant rock species within the whole history of the Mutnovsky volcanic activity. According to the literature, Mutnovsky mafic rocks may be divided into 3 petrographic groups, containing various set of main phenocrysts: (1) Plag-CPx-Ol-bearing, (2) Plag-bearing and (3) Plag-Ol \pm CPx-bearing basalts. First two groups are more typical for the oldest stages of the volcanic activity (Mutnovsky-I), while the third association (with scarce CPx phenocrysts) is typical for the current stage (Mutnovsky-IV) (Chashchin et al., 2011).

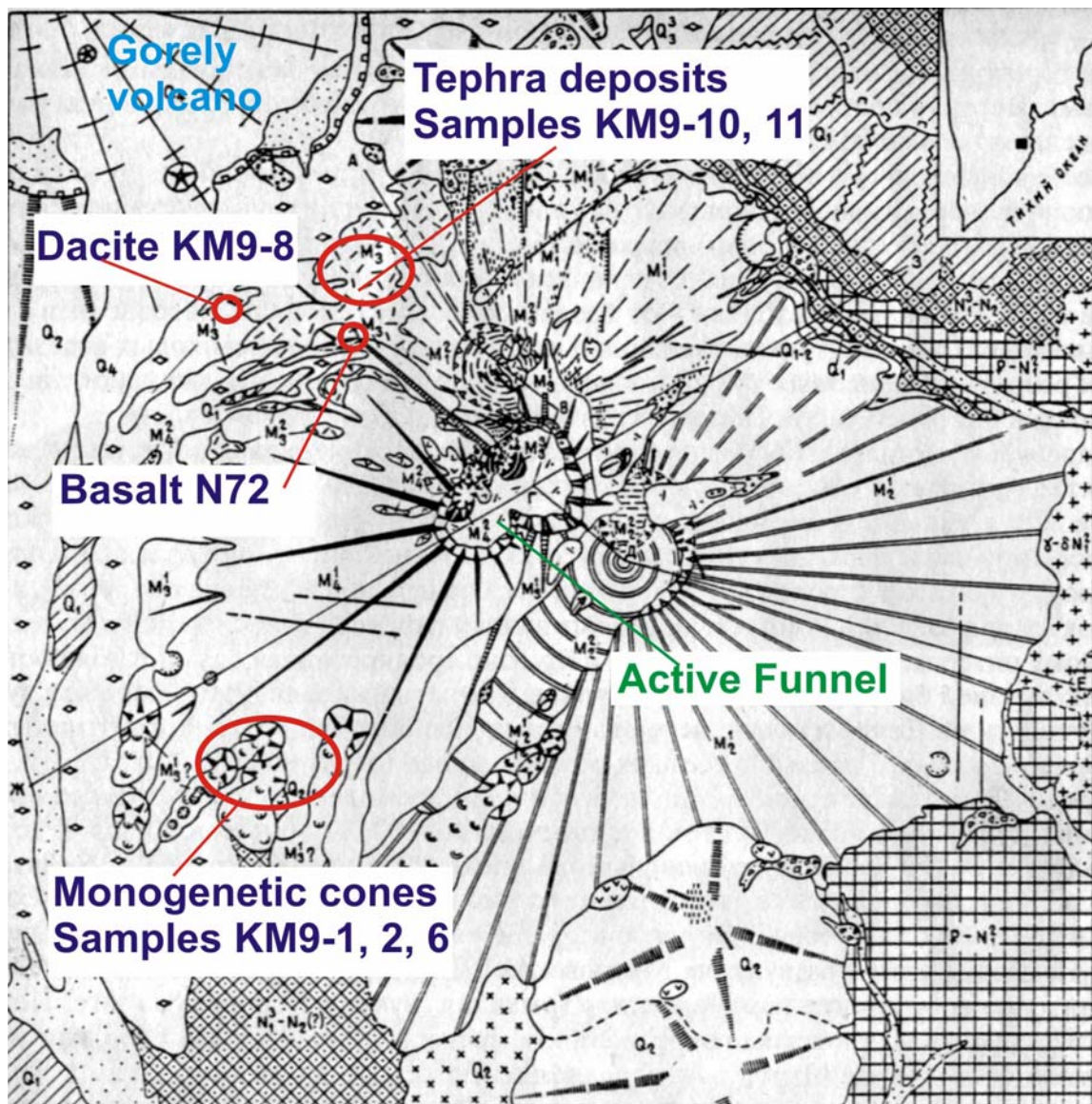


Fig. 1-3. Geological scheme of Mutnovsky volcano (after Selyangin, 1993) with localities of studied samples

The eruptive products of Mutnovsky represent classical low to medium-K high-Al island arc tholeiitic series of rocks and have only small variations of the petrochemical and petrographical features with time (Chashchin et al., 2011). In general, mafic eruptive products of the stage Mutnovsky-I can be referred to low-K high-Al ($al^*=1.15-1.80$, where $al^*=Al_2O_3/(FeO+Fe_2O_3+MgO)$) basalts and andesites with tholeiitic characteristics (enrichment in FeOtot). Whereas basalts of Mutnovsky-IV stage can be characterized as low- to moderate-K moderate-Al ($al^*=0.85-1.04$) basalts and are located close, or on the border between tholeiitic and calc-alkaline series on Miyashiro diagram (Fig. 1-4) (Chashchin et al., 2011).

The younger basalts are slightly enriched in MgO and CaO but contain less SiO₂, TiO₂, Al₂O₃ and Na₂O in comparison to basalts of the older stages of activity (Chashchin et

al., 2011). The geochemical features of the Mutnovsky magmas (typical for island arcs enrichment of fluid-mobile elements relative to less fluid-mobile or immobile, negative anomalies for Zr and Hf and weak Ti- and Eu-anomalies, $\delta^{18}\text{O}_{\text{Cpx}}$ slightly lower than in MORBs) has been attributed to the combination of two important processes in the zone of magma generation - partial melting in the mantle wedge and dehydration of the subducted sediments (Duggen et al., 2007).

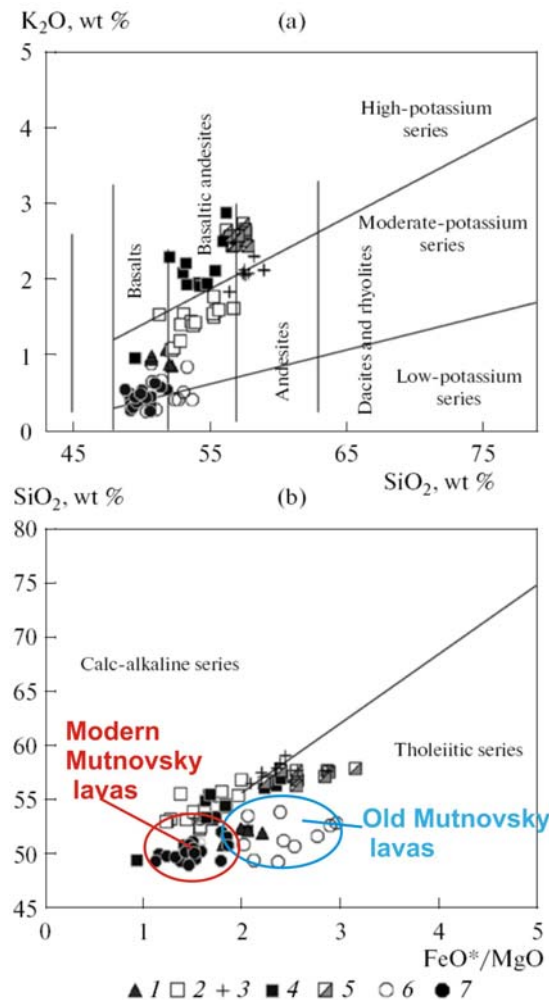


Fig. 1-4. (a) $\text{SiO}_2\text{-K}_2\text{O}$ and (b) $\text{SiO}_2\text{-FeO}^*/\text{MgO}$ for the rocks of the Gorely and Mutnovsky volcanoes (after Chashchin et al., 2011). **(1-5) Gorely volcano:** (1) basalts of the early postcaldera complex, (2) basalts and basaltic andesites of the three first cycles of the activity of modern edifice, (3) andesites of three first cycles of the evolution of modern edifice, (4) basalts and basaltic andesites of the two last cycles of the modern edifice, (5) andesites of the two last cycles of the formation of modern edifice; **(6-7) Mutnovsky volcano:** (6) basalts of the Mutnovsky-I old edifice; (7) basalts of the Mutnovsky-IV modern edifice.

The recent activity of the Mutnovsky volcano related to the current position of the magmatic conduit is located in the Active Funnel (Aktivnaya Voronka), which was formed approximately 1200-1300 years ago (Melekestsev et al., 1987). Active Funnel was the center of a number of historical eruptions (last eruptions occurred in 1960-1961, 2000 and 2007).

Exceptionally intensive and constant fumarolic activity in Mutnovsky crater(s) is observed during at least last 30 years (Selyangin, 1993). There are several fumarolic fields with high-temperature gases within the crater: Active Funnel (up to 620°C), Upper Field (more than 300°C) and Bottom Field (up to 150°C) (Bortnikova et al., 2007; Zelensky&Taran, 2011). Moreover, there are several high-temperature (about 300°C) geothermal fields located about 8 km to the north-east from Mutnovsky volcano (Dachny and Verkhne-Mutnovsky Fields). Economical exploration of these fumarolic fields was started in 1960-70s (Vakin, 1976). Since 1999 and 2002 respectively, Verkhne-Mutnovsky (12 MWe) and Mutnovsky (50 MWe) power plants were started to provided about one-third of electrical power for Petropavlovsk-Kamchatsky, the biggest city in Kamchatka (Kiryukhin, 2006; Eichelberger et al., 2009).

Hydrogeological studies of the Mutnovsky geothermal field(s) demonstrate that the plane of the main production zone of these fields intersects the feeding structure of the Mutnovsky volcano (Kiryukhin et al., 2005). The glacier inside the volcano's crater may serve as one of the source(s) of *meteoric* waters. A shallow hot magma body was proposed to be existed beneath the Northern Mutnovsky volcano-tectonic zone and may act as sources of heat and *magmatic* fluids in Mutnovsky geothermal fields (Kiryukhin, 2006). The long-term and powerful emanations of gases in the main crater of Mutnovsky volcano also require the presence of a shallow hot magma reservoir which should be fed by fresh portions of magma coming from the deeper levels (Selyangin, 1993).

Determination of the location(s) and estimations of the depth(s), sizes and shape of magmatic bodies below Mutnovsky volcano have been already performed during last decades of intense (1) geophysical observations (magneto-telluric sounding, seismic methods) (Grib, 1989; Active volcanoes..., 1991; Fedotov et al., 2005), (2) geochemical studies of the hydrothermal system (fluid composition, isotope data, volumes of degassing, changes in temperatures, Hg concentration) (Trukhin et al., 1986, book; Taran et al., 1992 (engl, JVGR); Rychagov et al., 2009; Bortnikova et al., 2007) and (3) numerical modeling (Fedotov et al., 2005; Utkin et al., 2005; Potapov, 2002; Nurmukhamedov et al., 2010 engl). There are many indications on the presence of the shallow (1 to 10 km depth) hot magma body (or bodies) with diameter(s) of 1 to 3 km below Mutnovsky volcano, that serve as a «feeding system» for the active hydrothermal system of Mutnovsky and is responsible for the current volcanic activity. According to the numerical modeling performed by Fedotov et al. (2005) and Utkin et al. (2005) there is a shallow magma chamber below Mutnovsky IV with following parameters: elevation of -1.7 km from the

sea level (about 3 km depth from the top of the volcano), radius of 1.5 km, temperatures of 950-1250°C; heat capacity of the chamber and host rocks are estimated as $0.3 \cdot 10^{20}$ J.

Extremely high concentrations of Cr, Ni, Co, Ti, V, B and Sr in hot springs in Active crater could be extracted from underlying basalts by oxidized high-temperature gases formed by mixing of surface waters with hot magmatic fluids which requires presence of a shallow magma reservoir (Bortnikova et al., 2007). Based on the detailed study of geochemistry of volcanic and hydrothermal gases in fumarolic fields in Mutnovsky crater Zelensky & Taran (2011) suggested the presence of at least two separate shallow magma bodies below Mutnovsky crater, responsible for different geochemical diversity of existing fumarolic gases (Fig. 1-5). The hottest fumaroles of Active Funnel require the presence of large hot convecting magma reservoir emitting magmatic gas(es) with typical subduction-related signature (Zelensky&Taran, 2011). The hydrothermal system of the Bottom Field is probably fed by a separate magma body with „rear-arc“ volatile characteristics and contribution of the volatiles mostly from the mantle wedge with weaker slab favour. Probably this body contains crystallizing and degassing basaltic magma which was observed during the last eruptions of Mutnovsky volcano (Zelensky & Taran, 2011).

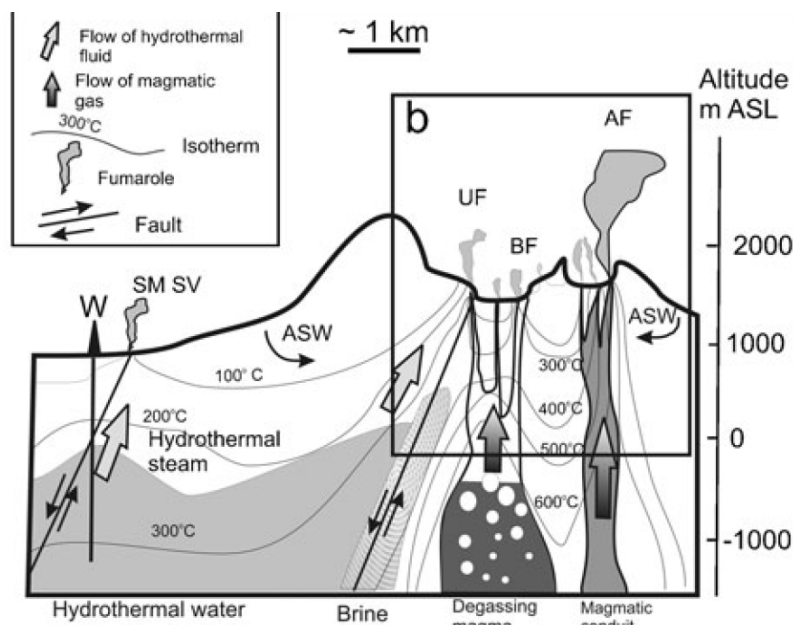


Fig. 1-5. A conceptual model of the volcano-hydrothermal system of Mutnovsky presented by Zelensky and Taran (2011). A cross-section is drawn through Mutnovsky crater (appx SW-NE) and the Mutnovsky edifice (appx N-S) showing temperature distribution and main fluid flows. AF, BF, UF are Active Funnel, Bottom and Upper Fields, respectively. SM-SV denotes “Severo-Mutnovsky steam vents”, W—geothermal well

It should be emphasized that only few petrological attempts were made for the evaluation of magma storage conditions beneath Mutnovsky volcano. Recently Chashchin

et al. (2011) performed modeling of the phase equilibria using primitive Mutnovsky basaltic melts (9-10 wt.% MgO) and utilizing the COMAGMAT model (Ariskin and Barmina, 2004). They found that natural crystallization sequence and compositions of minerals can be reproduced in the course of fractional crystallization at 100-200 MPa, with 0.25-0.9 wt.% H₂O in initial melt, and at redox conditions ranging between QFM-0.5 to QFM+0.9. The sequence of crystallized minerals was found to be as follows: Plag (1370-1200°C) – Ol+Plag (1188-1139°C), Ol+Plag+CPx (1134-1025°C) with the final appearance of OPx and Mt at lower temperatures (below 1100°C). Temperatures of plagioclase crystallization were found to be similar to those determined by homogenization of melt inclusions hosted in plagioclase (Chashchin et al., 2011). The estimates of redox conditions were supported by data from high-temperature gas-chromatography, indicating that in Mutnovsky basalts at 1100°C fO_2 varies between -12.5 and -13.3 log units (23 Chashchin et al., 2001). It should be noted however, that the natural LLD (liquid line of descent - the proxy of residual melt evolution) was not reproduced by the model mostly due to the low water concentrations assumed in the study of (Chashchin et al., 2011), which was resulted in enhanced plagioclase precipitation along Ol+Pl cotectic crystallization, reminiscent the dry MORB magma evolution. It seems that petrochemical trends of Mutnovsky volcanics require the presence of Cpx in solid assemblage from the earlier stages of magma differentiation (parental melts should be saturated or very close to saturation with Ol+Pl+Cpx mineral assemblage).

1.2 Mutnovsky Scientific Drilling Project (MSDP)

In 2006 Mutnovsky volcano was proposed as a possible object for the scientific drilling (ICDP - international continental drilling program). The scientific ICDP proposal was aimed at investigation of the interaction between magmatic and hydrothermal systems (Kiryukhin, 2006; Eichelberger et al., 2009). It was planned to (1) drill a borehole within the transition zone between the active craters of Mutnovsky and the geothermal production field (Fig. 1-6); (2) to sample rock cores and fluids as well as (3) to conduct a variety of surface investigations in the area of the volcano (surface electromagnetic methods, magneto-telluric soundings, seismic and geodetic observations) (Eichelberger et al., 2009). The proposed project included investigations of aqueous geochemistry of the system (element and isotopic composition of surface and borehole fluids), core petrography, geochemistry and physical parameters (density, porosity, gas permeability, pore space structure, geo-mechanical characteristics, thermal and magnetic properties). Main objectives of the scientific drilling on Mutnovsky were: (1) the identification of magmatic

components in fluids proximal to the conduits and their genetic relationship to fluids in the producing system; (2) interpretation of magma evolution and the history of Mutnovsky volcano; (3) determination the overall volatile and thermal budget of the volcano (Kiryukhin, 2006). The authors of the drilling project also proposed more challenging subsequent stage, assuming that drilling conditions after the first stage is favorable. They assumed to penetrate the Mutnovsky's active conduit and to obtain direct probes of the magmatic magma chamber material (Eichelberger et al., 2009). Unfortunately due to organization and financial problems the Mutnovsky Scientific Drilling was not started yet.

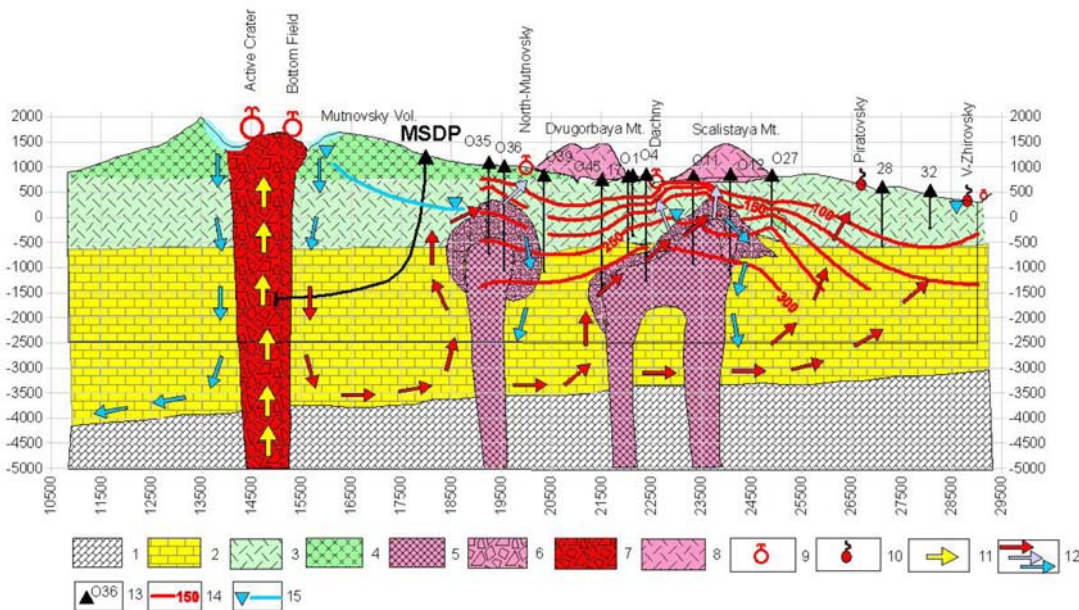


Fig. 1-6. Cross-section and conceptual hydrogeological model of the Mutnovsky volcano – Mutnovsky geothermal field system (after Kiryukhin and Eichelberger, 2006: 1 – Crystal basement, 2 – Cretaceous basement and Miocene sandstones, 3- Neogene volcanogenic and sedimentary rocks, 4 – Mutnovsky stratovolcano, 5 – Diorite intrusions, 6 – Diorite contact zone, 7 – Mutnovsky volcano magmatic system, 8- Acid extrusions, 9- fumarole fields, 10 – Hot springs, 11- Magma and magmatic fluids, 12 – Hydrothermal fluids, 13 – Geothermal wells, 14 – Temperature distribution (Mutnovsky geothermal field), 15 – Water levels in Mutnovsky hydrothermal system (referenced to m.a.s.l.). MSDP – potential drilling site for the Mutnovsky Scientific Drilling Program

The current work was conducted as DFG project in the frame of above mentioned Mutnovsky ICDP initiative. The obtained results provide new petrological data which can be used by other research groups, if the Mutnovsky drilling program will be successful in future. The samples used in this study (see below) have been collected by author during field campaign in summer 2009 (Fig. 1-3). **The sample of primitive basalt N72 used as starting material in our experimental studies** was provided by M. Portnyagin and was previously geochemically characterized in (Duggen et al., 2007).

2. METHODS OF INVESTIGATION

2.1. Studied natural samples

This work is mostly focused on experimental simulation of magma differentiation processes beneath Mutnovsky volcano and therefore we did not plan detailed analytical study of mineralogy and petrography of volcanic lavas of Mutnovsky volcano. This information is provided by a number of previous investigations (e.g. Martynov, Chashchin, 1989; Frolova et al., 2001; Hetchikov et al., 2001; Chashchin et al., 2011). However, in the course of the study we studied melt inclusions hosted in olivine phenocrysts. Melt inclusions are unique probes of unmodified magmas which provide very important information on major-element compositions of primitive magmatic liquids and pristine (undegassed) concentrations of dissolved volatiles such as H₂O, CO₂, S, Cl (Danyushevsky et al., 2002). Very often melt inclusions collected in slowly cooled lavas are partly crystallized or exhibit post-entrapment modification. Melt inclusions which presumably preserve initial volatiles concentrations can be only found in tephra which is the best material for studies of melt inclusions: it is formed by rapid magma ascent and fast cooling during explosive volcanic eruptions. Basaltic melt inclusions enclosed in phenocrysts of tephra undergo fast quench to almost clear glass and therefore do not require re-homogenization via heating experiments which may affect initial melt composition. For this purpose samples from **tephra deposits** were collected on the north-western slope of Mutnovsky (**samples KM9-10 and KM9-11**; N52°29,245', E158°08,244', h=1115m) (Mutnovsky III) (Fig. 1-3). Tephra samples contain olivine and plagioclase phenocrysts, rare clinopyroxene phenocrysts and volcanic glass. According to the bulk rock analyses, studied tephra have composition of basaltic andesites (Table 1-2).

In addition, classical **petrographical and mineralogical study of three representative basalts (KM9-1, KM9-2, KM9-6) and one dacite (KM9-8)** were performed (Table 1-2). Basaltic samples from monogenetic cones on the south-western slope of the volcano (N52°25,201', E158°06,442', h=816) were primarily collected in attempt to find most primitive Mutnovsky basalts and to obtain melt inclusions in these samples. According to the geological studies, they were formed during third stage of Mutnovsky activity (Mutnovsky-III) in Late Pleistocene (age Q₃⁴, M₃¹) (Selyangin, 1993) (Fig. 1-3). These lavas are represented by porphyritic massive lava (KM9-1), phryic vesicular lava (KM9-2) and subaphyric porous lava (KM9-6). KM9-1 and KM9-2 are characterized by the presence of different proportions of Plag, Ol and subordinate CPx phenocrysts, whereas subaphyric basalt KM9-6 has no phenocrysts and contain only Plag

subphenocrysts in the groundmass composed of Ol+Pl+Cpx+Mt. These samples provide detailed information on natural mineral associations, mineral compositions and are used for comparisons with their experimental counterparts. The sample of two-pyroxene-plagioclase dacite (KM9-8) was collected from the lava flow on the north-western slope of Mutnovsky (age $Q_3^4 M_3^1$; N52°29,134', E158°06,357', Fig. 1-3) and represents the differentiated probe of Mutnovsky liquid lines of descent. Compositions and proportions of phases were also determined in Ol-Plag-(±CPx)-bearing basalt N72 used as a starting composition for our crystallization and solubility experiments. Major-element bulk rock compositions, phase proportions and estimations of compositions of residual melts of the studied samples (N72, KM9-1, KM9-2, KM9-6, KM9-10, KM9-11) are reported in Table 1-2). The mineralogy and petrography of the studied samples are described in a paragraph 3.1.1. in more details.

2.2. Methods applied for melt inclusions

Preparation of melt inclusions (naturally quenched)

Olivine phenocrysts with sizes of 0.5 to 1 mm containing naturally quenched melt inclusions were hand-picked from the natural tephra material (samples KM9-10, 11). Grains were mounted with a mixture of epoxy Araldite D and hardener HY956 (proportion 5:1) into an Al-ring of inch-diameter. Mount was polished with different abrasive materials (diamond suspensions and pastes) until any of inclusions was opened on the surface of one of the grains. The grain containing the opened inclusion was removed from the mount with a heated needle and placed into acetone. Grains with opened inclusions were then re-mounted together into a Al-ring using the same mixture of epoxy and hardener and polished with 0.05 μm diamond paste to be analyzed for major-elements with Electron Microprobe and for H₂O and CO₂ with SIMS.

Re-homogenization experiments on melt inclusions

Re-homogenization experiments were performed on melt inclusions in olivine with an aim to dissolve volatiles (H₂O and CO₂) from shrinkage bubbles back into melt. Olivines containing melt inclusions were placed into AuPd capsules welded on the one site and squeezed with pliers on the second site to allow access of Ar during the experiment and therefore prevent oxidation of grains. Capsules were placed into an internally heated pressure vessel (paragraph 2.3.) at 200 MPa, heated up to 1150°C, held at this temperature for 5 minutes and subsequently quenched with a cooling rate about 150°C/sec. The re-heated melt inclusions were opened to the surface using the same procedure as naturally

quenched. On the last stage of polishing corundum powder was used to prevent contamination of the surface with carbon.

The temperature for the re-heating experiments was estimated to be slightly above the liquidus for the basaltic glass containing 2 wt.% H₂O with an aim to dissolve all daughter crystal phases or olivine precipitated on the walls of inclusion during cooling of tephra after eruption. It seems to be that the chosen temperature of 1150°C was relatively high and caused dissolution of some amount of olivine-host into melt inclusion. This resulted in an increase of $Kd^{Fe-Mg}_{Ol-Melt}$ in re-heated melt inclusions to values of 0.33 – 0.46, which are higher than $Kd=0.3$ estimated as olivine-melt equilibrium (Danyushevsky et al., 2000). Thus major-element compositions of re-heated melt inclusions (as well as naturally quenched) were recalculated to the equilibrium with olivine-host (paragraph 3.1.3.).

2.3. Phase relation experiments

Experimental strategy

Phase relations in the Mutnovsky basalt were studied as a function of pressure, temperature, a_{H_2O} and fO_2 . Two sets of experiments were conducted at pressures of 100 and 300 MPa in a range of temperatures from 950 to 1200°C at 300 MPa and 1000 to 1200°C at 100 MPa. These conditions correspond to the supposed depth(s) of magma chamber(s) below Mutnovsky volcano (1-10 km). The temperature interval 950-1200°C covers conditions from above-liquidus to below-solidus for the studied basalt composition depending of H₂O content in the melt. Experiments were performed at every 25°C temperature step.

In performed experiments water activity (a_{H_2O}) was set for every capsule by addition of mixture of H₂O and CO₂ (as Ag₂C₂O₄) in different proportions and usually varied between $a_{H_2O}=0$ and 1 at the same pressure and temperature to determine effect of water on phase assemblages and liquidus temperatures of mineral phases.

Redox conditions in experiments were dependent on a_{H_2O} inside the capsule and varied between $NNO+2.6$ in H₂O-saturated experiments ($a_{H_2O}=1$) to $NNO+0.7$ in anhydrous experiments ($a_{H_2O}=0$). This redox interval is a typical for island-arc magma systems (e.g.: Ballhaus, 1993; Parkinson and Arculus, 1999).

Starting material and capsule preparation

As a starting composition for all the performed phase relations experiments we have used basalt from the last stage of Mutnovsky activity (sample N72 provided by M. Portnyagin and described in Duggen et al., 2007). It was the most primitive composition (7

wt.% MgO and 50 wt.% SiO₂) of available samples at the time of performing experiments (Table 1-2). The same sample was also used for studies of solubility of mixed H₂O- and CO₂-bearing fluids in basaltic melts at pressures 50 to 900 MPa (Chapters 2, 3 of this work; Shishkina et al., 2010; Shishkina et al., 2012 submitted).

Bulk rock was ground into a powder and melted in Pt-crucible at 1600°C and air-conditions for 3 hours with subsequent quenching of the melt. The glass was crushed into a powder and melted additionally for 0.5 hours at the same conditions. The resulting glass was ground and mixture of two grain size fractions (0.125 m and 0.250) was used for filling the capsules with an aim to decrease the free volume between grains. The composition and homogeneity of the starting glass was checked by electron microprobe.

Experiments at temperatures below 1050°C were performed in golden capsules, at higher temperatures – in Au₈₀Pd₂₀-capsules. Every capsule (about 15 mm long and 2.6 mm inner diameter) was filled with 30-50 mg of basaltic glass powder and different amounts of distilled water and silver oxalate (as a source of CO₂) in proportions required for obtaining XH₂O^f planned in the run.

Capsules were not pre-saturated with Fe. As it was shown in the earlier study with the same starting composition (Shishkina et al., 2010) in a same range of redox-conditions, the only significant Fe-loss (up to 45 rel.%) from the melt into the capsule-walls was detected in nominally dry runs, with aH₂O=0-0.1. In all other runs with higher aH₂O, Fe-loss was less than 6 rel.%.

Experimental technique

The experiments were conducted in an internally heated pressure vessel (IHPV) equipped with a rapid-quench facility (Berndt et al., 2002) with Ar-gas as a pressure medium. The total pressure in the vessel was recorded continuously during the experiments with a calibrated Burster Type 8221 digital pressure transducer (pressure uncertainty ±1 MPa). The variations of pressure during the experiments were less than 5 MPa. Temperature in the runs was controlled by four S-type thermocouples (Pt-Pt₉₀Rh₁₀). Temperature oscillations were within ±10°C and temperature gradient along the capsules was less than 10°C.

Four to five capsules with starting material and different XH₂O_{ini} were run simultaneously. Duration of the experiments varied between 2 and 168 hours depending on the temperature. According to the previous experimental studies with basaltic compositions, such run durations are long enough to reach equilibrium (for refs. see paragraph Attainment of equilibrium). In the end of the run capsules were quenched rapidly by falling down to a cold zone of the vessel after melting the holding Pt-wire by electrical

shot (Description of the rapid-quench device is given in Berndt et al., 2002). The quench rate is about 150°C/sec.

The intrinsic redox (fO_2) conditions in the vessel at $aH_2O=1$ are on the level of $fO_2=NNO+2.6$. The fO_2 in every run (capsule) is controlled by the reaction $1/2O_2+H_2=H_2O$ and therefore is dependent on aH_2O inside the capsule (see following paragraph).

Determination of fluid composition after experiment

Fluid composition (mole fractions of H_2O ($X^{fl}H_2O$) and CO_2 ($X^{fl}CO_2$)) after experiments was determined using a conventional weight-loss procedure. A detailed description of the method can be found in Chapter 2 of this work. The results of fluid composition determination are presented in Appendix. Table A-1-4.

Determination of redox conditions

The oxygen fugacity prevailing in each individual capsule is dependent on water activity because it is controlled by the equilibrium reaction of water dissociation ($H_2 + 1/2 O_2 = H_2O$) inside the capsules. The fO_2 was calculated for each experiment using the expression $\log fO_2^{capsule} = \log fO_2^{intrinsic} + 2\log (aH_2O)$ (e.g. Botcharnikov et al., 2005b). The intrinsic redox conditions in the used IHPV ($fO_2^{intrinsic}$) at $aH_2O=1$ are close to $\log fO_2 = NNO+2.6$ (the oxygen fugacity is higher than that buffered by the Ni/NiO assemblage by 2.6 orders of magnitude) according to the recent determinations reported by Schuessler et al. (2008).

Water activity can be determined in two ways: (1) by determination of XH_2O in fluid inside a capsule and using activity coefficients after Aranovich and Newton (1999) and molar volumes of pure H_2O after Pitzer and Sterner (1994); (2) by model of Burnham (1979) using H_2O concentration in residual melt.

The calculated values of fO_2 for each experiment are reported in Appendix. Table A-1-4.

Attainment of equilibrium

Special procedures (i.e. reversal experiments) for testing the attainment of equilibrium in the crystallization experiments were not performed in this study. But the textural and compositional criteria can be used to prove that equilibrium in the system was achieved.

Duration of runs varied between 24 and 72 hours depending on a run temperature, the longest experiments were performed at lower temperatures where kinetics of element

diffusion is slower. Such experimental durations are long enough to reach equilibrium in low-viscous basaltic systems, as was proved by previous experimental studies (e.g. Sisson and Grove, 1993 a, b; Barclay and Carmichael, 2004; Baker and Eggler, 1987; Bartels et al., 1991; Di Carlo et al., 2006). Crystallization kinetics is much faster in presence of H₂O.

Another proof of attainment of equilibrium is morphology of crystals in run products: the observed crystals in performed experiments have euhedral shapes (tabular, equant or elongated) typical to these mineral species (Fig. 1-19). No quench forms are observed. Mineral phases are distributed homogeneously within a capsule.

Homogeneous composition of every phase (glass or mineral) for a single run was proved by multiple analyzes (3 to 10 times in different points for every phase in single run). Compositions of phases vary regularly (logically) with changes in temperature or aH₂O (fO₂).

Replicate runs were performed for several P-T-aH₂O-conditions and phase assemblages and phase compositions were reproduced.

The important parameters that may characterize equilibrium are distribution coefficients (K_d) of chemical compounds between pair of coexisting phases. In studied basaltic system distribution of Fe and Mg between melt and olivine can give an important information. In performed runs $Kd^{Fe-Mg}_{Ol-Melt}$ varied between 0.3 and 0.5 (Appendix. Table A-1-4).

Only values of $Kd^{Fe-Mg}_{Ol-Melt}$ below 0.33 can be assigned to equilibrium while higher numbers may point to the disequilibrium crystallization. Usually high $Kd^{Fe-Mg}_{Ol-Melt}$ are observed in runs with high H₂O contents. One of the explanations is that too high $Kd^{Fe-Mg}_{Ol-Melt}$ could be attributed to the wrong estimation of Fe²⁺/Fe-t in the melts. Proportion of Fe²⁺ together with fO₂ values was calculated by model of Kress and Carmichael (1991) using aH₂O determined by model of Burnham (1979) from H₂O concentrations in residual experimental glasses. It seems to be that model of Burnham (1979) overestimates aH₂O in melts (especially in hydrous) inducing overestimations of fO₂ (more oxidized conditions than indeed) and underestimations of Fe²⁺ in melts. Subsequently $Kd^{Fe-Mg}_{Ol-Melt}$ have too high values. In this study we have used data on phase compositions obtained from runs with high values of $Kd^{Fe-Mg}_{Ol-Melt}$, though the real reason of such high estimations still must be clarified.

2.4. Analytical methods

2.4.1. Electron microprobe

Major-element compositions of the minerals in natural samples (thin-sections), glassy inclusions in phenocrysts, as well as mineral phases and residual glasses in experimental products and air-melted glasses representing whole-rock compositions of studied natural samples from Mutnovsky (including starting composition for phase relations experiments) were analyzed by electron microprobe Cameca SX100. Mineral phases were analyzed with focused beam, 15 keV acceleration voltage and 15 nA beam current. Glasses were analyzed with defocused electron beam (5 to 20 μm diameter) 15 keV accelerating voltage and 4 nA beam current. Sodium and potassium were analyzed first to minimize alkali-loss. Concentrations of S, Cl and F in melt inclusions were determined together with major-elements using the setting with 40nA beam. Mineral and glass standards were used for calibration of obtained analyses.

Three to ten measurements of every phase in experimental products for every run were made to check for the homogeneity of phase compositions. Compositions of glasses prepared from the remelted rock-powders of studied natural samples (KM9-1, 2, 6, 8, 10, 11) were determined as average of at least 15 analyzes.

2.4.2. Determination of H₂O content in experimental glasses

Different methods were applied for the determination of concentrations of H₂O concentration in residual glasses in run products depending on degree of crystallinity and sizes of glass areas.

1) Karl-Fischer Titration (KFT) was used for determination of H₂O-content in above- or close- to liquidus runs performed at 300 MPa (runs N1-5 at 1150°C and N23-27 at 1200°C). The detailed description of the method is given in Chapter 2 of this work; Shishkina et al., 2010).

2) Fourier-transform infrared spectroscopy (FTIR) was applied for run products with relatively low crystallinity where glass areas could be visually found in microscope and diameter of spot for the analysis was adjusted to the size of glass area. Both mid-infrared (MIR) and near-infrared (NIR) ranges were used depending on H₂O-concentration in the glass.

The use of the method is described in details in Chapters 2 and 3 of this work. Molar absorption coefficients for basaltic glasses determined by Shishkina et al. (2010)

were used for calculations: 60 g/(mol*1) for 3550 cm⁻¹ band of H₂O, 0.79 g/(mol*1) for 4500 cm⁻¹ band (hydroxyl group) and 5200 cm⁻¹ band (molecular water).

3) „By-difference“ method with Electron Microprobe

In many cases the crystallinity of run products was too high to perform IR-measurements and therefore H₂O concentrations in residual glasses could be estimated only with „by-difference“ method using electron microprobe analyses. H₂O content is determined as 100 – total of major-element analytical total (wt.%). It is well known that this method of determination of H₂O content is not very precise and accurate (e.g. Devine et al., 1995). To improve accuracy and estimate an error of H₂O determination a set of standard basaltic glasses with known H₂O contents was analyzed during every analytical session. As standard glasses produced from solubility experiments were used (Chapter 2; Shishkina et al., 2010). It was observed after a number of analytical with standard glasses that accuracy of the method is quite low. Every standard was analyzed 5-10 times within every session and H₂O contents determined with „by-difference“ method varied in a range ±1-2 wt.% H₂O from an average value. Though the average values of H₂O contents in standard glasses were very close to those determined by independent methods (KFT or FTIR).

Comparison of H₂O concentrations in residual glasses determined with „by-difference“ method with results from FTIR (when it was possible) is shown on Fig. 1-7. A good agreement is observed for relatively high concentrations of H₂O (above 3 wt.%), while at lower H₂O-contents discrepancy is too high (up to 4 wt.% of difference). In some cases H₂O-contents determined by electron microprobe were higher, in others lower than IR-data, showing that „by-difference“ method may overestimate as well as underestimate H₂O concentrations.

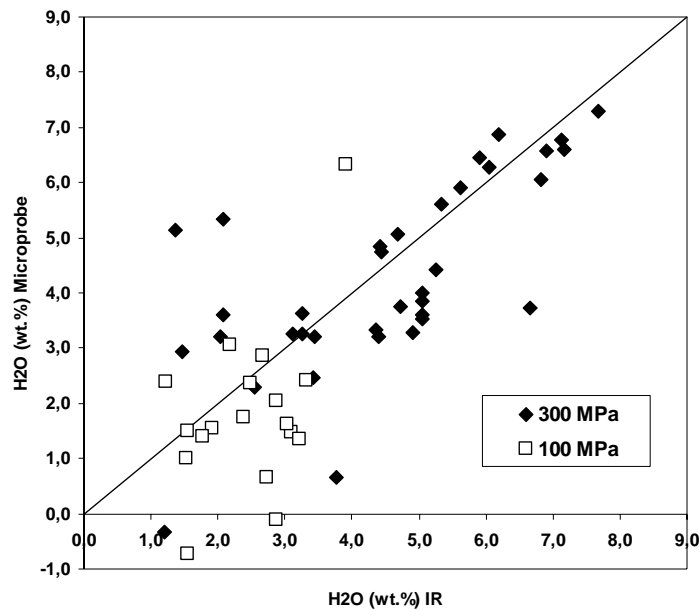


Fig. 1-7. Comparison of H₂O concentrations glasses determined with „by-difference“ method with results from FTIR in residual glasses of run products at 100 and 300 MPa.

In cases when both methods were applied, H₂O-contents determined by FTIR were used for description and discussion of run products. But since in many of crystallized run products it was not possible to apply FTIR, the data obtained by electron microprobe were used for estimations of H₂O contents in residual glasses assuming a large analytical error of $\pm 1-2$ wt.%.

2.4.3. Secondary ion mass-spectrometry (SIMS)

Determinations of concentrations of H₂O and CO₂ dissolved in the melt inclusions were performed by SIMS in two different laboratories.

1) **The concentrations of water in non-heated (naturally quenched) melt inclusions were measured with CAMECA ims4f at the Institute of Microelectronics (Yaroslavl', Russia).** The procedure of analyses was in details described in previous works on determinations of H₂O in melt inclusions (e.g. Sobolev, 1996; Portnyagin et al., 2007; Portnyagin et al., 2008). Surface of the mount with melt inclusions was coated with a 30 nm thick gold film. During analyses inclusions were bombarded by a primary beam of O²⁻ ions. With an aim to remove surface contamination the area for analysis was first sputtered for 3 min with 70 μ m diameter beam.

During analysis the beam was focused to a spot 10–20 μ m. The primary-ion energy was 14.5 keV at 15–20 nA current. The secondary ions of ¹H⁺, emitted from the sample were filtered by the high accelerating-voltage offset (-100 V, bandwidth ± 50 V) and analyzed at a mass spectrometer resolution of $M/\Delta M=300$ in pulse-counting mode.

Counting time was dynamically corrected and varied between 5 and 120 s depending on current counting statistics. Single analyses are average values from 5 cycles of measurements. The total analysis time varied from 50 to 70 min. Secondary ion intensities were normalized to $^{30}\text{Si}^+$ and converted to weight concentrations using calibration curves based on a set of well characterized natural and artificial glasses (Sobolev and Chaussidon, 1996; Rocholl et al., 1997; Jochum et al., 2006). Accuracy and precision for hydrogen were estimated to be better than 15%. Background signal for $^1\text{H}^+$ converted to weight percent of water equivalent was 0.01–0.02 wt.% as measured on nominally anhydrous olivine phenocrysts from highly depleted MORB from Sequeiros Fracture Zone.

2) The concentrations of H₂O and CO₂ in re-heated melt inclusions were measured with Cameca 1270 Ion Microprobe at the CRPG-CNRS (Nancy, France).

Olivine grains with the melt inclusions and pieces of basaltic glasses with known H₂O and CO₂ concentrations were mounted into an inch-size Al-ring using special epoxy (mixture of Araldite D and hardener HY956) and coated with Au. Prior to measurements samples and standards were held in a vacuum gas chamber for degassing and the analyses were started when the vacuum on the level of 10^{-8} to 10^{-9} Torr was achieved. Cs⁺ beam was used to produce negatively charged secondary ions: C, OH and O. The glasses were sputtered with a 10 kV Cs⁺ primary beam of the 10-15 nA intensity with a size of approximately 20x30 μm. The duration of a single measurement with 16 cycles was about 15 minutes.

Before and after each analytical session a series of representative standards were measured for calibration of carbon and water concentrations. Standards were basaltic glasses containing 0.77 to 5.7 wt.% H₂O and 0.0114 to 0.3277 wt.% CO₂ and were synthesized for study of H₂O-CO₂-solubility in tholeiitic basalt from Mutnovsky (Chapter 2; Shishkina et al., 2010).

The quantification of C and H concentrations was based on calibration curves that show linear correlation between known H₂O and CO₂ contents and OH/O and C/O ratios, respectively, for the whole range of analyzed concentrations in the standard glasses (Fig. 1-8).

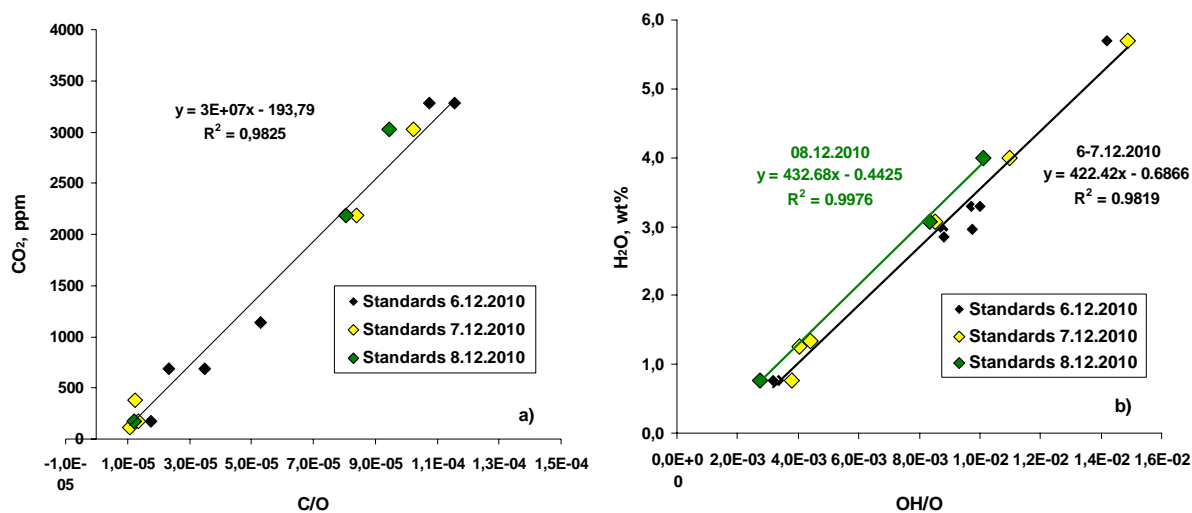


Fig. 1-8. Calibration lines for determination of CO₂ (a) and (H₂O) concentrations with Cameca 1270 Ion Microprobe at the CRPG-CNRS (Nancy, France) determined by analyses of standard glasses for every analytical session.

It must be noted, however that the analytical technique was not completely successful, because the intensity for both OH/O and C/O showed continuous drift of the obtained signal even after 16 cycles of the analysis. The reason for that might be a contamination of the surface with organic material or continuous evaporation of epoxy in the sample chamber. Another indication for such contamination is the relatively high detection limit for both H and C, as evidenced by the intersection of the calibration curve with the concentration axis (at about 0.7 wt.% for H₂O and 195 ppm for CO₂). These observations indicate that improved analytical approaches should be used in future, e.g., organic-free matrix and “pre-cleaning” of the surface with large beam and long exposure time with consequent analysis using smaller beam size.

2.4.4. Determination of the oxidation state of S species in melt inclusions by X-ray Absorption Near Edge Structure (XANES) spectroscopy

XANES spectra at the S K-edge were collected for 10 naturally quenched glassy inclusions in olivines using ANKA’s SUL-X beamline in Karlsruhe, Germany. Diameter of the beam was about 60 μm which usually was larger than size of inclusion (30 to 100 μm). Two measurements were performed on every inclusion.

In most of the glasses sulfur is presented in three forms: sulfide (S²⁻), sulfite (S⁴⁺) and sulfate (S⁶⁺) (Fig. 1-9). In 3 of studied glasses no sulfide species were detected.

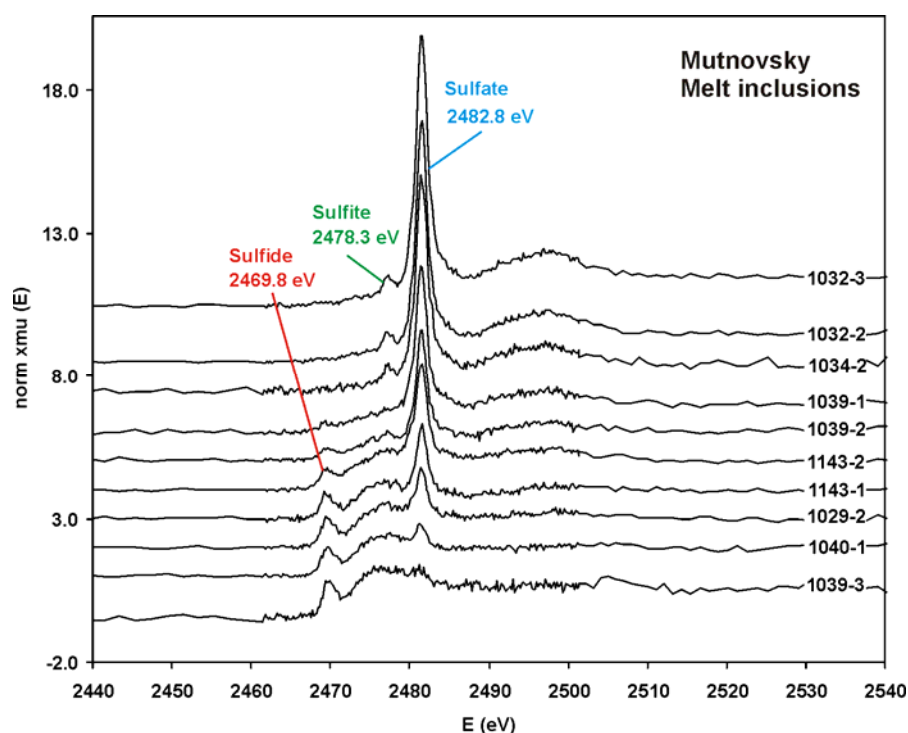


Fig. 1-9. XANES spectra for determination of sulfur speciation in melt inclusions in olivines from Mutnovsky tephra (samples KM9-10, 11).

$S^{6+}/\Sigma S$ values in melt inclusions were determined by the intensities of characteristic peaks for sulfide (S^{2-}) and sulfate (S^{6+}) on XANES-spectra (Fig. 1-9) applying method of Jugo et al. (2010). Oxygen fugacity was calculated using $S^{6+}/\Sigma S$ ratios in glasses according to a method described in Jugo et al. (2010).

$$\Delta QFM = -(\log_{10}(1/(S^{6+}/S^{tot}) - 1) - 2.1)/2$$

In the melt inclusions of Mutnovsky $S^{6+}/\Sigma S$ vary between 0.4 and 1 which corresponds to fO_2 within the range of QFM+0.9 to QFM+2 (Table 1).

Table 1. Intensities of characteristic peaks for sulfide (S^{2-}) and sulfate (S^{6+}) on XANES-spectra and calculated $S^{6+}/\Sigma S$ and oxygen fugacity.

Melt inclusion	$S^{6+}/\Sigma S$	d QFM
KM9-10-29-2-1	0.49	1.04
KM9-10-32-2-1	1.11	≥ 2
KM9-10-32-3-1	1.11	≥ 2
KM9-10-34-2-1	1.11	≥ 2
KM9-10-39-1-1	0.94	1.65
KM9-10-39-2-1	0.88	1.49
KM9-10-40-1-1	0.38	0.94
KM9-10-43-1-1	0.61	1.15
KM9-10-43-1-2	0.59	1.13
KM9-10-43-2-1	0.73	1.27

3. RESULTS

3.1. STUDY OF NATURAL SAMPLES:

3.1.1. Petrography and mineralogy of Mutnovsky natural samples

In this work petrography and mineralogy was studied for 7 samples of lava and tephra depositis that represent the last stages of the activity of Mutnovsky volcano (Mutnovsky III and IV) (Fig. 1-10). All studied samples are basalts and basaltic andesites except of one sample of dacite. Bulk rock compositions are presented in Table 1-2. For comparison of natural mineral and melt compositions with experimental products in discussion the new data are used together with previously published analytical data for Mutnovsky eruptive products (Martynov, Chashchin, 1989; Frolova et al., 2001; Hetchikov et al., 2001; Chashchin et al., 2011).

Four samples of basaltic lavas (N72, KM9-1, KM9-2 and KM9-6) have different petrographical characteristics: texture, structure, proportion of phenocrysts (Fig. 1-10). **Basalt KM9-1** is a massive lava containing euhedral and subhedral phenocrysts of plagioclase (15 %), olivine (5 %) and clinopyroxene (3 %), with sizes up to 1cm. **Basalt KM9-2** is a piece of volcanic lava bomb with porous structure containing the same association of phenocrysts (Plag+Ol+CPx) with 10% plagioclase, 6% olivine and about 1% clinopyroxene. In both samples groundmass is consisted of microlites of Ol+CPx+Plag+Mt. **Basalt KM9-6** is a subaphiric lava containing rare (less then 1%) phenocrysts of plagioclase (anorthite) and microphenocrysts of plagioclase, olivine (euhedral shapes but skeletal (hollow) texture) and clinopyroxene, groundmass is formed by microlites of Plag, CPx, OPx and Mt. **Basalt N72** is a massive basaltic lava with phenocrysts of plagioclase (15 %) and olivine (4%) and rare CPx (less then 1%), groundmass consists of Plag, CPx and Mt with rare OPx. In all samples of basaltic lavas groundmass has holocrystalline texture formed by microlites without detectable residual glass.

Bulk compositions of ground masses (microlites+microphenocrysts) in studied basaltic samples were estimated by mass-balance between compositions of bulk rocks and phenocrysts (Table 1-2). According to the mass-balance calculations studied samples represent portions of parental magma that was crystallized by 18-22 % after crystallization of Plag+Ol±CPx phenocrysts association.

The phenocrysts assemblage in two samples of **tephra (KM9-10 and KM9-11)** is mostly presented by olivine and plagioclase with rare Ca-pyroxene. Groundmass of tephra

consists of quenched residual glass with distributed needle-like (skeletal) microlites of Plag, isometrical or elongated Cpx and OPx, while Mt is absent.

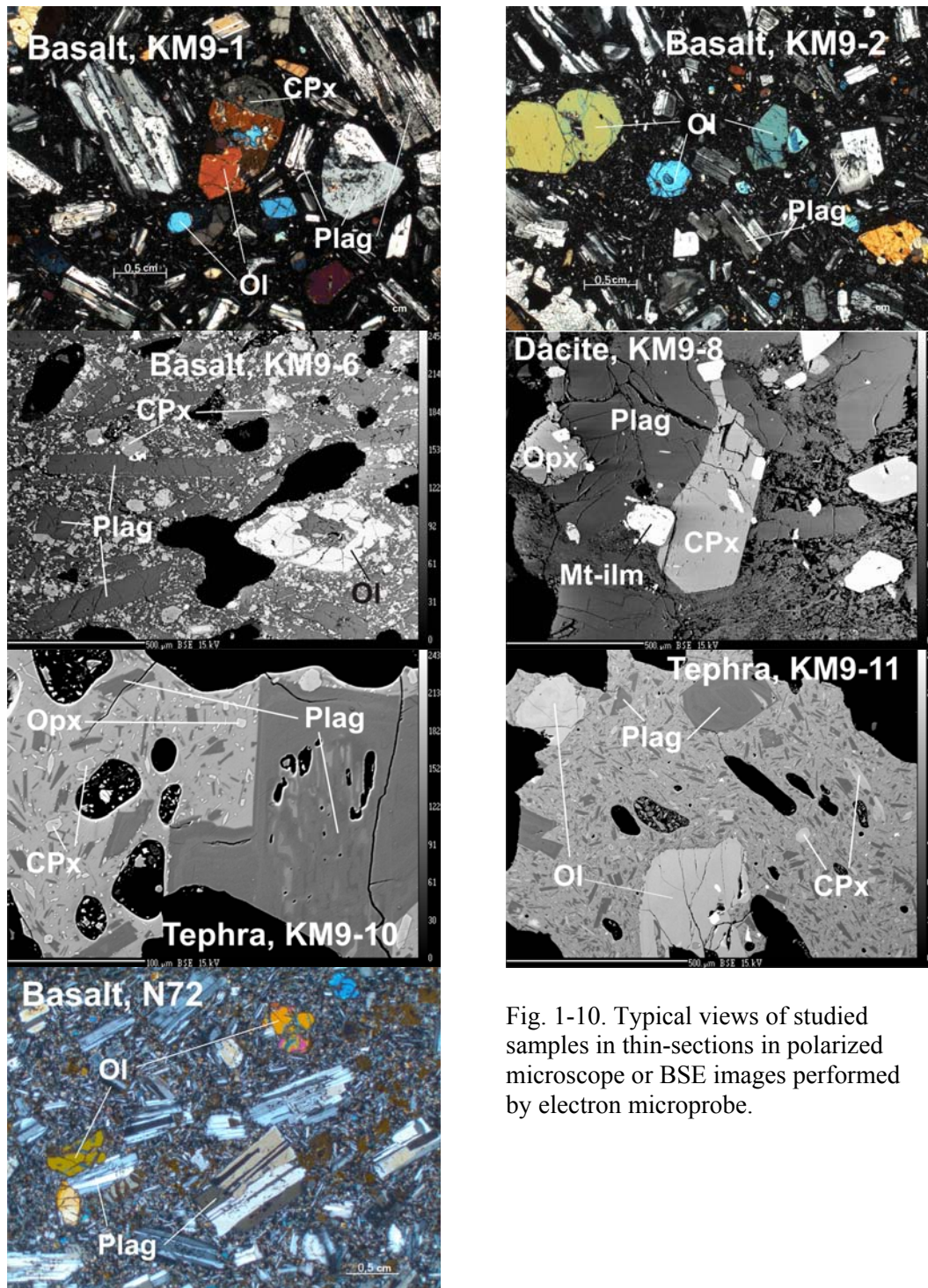


Fig. 1-10. Typical views of studied samples in thin-sections in polarized microscope or BSE images performed by electron microprobe.

The only studied silicic species from Mutnovsky is a **dacitic lava (KM9-8)** representing 3d stage of activity (Mutnovsky-III). Phenocrysts in dacite are presented by Plag, CPx, OPx and Mt (Mt-ilm dissolution). Its groundmass is formed by highly porous silicic glass with distributed microlites of plagioclase (albite), KFsp, Qtz, CPx and Mt.

Table 1-2. Bulk analyses of studied samples, proportions of phenocrysts and compositions of groundmasses

	N72* Basalt	KM9-1# Basalt	KM9-2# Basalt	KM9-6# Basalt	KM9-8 Dacite	KM9-10 tephra	KM9-11 tephra
SiO₂	50,06	49,95	49,80	52,01	65,53	55,87	54,23
TiO₂	0,90	0,90	0,91	1,22	0,98	0,95	0,76
Al₂O₃	18,35	17,86	18,02	17,48	16,42	16,71	17,47
FeO-t	9,36	9,48	9,52	10,94	3,94	8,32	7,87
MnO	0,17	0,16	0,16	0,19	0,15	0,18	0,15
MgO	7,01	7,92	7,94	4,94	1,40	5,42	6,86
CaO	11,32	10,62	10,62	9,36	3,59	8,35	9,15
Na₂O	2,45	2,43	2,35	3,10	5,34	3,16	2,68
K₂O	0,22	0,49	0,48	0,58	2,37	1,04	0,84
P₂O₅	0,15	0,18	0,19	0,18	0,28	0,00	0,00
Total	100,00	100,00	100,00	100,00	100,00	100,00	100,00
Proportions of phenocrysts and groundmass (GM)							
Plag	14,7	14,8	9,9				
OI	3,6	4,8	6,3				
CPx	0,0	2,5	1,1				
Mt	0,0	0,1	0,4				
GM	81,6	77,9	82,4				
Composition of groundmass							
SiO₂	51,36	51,52	50,99				
TiO₂	1,10	1,13	1,08				
Al₂O₃	16,33	16,99	17,70				
FeO-t	10,44	10,43	9,89				
MnO	0,19	0,19	0,17				
MgO	6,76	5,96	6,44				
CaO	10,61	10,43	10,30				
Na₂O	2,75	2,89	2,67				
K₂O	0,26	0,28	0,58				
P₂O₅	0,18	0,19	0,18				
Total	100,00	100,00	100,00				

* -composition from Duggen et al., 2007,

- compositions determined by XRF in AcmeLab (Canada)

Other compositions – electron microprobe analyses of glasses produced from remelted rock-powders.

Proportions of phenocrysts were calculated with „point-counting“ method

Compositions of groundmasses were determined by mass-balance between bulk rocks and phenocrysts composition in determined proportions.

All analyses are normalized to 100 wt.%.

Mineralogy of Mutnovsky natural samples

Compositions of minerals from studied natural samples are reported in Table 1-3 In general determined mineral compositions are in a good agreement with data reported in other sources (e.g. Martynov, Chashchin, 1989; Frolova et al., 2001; Hetchikov et al., 2001; Chashchin et al., 2011).

Table 1-3. Compositions of minerals in studied samples

	Olivine (Fo)					Plagioclase (An)					Clinopyroxene (Mg#)					Orthopyroxene (Mg#)				
Phenocrysts (cores)																				
Sample	Min	Max	Aver	StD	n	Min	Max	Aver	StD	n	Min	Max	Aver	StD	n	Min	Max	Aver	StD	n
N72	75,6	80,7	78,6	1,2	22	84,4	90,3	87,9	1,6	25			78,8		1					
KM9-1	72,1	83,2	78,9	3,1	38	85,7	93,3	88,4	2,1	20	77,6	79,5	78,4	0,7	8					
KM9-2	73,6	83,6	79,2	3,2	19	81,8	91,8	87,2	3,4	13	76,9	79,7	78,1	1,1	6					
KM9-6						88,0	88,2	88,1		2										
KM9-8						33,6	45,8	39,7	3,2	11	74,7	76,3	75,3	0,8	3	70,3	73,9	72,5	1,40	8
KM9-10	76,3	79,2	78,2	0,5	58	87,2	91,0	88,7	1,4	8			80,1		1					
KM9-11	77,3	80,6	78,5	0,6	48	87,0	91,6	89,5	1,4	8	76,9	78,8	77,9	1,3	2					
Phenocrysts (rims)																				
Sample	Min	Max	Aver	StD	n	Min	Max	Aver	StD	n	Min	Max	Average	StD	n					
N72	63,3	75,7	72,0	4,1	11	50,7	89,8	72,3	9,7	18			68,6		1					
KM9-1	68,4	74,2	71,3	2,9	3	66,9	84,8	72,9	5,2	9										
KM9-2					1	60,8	67,3	64,1	4,6	2										
KM9-6								77,8		1										
KM9-8						39,2	41,5	40,3	1,6	2			75,6		1					
KM9-10						67,8	73,2	70,7	2,7	3										
KM9-11			73,6		1	61,8	72,2	67,4	4,3	4										
Microphenocrysts (cores)																				
Sample	Min	Max	Aver	StD	n	Min	Max	Aver	StD	n	Min	Max	Aver	StD	n					
N72	77,5	79,8	78,5	0,8	10	70,7	85,3	78,0	10,3	2	75,8	77,8	77,0	1,0	3					
KM9-1	68,9	80,5	76,4	3,9	8	84,2	90,0	86,7	2,7	4			73,6		1					
KM9-2	73,3	76,3	74,8	2,1	2								78,8		1					
KM9-6	58,8	69,3	63,7	3,3	15	69,7	76,1	72,8	2,0	13	65,9	75,2	71,4	2,6	14					

Olivine (Fo)						Plagioclase (An)					Clinopyroxene (Mg#)					Orthopyroxene (Mg#)				
Microphenocrysts (rims)																				
Sample	Min	Max	Aver	StD	n	Min	Max	Aver	StD	n	Min	Max	Aver	StD	n	Min	Max	Aver	StD	n
KM9-1	66,9	70,1	68,9	1,7	3	67,6	74,1	71,6	3,5	3										
KM9-6	62,0	63,0	62,3	0,4	5			70,8		1	57,3	64,1	61,4	3,6	3					
Microlites (ground mass)																				
Sample	Min	Max	Aver	StD	n	Min	Max	Aver	StD	n	Min	Max	Aver	StD	n	Min	Max	Aver	StD	n
N72						48,0	71,1	65,1	6,4	11	67,3	76,0	72,7	2,4	10					
KM9-1	58,2	63,2	61,1	2,2	4	62,1	70,2	67,3	3,1	5	66,9	75,0	72,3	3,6	5					
KM9-2	61,7	65,6	63,1	2,2	3	60,3	68,6	63,5	4,4	3	72,5	75,8	73,9	1,7	3					
KM9-6						66,3	70,0	68,1	2,6	2	58,2	71,2	64,7	4,9	8	58,1	61,7	59,9	2,6	2
KM9-8								23,6		1	69,2	70,2	69,6	0,5	3					
KM9-10						55,2	60,4	57,9	2,6	3	69,9	70,7	70,4	0,4	3	71,6	77,5	74,2	3,0	3
KM9-11						59,1	64,3	61,8	2,7	3			69,9		1	71,0	73,7	72,3	1,9	2

Minimal (Min), maximal (Max) and average (Aver) values of mineral compositions in terms of Fo for olivine, An for plagioclase, Mg# for CPx and OPx (mol.%) determined for studied samples. StD – standard deviations for n analyses.

Plagioclase

Compositions of plagioclase are presented in Table 1-3 and on Figure 1-11..

Plagioclase is the most abundant mineral in phenocrysts association of Mutnovsky basalts comprising up to 15% of rocks and up to 80% of phenocrysts. Plagioclase phenocrysts in lavas and tephros are presented by euhedral to subhedral prismatic crystals with dimensions from 0.2 to 2 mm. We can divide phenocrysts into two groups according to the character of their zoning. Most of the phenocrysts have homogeneous high-Ca (anorthite to bytownite) cores sometimes with not well pronounced oscillatory zoning and obvious rim (thickness up to 100 μm) of less Ca-plagioclase (labradorite). Another smaller part of plagioclase phenocrysts is presented by well-zoned crystals with cloudy Ca-rich cores surrounded with irregular zones of less-Ca plagioclase. Sometimes two or several cores are grown together and form glomero-porphyrific aggregates surrounded with common rims. In a number of phenocrysts no pronounced low-Ca rims were observed. Cores or other zones in some crystals are resorbed (decayed).

Compositions of plagioclase phenocrysts in all studied basaltic samples are very constant. In general proportion of anorthitic component (An) in cores of phenocrysts varies between 82 and 93 with an evident maximum at An 86 to 90 for all studied samples (Fig.4 a. b histogramm). Compositions of rims vary from An 50 to An 90 with an average (maximum) of An 64-73.

Another generation of plagioclases in basalts is presented by microphenocrysts which are crystals with subhedral shapes and sizes smaller than 200 μm but bigger than microlites of groundmass. Microphenocrysts usually have homogeneous cores (bytownite: An 70-85 with average of An 72-78) and less-Ca rims (labradorite, An 68-74).

Plagioclase is also a most abundant mineral in groundmass where it mainly has composition of labradorite and varies between An48 to An77 with an average of An 57 to 73 for different samples. In general compositions of plagioclase microlites are similar but still less-Ca-rich than compositions of rims of phenocrysts or microphenocrysts.

In dacite (KM9-8) plagioclase forms phenocrysts of subhedral form with sizes up to 1mm. Crystals have very homogeneous composition without pronounced zoning and usually do not have contrasting rims. Composition of cores of plagioclases is andesine and varies between An37 and An46 with an average of An40, rims of crystals have the same composition. Groundmass of dacite contains very rare microlites of plagioclase (oligoclase An24), while higher proportions of KFsp and Qtz.

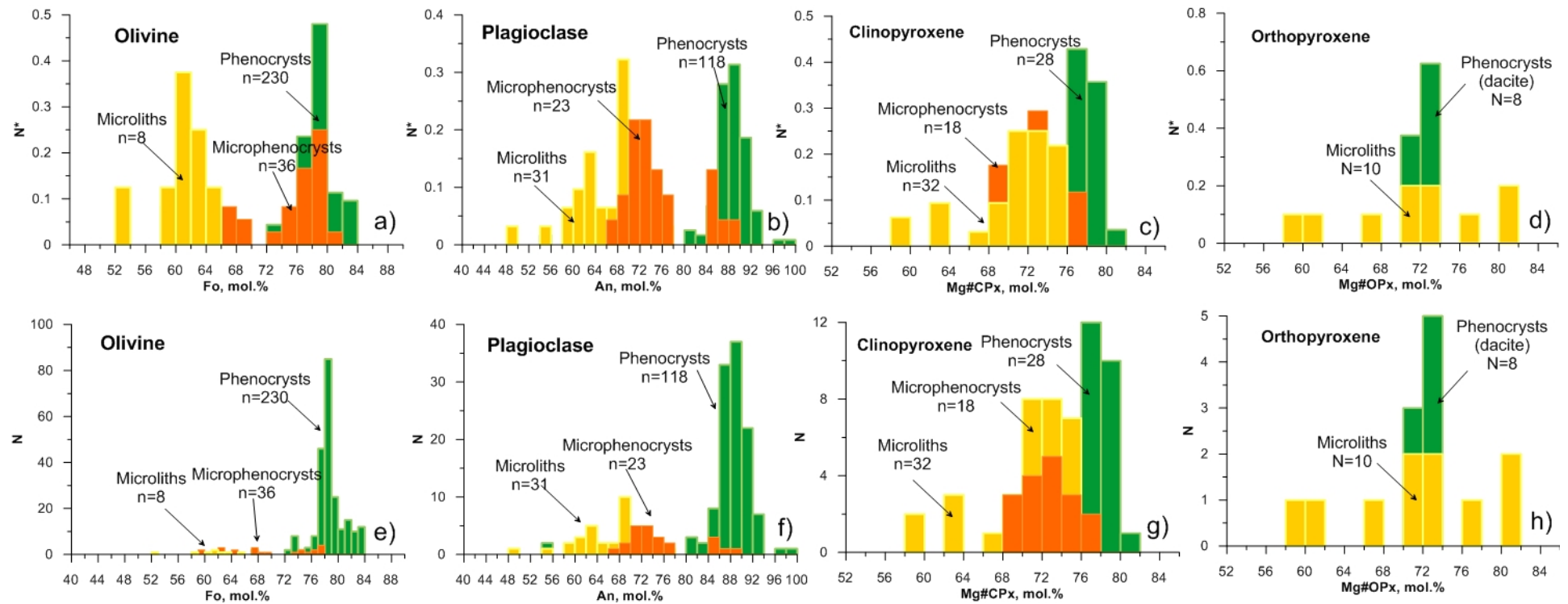


Fig. 1-11. Histograms of mineral compositions in studied Mutnovsky basalts presented as Fo for olivine, An for plagioclase, Mg# for CPx and OPx (mol. %). For orthopyroxene compositions of phenocrysts in dacite (KM9-6) are presented. Figures a-d display relative frequencies, figures e-h – real frequencies.

Olivine

Compositions of olivine are presented in Table 1-3, Figures 1-11, 12.

In all studied basalts olivine is a second important mineral of phenocrysts association. It comprises up to 6% of rock and 35% of phenocrysts and presented by euhedral to subhedral crystals with size up to 2 mm without pronounced zoning. Crystals have homogeneous Mg-rich cores and sometimes more Fe-rich rims of different thickness 10 to 50 μm can be distinguished. A few olivine crystals with reverse zoning: more Fe-rich cores surrounded with Mg-rich rims were found in studied samples (sample N72: core Fo67, rim Fo77; KM9-2: core Fo72, rim Fo80).

Compositions of olivine cores in studied basalts vary between Fo72 and Fo84 with a pronounced maximum of compositions at Fo78-80, in several samples a smaller maximum can be distinguished at Fo81-84. Fe-rich rims of olivine phenocrysts vary in composition between Fo63 and Fo 76 with an average of Fo 71-73 for different samples.

Microphenocrysts of olivine have subhedral shapes and sizes less than about 200 μm . They also have homogeneous compositions with Mg-rich cores and Fe-rich rims. Cores of microphenocrysts in samples N72, KM9-1 and KM9-2 have similar compositions to cores of phenocrysts and vary in a range of Fo 69 to Fo81 with averages of Fo 75-79. In sample KM9-6 where no Ol-phenocrysts were detected, Ol-microphenocrysts have skeletal textures and quite homogeneous cores of Fo 59 to Fo 69 with an average of Fo64.

In two samples of KM9-1 and KM9-2 olivines also were found in groundmass, where they form isometrical microlites usually surrounded with a rim of tiny crystals of Ca-pyroxene. Olivine of microlites has composition of Fo58 - 65.

Clinopyroxene

Compositions of clinopyroxene in studied samples are presented in Table 1-3, Figures 1-11, 12).

In all studied samples of basalts clinopyroxene was found among phenocrysts but proportion of this mineral is quite low (less than 3% of rock and less than 10% of phenocrysts). CPx form subhedral crystals which can be as big as 2 mm. Similarly to phenocrysts of plagioclase and olivine, crystals of CPx usually have homogeneous Mg-rich cores without pronounced zoning. Fe-rich rims were observed only in a few grains. In all samples compositions of CPx cores (Fs10-23 Wo131-44 En39-51) vary in a range of Mg# 74 to 80 with a pronounced maximum of compositions at Mg#77-79 for almost all samples. Compositions of CPx microphenocrysts cores in N72, KM9-1 and KM9-2 are similar to

those of phenocrysts and vary in a range of Mg#76-79. Microphenocrysts in subaphyric basalt KM9-6 are more Fe-rich: Mg#66-75 with an average of Mg#CPx71.

Clinopyroxene together with plagioclase is an important mineral phase of groundmass in basalts where it forms isometric microlites. CPx of microlites in all basaltic samples have very constant composition: Mg# 67 to 76 with an average at Mg#70-74 (Table 1-3). Only in sample KM9-6 CPx-microlites are more Fe-rich: Mg# 58-71 (average Mg#65).

Compositions of CPx phenocrysts (Mg# 75-76) and microlites (Mg#69-70) in dacite (KM9-8) are coinciding with those from basalts.

Orthopyroxene

Compositions of orthopyroxene in studied samples are presented in (Table 1-3, Fig. 1-11, 12).

Orthopyroxene is not a typical mineral of phenocrysts association in Mutnovsky basalts. Low-Ca pyroxene is presented among microlites in samples of basaltic tephra (KM9-10 and KM9-11) where it has composition Mg#71-77. Also OPx was detected in a groundmass of sample KM9-6 where it has composition Mg# 58-62. In previous works OPx was also described in groundmass of Mutnovsky basalts Mg#Opx 60-65 (Chashchin et al., 2011).

As an important mineral of phenocrysts association, OPx is presented in dacite KM9-8, where it forms subhedral grains in co-growth with CPx and Plag and have homogeneous compositions with absence of zoning: En68-72 Wo13 Fs25-29, Mg#70-74.

Oxides

In studied samples of basalts phenocrysts of Fe-Ti-oxides are rare and were not analyzed. Ti-magnetite is an important mineral in groundmass of Mutnovsky basaltic lavas, though almost not presented in tephra samples. In studied dacite (KM9-8) phenocrysts of oxides are presented and characterized by Magnetite-Ilmenite exsolutions.

Phenocrysts of magnetite were described in basalts, andesites and dacites of old Mutnovsky structure (Mutnovsky-I) and in young basalts of Mutnovsky-IV (Chashchin and Martynov, 2011). Compositions of Mt microlites were reported for basalts of Mutnovsky-IV (Chashchin and Martynov, 2011).

No hydrous phases like amphibole or biotite are observed in studied samples. These minerals were described in dacites and rhyolites of early stages of Mutnovsky activity (Selyangin, 1993).

Mineral inclusions in phenocrysts

Inclusions of **Cr-Spinel** in olivine phenocrysts (Fo 76.3-83.2) are quite often in studied basalts. Single phenocryst grain may contain several Cr-Spinel inclusions which have isometric shape and sizes from 10 to 70 mkm. Sometimes these inclusions are surrounded with portions of glass (melt inclusions) (Fig. 1-13). Cr# of Cr-Spinel inclusions vary from 0.03 to 0.23.

Very often phenocrysts of olivine (Fo 77.7-80.3) contain inclusions of small grains of plagioclase (An77.5–92.8; average An 86.5±4) or clinopyroxene (Mg# 77.3-78.9) which sometimes are surrounded by portions of glass (melt inclusions) (Fig. 1-13).

3.1.2. Mineral associations (paragenesis) in Mutnovsky natural rocks

Usually studies of mineral paragenesis (association of minerals that were formed (crystallized) simultaneously at the same conditions) are based on analyses of minerals (pairs or more mineral phases in association) that are evidently were growing simultaneously, for example glomeroporphyric aggregates, intergrowth and co-growth of different mineral phases or mineral inclusions of one phase in another. In cases of such obvious proves of simultaneous growth (belonging of minerals to the same paragenesis), application of different petrological tools, such as mineral geothermometers and geobarometers based on studies of mineral pairs are permissible.

Unfortunately, in studied Mutnovsky samples such co-growth of mineral phases are quite rare and not enough for any discussion or statistics. Most of the phenocrysts and microphenocrysts are presented as single euhedral or subhedral crystals. 3 main parageneses (stages of crystallization) may be distinguished in Mutnovsky mafic rocks: phenocrysts (cores and rims), microphenocrysts (cores and rims) and microlites. It is suggested that different mineral phases that belong to the same paragenesis were crystallized at the same conditions: temperature, pressure, water activity and redox conditions and were in equilibrium with each other and with the same magma (melt) composition.

For every studied sample an average composition (as well as minimum, maximum and standard deviation) was calculated for every mineral phase in paragenesis (presented as

Fo for olivine, An for plagioclase, Mg# for CPx and OPx (mol. %)). It is assumed that these minerals are in equilibrium (Table 1-3, Fig. 1-12).

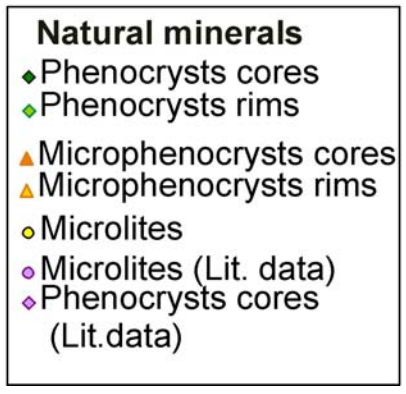
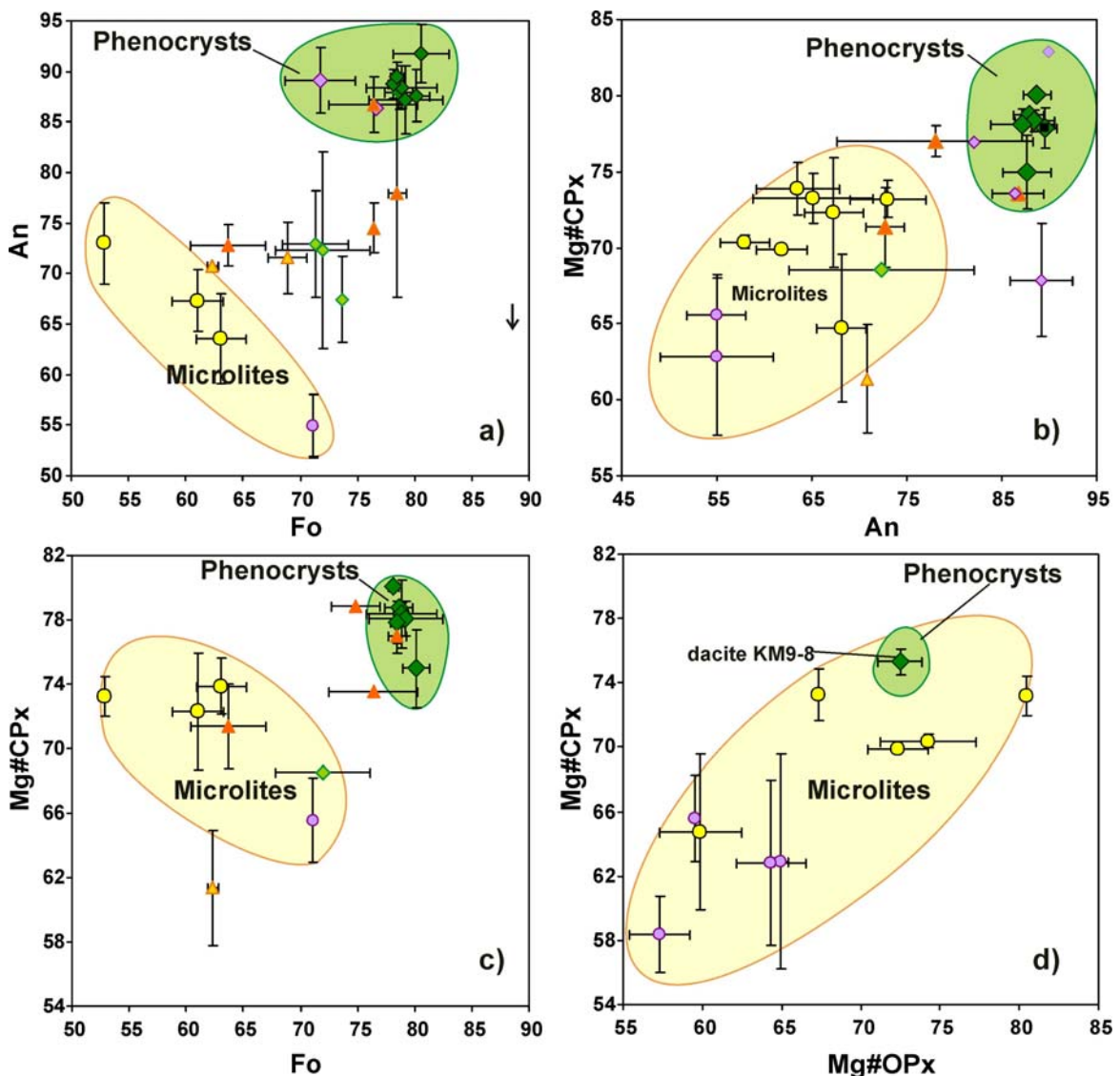


Fig. 1-12. Compositions of coexisting minerals in Mutnovsky rocks. Studied samples are presented together with literature data (Martynov, Chashchin, 1989; Chashchin et al., 2011).

Compositions of coexisting mineral pairs are presented on Figure 1-12. When it is possible, compositions of coexisting minerals that were reported in earlier studies of Mutnovsky mineralogy are also plotted together with data from this study.

Compositions of **phenocrysts cores** from studied Mutnovsky lava and tephra samples are very close to each other and altogether form small areas on diagrams Fo-An,

An-Mg#CPx, Fo-Mg#CPx (Fig. 1-11, 12). It is in agreement with the observation made on histograms of compositional distribution for every mineral where phenocrysts cores form pronounced maxima at the same compositional range for all studied samples. Therefore first mineral paragenesis (phenocrysts) in Mutnovsky basalts is composed by olivine (Fo 72-84, average 77-80), plagioclase (An 85-94, average 87-90) and high-Ca-pyroxene (Mg# = 74–81, maximum 77-80).

Compositions of coexisting minerals in **microphenocrysts** in different samples do not show the same consistency as phenocrysts, but in general they consist of less-Ca-plagioclase and more Fe-rich olivine and clinopyroxene (Fig. 1-11, 12). Probably second paragenesis (microphenocrysts) was crystallized from relatively evolved magma in comparison to phenocrysts and also reflects changes in conditions of crystallization.

Compositions of rims of phenocrysts and microphenocrysts follow the general trend of simultaneous decrease of Ca-content in plagioclases and magnesium number of olivine and CPx. The last stage of crystallization of studied rocks happened during eruption of magma to the surface when residual melt was completely crystallized into **microlites** of Plag+Ol+CPx+Ti-Mt (KM9-1 and KM9-2), Plag+CPx+OPx+Mt (KM9-6, N72) or Plag+CPx+OPx(±Mt?) (tephra KM9-10, 11) associations (Fig. 1-12).

3.1.3. Melt inclusions in olivine phenocrysts

Melt inclusions in olivine are round-shaped and have sizes from 15 to almost 200 μm (Fig. 1-13). All the inclusions in phenocrysts from lava and scoria samples and part of the inclusions from tephra samples are completely or partly crystallized during cooling after entrapment. Usually the daughter-phases are needle-like skeletal crystals distributed in the volume of inclusion or growing on its walls (Fig. 1-13 c). In few cases when these daughter-phases of melt inclusions were relatively big, we could analyze them with electron microprobe, they were identified as plagioclase (1 analysis An30), high-Ca-pyroxene (enriched in Al_2O_3 and depleted in SiO_2) and amphibole (Fig. 1-13 d). Quite often melt inclusions were trapped into phenocrysts together with mineral inclusions of Cr-Spinel, plagioclase or clinopyroxene (Fig. 1-13 b,c,d). These mineral inclusions within the melt inclusions have isometric subidiomorphic shapes and dimensions of dozens μm . Compositions are similar (overlap) with compositions of natural phenocrysts (paragraph 3.1.1). Therefore we can prove that they were crystallized before entrapment and not as a result of crystallization of melt inclusion.

Most of the melt inclusions in phenocrysts from the tephra-samples were naturally quenched into glass as a result of fast cooling during explosive eruption(s). Such naturally

quenched melt inclusions consist of silicate glass and usually contain one or several shrinkage bubbles and quite rare skeletal quench crystals or cryptocrystalline aggregates are formed in the glasses (Fig. 1-13e).

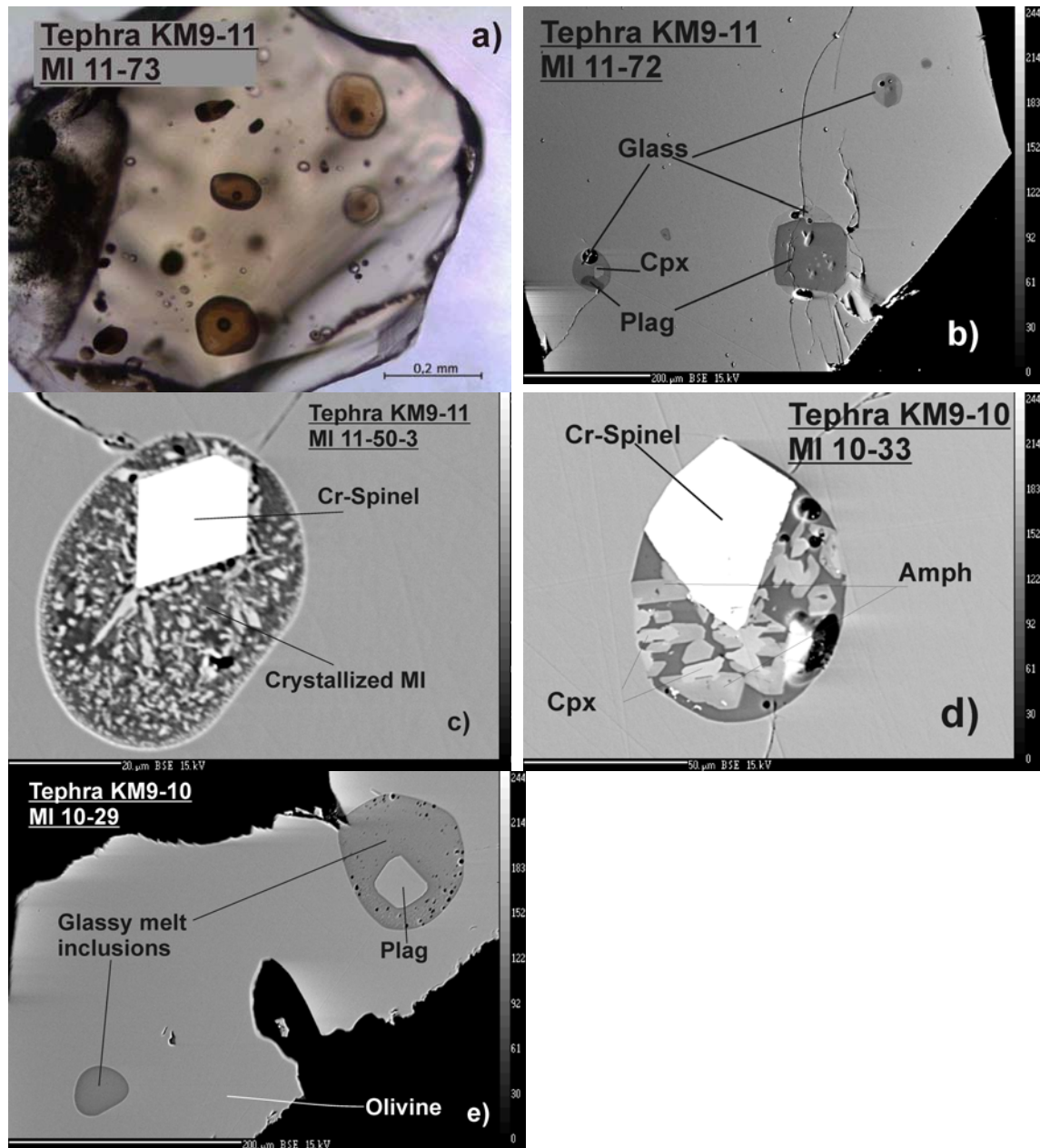


Fig. 1-13. Melt inclusions in olivines. a – microscopic foto of group of melt inclusions in olivine from tephra KM9-11 after re-homogenization experiment. b-e - BSE images performed by electron microprobe. b - Melt inclusions containing «primary» mineral inclusions of Plag and CPx; c, d – partly crystallized melt inclusions with daughter phases of CPx, Plag and Amphibole and enclosed inclusions of Cr-Spinel; e – naturally quenched melt inclusions.

For 10 naturally quenched melt inclusions major-element composition (electron microprobe (Hannover)) and H₂O concentrations (SIMS (Yaroslavl', Russia)) were determined (Appendix Table A-1-3). For 10 of these melt inclusions S⁶⁺/S^{total} ratio was determined by XANES and varies from 0.4 to 1. This sulfur speciation corresponds to the oxygen fugacity of QFM+1 to QFM+2 according to the method of Jugo et al. (2010).

Information about H₂O and CO₂ concentrations in melt inclusions can be used for the estimations of the pressure in magma reservoir at the moment of melt inclusion trapping by phenocrysts. Experimentally determined volatile solubility isobars for Mutnovsky tholeiite can be used for the quantitative estimations of volatiles saturation pressure (Chapter 2; Shishkina et al., 2010). The common problem is to measure volatiles in inclusions because most of naturally quenched melt inclusions contain shrinkage bubble(s) which presumably accumulate volatiles (especially CO₂) extracted from the melt after enclosure in the host mineral. Therefore melt inclusions must be re-homogenized with an aim to dissolve volatiles from the shrinkage bubble(s) back to the silicate melt and try to quench them into volatile-containing glass.

Re-homogenization experiments (paragraph 2.2.) with melt inclusions in olivines from tephra samples KM9-10 and KM9-11 were performed. After “re-homogenization” procedure all melt inclusions became pure glasses without quench crystals though shrinkage bubbles were not disappeared probably showing that volatiles were not completely dissolved back to melt). It can be due to the partial loss of H₂O from inclusion after its trappment which results in changing of volatile activities in melt/bubble and reduces of CO₂-solubility. 30 to 40 of re-heated melt inclusions were analyzed for major-element compositions with electron microprobe (Hannover) and for H₂O and CO₂ concentrations with SIMS (Nancy).

It is well known (*e.g.* Danyushevsky et al., 2000) that composition of melt inclusion in olivine differs from the initial composition of the melt. The very common effect of “Fe-loss” occurs due to the re-equilibration of the trapped melt with crystallized Fe-enriched olivine rim on the walls of an inclusion during cooling after entrapment (Danyushevsky et al., 2000). This effect must be taken into account when working with naturally quenched melt inclusions if $Kd^{Fe-Mg}_{Ol-Melt}$ differs significantly from 0.3. In studied naturally quenched melt inclusions of Mutnovsky Kd vary between 0.16 and 0.25. On the contrary, during „re-homogenizing” experiments some amount of host-olivine was dissolved in the melt of an inclusion because experimental temperatures were higher than those during trappment. Re-heated melt inclusions were enriched in MgO and $Kd^{Fe-Mg}_{Ol-Melt}$ for re-heated inclusions varies in the range of 0.33 to 0.46. Therefore analyzed compositions of glasses must be recalculated to equilibrium with composition of host-olivine. We have performed calculations using the software for crystallization modeling Petrolog3 (Danyushevsky&Plechov, 2011). Not-heated (naturally quenched) inclusions were recalculated using option „Reverse crystallization“, whereas re-heated inclusions with option “Fractional crystallization”. In both cases calculation conditions were set as pressure

equal to 100 MPa, oxygen fugacity on the level of QFM+1. Fo-number of the host-olivine was used as a parameter for stop calculations; model of Danyushevsky (2001) was applied for olivine. Initial and recalculated compositions of melt inclusions are presented in Appendix, Table A-1-1 and 2 (Fig. 1-14, 15). According to the performed calculations 2-8 % of olivine must be dissolved back to melt to achieve equilibrium for naturally quenched. In re-heated samples 4 to 9 % of olivine must be crystallized from melt. Temperatures of melts-olivine equilibrium vary from 986°C to 1084°C with an average temperature of 1040°C. Compositions of host-olivine vary between Fo 77.5 and Fo 80.5. In following discussion re-calculated compositions of melt inclusions are used.

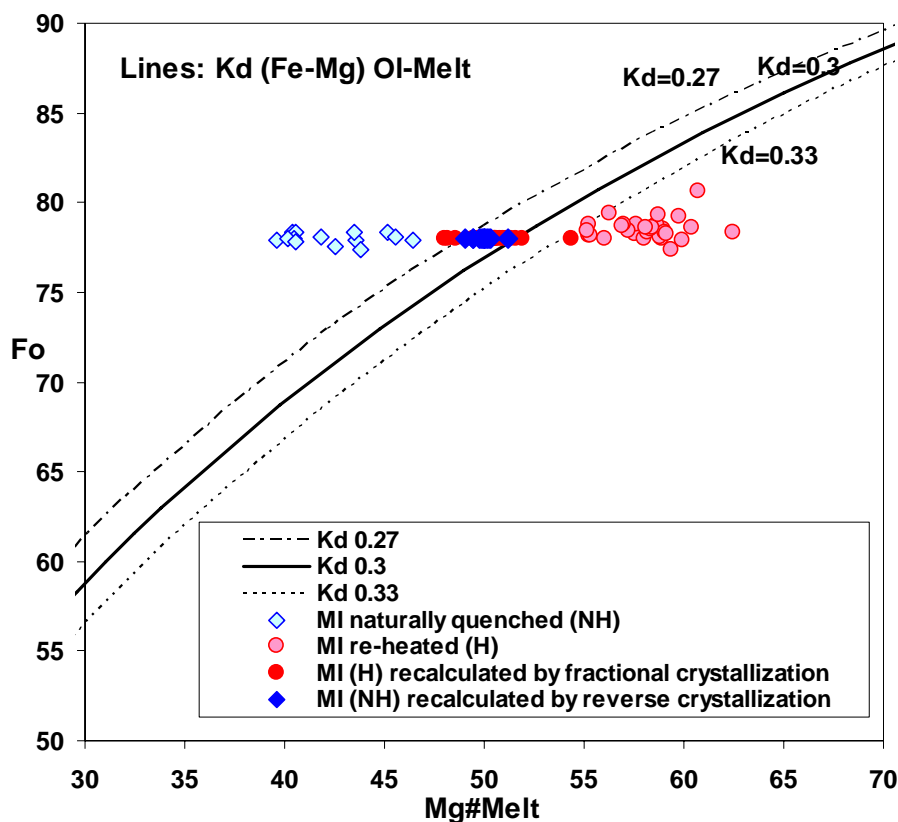


Fig. 1-14. Compositions of melt inclusion – host-olivine pairs from the studied samples before and after recalculation in Petrolog3 (Danyushevsky&Plechov, 2011).

All studied melt inclusions are basalts to basaltic andesites (50-54 wt.% SiO₂; 4-6.5 wt.% MgO). On Harker diagrams in coordinates of major-oxides vs. MgO or SiO₂ compositions of the melt inclusions form short evolutionary trends and overlap with bulk rock compositions of eruptive products of Mutnovsky (Fig.1-15). Compositions of the most primitive inclusions are very close to basalt N72 that was used in this work as a starting material for the phase relation experiments.

Volatile-contents in studied melt inclusions are presented in Appendix, Table A-1-3. Water concentrations in naturally quenched inclusions vary between 1.5 and 2.0 wt.%

H₂O, in re-heated melt inclusions - from about 2.0 to 2.5 wt.% H₂O. In most of analyzed re-heated inclusions no presence of CO₂ is found. Only in six of analyzed inclusions low concentrations of CO₂ (20 to 180 ppm) were detected. Absence of CO₂ can be explained in different ways. Either volatile was not dissolve from the shrinkage bubbles during re-homogenization experiments and subsequent quenching, or melts were already degassed (lost CO₂) before capture into crystals.

S and Cl in the melt inclusions were analyzed by electron microprobe. Both naturally quenched and re-heated melt inclusions contain similar amounts of the volatiles: 500 to 3100 ppm S (average 1400 ppm) and 200 to 900 ppm Cl (average 600 ppm) (Appendix Table A-1-1).

3.1.4. Natural LLDs (bulk rocks, melt inclusions, ground masses)

As was mentioned above, Mutnovsky eruptive products are presented by a wide range of compositions: from basalts to rhyodacites with a dominant role of basalts and basaltic andesites throughout all the history of volcanic activity. Bulk compositions of Mutnovsky rock from different stages of its activity are presented on Fig (1-15a,b) showing variations of major petrochemical oxides vs. SiO₂ and MgO. Data presented are from Chashchin et al., 2011; Kepezshinskas et al., 1981; Hochstaedter et al., 1996; Pineau et al., 1999; Alves et al., 2002; Popolitov et al., 1981; Duggen et al., 2007 Active volcanoes of Kamchatka, 1991; Martinov, Chashin, 1989; Hetchikov, Chashin et al., 2001.

Concentration of SiO₂ varies from about 49 to 71 wt.% with simultaneous decrease of MgO from 8.4 wt.% (our most Mg#-rich sample contain 8.0 wt.% MgO) to 0.5 wt.% MgO. In mafic rocks (49-54 wt.% SiO₂) concentration of MgO vary greatly at same SiO₂ content: for example at about 50 wt.% SiO₂ it changes between 3.5 and 8.5 wt.% MgO which is typical for island arc tholeiites. In more evolved rocks concentration of MgO at constant SiO₂ vary in a narrow range and linearly decrease with increase of SiO₂.

Accumulation of high-Ca plagioclase phenocrysts may be a reason of the wide range of Al₂O₃ content in Mutnovsky basalts and basaltic andesites between about 17 and 24 wt.% Al₂O₃. In andesites concentration of Al₂O₃ stays almost constant on the level of 16-18 wt.% Al₂O₃ and decreases down to 14 wt.% Al₂O₃ in the most silicic species (Fig. 1-15, 16). Large variation of Al₂O₃ content in Mutnovsky mafic rocks is also pronounced on diagram Al₂O₃ vs. MgO in a range of 3-6 wt.% MgO (Fig. 1-16).

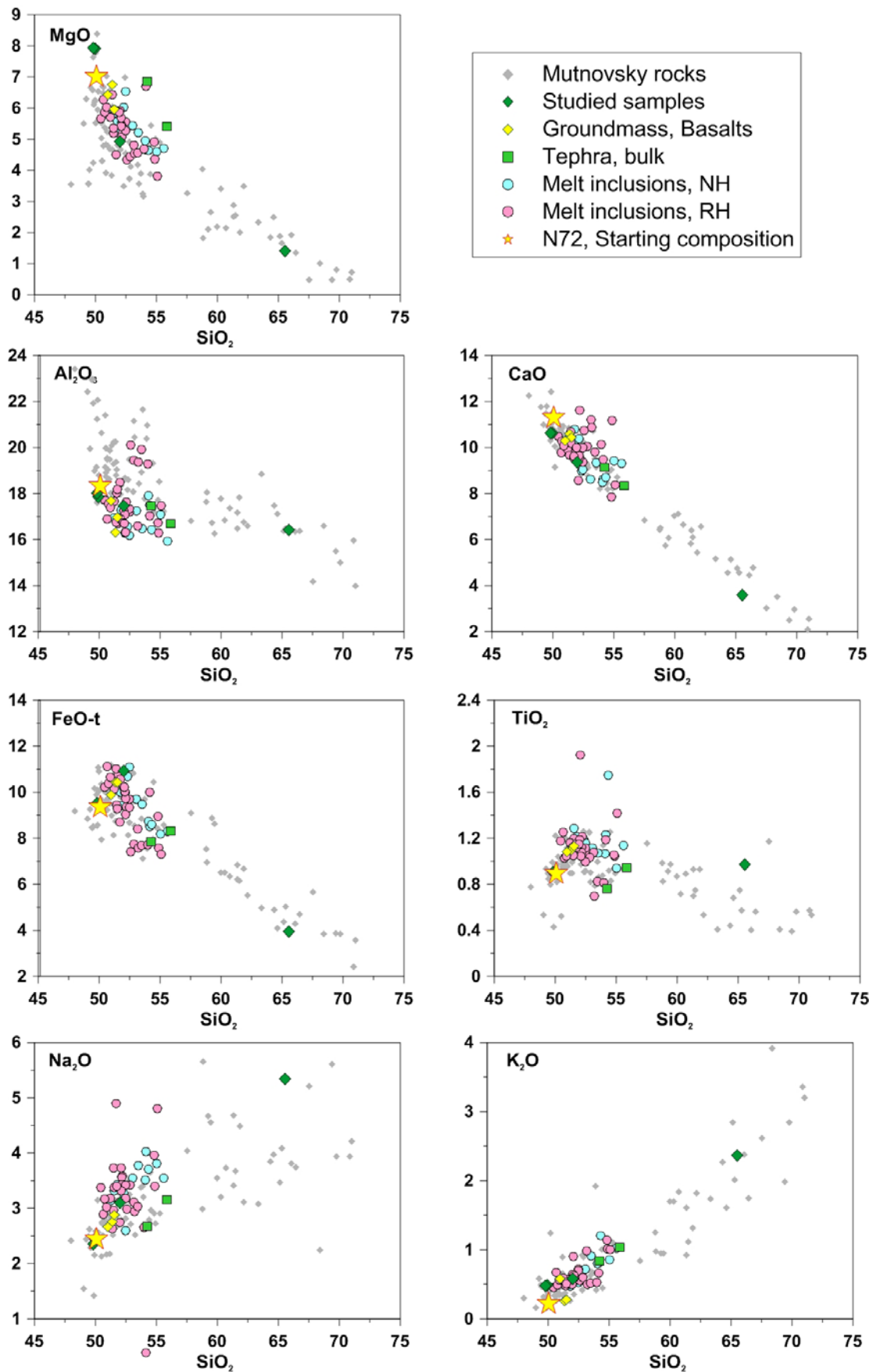


Fig. 1-15. Variational diagrams in oxides vs. SiO_2 for Mutnovsky rocks (grey diamonds), melt inclusions (NH – not heated, naturally quenched MI; RH – re-heated MI). Studied samples of basalts, tephra and calculated compositions of groundmasses in basalts are shown.

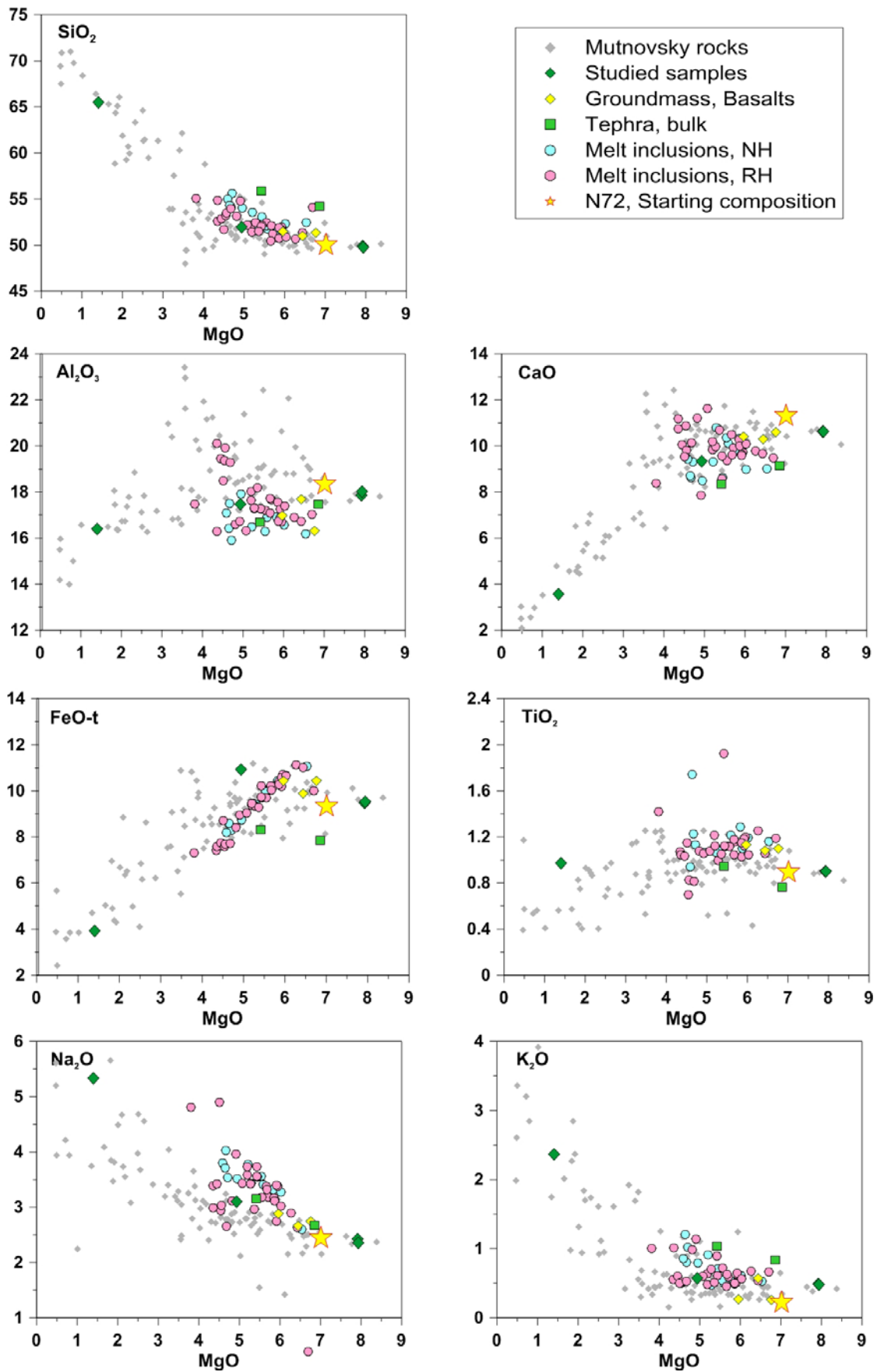


Fig. 1-16. Variational diagrams in oxides vs. MgO for Mutnovsky rocks (grey diamonds), melt inclusions (NH – not heated, naturally quenched MI; RH – re-heated MI). Studied samples of basalts, tephra and calculated compositions of groundmasses in basalts are shown.

Concentration of FeO-tot in mafic rocks follows typical tholeiitic trend of constant enrichment with evolution of melt and vary between approximately 8 and 11 wt.% FeO-tot (Fig. 1-15, 16). In more evolved rocks FeO-tot constantly decreases with increase of SiO₂ or decrease of MgO.

CaO linearly decrease from 12.5 to 2 wt.% CaO with decrease of SiO₂ within the all range of Mutnovsky eruptive products (Fig. 1-15, 16) and vary in a narrow range at constant SiO₂.

Two main evolutionary trends can be recognized for Mutnovsky mafic rocks using concentration of TiO₂. One trend does not show a dependence of TiO₂ concentration on SiO₂ or MgO content and tends to be almost constant on a level of 0.9-1 wt.% TiO₂. While a number of basalts follow a trend of enrichment in TiO₂ typical for island arc tholeiites with concentration of TiO₂ up to 1.25 wt.% (Fig. 1-15, 16). In the most evolved silicic rocks TiO₂ content is depleted to 0.4 wt.% TiO₂.

Concentration of Na₂O increases from about 2 to 5.6 wt.% with SiO₂ increase and MgO decrease within the whole range of rock compositions (Fig. 1-15,6). Concentration of K₂O increases from about 0.2 to 3.5 wt.% within the range of Mutnovsky rocks. Mutnovsky basalts contain 0.2 to 0.9 wt.% K₂O (Fig. 1-15,16). According to the classification of Gill (1981) Mutnovsky eruptive products belong to Low and Medium-K series.

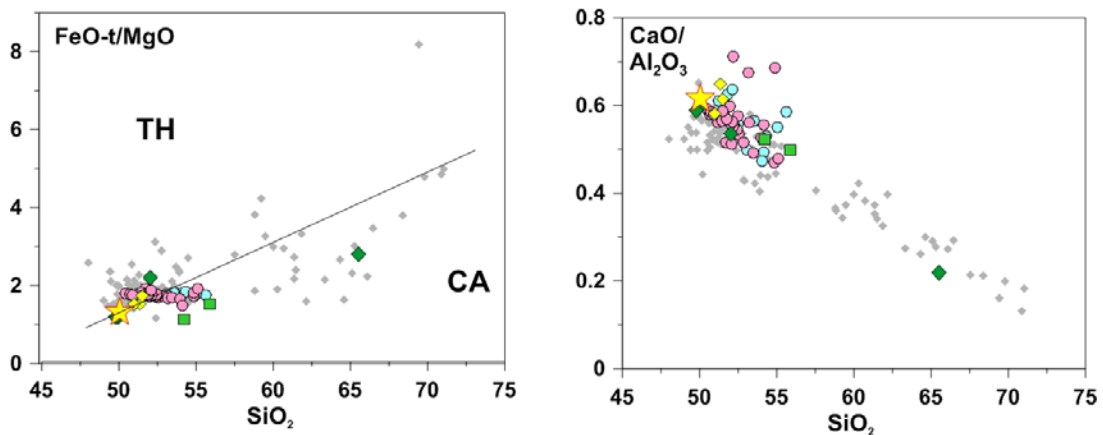


Fig. 1-17. (a) FeO-t/MgO – SiO₂ classification diagram (Miyashiro, 1974); (b) CaO/Al₂O₃ vs. SiO₂ diagram. Mutnovsky rocks (grey diamonds), melt inclusions (NH – not heated, naturally quenched MI; RH – re-heated MI). Studied samples of basalts, tephra and calculated compositions of groundmasses in basalts are shown.

CaO/Al₂O₃ in Mutnovsky rocks decreases linearly from 0.62 to 0.13 with increase of SiO₂ and decrease of MgO (Fig. 1-17b).

On classification diagram of FeO-tot/ MgO vs. SiO₂ diagram of Miyashiro (1974) most of the mafic Mutnovsky rocks are plotted in a field of tholeiitic series or close to the differentiation line between tholeiitic (TH) and calc-alkaline (CA) series. Compositions of more evolved rocks are found to be in both TH and CA fields (Fig. 1-17a).

On the AFM-diagram (Kuno, 1968; Irvine and Bargar, 1971) most of the Mutnovsky mafic rocks are located along the discriminant boundary between tholeiitic and calc-alkaline series, most of the evolved rocks are plotted within the field of CA-series (Fig. 1-18).

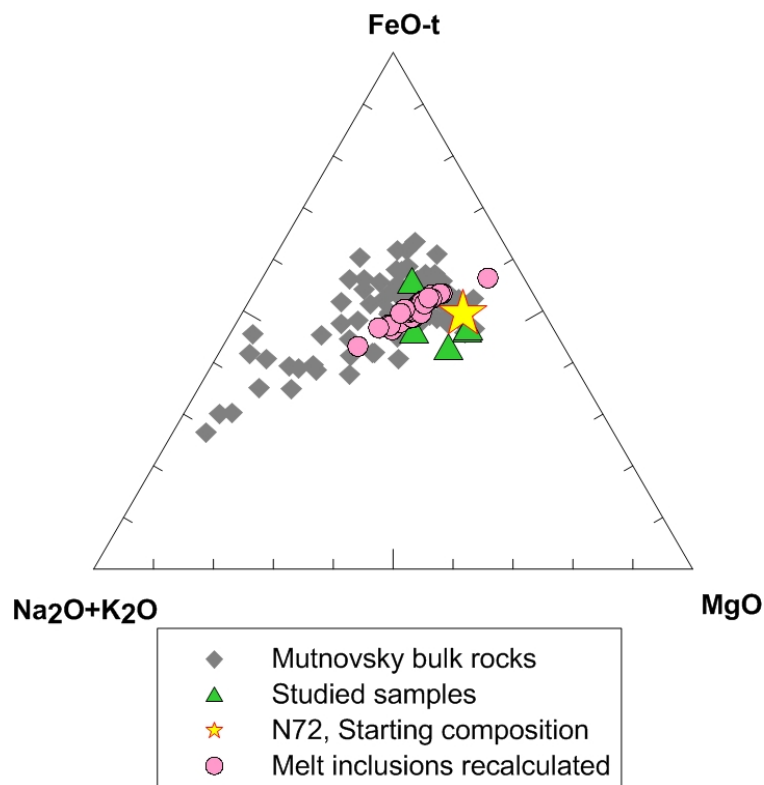


Fig. 1-18. AFM diagram. Mutnovsky rocks (grey diamonds), melt inclusions (pink circles). Studied samples of basalts and tephra.

Composition of basalt that was chosen as a starting material for phase relation experiments in this study (N72) on both diagrams is located near the discrimination lines between TH and CA series.

According to the classification diagrams majority of Mutnovsky mafic rocks can be classified as low to middle-K island-arc tholeiitic series.

The melt inclusions in olivines from studied Mutnovsky tephra and lava samples are basalts to basaltic andesites with 50.5 – 55.5 wt.% SiO₂ and 4.3 (min 3.8) – 6.7 wt.% MgO (Appendix). Compositions of primary trapped melts form continuous irregular-shaped fields of the Harker diagrams and overlap with Mutnovsky bulk rock compositions for most of the major oxides (Fig. 1-15, 16).

Compositions of primary melts follow the same evolutionary trends as bulk rocks for SiO₂, MgO, CaO, TiO₂. Since during re-calculation of the glass composition to the equilibrium with olivine-host, Fe-Mg-distribution between olivine and melt was kept constant (K_d=0.3) it resulted in a linear trend between FeO-t and MgO. Such linear decrease of FeO-t with decreasing of MgO is not typical for Mutnovsky volcanic series. On FeO-t/MgO vs. SiO₂ diagram (Miyashiro, 1974) compositions of melt inclusions form a horizontal line and most of them are plotted to the field of tholeiitic series following to the discrimination border (Fig. 1-17).

The main deviations between compositions of melt inclusions and eruptive products of Mutnovsky are found to be in Al₂O₃, K₂O and Na₂O contents. Concentrations of Al₂O₃ in most of analyzed primary melts (except of 7 inclusions) are systematically lower than in bulk rocks: 16-18 wt.% Al₂O₃ in melt inclusions in comparison to 17-24 wt.% in basalts. Such strong enrichment of bulk rock compositions is caused by a high proportion of phenocrysts of high-Ca-plagioclase in Mutnovsky basalts. Therefore compositions of melt inclusions may record a correct way of evolution of basaltic melt in terms of Al₂O₃ content, showing depletion of melt in Al₂O₃ due to the crystallization of (Ca-rich) plagioclase. Melts of inclusions are systematically enriched in alkalis (Na₂O and K₂O) in comparison to bulk rocks and follow trends of K₂O and Na₂O enrichment with evolution of melt composition parallel to main Mutnovsky series.

Melts trapped in olivines are genetically related to volcanic products and may present different portions of magma which was parental to Mutnovsky volcanic series. Therefore study of the melt inclusions (major-elements, volatile components, parameters of equilibrium with host olivine etc.) may give important information about magma storage conditions below Mutnovsky (see Discussion).

3.2. RESULTS. PHASE RELATIONS EXPERIMENTS AT 100 AND 300 MPA

3.2.1. Phase assemblages in experimental products

Experimental conditions (pressure, temperature, run duration, $X_{H_2O}^{ini}$, fO_2^{run} , a_{H_2O}) together with obtained phase assemblages and phase proportions are presented in Appendix (Table A-1-4). Run products were solid materials (partly or completely crystallized glasses) and co-existing H₂O-CO₂-bearing fluid (Fig. 1-19). The crystallized phases at both pressures are olivine (Ol), plagioclase (Pl), clinopyroxene (Cpx), orthopyroxene (OPx) and titanomagnetite (Mt). Amphibole (Amph) was presented in several H₂O-rich runs below 1000°C at 300 MPa.

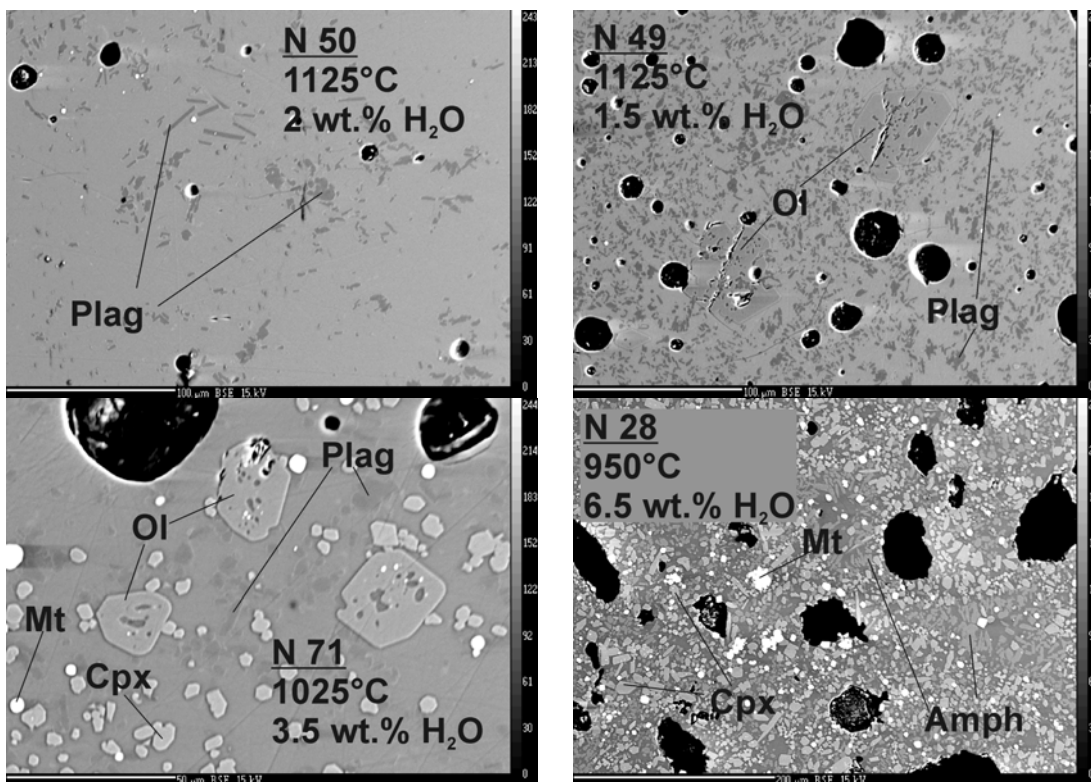


Fig. 1-19. Representative images of run products at 300 MPa and different temperatures and H₂O contents (BSE images).

Stabilities of the mineral phases depend on pressure, temperature, a_{H_2O} and fO_2 in the system. Phase diagrams with mineral stability fields as a function of temperature and H₂O-content in residual glasses at 300 and 100 MPa are constructed and are shown on Fig. 1-20. Oxygen fugacity in the system is marked on these diagrams. At both pressures crystallization degree of the starting melt logically increases with decreasing temperature. Liquidus temperatures for silicate minerals (except Amph) decrease with increasing of a_{H_2O} in the system (or with H₂O-content of the residual melt).

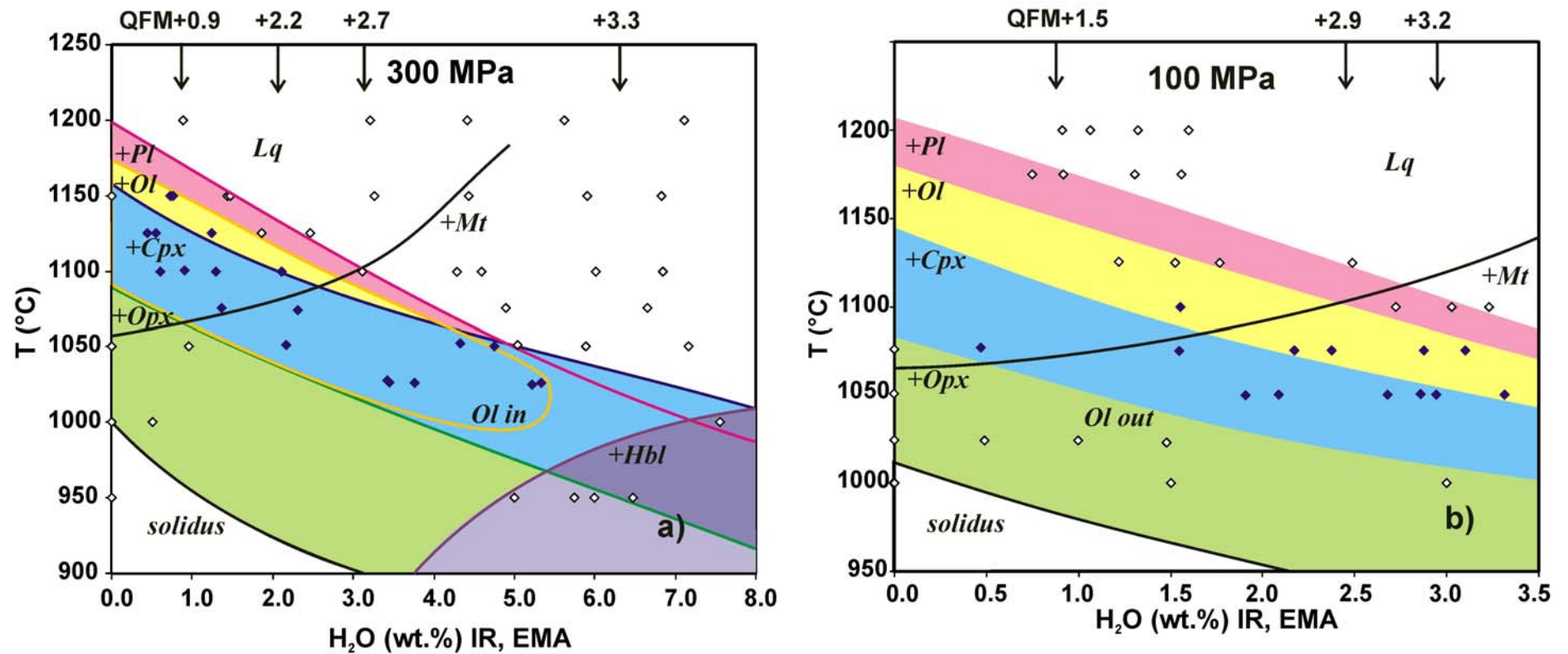


Fig. 1-20. Phase diagrams for Mutnovsky tholeiitic basalt determined after phase relation experiments at 100 and 300 MPa. Every diamond represent single run. Field of stabilities for different mineral associations are shown in different colours. Oxygen fugacity (in terms of QFM buffer) relevant to H₂O contents in the melts is shown by arrows above.

Sequence of silicates crystallization is similar at both pressures and is as follows: Pl → Pl + Ol → Pl + Ol + CPx → Pl + CPx + OPx. More detailed sequences of mineral crystallization and phase relations are discussed below for every pressure.

300 MPa experiments (950-1200°C) (Fig. 1-20a)

At 1200°C Mutnovsky basalt is above the liquidus for the whole range of investigated $a_{\text{H}_2\text{O}}$. Plagioclase is the first mineral phase crystallized from melts with less than 3 wt.% H₂O, followed by Ol. In dry system plagioclase starts to crystallize at about 1200°C and olivine – at 1180°C. Clinopyroxene is the next mineral in the crystallization sequence, which appears at about 1155°C in dry melt. With decreasing temperature all three minerals (Plag+Ol+CPx) crystallize together until about 1090°C, where orthopyroxene replaces olivine owing to peritectic reaction. Two-pyroxenes-plagioclase association is stable down to solidus. In dry system magnetite is a late phase, found in runs with temperatures below 1050°C.

Since liquidus of magnetite has a positive slope with increasing of H₂O content in the melt (this causes increase of f_{O_2} in the system) it becomes first crystallizing phase from the melts with more than 3 wt.% H₂O (that corresponds to $f_{\text{O}_2} > \text{QFM}+2.6$ or $\text{NNO}+1.9$).

Increase of H₂O in melt (and accordingly $a_{\text{H}_2\text{O}}$ and f_{O_2} in the system) causes significant decrease of liquidus temperatures for silicate minerals (Plag, Ol, CPx, OPx). Until 4 wt.% H₂O in the melt sequence of the silicate minerals crystallization remains the same. At higher water content CPx crystallizes ahead of olivine. In melts with more than 5 wt.% H₂O CPx is the first silicate mineral on a liquidus at 1050°C followed by plagioclase and olivine. It seems to be that the olivine is not stable in melts containing more than 5.5 wt.% H₂O (to $f_{\text{O}_2} > \text{QFM}+3$). The crystallization of OPx is accompanied by the absence of Ol. Only in two runs (N 42, 47) Ol and OPx were found as co-existing phases.

At higher water activities the crystallization sequence is complicated by the presence of amphibole (Amph) at temperatures below 1000°C. In the presence of Amph, CPx and OPx do not crystallize simultaneously.

100 MPa experiments (1000-1200°C) (Fig. 1-20b)

At 100 MPa sequence of crystallization of silicate minerals is as follows: Pl → Pl + Ol → Pl + Ol + CPx → Pl + Cpx + Opx within the all range of H₂O-content in the melt (corresponding to $a_{\text{H}_2\text{O}}$ from 0 to 1). Liquidus surfaces of silicates have negative slope with increasing of H₂O. At dry conditions plagioclase starts to crystallize at about 1200°C, olivine – at 1170°C, CPx – at 1145°C, OPx – at 1075°C. At H₂O-saturated conditions

(melts with around 3.5 wt.% H₂O) liquidus temperatures are much lower and are: 1080°C for Plag, 1070°C for Ol, 1045°C for CPx, 1000°C for OPx. In contrast to experiments at 300 MPa no amphibole was detected in any runs at 100 MPa. Magnetite starts to crystallize at higher temperatures in water-saturated conditions (about 1125°C), whereas only at 1050°C at dry conditions, which is caused by increase of fO_2 in the system with increase of H₂O-content of the melt.

3.2.2. Phase proportions at 100 and 300 MPa (as a function of T, aH₂O)

Phase proportions in run products were calculated by mass-balance between the bulk composition of starting material and compositions of coexisting phases (melt and minerals) in every run (Appendix, Table A-1-4). Anhydrous composition of melt was always recalculated to 100 %.

The fraction of residual melt decreases almost linearly with decrease of temperature and subsequent progressive crystallization in systems with different aH₂O from dry to H₂O saturated. The lowest melt proportion was calculated as 27% in H₂O-rich melts at 1000°C at 300 MPa and 37% in H₂O-saturated melts at 950°C at 100 MPa (Fig. 1-21). In runs with higher crystallization degree analyses of glasses were not performed because of too small glass areas between crystals. This resulted in high residual $R^2 = 1$ to 6 in runs where glass was not analyzed. Linear extrapolations of melt fraction down to 0 % let us to suggest that solidus temperature in dry system is about 1025-1050°C, in H₂O-saturated is slightly lower 900°C.

Phase proportions of minerals constantly increase with decreasing of temperature. Plagioclase and clinopyroxene show almost linear parallel trends of increasing of mineral fraction with temperature decrease depending on aH₂O (Fig. 1-21). Similar observation can be made for olivine and magnetite fractions in runs at 300 MPa, though no clear dependence on aH₂O can be made for these minerals at 100 MPa (Fig. 1-21). There is not enough data to make conclusions about effects of H₂O or fO_2 on crystallization of OPx and Amph. Highest proportions of minerals in runs with highest crystallinity where glass could be still analysed are 40 - 42 % for plagioclase, 6.5-7 % for olivine, 16-18 % for clinopyroxene, about 9% orthopyroxene, 5-6 % magnetite. Proportion of amphibole varies between 3 and 26 %.

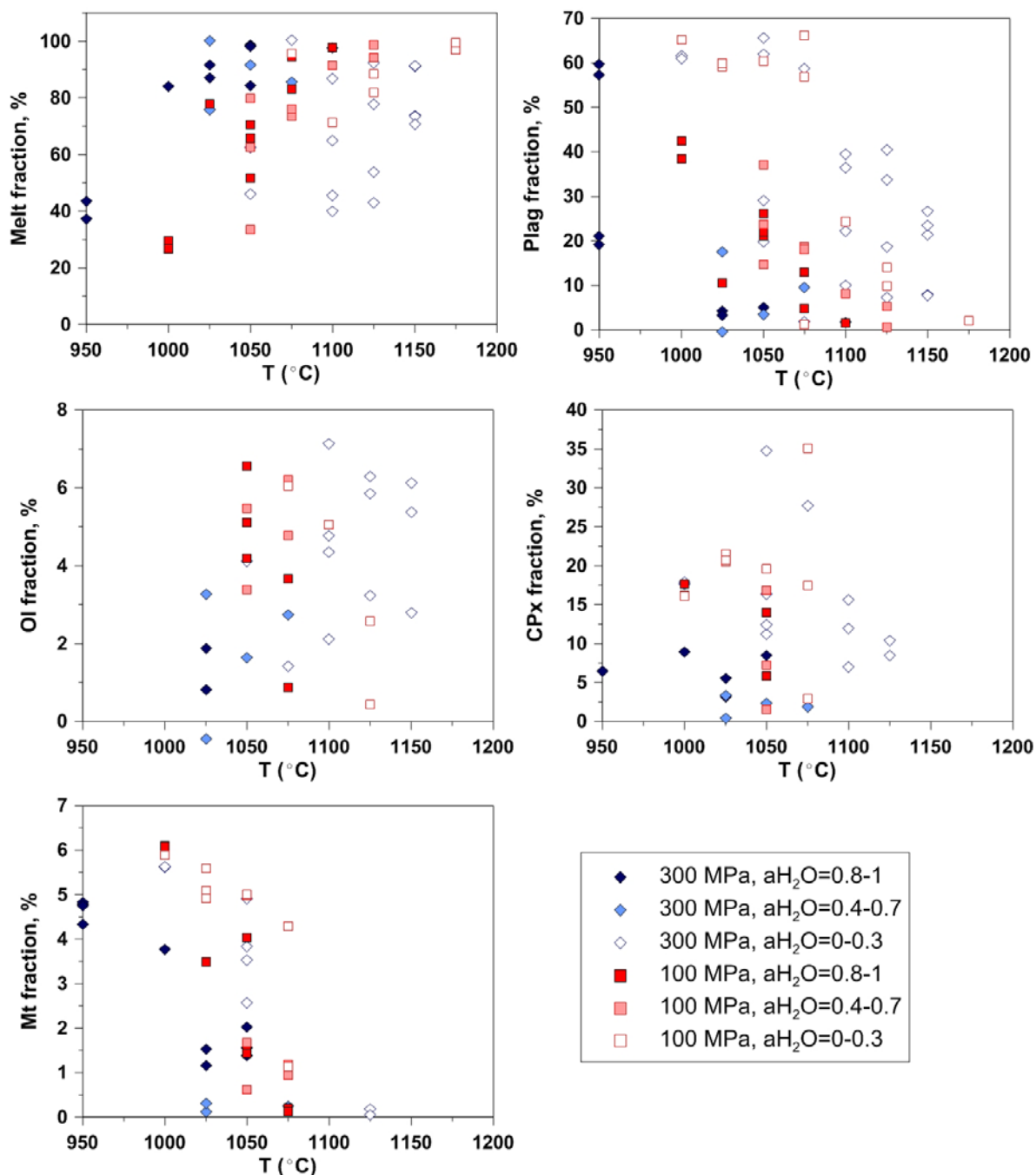


Fig. 1-21. Calculated phase proportions in run products at 300 MPa (blue symbols) and 100 MPa (red symbols) as a function of temperature and $a_{\text{H}_2\text{O}}$ (noted in the legend)

3.2.3. Phase compositions in experimental products

The compositions of minerals and glasses observed in the crystallisation experiments were analyzed by electron microprobe and are presented in Appendix, Tables A-1-5 to A-1-11).

With an aim to understand an effect of H_2O on evolution of the basaltic melt, run products were divided into three groups according to the water activity: $a_{\text{H}_2\text{O}}$: 0 – 0.3; 0.4 – 0.7 and 0.8 – 1.

Glass

300 MPa

Compositions of residual glasses in experimental products at 300 MPa vary from basaltic to andesitic (Appendix, Table A-1-5). Compositional differences between melts formed in the systems with different $a\text{H}_2\text{O}$ (from 0.0 to 1.0) as a function of temperature are shown in Figure 1-22). In temperature range from 1200°C to 1050°C melts almost do not differentiate, concentration of SiO_2 , MgO , CaO keeps almost constant, while slight enrichment in FeO-t is observed, which is typical for tholeiitic evolutionary trends. H_2O -saturated melts ($a\text{H}_2\text{O}=0.9-1.0$) start to differentiate only at temperatures below 1050°C, when crystallization of Cpx , Amph and Plag begins, and reach andesitic composition (2.7 wt.% MgO at 63.0 wt.% SiO_2) at 950°C (runs N28, 30).

Behavior of MgO , CaO and Al_2O_3 in melts is controlled by crystallization of silicates from the melt and depletion of these elements starts with the beginning of crystallization and starts at higher temperatures in H_2O -poor systems, than in H_2O -saturated. Differentiation of the dry systems is expressed in strong enrichment of residual melts with K_2O in course of crystallization due to decreasing of temperature (Fig. 1-22). At 1100°C dry melts contain around 0.54 wt.% K_2O , while H_2O -saturated melts preserve original concentration of about 0.2 wt.%.

There is no pronounced effect of $a\text{H}_2\text{O}$ on concentration of Na_2O in the residual melts. In general it acts as incompatible compound, its concentration increases in the melts with decreasing of temperature (Fig. 1-22).

Contents of FeO-t and TiO_2 in the residual melts are strongly dependent on crystallization of titanomagnetite. In dry systems Mt appears only at temperatures of about 1050°C that causes strong enrichment of the residual melts with FeO-t and TiO_2 in course of crystallization of silicates at temperature interval of 1200-1050°. Concentrations reach maximum of about 13 wt.% FeO-t and 2 wt.% TiO_2 . In dry melts below 1050°C concentrations of FeO-t and TiO_2 drop due to the crystallization of Ti-Mt and lie within the trend of hydrous-melts. Down to 1025°C melts with $a\text{H}_2\text{O}>0.3$ have almost constant content of FeO-t and TiO_2 (similar to the starting material). The most evolved compositions (N28, 30) contain about 4.6 and 0.7 wt.% of FeO-t and TiO_2 respectively. In performed experiments redox conditions were controlled by $a\text{H}_2\text{O}$, therefore hydrous conditions were simultaneously more oxidized and favored for early crystallization of magnetite.

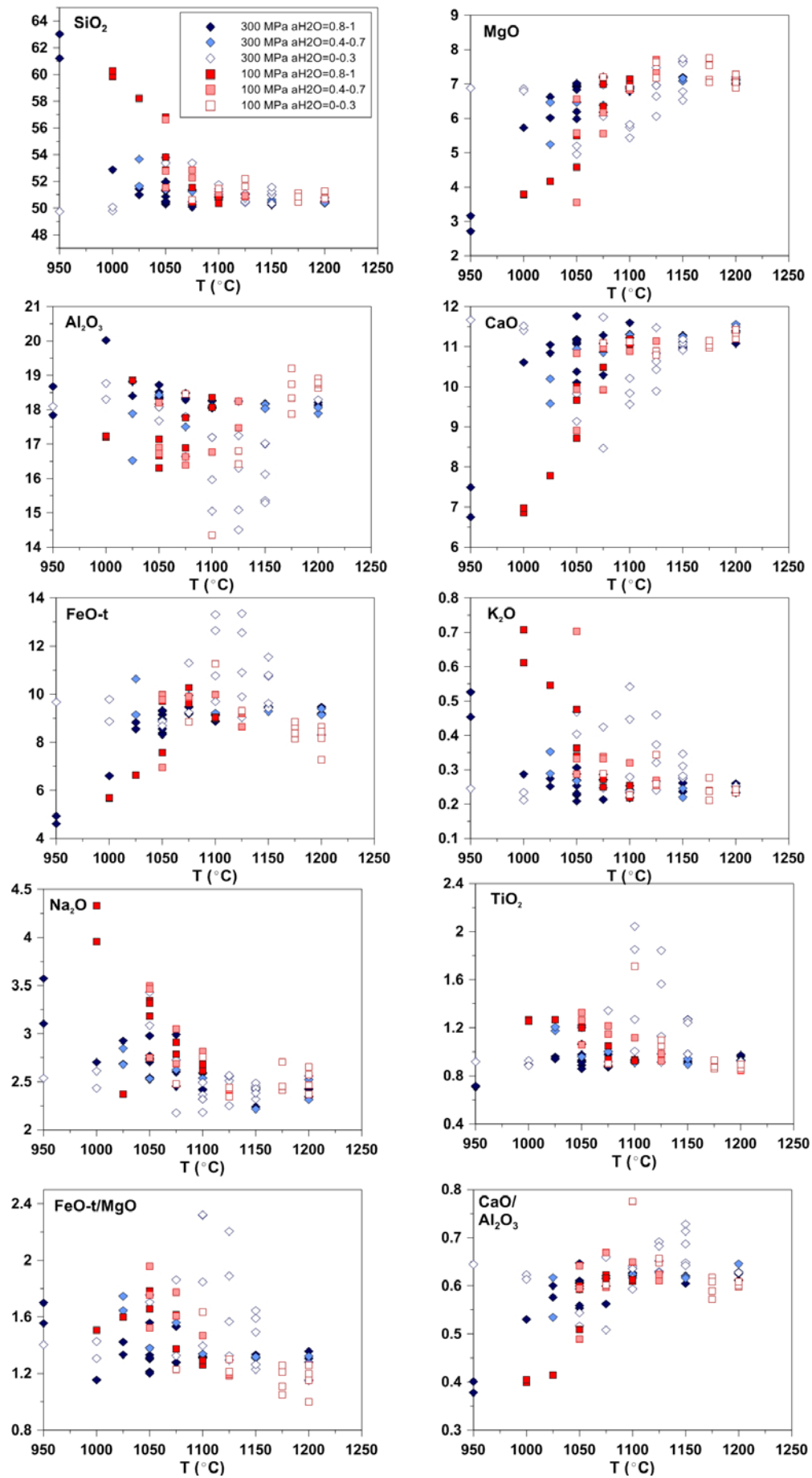


Fig. 1-22. Compositions of experimental melts as a function of temperature and $a_{\text{H}_2\text{O}}$ at 300 MPa (blue symbols) and 100 MPa (red symbols).

100 MPa

Compositions of residual glasses in experimental products at 100 MPa vary from basaltic to andesitic (Appendix, table A-1-5).

No pronounced systematic dependence of the major-element compositions of the residual melts on $a\text{H}_2\text{O}$ is observed in experiments at 100 MPa (Fig. 1-22). Dry glasses are characterized by strong FeO-t and TiO_2 , while depletion in Al_2O_3 , CaO and MgO with decrease of temperature and almost constant SiO_2 . Depletion of MgO in hydrous-melts ($a\text{H}_2\text{O}>0.3$) starts at temperatures of below 1125°C with the beginning of Ol crystallization. Since crystallization of plagioclase starts at about 1175°C in melts with $a\text{H}_2\text{O}=0.1$, that these melts are more depleted in Al_2O_3 than more hydrous where crystallization of Plag is delayed (Figs. 1-22).

Crystallization of titanomagnetite starts at about 1075°C in melts with $a\text{H}_2\text{O}$ below 0.6 and at higher temperature of $1100\text{-}1125^\circ\text{C}$ in more hydrous melts) (Figs. 1-22). This fact together with higher crystallization of the melt due to decreasing of temperature causes faster differentiation of the melt composition. FeO-t content in the melts increase until 1075°C where crystallization of magnetite starts and followed by sharp depletion of FeO (Fig. 1-22).

The most evolved melts at 100 MPa were reached at 1000°C in melts with $a\text{H}_2\text{O}=0.8$ (runs N128, 129) and contain about 60.0 wt.% SiO_2 and 3.8 wt.% MgO (Fig. 1-22).

Glass composition on Harker diagrams (100 and 300 MPa)

Differentiation trends of residual melts are presented on Harker-diagrams in coordinates of major-element oxides concentrations vs. SiO_2 (Fig. 1-23, 24) and vs. MgO (Fig. 1-25, 26). Effect of $a\text{H}_2\text{O}$ on the character of melt differentiation can be better observed for experiments at 300 MPa. Depletion of MgO from the melts starts after beginning of olivine crystallization. Plagioclase is a first phase on liquidus in H_2O -poor melts at 300 MPa leading to strong decrease of Al_2O_3 in dry melts in contrast to more hydrous melts. H_2O -saturated melts do not show depletion of Al_2O_3 due to very late crystallization of plagioclase. At 100 MPa plagioclase crystallizes before Ol and CPx in all range of $a\text{H}_2\text{O}$, so depletion in Al_2O_3 for all melts is observed, though for dry melts decrease in Al_2O_3 is faster. Dry and H_2O -poore ($a\text{H}_2\text{O}<0.2$) melts at 300 MPa are slightly depleted in CaO and Na_2O and noticeably enriched in K_2O in comparison to more hydrous melts. Significant increase of FeO-t and TiO_2 contents in dry and H_2O -poor melts

($a_{\text{H}_2\text{O}} < 0.2$) is caused by delayed crystallization of magnetite and large degree of crystallization of silicate minerals (Plag).

A general observation may be concluded: there are significant deviations of evolutionary trends between dry (H_2O -poor melts with $a_{\text{H}_2\text{O}}$ below 0.3) and hydrous glasses ($a_{\text{H}_2\text{O}}$ from 0.3 to 1).

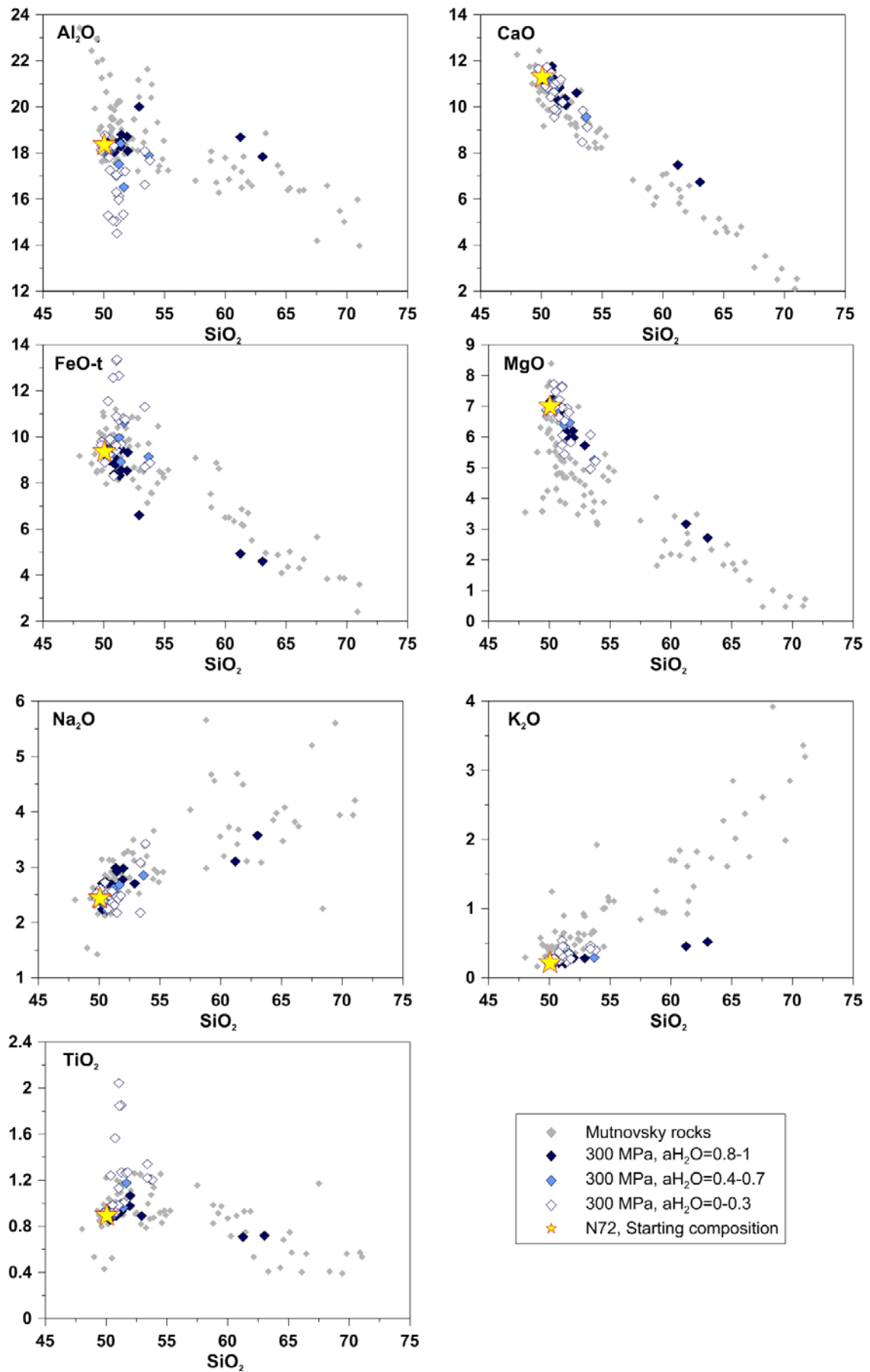


Fig. 1-23. Compositions of experimental melts as a function of SiO_2 (Harker diagrams) and $a\text{H}_2\text{O}$ at 300 MPa. Compositions of Mutnovsky rocks are shown for comparison.

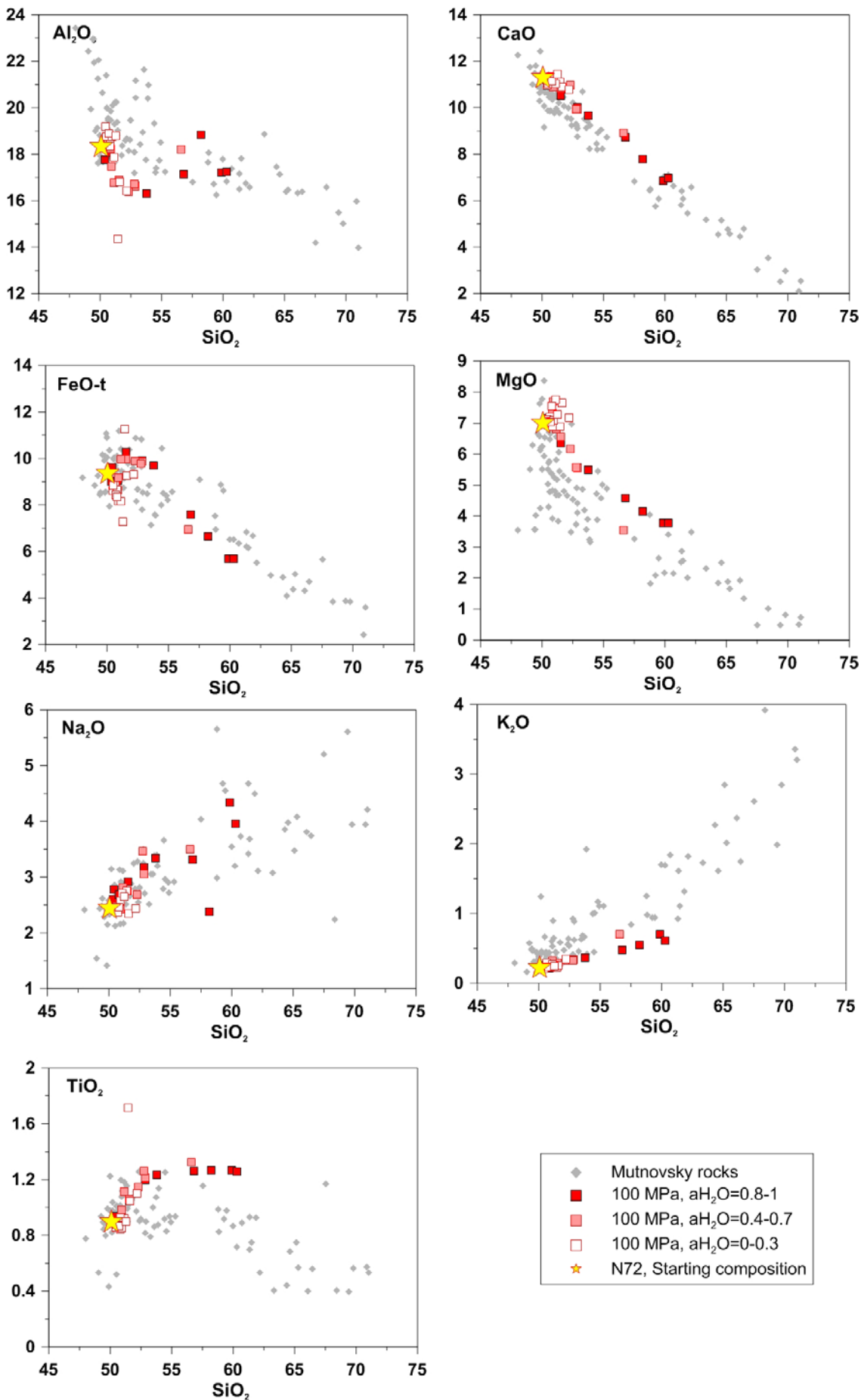


Fig. 1-24. Compositions of experimental melts as a function of SiO_2 (Harker diagrams) and $a_{\text{H}_2\text{O}}$ at 100 MPa. Compositions of Mutnovsky rocks are shown for comparison.

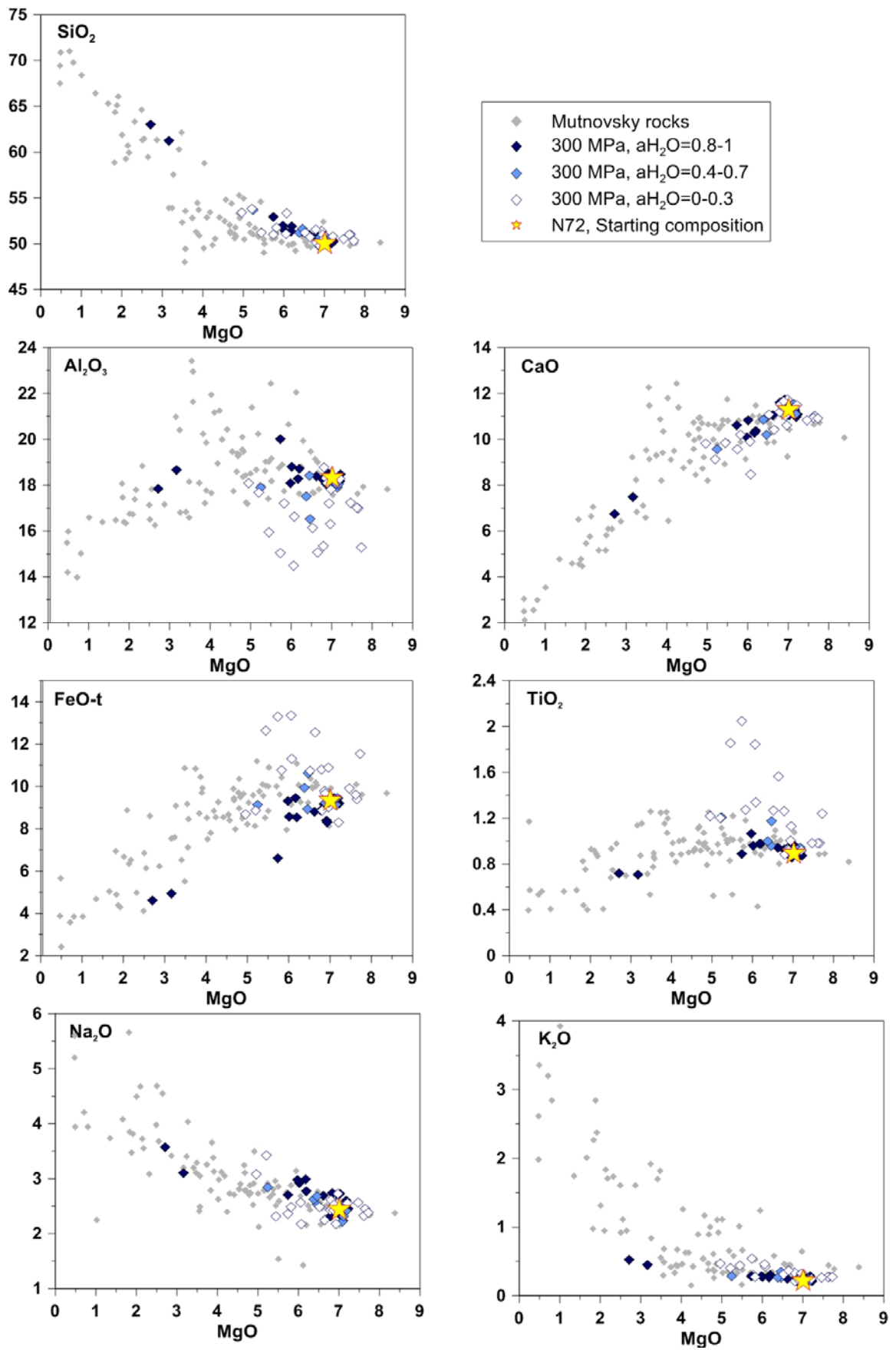


Fig. 1-25. Compositions of experimental melts as a function of MgO (Harker diagrams) and a_{H_2O} at 300 MPa. Compositions of Mutnovsky rocks are shown for comparison.

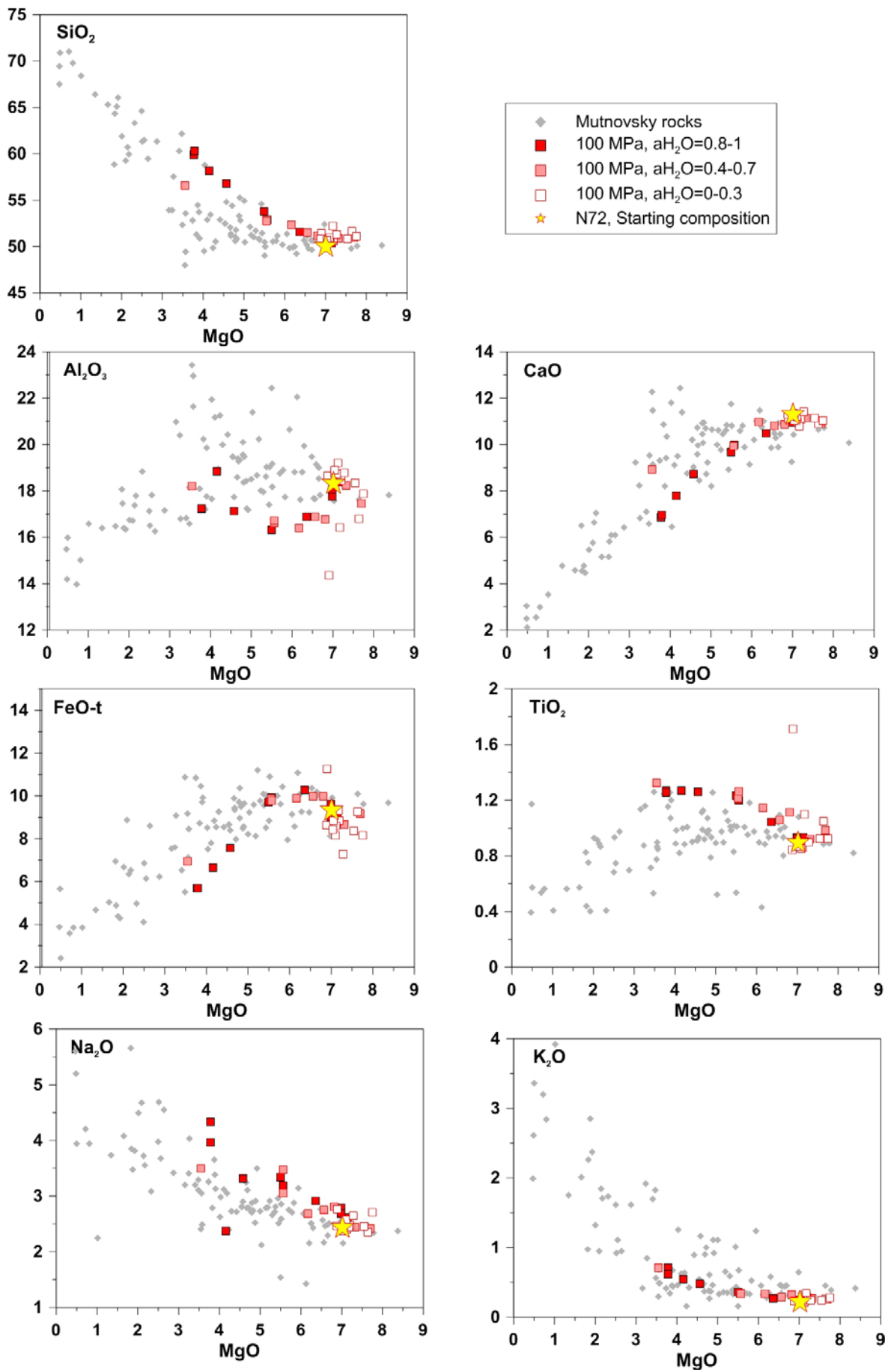


Fig. 1-26. Compositions of experimental melts as a function of MgO (Harker diagrams) and a_{H_2O} at 100 MPa. Compositions of Mutnovsky rocks are shown for comparison.

Plagioclase

Major-element compositions of experimental plagioclase in run products at 100 and 300 MPa are presented in Appendix, Table A-1-7.

Plagioclase is a first silicate mineral crystallized from melts in all range of a_{H_2O} at 100 MPa and in melts with less than about 5 wt.% H_2O at 300 MPa (corresponds to $a_{H_2O} < 0.7$) and crystallizes until solidus (Fig. 1-20). Plagioclase in run products forms elongated prismatic (rarely isometric) crystals (Fig. 1-19).

Composition of plagioclase varies from An61.3 to An89.6 in experiments at 300 MPa, and from An66.1 to An89.7 in experiments at 100 MPa. Positive temperature dependence on An-composition of plagioclase can be noticed for all range of a_{H_2O} (Fig. 1-27). More An-rich plagioclases crystallize at higher temperatures from the melts with constant a_{H_2O} . At the same temperature plagioclases formed from hydrous melts are significantly more enriched in An-component in comparison to plagioclase from dry runs (Fig. 1-27).

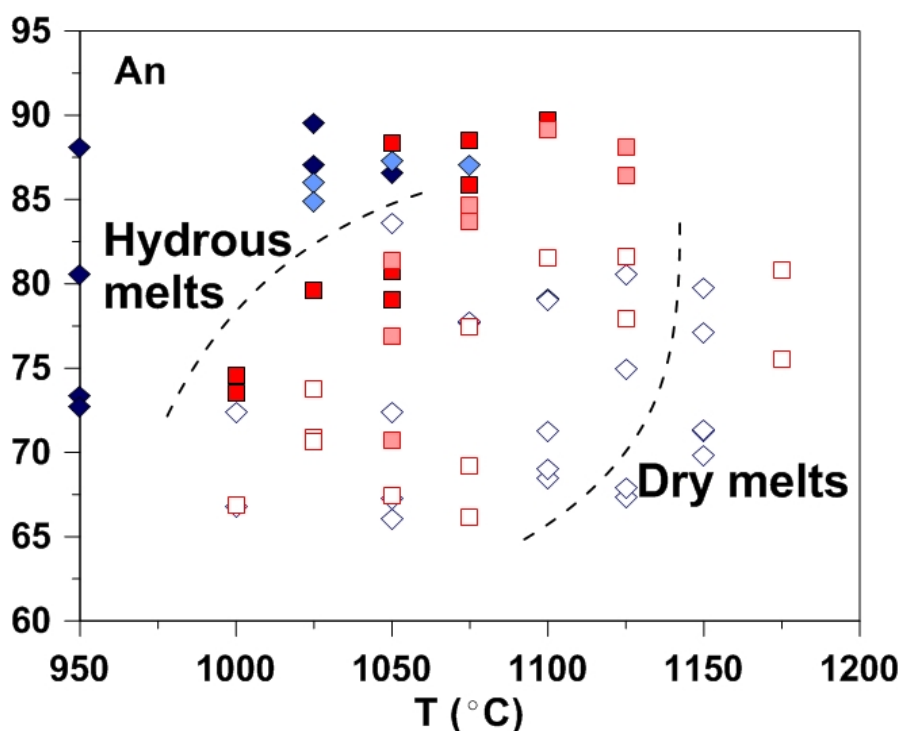


Fig. 1-27. Compositions of plagioclase vs. temperature and as function of a_{H_2O} at 300 and 100 MPa (symbols are the same as on Fig. 1-22).

Olivine

Major-element compositions of experimental olivine in run products at 100 and 300 MPa are presented in Appendix, Table A-1-6.

Olivine was crystallized in experiments at both pressures within wide ranges of temperatures and $a_{\text{H}_2\text{O}}$ (f_{O_2}) (Fig. 1-20). Usually olivine forms subidiomorphic isometric to elongated crystals, which in many cases contain poikilitic inclusions of plagioclase (Fig. 1-19).

Composition of olivine varies from Fo71.3 to Fo84.5 at 300 MPa and from Fo75.4 to Fo85.9 at 100 MPa. Clear dependence of olivine composition (Fo-number) on temperature, $a_{\text{H}_2\text{O}}$ in the system is observed (Fig. 1-28). Fo-number of olivine is positively correlated with temperature for all range of $a_{\text{H}_2\text{O}}$ and f_{O_2} . This dependence can be described as linear trend and has different slope for different $a_{\text{H}_2\text{O}}$ (and f_{O_2}). Trends of temperature-dependence for olivines from dry (more reduced) experiments have steeper slope then for olivines from hydrous (more oxidized) experiments.

Fo-numbers of olivines are positively correlated with Mg-numbers [$\text{Mg}/(\text{Mg}+\text{Fe}^{2+})$] of the coexisting residual melts with a distinct effect of $a_{\text{H}_2\text{O}}$ (Fig. 1-29). Olivine crystallized in dry conditions has less Fo-number then from hydrous experiments because of increase of $\text{Fe}^{3+}/\text{Fe}^{2+}$ in coexisting melt.

As it was discussed in a paragraph „Attainment of equilibrium“, in many of performed experiments values of K_d are too high (0.3 – 0.5) (Fig. 1-29) which may be attributed to overestimated $a_{\text{H}_2\text{O}}$ and therefore Fe^{3+} proportion in melts.

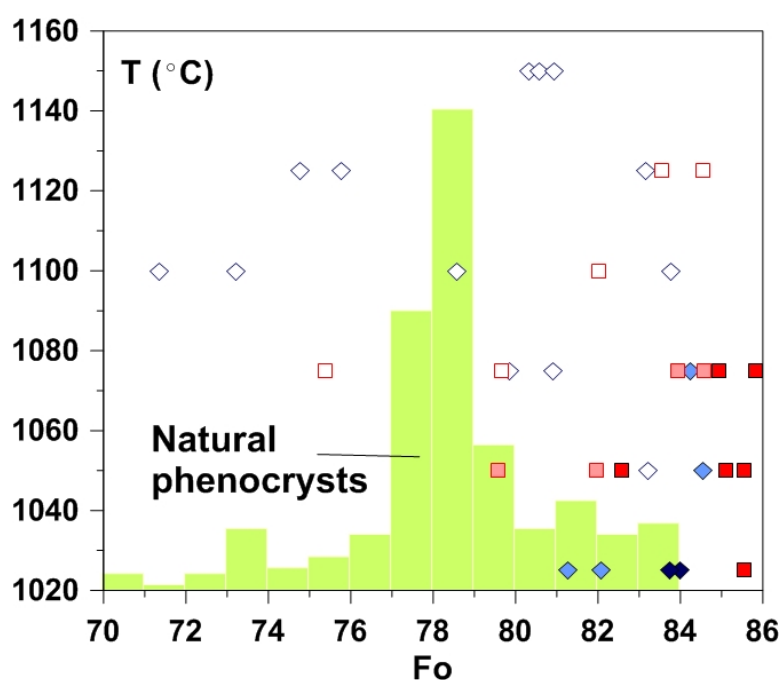


Fig. 1-28. Compositions of experimental olivines (Fo) vs. temperature and as function of $a_{\text{H}_2\text{O}}$ at 300 and 100 MPa (symbols are the same as on Fig. 1-22). For comparison histogram of compositions of natural phenocrysts from Mutnovsky basalts is shown.

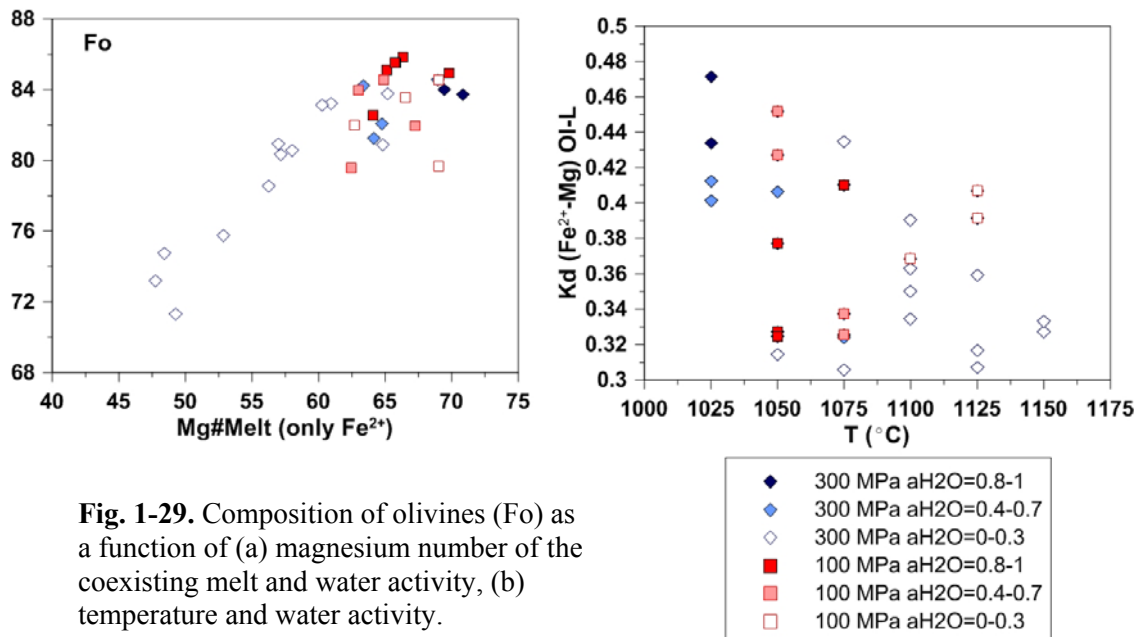


Fig. 1-29. Composition of olivines (Fo) as a function of (a) magnesium number of the coexisting melt and water activity, (b) temperature and water activity.

Clinopyroxene (high-Ca pyroxene)

Major-element compositions of experimental clinopyroxenes in run products at 100 and 300 MPa are presented in Appendix, Table A-1-8.

Mg#-number of clinopyroxene varies from 63.6 to 80.6 in experiments at 300 MPa, and from 58.6 to 81.4 in experiments at 100 MPa. From our experimental data a positive correlation between Mg#-number of clinopyroxene and temperature can be recognized (Fig. 1-30). The slopes of these trends are different for various *a*H₂O in the system. For experiments at 300 MPa a wider range of Cpx-compositions (Mg#-number) was formed from dry melts, whereas composition of clinopyroxenes almost does not change in H₂O-saturated melts with decrease of temperature. (similar observation in Botcharnikov et al., 2008). Similarly to olivines dry (reduced) melts produce less Mg#-rich clinopyroxenes than hydrous (oxidized) ones, where activity of Fe²⁺ in melts is decreased.

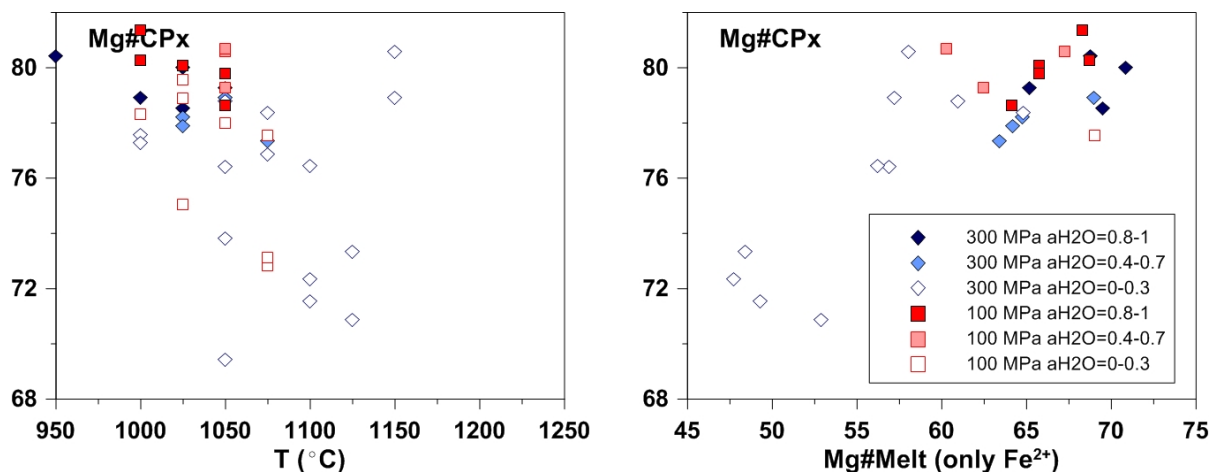


Fig. 1-30. Composition of clinopyroxenes (Mg#) as a function of (a) temperature and water activity, (b) magnesium number of the coexisting melt and water activity.

Orthopyroxene (low-Ca pyroxene)

Major-element compositions of experimental clinopyroxenes in run products at 100 and 300 MPa are presented in Appendix, Table A-1-9.

Mg#-number of orthopyroxene varies from 73.2 to 82.6 in experiments at 300 MPa, and from 71.3 to 84.3 in experiments at 100 MPa. Positive correlation of Mg#-number with temperature at the same $a_{\text{H}_2\text{O}}$ is observed (Fig. 1-31). Orthopyroxene crystallized from H_2O -saturated melts has significantly more Mg#-number, then from dry melts.

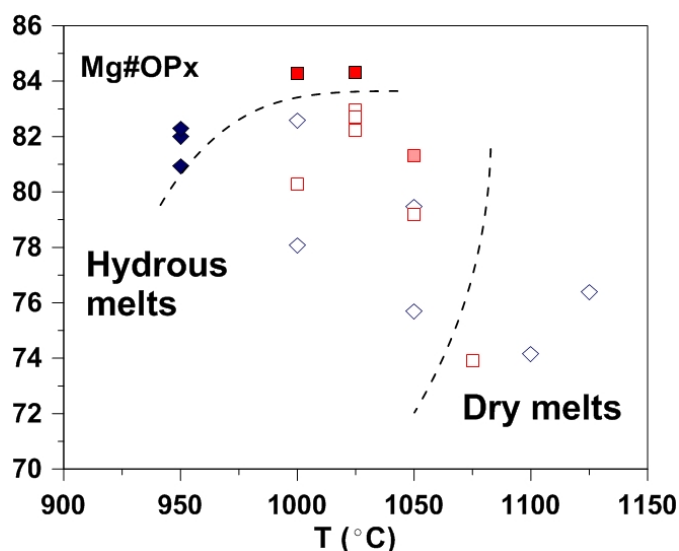


Fig. 1-31. Compositions of orthopyroxene (Mg#) vs. temperature and as function of $a_{\text{H}_2\text{O}}$ at 300 and 100 MPa (symbols are the same as on Fig. 1-22).

Amphibole

Major-element compositions of experimental amphiboles in run products at 300 MPa are presented in Appendix, Table A-1-10.

Ca-amphiboles (hornblende: magnesiohastingsite, according to the classification from Leake et al., 1997) were observed in five runs at 300 MPa and 950 and 1000°C (Fig. 1-19, 1-20). Mg#-number of amphiboles is 72.9 to 75.7 at 950°C and 77.2 at 1000°C. The dataset is not enough to make any conclusions about temperature or $a_{\text{H}_2\text{O}}$ effects on the amphibole composition.

Titanomagnetite

Major-element compositions of experimental titanomagnetites in run products at 100 and 300 MPa are presented in Appendix, Table A-1-11.

Content of Mt-component in experimental titanomagnetites vary between 0.55 and 0.8. At a constant temperature magnetites from more H_2O -rich experiments are enriched in Mt-component in comparison to more dry ones. Positive correlation between Mt-number (X Mt) and $a_{\text{H}_2\text{O}}$ and f_{O_2} can be definitely detected.

4. DISCUSSION

4.1. Comparison of natural and experimental phase associations

As it has been shown before (Results, part 3.3. – 2, Table 1-3), several stages of mineral crystallization (generations of phenocrysts) can be identified in natural magmas (basalts and basaltic andesites), considering their petrographical features such as size and crystal shape and their mineral compositions: phenocrysts (cores), microphenocrysts (cores) and microlites in groundmass. The mineral association observed in phenocrysts and microphenocrysts are similar for most of the studied samples and is represented by **Plag+Ol±CPx (+Mt) - association**. Mineral associations in groundmass of basalts differs from sample to sample by the presence additional Opx and the lack of Ol: Plag+Ol+CPx+Ti-Mt, Plag+CPx+OPx+Ti-Mt or Plag+CPx+OPx (Table 1-3). In dacite KM9-8 we 2 main parageneses have been distinguished: phenocrysts of Plag+CPx+OPx+Mt-Ilm and groundmass consisting of glass with microlites of Plag, KFsp, Qtz, CPx and Mt. Our new observations of phenocrysts and microphenocrysts associations in mafic samples are in a good agreement with the previous studies, which reported that Plag-Ol±CPx-phyric basalts are the most typical rock species of the last stages of Mutnovsky volcanic activity (Mutnovsky-III, IV) (Selyangin, 1993; Chashchin et al., 2011).

The set of main mineral associations of Mutnovsky basalts have been reproduced in our **experiments at both 100 and 300 MPa** (Fig. 1-20a,b; 32a,b). For both pressures, different mineral associations can be observed within restricted ranges of temperatures and melt water concentrations, as it is shown on phase diagrams by colored fields (Fig. 1-20, 32).

Plag+Ol±CPx (+Mt) association of natural **phenocrysts** (microphenocrysts and some groundmasses) is well bracketed by mineral stability curves and corresponds to two fields on the phase diagrams: Plag+Ol and Plag+Ol+CPx.

At 300 MPa association of plagioclase with olivine (Plag+Ol without CPx, yellow field on phase diagrams, Fig.1-32a) is stable in a narrow range of temperatures. At nominally dry conditions Ol and Pl crystallize together at temperatures between 1155 and 1175°C. Increase of H₂O content in the system causes shifting of temperature interval of Plag+Ol-stability field downwards to lower temperature values. The maximum melt H₂O content at which Ol+Pl-association is still stable is about 3 - 3.5 wt.% H₂O which corresponds to *a*H₂O of about 0.5 and *f*O₂ close to QFM+2.7 (T=1075°C). It should be noted that a large part of Plag+Ol stability field at 300MPa is located above the stability field of magnetite (Fig.1-32), which became a liquidus phase at 1100°C and ~3 wt.% H₂O.

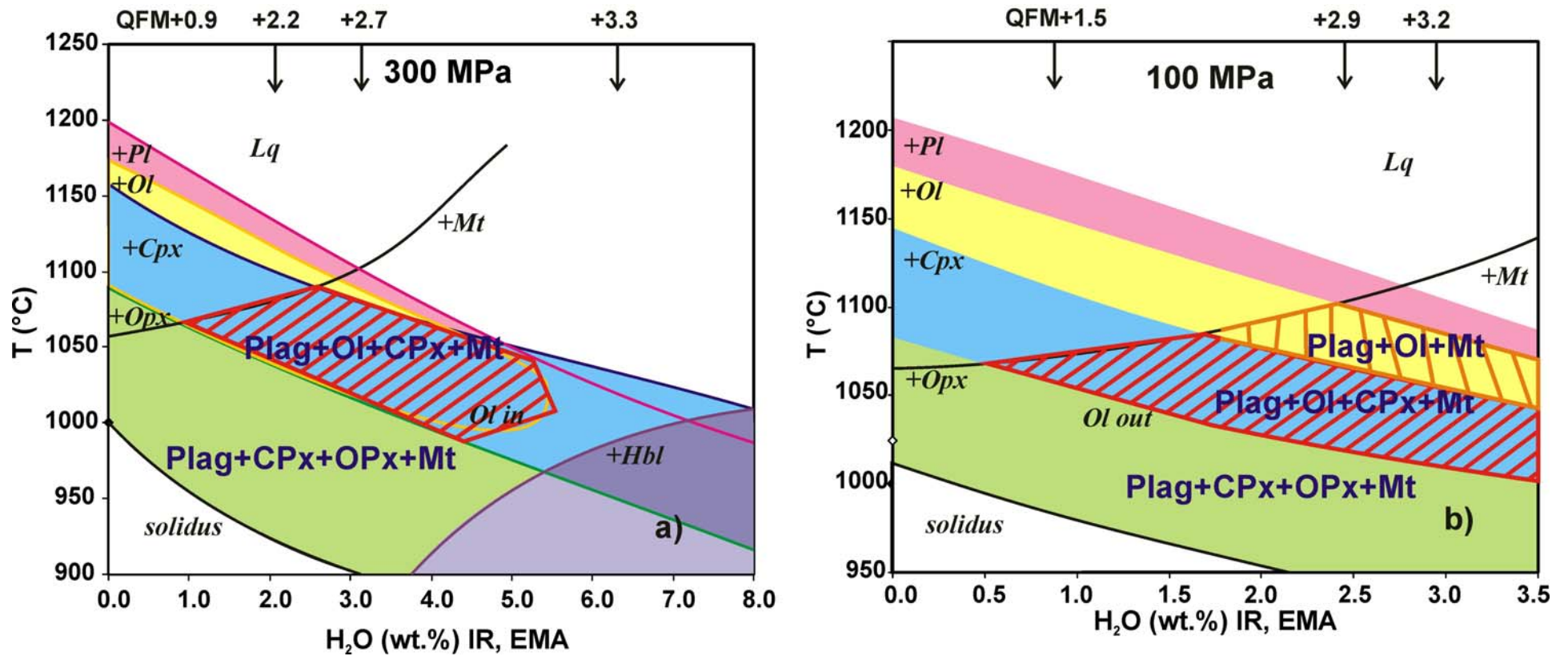


Fig. 1-32. Phase diagrams for Mutnovsky tholeiitic basalt determined after phase relation experiments at 100 and 300 MPa. Fields of stabilities for different mineral associations are shown in different colours. Dashed fields represent natural associations of phenocrysts in Mutnovsky basalts.

Though in natural lavas magnetite is scarce phenocryst, the presence of small proportion of Mt in Mutnovsky parental magma is required due to the prominent lack of TiO₂ enrichment in whole rock compositions. According to our experimental observations, the Cpx-free Ol+Plag+Mt association can exist only within a narrow range of conditions: 2.5 - 3.5 wt.% H₂O and 1075-1090°C (Fig.1-20, 32a).

In contrast, the main phenocrysts association of Mutnovsky basalts Plag+Ol+CPx was reproduced at lower temperatures (blue field on phase diagrams, Fig.1-20, 32a) in a wide range of melt water contents up to 5.5 wt.% H₂O (from nominally dry conditions to almost water-saturated, $a_{\text{H}_2\text{O}}=0.9$). Temperature interval of the stability field for Plag+Ol+CPx association varies from about 1090 - 1155°C at dry conditions to 1000 - 1025°C at H₂O-saturated. At lower $a_{\text{H}_2\text{O}}$ only three silicate crystallize from the melt, whereas at conditions with higher $a_{\text{H}_2\text{O}}$ (f_{O_2}) magnetite also becomes stable phase in addition to Plag+Ol+CPx. **In general, crystallization of natural Plag+Ol+CPx+Mt phenocrysts associations can be reproduced at 300 MPa in melts containing 1 to 5.5 wt.% H₂O.**

At 100 MPa associations of Plag+Ol and Plag+Ol+CPx are stable within the whole range of $a_{\text{H}_2\text{O}}$: from nominally dry to H₂O-saturated conditions (Fig. 1-32b). Similarly to the experiments at 300 MPa, association of Plag+Ol crystallizes at higher temperatures than that of Plag+Ol+CPx. For Plag+Ol association temperature intervals are about 1145-1175°C at $a_{\text{H}_2\text{O}}=0$ and 1050-1075°C at $a_{\text{H}_2\text{O}}=1$. Crystallization of Plag+Ol+CPx association occurs between 1075 and 1145°C at dry conditions and 1000 and 1050°C at H₂O-saturated conditions. Plag+Ol+Mt association is crystallizing from melts with more than about 1 wt.% H₂O ($a_{\text{H}_2\text{O}}$ higher 0.15 or f_{O_2} higher then QFM+1.5) at temperatures above 1105°C. **Crystallization of Plag+Ol+CPx+Mt association at 100 MPa is observed for dry to H₂O-saturated melts.**

The typical association of groundmass **microlites** Plag+CPx+OPx±Mt was experimentally reproduced at both pressures (green field on phase diagrams, Fig. 1-32). For all $a_{\text{H}_2\text{O}}$ investigated, this mineral association is stable at lower temperatures than Plag+Ol+CPx-association. Low-Ca-pyroxene (Opx) replaces olivine as a result of peritectic reaction, and these two minerals were not found together in natural rocks. However in our experiments there are two runs at 300 MPa (N42, N47) and one run at 100 MPa (N99) where Opx and Ol were coexisted. In addition, due to lower temperature of Opx stabilization, in experiments at both pressures Opx always joins the magnetite-bearing solid assemblage (Plag+CPx+Mt). Magnetite is always presented in groundmass of Mutnovsky basaltic lavas where it crystallizes together with silicate minerals: Plag+Ol+CPx or

Plag+CPx+OPx. But in studied tephra samples (KM9-10 and 11) microlites of Mt are absent in quenched residual glass. Probably this observation shows that redox conditions during crystallization of groundmass of lavas were relatively reduced, which prevented Mag crystallization.

Thus, comparison of natural and experimental data demonstrate that mineral associations observed in Mutnovsky basalts were successfully reproduced for both pressures 100 and 300 MPa at following conditions:

Phenocrysts: 1000-1075°C, at least 1.5–2.0 wt% H₂O;

Microlites in groundmass: 1050-1075°C, dry systems.

4.2. Comparison of natural and experimental mineral compositions

To discuss chemical evolutionary trends for both natural and experimentally produced minerals, mineral major element compositions were recalculated to mineral components and element ratios: forsterite component (Fo) for olivine, anorthite component (An) for plagioclase, magnesian number ($Mg\# = (Mg/Mg+Fe^{total}) \text{ mol.}\%$) and En (enstatite) – Fs (ferrosillite) – Wol (wollastonite) for CPx and OPx. Histograms of natural mineral compositions summarized in Fig. 1-33 illustrate the general progression of mineral compositional evolution for different mineral generations in the sequence phenocrysts - microphenocrysts - microlites.

Compositional ranges of experimental **olivines** at 100 MPa (Fo 72-86) and 300 MPa (Fo76-84) overlap with the range of natural olivine compositions (Fo52-84). Compositions of natural olivine phenocrysts (cores) form a very pronounced maximum on the histogram in a narrow interval of Fo77-80 with a second smaller maximum at Fo80-84. The first interval (Fo77-80) was reproduced only in a few experiments at 100 and 300 MPa with intermediate water activities ($a_{H_2O} = 0.1 - 0.4$) (corresponds to QFM+0.5 to QFM+1.5 at 300MPa and about QFM+3 at 100MPa) at temperatures 1050-1100°C. More Mg-rich olivines (>Fo80, up to Fo86 at 100MPa) were crystallized in a wide range of experimental conditions at both pressures (Fig. 1-28): from H₂O-poor melts ($a_{H_2O} \approx 0.1-0.3$) at higher temperatures (1150°C) to almost H₂O-saturated ($a_{H_2O}=1$) with decrease of temperatures down to about 1025°C. At the same time a wide range of more Fe-rich natural olivines (Fo52-71) (typically microlites or microphenocrysts) was not reproduced in the performed experiments at both pressures at any studied temperature within all range of water activities.

Natural **plagioclases** in Mutnovsky basalts from different mineral parageneses: phenocrysts, microphenocrysts and microlites, form a very wide range of compositions in

terms of their anorthite component: An46 – An98. Compositions of experimental plagioclases at both pressures (An66–90 at 300 MPa, An67–90 at 100 MPa) are located within the natural range. High-Ca plagioclases (An85-94, bytownite-anorthite) represent typical natural phenocrysts in Mutnovsky basalts and were reproduced in experiments at both pressures, though experimentally produced Pl never more anorthitic than An90. Usually, the most Ca-rich plagioclases were crystallized in runs with high water activity ($a_{\text{H}_2\text{O}}=0.8-1$) in a wide temperature range of 950-1075°C (Fig.1-27). Natural microphenocrysts and microlites are less calcic plagioclases (An 59-77) which form another maximum on the histogram (Fig. 1-11). This compositional range was completely reproduced in our experiments. The least Ca-plagioclases in experiments at 100 and 300 MPa are An 66-67 (only one run with An 61 at 300 MPa), they were crystallized in runs with nominally dry ($a_{\text{H}_2\text{O}}\approx 0$) or water-poor ($a_{\text{H}_2\text{O}}=0.1-0.3$) conditions at temperatures of 1000-1125°C at 300 MPa and 1000-1075°C at 100MPa (Fig. 1-27).

Compositions of experimentally produced **high-Ca-pyroxenes** almost completely reproduce natural clinopyroxenes (Fig. 1-33). In terms of magnesian number (Mg#) compositions of CPx phenocrysts vary in the range of 74 to 81 with a maximum at 77-80, while more Fe-rich microlites and microphenocrysts vary in the range of Mg#69-78. In performed experiments at 300MPa (Mg#CPx=70–81) and 100MPa (Mg#CPx=72–82) compositions of CPx similar to natural phenocrysts were produced in a wide range of temperatures (950-1150°C at 300MPa and 1000-1050°C at 100MPa) and water activities from H₂O-poor to H₂O-saturated (Fig. 1-30).

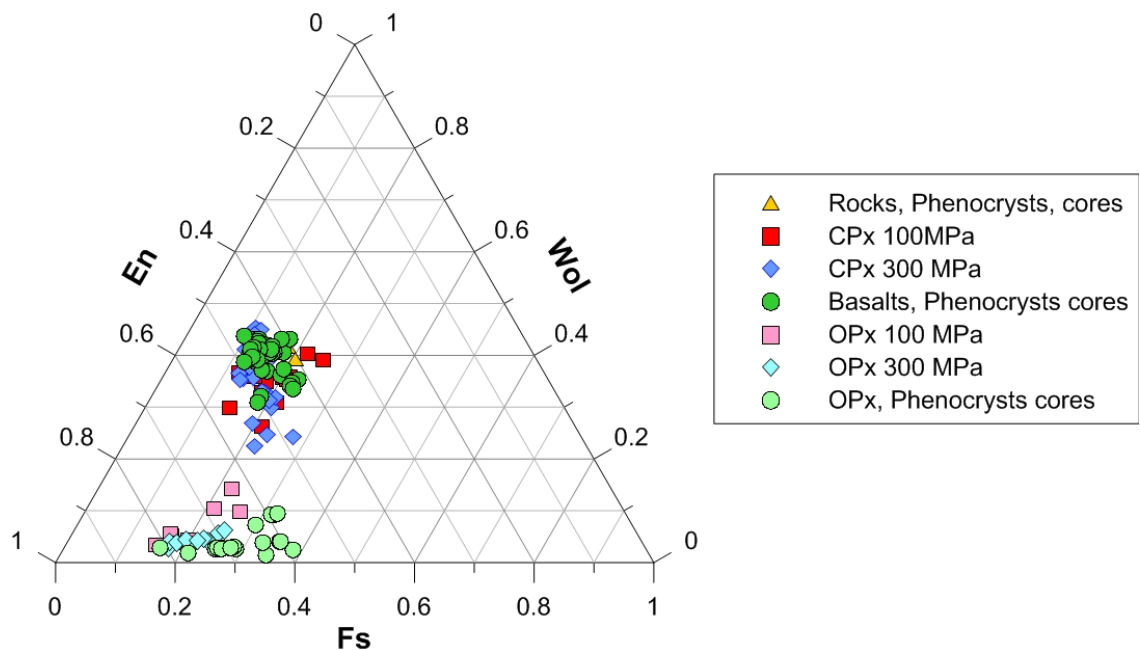


Fig. 1-33. Compositions of experimental and natural clino- and orthopyroxenes shown in the triangular projection ferrosillite (Fs) - wollastonite (Wo) – enstatite (En)

On the projection of compositions of pyroxenes onto the triangular diagram in coordinates Fs-Wol-En (Ferrosillite-Wollastonite-Enstatite) compositions of natural CPx-phenocrysts in basalts (Fs10-23 Wol31-44 En39-51) and experimental compositions at 100 MPa (En36-52 Wol26-43 Fs11-25) and 300 MPa (En42-55 Wol23-47 Fs11-28) are overlapping and therefore show that CPx phenocrysts could crystallize at both of studied pressures at various aH₂O and temperatures (Fig. 1-33).

Low-Ca-pyroxene (orthopyroxene) does not belong to phenocryst association of Mutnovsky basalts, but does occur in andesites and dacites. In studied samples of dacite OPx phenocrysts have a composition of En68-72 Wol3 Fs25-29, Mg#70-74. In general OPx from andesites and dacites are different from those from experiments at both pressures (Fig. 1-33)

In studied mafic samples **OPx** usually were presented only as microlites in groundmass (mainly Mg#OPx=71-78), though more Fe-rich (Mg# 55-65) OPx-microlites were found in one studied sample (KM9-6) and reported in earlier studies (e.g. Chashchin, 2011). Compositions of the experimentally produced OPx are shifted to more Mg-rich values in comparison to natural: Mg#CPx74–83 at 300MPa and Mg#CPx72–85 at 100MPa (Fig. 1-31, 33). They reproduce part of the compositional range of natural OPx-microlites (Mg#72-78). They were crystallized in nominally dry runs at both pressures in temperature range of 1000-1125°C at 300 MPa and 1050-1075°C at 100MPa (Fig. 1-31). More Mg-rich (>Mg#80) OPx were crystallized at relatively high aH₂O and lower temperatures (below 1050C) in association with CPx and Plag.

4.3. Compositions of coexisting minerals in natural rocks and experimental products

More accurately crystallization conditions of natural mineral generations can be bracketed by comparison of compositions of coexisting minerals in natural samples with their experimental counterparts (Fig. 1-34).

Compositions of experimental minerals at 100 and 300 MPa in an every chosen pair (Ol-Plag, Plag-CPx, Ol-CPx, CPx-OPx) vary systematically following a certain trend from more primitive to more evolved compositions for every mineral in a pair (Fig. 28 a-d). This behavior is similar to evolutionary trend observed in coexisting natural phenocrysts, microphenocrysts and microlites. Moreover, compositions of coexisting minerals in run products are very close to natural ones and even overlap with them. This observation shows that at certain experimental conditions not only compositions of natural single mineral phases were reproduced, but also, more importantly, cotectic compositions (mineral phases

crystallized simultaneously). Since, compositional trends at 100 and 300 MPa are almost identical, we may conclude that natural associations could crystallize at both pressures.

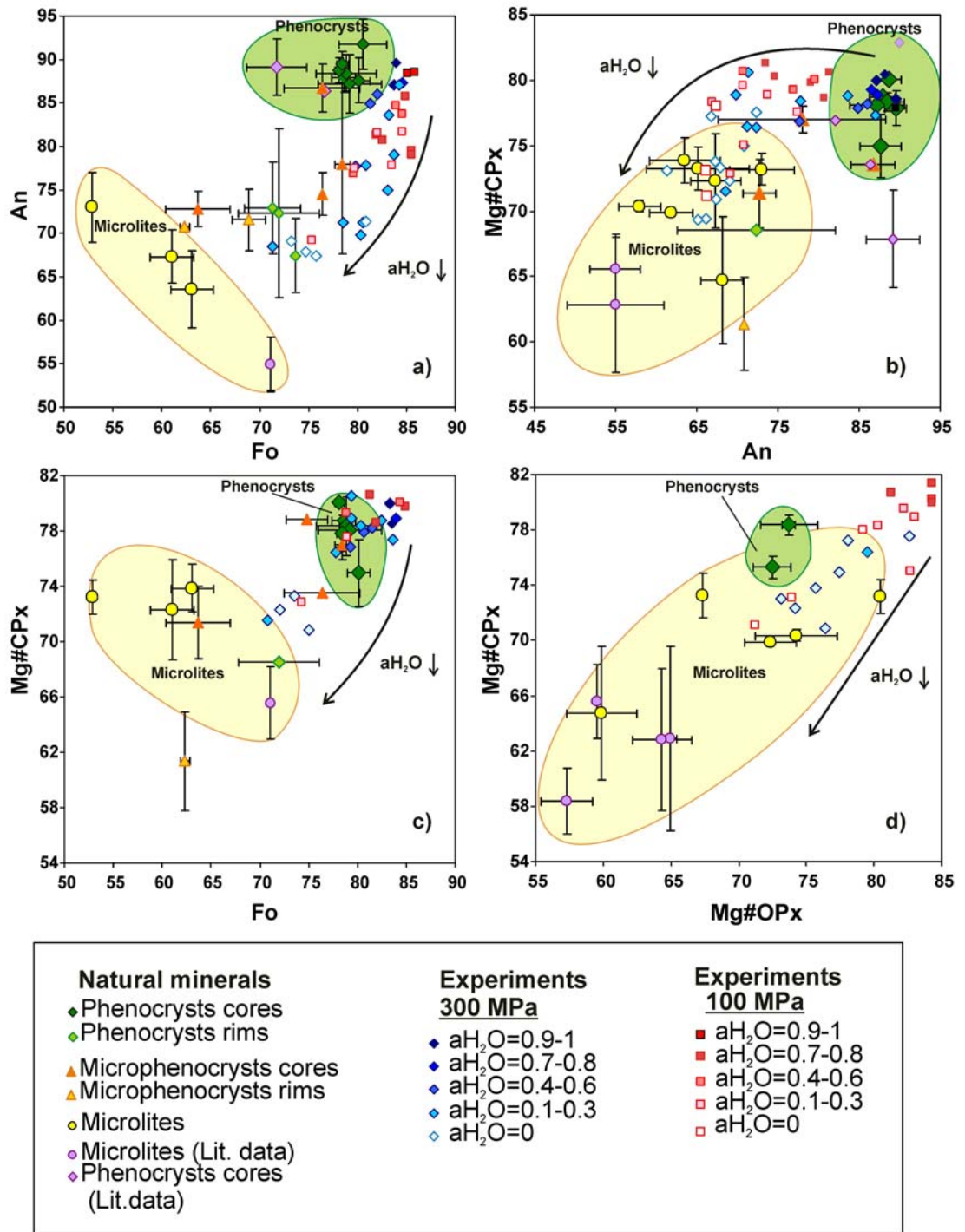


Fig. 1-34. Comparison of compositions of coexisting minerals from natural associations of Mutnovsky and experimental products at 100 and 300 MPa. Effect of aH_2O on compositions of experimental phases is shown (see Legend). Studied samples are presented together with literature data (Martynov, Chashchin, 1989; Chashchin et al., 2011).

The effect of water (in terms of aH_2O) in the system on compositions of coexisting minerals is shown on Fig. 1-34. Similarly to the relationship between composition of single mineral and intensive parameter (Discussed in paragraphs 3.2.3, Figs.1-27-31) we can

conclude that: at the same temperature compositions of minerals (single or co-existing) vary in a wide range depending on $a\text{H}_2\text{O}$ (since water has a significant effect on liquidus temperatures of silicates, especially plagioclase). The most primitive compositions were crystallized from H_2O -rich melts (and also more oxidized), while the most evolved – from dry melts at relatively reduced conditions.

The most primitive mineral pairs (high-Ca-Plag + Mg-rich Ol and CPx) were crystallized from H_2O -rich melts ($a\text{H}_2\text{O}=0.4-1.0$). In general, decrease of $a\text{H}_2\text{O}$ causes shifting of compositions of coexisting minerals to more evolved region. The main effect changes in $a\text{H}_2\text{O}$ produce on the composition of plagioclase: increase of $a\text{H}_2\text{O}$ (H_2O content in melt) causes crystallization of more Ca-rich plagioclase (at the same temperature) (Fig. 1-27, 34) in an association with Ol or (and) CPx, while compositions of these mafic minerals remain almost constant in a wide range of $a\text{H}_2\text{O}$ (Fig. 1-34). Significant increase of Fe# of Ol and CPx is observed only in the most H_2O -poor (dry) and reduced conditions.

The most Ca-rich plagioclases (An85-90) corresponding to the natural phenocrysts were crystallized from melts with $a\text{H}_2\text{O}=0.4-1$ in association with Ol or with Ol+CPx at 300 MPa (Fig. 1-34). At 100 MPa plagioclase of similar Ca-rich (An 86-90) composition crystallizes only in association with olivine from the melts with H_2O more than 2 wt.%. However, as soon as CPx joins the onset of Plag+Ol crystallization, coexisting plagioclase becomes less Ca-rich (An77-82). One of the explanations can be that Ca is also distributed to the Ca-rich pyroxene instead of plagioclase, though at 300 MPa we do not see such a behavior. Olivines coexisting with such An-rich plagioclases are a more Mg-rich, than natural ones at both pressures. Experimental olivines can be as Mg-rich as Fo86, while natural olivine phenocrysts are always below Fo84 with average Fo78-80. Compositions of CPx in equilibrium with the most Ca-rich plagioclases and Mg-rich olivines in H_2O -rich experiments at 300 MPa are completely overlapped with natural ones (Mg#77-81). At the same time CPx from performed most H_2O -rich ($a\text{H}_2\text{O}=0.7-0.8$) experiments at 100 MPa have similar composition to natural CPx phenocrysts but they are in equilibrium with less Ca-rich plagioclases (only up to An81). Probably in H_2O -saturated experiments at 100 MPa we would also observe crystallization of high-Ca-plagioclase (An90) in association with Ol+CPx.

According to the phase diagram in Figs. 1-32 the best conditions for crystallization of natural Plag+Ol+CPx+Mt are observed at 300MPa pressure in a temperature interval of 1025-1075°C; magmas must have more than 2 wt.% H_2O ($a\text{H}_2\text{O}=0.3-1.0$ in melt). It is not clear from our experimental dataset if at 100 MPa crystallization of high-Ca-Plag with Ol+CPx is possible at H_2O -saturated conditions. Crystallization of two-mineral association

(Ol+Plag(+Mt)) could happen also at lower pressure (100 MPa) as a result of crystallization of H₂O-saturated basaltic magma at 1050-1075°C.

Crystallization of most evolved set of minerals (microphenocrysts, rims of phenocrysts and microphenocrysts) occur in melts with lower H₂O-content in magmas that were probably degassed during the ascending. Compositions of microlite association Plag+CPx+OPx±Mt were reproduced in nominally dry experiments at both pressures at temperatures of 1050-1075°C. Association of phenocrysts in studied dacite (Plag+CPx+OPx+Mt-Ilm) could not be reproduced by crystallization of basaltic melt at investigated conditions. Though compositions of coexisting CPx and OPx were very close to the natural ones in several experiments with nominally dry melts, but they are in equilibrium with more Ca-rich plagioclase (An 60-65) than Na-rich plagioclase An40 presenting as phenocrysts in natural dacite.

4.4 Comparison of natural and experimental LLDs

Evolutionary trends of Mutnovsky volcanic series (bulk rocks, residual glasses and melt inclusions) were described in a paragraph 3.1.4. Effects of experimental conditions (temperature and aH₂O) on compositions of residual melts in crystallization experiments at 100 and 300 MPa were discussed in a paragraph 3.2.3. Below we compare experimental and natural LLDs (Fig. 1-35, 36).

Compositions of experimental glasses follow distinct evolution trends depending on water activity (aH₂O) in the system and accordingly to redox conditions. These parameters affect liquidus temperatures and sequences of crystallization of mineral phases (especially plagioclase and magnetite) and subsequently cause variations in compositions of residual melts. For comparison of natural and experimental LLDs, compositions of Mutnovsky bulk rocks, residual glasses and melt inclusions are plotted on Harker diagrams (major-element oxides vs. SiO₂ and MgO) together with compositions of residual experimental glasses at 100 and 300 MPa, which, in turn, are divided into three groups with low, middle and high aH₂O (Fig. 1-35). For clarity, we demonstrate only compositions of experimental glasses that were in equilibrium with Plag+Ol (±Mt) and Plag+Ol+CPx (±Mt) mineral associations.

Experimental glasses produced at both pressures follow natural trend of Mutnovsky melt evolution for some of major-element oxides: SiO₂, MgO, CaO, Na₂O irrespective to the aH₂O. Concentrations of K₂O are slightly, but systematically lower in experimental glasses in comparison to natural rocks and melt inclusions at the given SiO₂. In basaltic region K₂O-content in experimental glasses overlap with low-K₂O natural compositions and difference becomes more pronounced for evolved melts (Fig. 1-35, 36). The

enrichment of natural lavas with respect to K_2O probably indicates on importance assimilation or contamination processes in magma genesis beneath Mutnovsky.

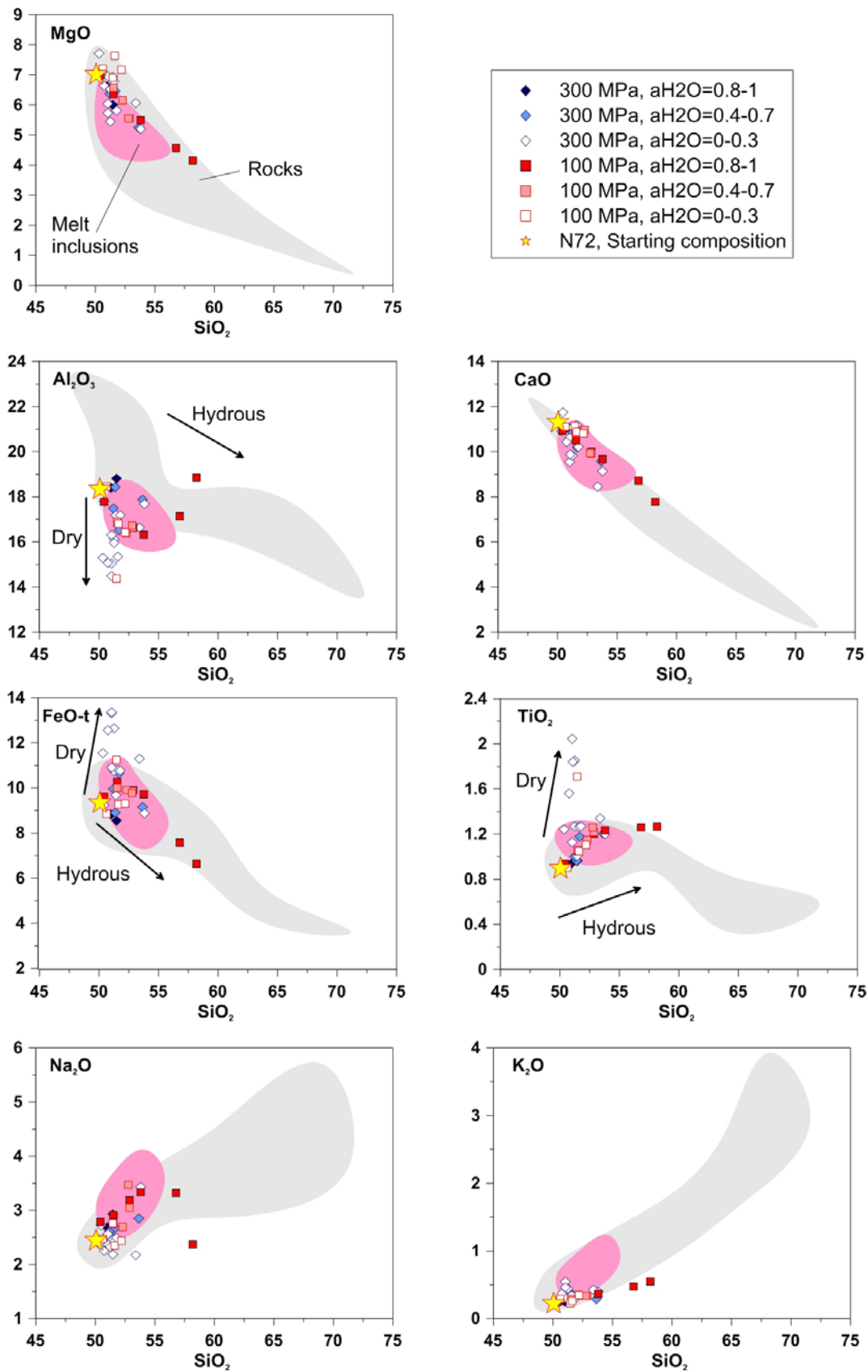


Fig. 1-35. Variational diagrams in oxides vs. SiO_2 for Mutnovsky rocks (grey fields), melt inclusions (pink fields) and experimental glasses at 300 and 100 MPa. Only experiments with stable associations of minerals Plag+Ol±CPx are presented.

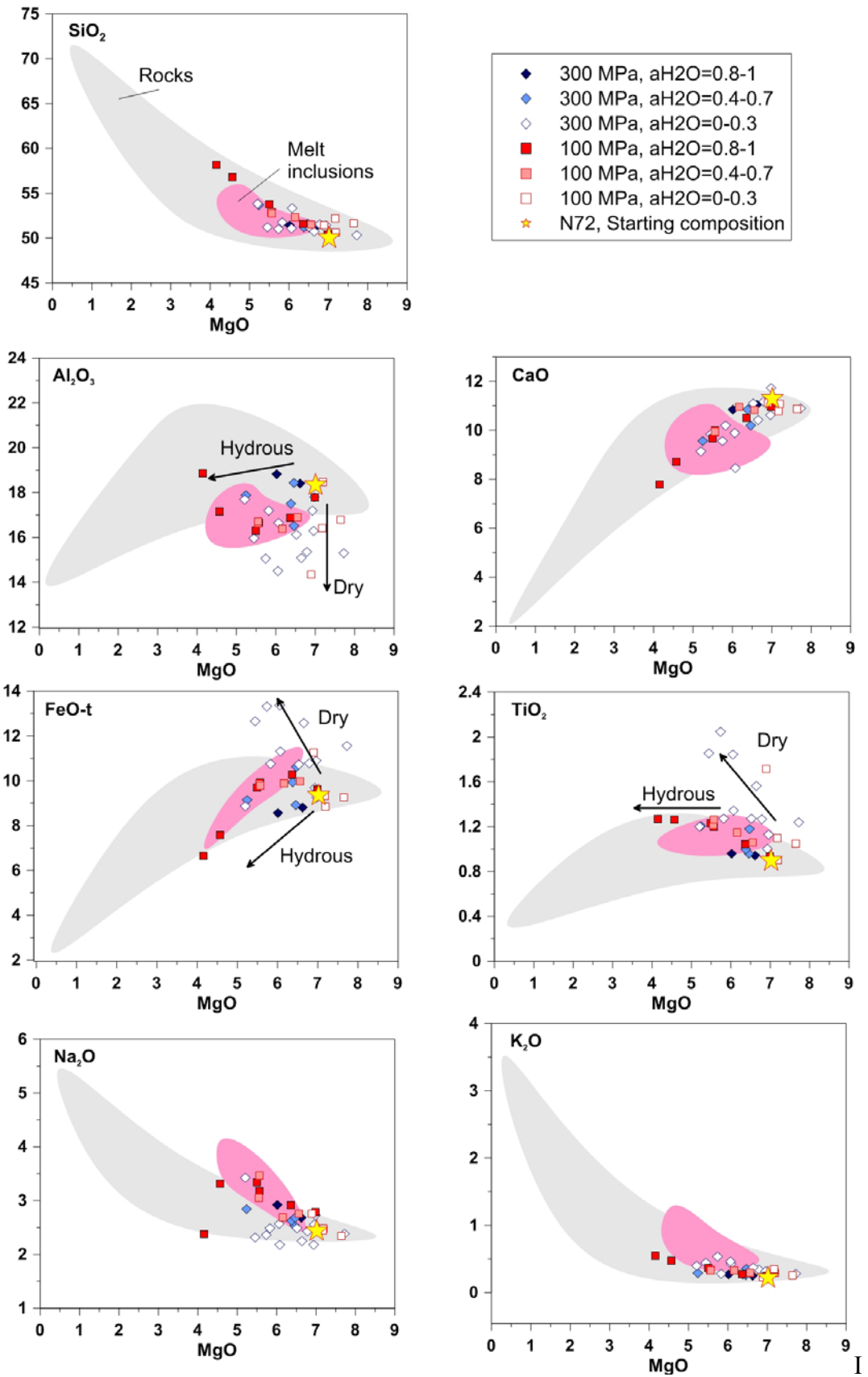


Fig. 1-36. Variational diagrams in oxides vs. MgO for Mutnovsky rocks (grey fields), melt inclusions (pink fields) and experimental glasses at 300 and 100 MPa. Only experiments with stable associations of minerals Plag+Ol±CPx are presented.

In contrast to other oxides, concentrations of Al_2O_3 , FeO-t and TiO_2 in experimental glasses follow two distinct trends for low and high $a\text{H}_2\text{O}$ runs. In H_2O -poor ($a\text{H}_2\text{O} < 0.3$) and relatively reduced experiments crystallization of Mt was delayed and residual melts are significantly enriched in FeO-tot (up to 13.5 wt.%) and TiO_2 (up to 2 wt.%) (Figs. 1-35, 36). The effect of FeO-t and TiO_2 enrichment is more pronounced for experiments at 300 MPa, since dry experiment at 100 MPa were not performed at temperatures above 1100°C. On Miyashiro classification diagram (Fig. 1-37a) H_2O -poor melts are located in the field of tholeiitic magmas (MORBs) showing very strong enrichment in FeO-tot (FeO-tot/MgO up to 2.3) at almost constant SiO_2 (50-51 wt.%). Such high FeO-tot/MgO values are also typical for natural Mutnovsky basalts. At the same time absolute FeO-tot contents in Mutnovsky basalts definitely does not show tendency of enrichment; instead they stays constant in basalts and are lowering down (below 11 wt.%) in more evolved andesites and dacites. In 300 MPa experiments at H_2O -saturated conditions ($a\text{H}_2\text{O} = 1$) crystallization of magnetite starts at early stages of melt evolution and therefore residual melts do not show enrichment in FeO^{tot} and TiO_2 and their compositions overlap with natural basalts and andesites. But on FeO^{tot}/MgO vs. SiO_2 diagram H_2O -saturated melts (300MPa) are found to be placed on the discrimination line (Fig.1-37a).

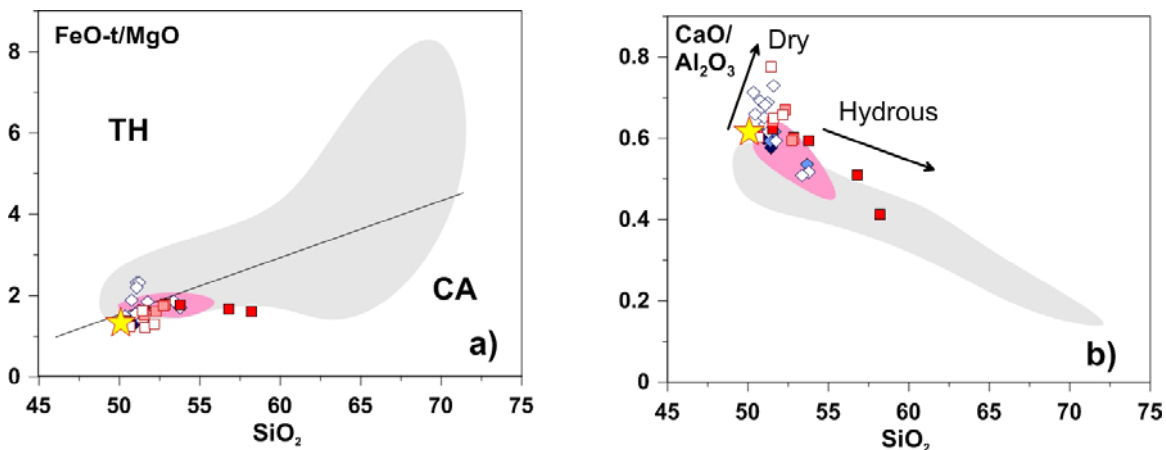


Fig. 1-37. (a) FeO-t/MgO – SiO_2 classification diagram (Miyashiro, 1974); (b) $\text{CaO}/\text{Al}_2\text{O}_3$ vs. SiO_2 diagram. Mutnovsky rocks (grey fields), melt inclusions (pink fields) and experimental glasses at 300 and 100 MPa are presented. Only experiments with stable associations of minerals Plag+Ol±CPx are presented.

Another oxide that shows very strong dependence on $a\text{H}_2\text{O}$ in the system is Al_2O_3 , which is related to effect of H_2O content in the melt on stability of plagioclase. Due to the early crystallization of Ca-rich plagioclase, H_2O -poor glasses ($a\text{H}_2\text{O} < 0.3$) at 300 MPa show strong depletion in Al_2O_3 concentration up to 14.5 wt.%, which is much lower than Al_2O_3 -contents in the whole rocks and melt inclusions (Fig. 1-37b). This effect is also can be seen

on CaO/Al₂O₃ vs. SiO₂ diagram, where H₂O-poor melts show increased values of CaO/Al₂O₃ up to 0.7 (Fig. 1-37b). On the contrary, relatively hydrous melts at both pressures (aH₂O>0.4) of basaltic composition show relatively small depletion in Al₂O₃ (down to 16.5 wt.%) which is in a very good agreement with compositions of melt inclusions (Fig. 1-37b). Thus, only hydrous experimental melts of more evolved (andesitic) composition at both pressures follow similar evolution trend as natural volcanic rocks.

As a result of comparison of natural and experimental LLDs we can conclude, that natural series of Mutnovsky could be principally reproduced as a result of crystallization of N72 primitive basaltic melt at both studied pressures of 100 and 300 MPa. Parental magma must contain relatively high amounts of water (at least 1.5 - 2.0 wt.% H₂O), which corresponds to water activity (aH₂O) higher than 0.2 at 300 MPa or 0.4 at 100 MPa and redox conditions of QFM+1.7 to QFM +3.5 at 300 MPa and QFM+3 to QFM+3.75 at 100 MPa.

4.5. Redox state of Mutnovsky magmas

Determinations of sulfur speciation in naturally quenched (non re-heated) glassy inclusions in olivines from tephra shows that S⁶⁺/ΣS vary between 0.4 and 1, which corresponds to *f*O₂ within the range of QFM+0.9 to QFM+2 (Jugo et al., 2010) (paragraph 2.4.4, Table 1, Fig. 1-9). Oxygen fugacity and temperatures determined for olivine- Cr-Spinel pairs in Mutnovsky basalts using geothermometer of Ballhaus (1991) vary between QFM+0.3 to QFM+2.6 and 1050-1120°C. Mt-Ilm exsolutions in phenocrysts and coexisting microlites in studied dacite represent redox conditions on level of QFM+0.3 (according to model of Spencer & Lindsley, 1981) and temperatures of 750-800°C (Carmichael, 1967). Considering the large uncertainties of analytical methods and model imperfections, the estimates of *f*O₂ obtained on natural samples is in principle agreement with the previous estimates of oxygen fugacities suggested fro island arc magmas (~QFM+0.7 QFM+2, Ballhaus, 1993; Parkinson and Arculus, 1999). These estimates are also in a good agreement with our phase equilibria experiments.

3.4.6. Volatiles saturation pressures (Melt inclusions)

Our study of the melt inclusions in olivine phenocrysts from lava and tephra samples supports the presence of 1.5 – 2.5 wt.% H₂O in Mutnovsky basaltic melts and the hydrous character of island arc tholeiitic magmatism. Using concentrations of H₂O and CO₂ determined in melt inclusions and our original H₂O-CO₂ solubility diagram (see

Chapter 2) the pressures of last equilibration of the melt with fluid phase was estimated to be between 50 and 110 MPa (Fig. 1-38). These volatile saturation pressures show a minimum possible pressure at the moment of melt inclusion entrapment.

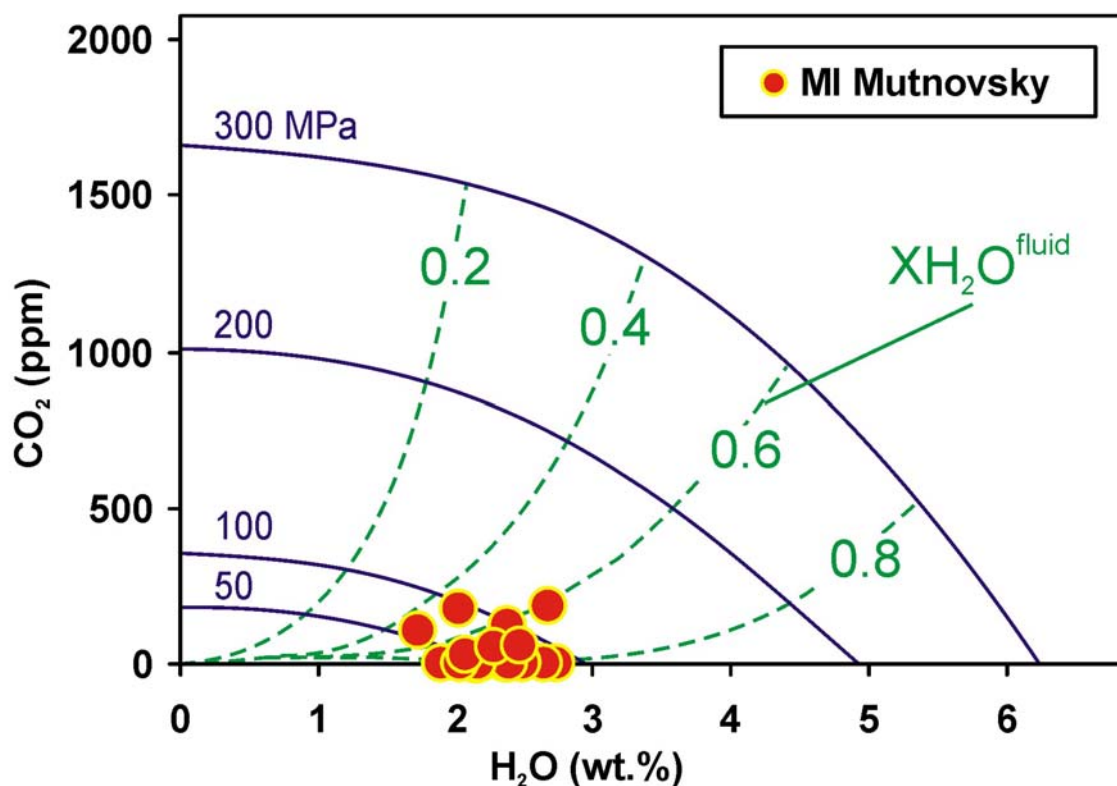


Fig. 1-38. H₂O and CO₂ concentrations in melt inclusions in olivines from Mutnovsky volcano. Solubility plot for H₂O- and CO₂-bearing fluids in basaltic melts at 1250°C and pressures from 50 to 300 MPa is after Shishkina et al., 2010 (Chapter II of the Thesis). The solid lines represent isobars, the dashed lines are isopleths of constant fluid composition for the melts saturated with H₂O-CO₂-bearing fluids.

4.7. Magma storage conditions of Mutnovsky volcano

The study of petrography, mineralogy and melt inclusions in natural volcanic rocks of Mutnovsky volcano in combinations with performed experimental investigation of phase relations in basaltic melt enables us to estimate parameters of crystallization and evolution of magma beneath Mutnovsky volcano.

Comparison of natural and experimental liquid lines of descent (LLDs) shows that volcanic series of Mutnovsky are well reproduced by differentiation of starting basaltic melt which initially must have ~1.5-2.0 wt.% H₂O. Crystallization of the main mineral assemblage of Plag+Ol±CPx phenocrysts in Mutnovsky basalts may proceed in a range of pressures between 100 and 300 MPa. Phenocrysts cores are forming at pressures ~ 300

MPa in water-bearing (2-5 wt%) basaltic melt at oxidized conditions (\sim QFM+2.2. to QFM+2.7). At 300 MPa crystallization of Plag+Ol+CPx mineral assemblage takes place in interval of temperatures between 1025 and 1075°C. At these conditions silicates crystallize nearly simultaneously with magnetite. Crystallization of parental melt also may proceed at lower pressure of 100 MPa. Although similar mineral association also crystallizes at 100 MPa at slightly higher water activities, at this pressure Pl compositions are more evolved (An 77-80) than natural phenocryst cores (An 84-90). This suggests that phenocrysts of Mutnovsky Plag+Ol+CPx-bearing basalts were last equilibrated at pressures higher than 100 MPa. In contrast, crystallization of Cpx-free basalts (Ol-Pl-bearing) is probably takes place at low pressures \sim 100 MPa; compositions of both Plag and Ol in these basalts are well reproduced at 100 MPa and at high a_{H_2O} . Thus low-pressure-crystallization is responsible for formation of Ol-Pl-bearing basalts, which are the most abundant rock species for the late stages of Mutnovsky activity (Mutnovsky-III, IV).

Thus, although the first (initial) stage of Mutnovsky volcano history (e.g. depths of primary magma origination) remains still unclear, its subsequent evolution is recorded in phenocrysts and lava compositions, to a certain extent reproduced in experiments and can be summarized as following. The portions of *hydrous* parental basaltic magma continuously ascended from the zone(s) of magma generation and may be stored and stagnated at different levels of magmatic column. Our experimental results and natural observations indicate at least one of such interval located at about 9 km depth and corresponding to 300 MPa pressure. At this level, parental melts were last equilibrated with Plag+Ol+CPx solid assemblage, and experienced fast ascend and eruption leading to formation of Plag+Ol+CPx-bearing basalts abundantly observed as eruptive products of the earliest stages (Mutnovsky-I and -II) of volcano evolution. With time the depth of magmatic chamber was probably changed to shallower levels. Its current locus can be assumed at depth not deeper than \sim 3 km (100 MPa) since only at this pressure crystallization of magma leads to formation of Ol+Pl-bearing basalts with phenocryst compositions reproduced only at 100 MPa. Importantly, at this depth crystallization must have proceeded at high water activities ($a_{H_2O}>0.7$) to maintain high-An contents of crystallizing Pl and to drive residual melt evolution along Mutnovsky natural IAT-trend. The lost of volatiles due to degassing might cause the oversaturation of the melts with respect to Pl+Ol+Cpx association driving melt compositions along classical tholeiitic trend of FeO and TiO₂ enrichment and strong Al₂O₃ depletion and leading to formation of the magmas (melts) represented by Mutnovsky tephra glasses. Thus, tephra material represent a portion of magma that was stored in a reservoir at depth corresponding to pressures of 50-

110 MPa and where crystallization of olivine and plagioclase phenocrysts occurred at conditions close to H₂O saturation. The presence of a hot magma reservoir at shallow depths of about 1-2 km below Mutnovsky volcano is also supported by geophysical observations and numerical modeling (e.g.: Fedotov et al., 2005; Utkin et al., 2005). Strong hydrothermal activity in the crater of Mutnovsky also requires a constant input of heat, which can be produced from a shallow hot magma reservoir.

5. CONCLUSIONS

1) The mafic part of volcanic series of Mutnovsky volcano from basalts to andesites can be experimentally reproduced at pressures 100 and 300 MPa. Mutnovsky parental magma (7.0 wt.% MgO, 50.1 wt.% SiO₂) should have 1.5-2.0 wt.% H₂O ($a_{\text{H}_2\text{O}} \sim 0.2$ at 300 MPa or $a_{\text{H}_2\text{O}} \sim 0.4$ at 100 MPa) and crystallization should proceed at oxidizing conditions ($> \text{QFM}+1.7$). The hydrous and oxidized conditions of crystallization favor earlier crystallization of magnetite and delayed crystallization of plagioclase and its lower proportion in solid phase. This is resulted in non-significant enrichment of residual melt in FeO^{tot} and TiO₂ and a weak depletion in Al₂O₃ at the early stages of crystallization of the basaltic melt. This compositional trends of Mutnovsky IAT magma evolution are transitional between pure calc-alkaline (water-rich magma crystallization) and pure tholeiitic (dry MORB-like crystallization). The subsequent stages of magma differentiation should proceed at higher water activities to follow the strong silica enrichment and FeO depletion path of Mutnovsky andesites and dacites.

2) Crystallization conditions of the natural association of phenocrysts (An₈₅₋₉₄, Fo₇₂₋₈₄, Mg#CPx₇₄₋₈₁) were experimentally reproduced at 300 MPa for parental magma containing 2 - 5 wt.% H₂O and at redox conditions corresponding to QFM+2.2 - QFM+2.7. The onset of Plag+Ol+CPx±Mt crystallization proceeds in temperature interval between 1025-1075°C. Basalts formed at these depths (~ 9 km) usually represent the earlier stages of magmatic activity (Mutnovsky-I, and -II).

3) Crystallization of Plag+Ol+CPx±Mt association is also observed at 100 MPa crystals in the wide range of $a_{\text{H}_2\text{O}}$. However at 100 MPa Cpx joins solid assemblage after a certain interval of melt evolution along the Ol+Pl cotectics. Crystallization of Cpx denotes precipitation of more albitic Pl, which is not observed in natural magmas. However Cpx-free Ol+Pl association reproduces mineral compositions of all historical and recent eruptions (Mutnovsky-III, and -IV).

4) The presence of a relatively shallow magma chamber (storage reservoir) is suggested below Mutnovsky volcano located on depth about 1.5 – 3 km and filled with partially degassed magma containing 1.5-2.5 wt.% H₂O. Crystallization of this magma produces association of high-Ca-plagioclase and olivine crystals (at 1050-1075°C) which represent the main type (Ol-Pl-bearing-) of basalts of all historical and recent eruptions. Strong hydrothermal activity in the crater of Mutnovsky also requires a constant input of heat, which can derive from a hot magma body located not far from the surface.

5) The performed crystallization experiments demonstrate crucial role of water in magma differentiation process of Mutnovsky magmas in particular and of island arc tholeiites in general. In agreement with previous experimental studies, crystallization at nominally dry conditions drives basaltic melt along Ol+Plag and later along Ol+Plag+CPx cotectics with the predominance of Plag in solid assemblage. At dry conditions magnetite crystallization in basaltic melt is significantly suppressed. Both factors are responsible for the realization of classical tholeiitic (MORB-like) trend of magma evolution. The presence of about ~2 wt% of H₂O in parental melts of IAT significantly affects stability fields of silicates and is required to produce island arc tholeiitic differentiation trend.

References

- Active volcanoes of Kamchatka. (1991) Nauka Publishers. Moscow. V.1. P. 316-337. (In Russian and English)
- Alves, S., Schiano, P., Capmas, F. And Allegre, C.-J. (2002) Osmium isotope binary mixing arrays in arc volcanism. *Earth Planetary Science Letters*. V. 198, p. 355-369
- Aranovich, L.Y., Newton, R.C. (1999) Experimental determination of CO₂-H₂O activity-concentration relations at 600–1000 C and 6–14 kbar by reversed decarbonation and dehydration reactions. *American Mineralogist* 84, 1319-1332.
- Ariskin, A.A., and Barmina, G.S. (2004) COMAGMAT: development of a magma crystallization model and its petrological applications. *Geochemistry International*, 42(Suppl. 1), S1–S157.
- Baker, D. R. and Eggler, D. H. (1987) Compositions of anhydrous and hydrous melts coexisting with plagioclase, augite, and olivine or low-Ca pyroxene from 1atm to 8 kbar. Application to the Aleutian volcanic center of Atka. *American Mineralogist* 72, 12-28.
- Ballhaus, C. G. (1993) Redox states of lithospheric and asthenospheric upper mantle. *Contributions to Mineralogy and Petrology* 114, 331-348.
- Ballhaus, C. G., Berry, R. F. and Green, D. H. (1991) High pressure experimental calibration of the olivine-orthopyroxene-spinel oxygen geobarometer: implications for the oxidation state of the upper mantle. *Contributions to Mineralogy and Petrology* 107, 27-40.
- Barclay, J. and Carmichael, I. S. E. (2004) A hornblende basalt from western Mexico: water-saturated phase relations constrain a pressure–temperature window of eruptibility. *Journal of Petrology* 45, 485–506
- Bartels, K. S., Kinzler, R. J. and Grove, T. L. (1991) High pressure phase relations of primitive high-alumina basalts from Medicine Lake volcano, northern California. *Contributions to Mineralogy and Petrology* 108, 253–270.
- Berndt, J., Liebske, C., Holtz, F., Freise, M., Nowak, M., Ziegenbein, D., Hurkuck, W. and Koepke, J. (2002) A combined rapid-quench and H₂-membrane setup for internally heated pressure vessels: Description and application for water solubility in basaltic melts. *American Mineralogist* 87, 1717-1726.
- Bortnikova, S.B., Sharapov, V.N., and Bessonova, E.P. (2007) Hydro-geochemical composition of springs at the Donnoe Fumarole Field, Mutnovsky Volcano (Southern Kamchatka) and problems of their relation with supercritical magmatic fluids. *Dokl Earth Sci.*, 413A (3):410–414

Botcharnikov, R.E., Koepke, J., Holtz, F., McCammon, C., Wilke, M. (2005b) The effect of water activity on the oxidation and structural state of Fe in a ferro-basaltic melt. *Geochim. Cosmochim. Acta* 69, 5071-5085.

Burnham, C.W. (1979) The importance of volatile constituents. In: Yoder, H.S. (Ed.), *The Evolution of the Igneous Rocks*. Princeton University Press, Princeton, NJ, pp. 439–482.

Carmichael, I.S.E. (1967) The iron-titanium oxides of salic volcanic rocks and their associated ferromagnesian silicates, *Contrib. Mineral. Petrol.* V. 14, p. 36-64.

Carmichael, I. and Ghiorso, M. S. (1990) The effect of oxygen fugacity on the redox state of natural liquids and their crystallizing phases. In: Nicholls, J. and Russell, J. K. (eds) *Modern Methods of Igneous Petrology: Understanding Magmatic Processes*. Mineralogical Society of America, *Reviews in Mineralogy* 24, 191-212.

Carmichael, I. (1991) The redox states of basic and silicic magmas: a reflection of their source regions? *Contributions to Mineralogy and Petrology* 106, 129-264.

Chashchin, A.A., Martynov, Yu.A., Perepelov, A.B., Ekimova, N.I. and Vladimirova, T.P. (2011) Physical and Chemical Conditions of the Formation and Evolution of Late Pleistocene–Holocene Magmas of the Gorely and Mutnovsky Volcanoes, Southern Kamchatka. *Russian Journal of Pacific Geology*. V. 5, N 4, pp. 348–367.

Chashchin, A.A., Khetchikov, L.N., Ivanov V.V, et al. (2001) Fluid Regime of the Formation of Magmatic Rocks and Au–Ag Mineralization of the Vilyuchinsk Volcanotectonic Structure, South Kamchatka/ Ore Deposits of Continental Margins (Dal'nauka, Vladivostok, 2001), V. 2, p. 341–366 (in Russian).

Danyushevsky, L. V. (2001) The effect of small amounts of H₂O on crystallisation of mid-ocean ridge and backarc basin magmas, *J. Volcanol. Geotherm. Res.*, 110, 265–280

Danyushevsky, L.V. and Plechov, P.Yu. (2011) Petrolog3: Integrated software for modeling crystallization processes, *Geochem.Geophys. Geosyst.*, 12, Q07021

Danyushevsky, L.V., Della-Pasqua, F.N., Sokolov, S. (2000) Re-equilibration of melt inclusions trapped by magnesian olivine phenocrysts from subduction-related magmas: petrological implications. *Contrib. Mineral. Petrol.* 138, 68–83.

Danyushevsky, L.V., McNeill, A.W., and Sobolev, A.V. (2002) Experimental and petrological studies of melt inclusions in phenocrysts from mantle-derived magmas: an overview of techniques, advantages and complications. *Chemical Geology*, 183(1-4), 5-24.

Devine, J. D., Gardner, J. E., Brack, H. P., Layne, G. D. and Rutherford, M. J. (1995) Comparison of microanalytical methods for estimating H₂O contents of silicic volcanic glasses. *American Mineralogist* 80, 319–328.

Di Carlo, I., Pichavant, M., Rotolo, S.G. and Bruno, S. (2006) Experimental Crystallization of a High-K Arc Basalt: the Golden Pumice, Stromboli Volcano (Italy). *Journal of Petrology*, v. 47, N. 7, p. 1317-1343

Duggen S., Portnyagin M., Baker J., Ulfbeck D., Hoernle K., Garbe-Schonberg D. and Grassineau N. (2007) Drastic shift in lava geochemistry in the volcanic-front to rear-arc region of the Southern Kamchatkan subduction zone: Evidence for the transition from slab surface dehydration to sediment melting. *Geochimica et Cosmochimica Acta* 71, 452-480.

Eichelberger, J., Kiryukhin, A. and Simon, A. (2009) The magma-hydrothermal system at Mutnovsky volcano, Kamchatka peninsula, Russia. *Scientific Drilling*, 7, p. 54-59.

Fedotov S.A. (2005) *Magmatic Feeding Systems and Mechanizm of Volcanoes Eruptions*. Moscow. Nauka Publ., 300 p. (in Russian)

Frolova, T.I., Plechov, P.Yu., Tikhomirov, P.L., and Churakov, S.V. (2001) Melt Inclusions in Minerals of Allivalites of Kuril–Kamchatka Island Arc, *Geokhimiya*, vol. 39, no. 4, pp. 336–346.

Gorbatov A, Kostoglodov V, Suarez G, Gordeev E (1997) Seismicity and structure of the Kamchatka subduction zone. *J Geophys Res* 102:17883–1789.

Gorbatov, A., Domiguez, J., Suarez, G., Kostoglodov, V., Gordeev, E. (1999) Tomographic imaging of the P-wave velocity structure beneath the Kamchatka pensinsula. *J. Geophys. Res.* 137, 269–279.

Grib, E.N. (1989) Composition and parameters of crystallization of lavas of volcanic structures of Severno-Mutnovsky volcanic zone. *Volcanology and Seysmology*, V. 4, p. 29-43 (in Russian)

Hetchikov, L.N., Chashin, A.A., Pahomova, V.A. and Odarichenko E.G. (2001) Phenocrysts of plagioclase in basalts of Gorely and Mutnovsky volcanoes (South Kamchatka) and conditions of its formation, data from melt inclusions study/Extending abstracts of X International Conference on Thermobarogeochemistry. p. 111-139. (in Russian)

Hochstaedter, A.G., Kepezhinskas, P., Defant, M., Drummond, M., Koloskov, A. (1996) Insights into the volcanic arc mantle wedge from magnesian lavas from the Kamchatka arc. *J. Geophys. Res. Solid Earth*. V. 101 (B1), p. 697–712.

Irvine, T.N. and Baragar, W.R.A. (1971) A guide to the chemical classification of the common volcanic rocks. *Canadian Journal of Earth Sciences*, 8: 523-548.

Ishikawa, T., Tera, F., Nakazawa, T. (2001) Boron isotope and trace element systematics of three volcanic zones in the Kamtchatka arc. *Geochim. Cosmochim. Acta* 65 (24), 4523–4537.

Jochum, K.P., et al. (2006) MPI-DING reference glasses for in situ microanalysis: New reference values for element concentrations and isotope ratios. *Geochem. Geophys. Geosyst.* 7. doi:10.1029/2005GC001060.

Jugo, P.J., Wilke, M., and Botcharnikov, R.E. (2010) Sulfur K-edge XANES analysis of natural and synthetic basaltic glasses: Implications for S speciation and S content as function of oxygen fugacity *Geochim. Cosmochim. Acta* 74, 5926-5938

Kepezhinskas, P., McDermott, F., Defant, M.J., Hochstaedter, A., Drummond, M.S., Hawkesworth, C., Kolosov, A., Maury, R.C., Bellon, H. (1997) Trace element and Sr–Nd–Pb isotopic constraints on a three-component model of Kamtchatka arc petrogenesis. *Geochim. Cosmochim. Acta.* V. 61, p. 577–600.

Kiryukhin A., Eichelberger J. C. and Izbekov P. (2006) Scientific drilling of the Mutnovsky magma-hydrothermal system (Kamchatka, Russia): testing the magma-hydrothermal connection. A workshop proposal to ICDP. *Petropavlovsk-Kamchatsky*, p.23.

Kiryukhin, A.V., Leonov, V.L., Slotvsov, I.B, Delemen, I.F., Puzankov, M.Y., Polyakov, A.Y., Ivanysko, G.O., Bataeva, O.P., Zelensky, M.E. (2005) Modeling of the exploitation of the Dachny geothermal field in relation to steam supply to Mutnovsky PP// *Volcanology and Seismology Journal* , 50 p. (in Russian)

Kress, V.C., Carmichael, I.S.E. (1991) The compressibility of silicate liquids containing Fe₂O₃ and the effect of composition, temperature, oxygen fugacity and pressure on their redox states. *Contrib. Mineral. Petrol.*, 108, pp. 82–92.

Leake, B.E., Woolley, A.R., Arps, C.E.S., Birch, W.D., Gilbert, M.C., Grice, J.D., Hawthorne, F.C., Kato, A., Kisch, H.J., Krivovichev, V.G., Linthout, K., Laird, J., Mandarino, J., Maresch, W.V., Nickel, E.H., Rock, N.M.S., Schumacher, J.S., Smith, D.C., Stephenson, N.C.N., Ungaretti, L., Whittaker, E.J.W., Youzhi, G. (1997) Nomenclature of amphiboles. Report of the Subcommittee on Amphiboles of the International Mineralogical Association Commission on new minerals and mineral names. *Eur J Min* 9:623–651

Martynov, Y. A. and Chashchin, A. (1989) Rock-forming minerals of the mafic effusives of Mutnovsky geothermal field. New data on petrology of the magmatic and metamorphic rocks in Kamchatka. Vladivostok: FarEast Branch, USSR Academy of Science, 112-123 (in Russian).

Martynov, Y. A., Perepelov, A. B. and Chashchin, A. (1995) Geochemical typization of the basaltoids from Mutnovsky volcanic field (Southern Kamchatka). *Geology of the Pacific Ocean (Tikhookeanskaya Geologiya)* 5, 72-83 (in Russian).

Melekestsev I. V., Braizeva O. A. and Ponomareva, V. V. (1987) The activity dynamics of Mutnovsky and Gorely volcanoes in Holocene and volcanic hazards for surrounding areas. *Volcanology and Seismology*, 3-18 (in Russian).

Nurmukhamedov, A.G., Chernev, I.I., Alekseev, D.A. and Yakovlev, A.G. (2010) 3D Geoelectric Model of the Mutnov Steam Hydrothermal Deposit. *Izvestiya, Physics of the Solid Earth*, Vol. 46, No. 9, pp. 739–750.

Parkinson IJ, Arculus RJ (1999) The redox state of subduction zones: insights from arc-peridotites. *Chem Geol* 160:409-423

Pineau, F., Semet, M.P., Grassineau, N., Okrugin, V.M., Javoy, M. (1999) The genesis of the stable isotope (O,H) record in arc magmas: the Kamchatka's case. *Chem. Geol.* V. 135, p. 93–124.

Pitzer, K.S., Sterner, S.M. (1994) Equation of state valid continuously from zero to extreme pressures for H₂O and CO₂. *Journal of Chemistry and Physics* 102, 3111-3116.

Popolitov, E.I., Volynets, O.N. (1981) Geochemical characteristics of quaternary volcanism of the Kurile-Kamchatka island arc and some problems of petrogenesis, *Nauka, Novosibirsk* 1-183 (in Russian)

Portnyagin, M.V., Hoernle, K., Plechov, P.Y., Mironov, N.L., Khubunaya, S.A. (2007) Constraints on mantle melting and composition and nature of slab components in volcanic arcs from volatiles (H₂O, S, Cl, F) and trace elements in melt inclusions from the Kamchatka Arc. *Earth Planet. Sci. Lett.* 255, 53–69.

Potapov, V.V. (2002) Physical model of heat- and mass-transport in magmatogenic hydrothermal system beneath Mutnovsky volcano. *Volcanology and seismology.* V. 2, p. 21-29 (in Russian)

Rocholl, A.B.E., Simon, K., Jochum, K.P., Molzahn, M., Pernicka, E., Seufert, M., Spettel, B., Stummeier, J. (1997). Chemical characterization of NIST silicate glass certified reference material SRM 610 by ICP-MS, TIMS, LIMS, SSMS, INAA, AAS and PIXE. *Geostandards* 21, 101–114.

Rychagov, S.N., Nuzhdaev, A.A. and Stepanov, I.I. (2009) Behavior of Mercury in the Supergene Zone of Geothermal Deposits, Southern Kamchatka. *Geochemistry International*, Vol. 47, No. 5, pp. 504–512.

Schuessler, J.A., Botcharnikov, R.E., Behrens, H., Misiti, V., Freda, C. (2008) Oxidation state of iron in hydrous phono-tephritic melts. *Am Mineralogist* 93, 1493–1504.

Selyangin O. B. (1993) New data on Mutnovsky volcano: Structure, evolution and prediction. *Volcanology and Seismology* 1, 17-35 (in Russian).

Sisson, T.W., and Grove, T.L. (1993a) Experimental investigations of the role of H₂O in calc-alkaline differentiation and subduction zone magmatism. *Contributions to Mineralogy and Petrology*, 113(2), 143-166.

Sisson, T.W., and Grove, T.L. (1993b) Temperatures and H₂O contents of low-MgO high-alumina basalts. *Contributions to Mineralogy and Petrology*, 113(2), 167-184.

Sobolev, A.V., 1996. Melt inclusions in minerals as a source of principal petrological information. *Petrology* 4, 209–220.

Sobolev, A.V., Chaussidon, M. (1996) H₂O concentrations in primary melts from island arcs and mid-ocean ridges: implications for H₂O storage and recycling in the mantle. *Earth Planet. Sci. Lett.* 137, 45–55.

Spencer, K. J. and Lindsley, D. H. (1981) A solution model for coexisting iron-titanium oxides. *American Mineralogist*. V. 66, p.1189-1201.

Taran, Y.A., Pilipenko, V.P., Rozhkov, A.M., Vakin, E.A. (1992) A geochemical model for fumaroles of the Mutnovsky volcano, Kamchatka, USSR. *Journal of Volcanology and Geothermal Research*, 49, 269-283.

Tatsumi, Y., Furukawa, Y., Kogiso, T., Yamada, Y., Yokoyama, T. and Fedotov S.A. (1994) A third volcanic chain in Kamchatka: Thermal anomaly at transform/convergence plate boundary. *Geophys. Res. Lett.* 21, 537–540.

Trukhin, Y.P. (2003) Geochemistry of the active geothermal processes and geotechnologies applications. Moscow, Nauka Publ., 376 p.

Utkin, I.S., Fedotov, S.A., Delemen, I.F., Utkina, L.I. (2005) Dynamics of the development of flowing magmatic chambers on Mutnovsko-Gorelovsky group of volcanoes, their thermal fields and underground heat capacity. *Volcanology and Seismology* 5, 30-40 (in Russian).

Vakin, E.A., Kirsanov, I.T. and Kirsanova, T.P. (1976) Thermal fields and hot springs of the Mutnovsky geothermal area. In “Geothermal systems and thermal fields of Kamchatka”. Moscow Nauka, pp 85–114 (in Russian)

Zelenski, M., Taran, Y. (2011) Geochemistry of volcanic and hydrothermal gases of Mutnovsky volcano, Kamchatka: evidence for mantle, slab and atmosphere contributions to fluids of a typical arc volcano. In: Inguaggiato S, Shinohara H, and Fischer T (eds) *Geochemistry of volcanic fluids: a special issue in honor of Yuri A. Taran*. *Bull Volcanol* 73(4): 373–394.

Chapter II.

Solubility of H₂O- and CO₂-bearing fluids in tholeiitic basalts at pressures up to 500 MPa

Results presented in Chapter II are modified after paper of Shishkina et al (2010) in Chemical Geology.

Shishkina, T., Botcharnikov, R.E., Holtz, F., Almeev, R.R., Portnyagin, M. (2010): Solubility of H₂O and CO₂-bearing fluids in tholeiitic basalts at pressures up to 500 MPa, Chemical Geology 277, 115-125

ABSTRACT

The solubility of H₂O- and CO₂-bearing fluids in tholeiitic basalts has been investigated experimentally at temperature of 1250°C and pressures of 50, 100, 200, 300, 400 and 500 MPa. The concentrations of dissolved H₂O and CO₂ have been determined using FTIR spectroscopy with an accurate calibration of the absorption coefficients for hydrogen- and carbon-bearing species using synthesized standards of the same tholeiitic composition. The absorption coefficients are 0.65±0.08 and 0.69±0.08 L/(mol*cm) for molecular H₂O and OH groups by Near-Infrared (NIR), respectively, and 68±10 L/(mol*cm) for bulk H₂O by Mid-Infrared (MIR). The carbonate groups determined by MIR have an absorption coefficient of 317±23 L/(mol*cm) for the band at 1430 cm⁻¹. The solubility of H₂O in the melt in equilibrium with pure H₂O fluid increases from about 2.3 ± 0.12 wt.% at 50 MPa to about 8.8 ± 0.16 wt.% at 500 MPa, whereas the concentration of CO₂ increases from about 175 ± 15 to 3318 ± 276 ppm in the melts which were equilibrated with the most CO₂-rich fluids (with mole fraction of CO₂ in the fluid, X^fCO₂, from 0.70 to 0.95). In melts coexisting with H₂O- and CO₂-bearing fluids, the concentrations of dissolved H₂O and CO₂ in basaltic melt show a non-linear dependence on both total pressure and mole fraction of volatiles in the equilibrium fluid, which is in agreement with previous studies. A comparison of new experimental data with existing numerical solubility models for mixed H₂O-CO₂ fluids shows that the models do not adequately predict the solubility of volatiles in basaltic liquids at pressures above 200 MPa, in particular for CO₂, implying that the models need to be recalibrated.

The experimental dataset presented in this study enables a quantitative interpretation of volatile concentrations in glass inclusions to evaluate the magma storage conditions and degassing paths of natural island arc basaltic systems. The experimental database covers the entire range of volatile compositions reported in the literature for natural melt inclusions in olivine from low- to mid-K basalts indicating that most melt inclusions were trapped or equilibrated at intermediate to shallow levels in magmatic systems (<12-15 km).

Key words: H₂O, CO₂, water, carbon dioxide, fluid, solubility, tholeiite, basalt, magma, Mutnovsky volcano, Kamchatka

1. INTRODUCTION

Natural subduction-related magmas contain a wide range of volatiles with significant proportions of H₂O and CO₂ as estimated on the basis of volcanic and hydrothermal gas discharges (e.g., Fischer & Marty, 2005). The results of Fischer & Marty (2005) indicate that primitive magmas may contain about 8-16 wt% H₂O and 3500-7600 ppm CO₂. Evidence for high volatile contents during arc magma genesis and evolution is also given by the analysis of glass inclusions preserved in phenocrysts usually containing up to 6-8 wt% H₂O and 2500-3000 ppm CO₂ (e.g., Sisson & Layne, 1993; Wallace, 2005). Volcanic gases of typical subduction-related volcanoes have also predominant abundances of H₂O and CO₂ with concentrations varying from ~80 to 99 mole% and from <1 to ~8 mole %, respectively (e.g., Symonds et al., 1994; Giggenbach, 1996). Considering that the solubility of H₂O and CO₂ in silicate melts is mainly dependent on pressure, the concentrations of H₂O and CO₂ determined in glass inclusions and volcanic gasses are commonly used to estimate magma storage conditions and magma evolution history, provided that the volatile solubility data and models are available.

The knowledge on the solubility of H₂O- and CO₂-bearing fluids in silicate melts with compositions ranging from rhyolites to basalts was greatly improved by numerous experimental studies in the last two decades (e.g., Blank et al., 1993; Blank and Brooker, 1994; Dixon et al., 1995; Jakobsson, 1997; Tamic et al., 2001; King and Holloway, 2002; Behrens et al., 2004a; Botcharnikov et al., 2005a; 2006). Based on the experimental datasets, several empirical and semi-empirical (thermodynamic) models have been proposed as tools to reconstruct magma degassing conditions (e.g., Dixon et al., 1995; Papale, 1999; Tamic et al., 2001; Newman and Lowenstern, 2002; Behrens et al., 2004a; Liu et al., 2005; Papale et al., 2006). However, our understanding of mixed H₂O and CO₂ volatile solubilities in typical basaltic magmas is limited by the very few available experimental data. Furthermore, published datasets are restricted to pressures < 200 MPa (Dixon et al., 1995; Botcharnikov et al., 2005a) and are only useful to model relatively shallow depths of magma degassing. The composition of a fluid phase, coexisting with an ascending magma body may change significantly during magma ascent as a result of a strong dependence of volatile solubilities on pressure and fluid composition (e.g., the solubility of H₂O is two orders of magnitude higher than that of CO₂). The volatile solubility extrapolations up to pressure of 500 MPa in the recent models of Newman and Lowenstern (2002) and Papale et al. (2006) are only weakly supported by the experiments, making estimates of degassing conditions for typical basaltic magmas inaccurate. A large

and growing database of volatile concentration measurements in glass inclusions (in particular of basaltic composition) obviously requires additional experimental data at high pressures and temperatures to better constrain degassing conditions of natural magmas.

Here we present new experimental data on the solubility of H₂O and CO₂-bearing fluids in basaltic magmas of Mutnovsky volcano, Kamchatka, Russia. Based on their major element composition, the erupted lavas of Mutnovsky are typical island arc high-Al, low-K tholeiitic basalts (Martynov and Chashchin, 1989; Martynov et al., 1995; Pineau et al., 1999; Duggen et al., 2007). The solubility data are obtained for pressures from 50 to 500 MPa, covering the wide range of typical pressures/depths of glass inclusion entrapment, and are useful for quantitative evaluation of magma storage conditions and degassing of natural basaltic magmas.

2. EXPERIMENTAL AND ANALYTICAL METHODS

2.1 Starting materials and capsule preparation for solubility experiments

The experiments on solubility of H₂O and CO₂ in basaltic melt were conducted using natural basalt from Mutnovsky volcano (sample N72 from Duggen et al. 2007). This sample is the most primitive basalt of the rocks collected at Mutnovsky volcano (see composition in Table 2-1). It is composed of phenocrysts of plagioclase and olivine distributed in a fine-grained groundmass consisting of plagioclase, clinopyroxene and magnetite. The sample was powdered and melted for 3 hours in a Pt-crucible in an oven at 1600°C and 1 atm, then rapidly quenched to a glass. This glass was crushed and the same melting procedure was repeated for 1.5 hours. The major element composition and homogeneity of the finally quenched basaltic glass were inspected by electron microprobe analysis (Table 2-1). The basaltic glass was crushed and sieved into two fractions: <125µm and 125-200 µm. Before loading into capsules, these fractions were mixed in proportion ~ 1:1 to minimize the free volume between grains and hence, the incorporation of atmospheric nitrogen.

Au₈₀Pd₂₀-capsules with a diameter of 2.6-3.4 mm, a length of 15-20 mm were used to conduct the experiments on volatile solubility. About 50 mg of basaltic glass powder was placed in each capsule. Distilled water (0 – 8 µl H₂O) and Ag₂C₂O₄ (0 – 15 mg) were used as sources of H₂O and CO₂, respectively. Water and silver oxalate were loaded into the capsules in different proportions to establish different mole fractions of water in the added fluid phase (XH₂O_{in}) before experiment (Table 2-2). Capsules were weighed after loading of each component. Capsules were closed with pliers and cooled using liquid

nitrogen to avoid loss of water and CO₂ during welding. After welding, the capsules were checked for leakage by heating in a drying furnace for at least 1 hour at 110°C and consequent weighing.

It must be noted that in this study the concentration of water and especially carbon-bearing species in the quenched glasses were determined using infrared spectroscopy. Considering that the main source of error on the absolute concentrations of water- and carbon-bearing species is related to uncertainties on the absorption coefficients (e.g., Ohlhorst et al., 2001), we synthesized four large (~500 mg) samples to determine the absorption coefficients for the basaltic composition used in this study (in particular the absorption coefficient for carbonate groups in the glasses). The Au₈₀Pd₂₀-capsules (diameter 5 mm, length 35 mm) were filled with 500 mg of basaltic glass powder, 5-30 µl of H₂O, 1.5-3 mg Ag₂C₂O₄ or 1-3 mg CaCO₃. To achieve homogenous distribution of the components, the capsules were filled in several steps (water and silver oxalate were added as small portions at different levels of the capsule). When CaCO₃ was used as a source of CO₂, it was mixed with basalt glass powder before loading.

Table 2-1. Composition of starting material in wt.% (sample N72, basalt from Mutnovsky volcano), recalculated to 100 wt.%

	SiO ₂	TiO ₂	Al ₂ O ₃	FeO-t	MnO	MgO	CaO	Na ₂ O	K ₂ O	P ₂ O ₅
1	50.07	0.90	18.36	9.35	0.17	7.02	11.32	2.45	0.22	0.15
2	50.17	0.92	18.28	9.37	0.17	7.00	11.37	2.33	0.23	0.15

Notes:

1 - XRF data (mas. %) for natural sample after Duggen et al. (2007)

2 – average of 50 microprobe measurements for the remelted sample used in the experiments

2.2 Experimental technique

We used a vertically oriented internally heated pressure vessel (IHPV) with Ar as pressure medium. The temperature in the IHPV was recorded with four unsheathed S-type (Pt – Pt₉₀Rh₁₀) thermocouples with a temperature gradient along the sample of ±3°C. Total pressure was recorded continuously with a calibrated Burster Type 8221 digital pressure transducer (pressure uncertainty ±1 MPa). The variation of pressure during the experiments did not exceed 5 MPa. Several sets of experiments were performed at the same temperature of 1250 °C and at pressures of 50, 100, 200, 300, 400 and 500 MPa. Five to six capsules with different proportions of H₂O and CO₂ (XH₂O_{in} from 0 to 1, Table 2-2) were placed in the pressure vessel for each experiment. The duration of each run was about 24 hours. The

samples were quenched isobarically with a quench rate of about 150°C/sec using a rapid-quench technique described by Berndt et al. (2002). The intrinsic redox conditions in the IHPV ($fO_2^{\text{intrinsic}}$) at $aH_2O=1$ are close to $\log fO_2 = NNO+2.6$ (the oxygen fugacity is higher than that buffered by the Ni/NiO assemblage by 2.6 orders of magnitude) according to the recent determinations reported by Schuessler et al. (2008). The oxygen fugacity prevailing in each individual capsule is dependent on water activity because it is controlled by the equilibrium reaction of water dissociation ($H_2 + 1/2 O_2 = H_2O$) inside the capsules. Water activities for every run were calculated from the composition of the fluid phase ($X^{\text{fl}}H_2O$, see §2.3) using activity coefficients after Aranovich and Newton (1999) and molar volumes of pure H_2O after Pitzer and Sterner (1994). The fO_2 was calculated for each experiment using the expression $\log fO_2^{\text{capsule}} = \log fO_2^{\text{intrinsic}} + 2\log (aH_2O)$ (see also Botcharnikov et al., 2005b) and the calculated values for each experiment are reported in Table 2-2.

Experiments designed for the determination of molar absorption coefficients (preparation of reference glasses) were carried out at 1250°C and 500 or 300 MPa for 24 hours followed by rapid quench.

Table 2-2. Experimental conditions and results of Karl-Fischer titration, determinations of redox state of Fe and infrared spectroscopy

Capsule NN	P (MPa)	XH ₂ O _{in} ^a	X ^H H ₂ O ^b	ΔNNO ^c	H ₂ O (wt.%) KFT ^d	FeO loss, % relative ^e	Fe(II)/ Fe total ^f	H ₂ O-t, wt.% (3550 cm ⁻¹) MIR ^g	H ₂ O-m, wt.% (5200 cm ⁻¹) NIR	OH, wt.% (4500 cm ⁻¹) NIR	H ₂ O total, wt.%, NIR ^h	CO ₂ , ppm (1430 cm ⁻¹) (MIR)
M13	50	1.00	1.00 (8)	2.60	1.67 (14)	—	n.a.	n.a.	n.a.	n.a.	—	0
M14	50	0.93	1.00 (5)	2.60	1.82 (12)	—	0.64 (2)	1.59 (21)	0.59 (6)	1.12 (12)	1.71 (13)	0
M15	50	0.78	0.48 (8)	2.00	1.54 (12)	—	0.68 (2)	1.43 (20)	0.54 (6)	0.98 (10)	1.52 (12)	60 (7)
M16	50	0.54	0.20 (8)	1.28	1.07 (12)	6.55	0.73 (2)	1.10 (17)	n.a.	n.a.	—	92 (8)
M51	50	0.94	0.98 (3)	2.58	2.24 (11)	—	0.66 (3)	n.a.	0.96 (10)	1.38 (14)	2.34 (17)	0
M50	50	0.83	0.67 (6)	2.27	2.43 (12)	—	0.70 (2)	n.a.	0.73 (8)	1.17 (13)	1.90 (15)	35 (3)
M49	50	0.52	0.31 (8)	1.64	1.25 (12)	6.04	0.75 (2)	n.a.	0.44 (5)	0.79 (8)	1.23 (10)	114 (10)
M48	50	0.00	0.20 (8)	1.24	0.77 (11)	12.47	0.79 (2)	0.70 (13)	0.34 (4)	0.51 (5)	0.85 (6)	176 (15)
M47	50	0.00	0.18 (8)	1.20	0.82 (12)	10.60	0.75 (2)	0.73 (12)	0.34 (4)	0.51 (5)	0.85 (7)	175 (14)
M6	100	1.00	1.00 (5)	2.60	2.80 (13)	—	0.64 (2)	n.a.	1.46 (16)	1.68 (17)	3.14 (23)	0
M7	100	0.94	0.60 (8)	2.18	2.97 (12)	—	0.66 (2)	n.a.	1.49 (15)	1.60 (16)	3.08 (22)	0
M8	100	0.77	0.49 (5)	2.02	2.26 (12)	—	0.71 (2)	2.06 (23)	0.94 (10)	1.27 (13)	2.21 (17)	157 (13)
M9	100	0.38	0.12 (6)	0.87	1.20 (12)	13.33	0.84 (2)	1.31 (20)	0.00	0.78 (9)	0.78 (9)	292 (24)
M10	100	0.00	0.08 (5)	2.60	0.75 (11)	16.84	0.88 (3)	0.84 (17)	0.00	0.55 (6)	0.55 (6)	341 (27)
M11	200	1.00	1.00 (3)	2.60	4.95 (12)	—	0.56 (2)	n.a.	2.92 (30)	2.06 (21)	4.98 (37)	0
M12	200	0.94	0.88* (5)	2.49	4.44 (13)	—	0.57 (2)	n.a.	2.31 (24)	1.91 (20)	4.22 (31)	195 (18)
M2	200	0.89	0.63 (4)	2.23	4.22 (13)	—	0.82 (3)	n.a.	2.09 (22)	1.88 (20)	3.97 (30)	296 (24)
M3	200	0.78	0.47 (5)	2.01	3.21 (14)	—	0.65 (3)	n.a.	1.36 (14)	1.65 (17)	3.00 (22)	598 (48)
M5	200	0.00	0.06 (5)	0.31	0.64 (13)	12.53	0.88 (3)	0.82 (17)	0.00	0.52 (5)	0.52 (5)	990 (83)
M33	300	1.00	1.00 (2)	2.60	6.25 (12)	—	n.a.	n.a.	4.16 (43)	2.23 (23)	6.39 (48)	0
M34	300	0.95	0.87 (3)	2.49	5.70 (13)	—	0.57 (2)	n.a.	3.62 (38)	2.22 (23)	5.84 (44)	375 (30)
M35	300	0.84	0.57 (4)	2.17	4.20 (12)	—	0.61 (2)	n.a.	2.28 (23)	1.94 (20)	4.23 (31)	1019 (81)
M36	300	0.71	0.34 (5)	1.78	2.82 (11)	—	0.66 (2)	n.a.	1.44 (15)	1.61 (17)	3.05 (22)	1392 (111)
M37	300	0.00	0.05 (5)	0.19	0.65 (12)	26.72	0.79 (3)	0.48 (9)	0.27 (3)	0.26 (3)	0.53 (4)	1627 (142)
M38	400	1.00	1.00 (5)	2.60	7.36 (12)	—	0.54 (2)	n.a.	n.a.	n.a.	—	0
M39	400	0.96	0.89 (3)	2.51	6.75 (12)	—	0.54 (2)	n.a.	4.59 (47)	2.30 (24)	6.89 (52)	681 (54)
M30	400	0.88	0.67 (4)	2.30	5.65 (12)	—	0.59 (2)	n.a.	3.22 (34)	1.97 (21)	5.18 (39)	1271 (101)
M40	400	0.63	0.31 (4)	1.73	3.07 (12)	—	0.64 (2)	n.a.	1.43 (15)	1.60 (16)	3.03 (22)	2183 (178)
M19	500	0.64	0.18 (4)	1.45	3.29 (13)	—	0.70 (2)	n.a.	1.49 (15)	1.68 (17)	3.16 (23)	3277 (266)

Table 2-2 continued.

Capsule NN	P (MPa)	X _{H₂O} ⁱⁿ ^a	X ^{H₂O} ^b	ΔNNO ^c	H ₂ O (wt.%) KFT ^d	FeO loss, % relative ^e	Fe(II)/ Fe total ^f	H ₂ O-t, wt.% (3550 cm ⁻¹) MIR ^g	H ₂ O-m, wt.% (5200 cm ⁻¹) NIR	OH, wt.% (4500 cm ⁻¹) NIR	H ₂ O total, wt.%, NIR ^h	CO ₂ , ppm (1430 cm ⁻¹) (MIR)
M20	500	0.87	0.64* (5)	2.28	5.72 (12)	—	0.61 (2)	n.a.	3.73 (38)	2.19 (22)	5.91 (44)	2421 (268)
M21	500	0.97	0.91* (5)	2.52	7.56 (14)	—	0.56 (2)	n.a.	n.a.	n.a.	—	1051 (98)
M22	500	1.00	1.00 (6)	2.60	8.81 (16)	—	0.54 (2)	n.a.	n.a.	n.a.	—	0
M42	500	0.23	0.07 (3)	0.55	1.33 (11)	5.44	0.75 (2)	1.42 (19)	0.69 (8)	0.96 (11)	1.65 (13)	3318 (276)
M43	500	0.52	0.16 (4)	1.24	2.62 (11)	—	0.67 (2)	n.a.	1.24 (13)	1.55 (16)	2.79 (21)	3172 (265)
M44	500	0.73	0.27 (5)	1.65	4.00 (12)	—	0.63 (2)	n.a.	2.20 (23)	1.91 (19)	4.11 (30)	3029 (244)
M46	500	0.91	0.76* (5)	2.39	6.69 (12)	—	0.57 (2)	n.a.	4.80 (49)	2.28 (23)	7.09 (55)	2189 (181)

Notes:

n.a. - was not analyzed; calculated errors are shown in brackets near values (1 sigma deviation)

^a - mole fractions of H₂O in fluid loaded to the capsules before experiments;

^b - mole fractions of H₂O in fluid in the capsules after experiments, * - values calculated by mass-balance when weight-loss procedure failed;

^c - deviation of oxygen fugacity from Ni/NiO buffer in log units (calculation procedure described in part 2.2);

^d - KFT represents a single measurement with error calculated by error propagation considering errors in titration rate of 0.02 mg/s, errors in sample weight of 0.1 mg, and uncertainty of unextracted water of 0.10 wt%;

^e - deviations of FeO-total concentrations in experimental glasses from initial composition (Table 2-1), only deviations higher than ±5 % relative are shown;

^f - 2σ error (calculated from analytical uncertainties) is shown;

^g - Errors of the calculated concentrations of H₂O and CO₂, determined by IR, calculated by error propagation considering errors of thickness (0.0002 cm), density (2% relative), reproducibility of absorbance (for each band respectively) and errors of the absorption coefficients (from Table 2-3);

^h - sum of H₂O-molecular and OH-group concentrations determined by near-infrared spectroscopy.

2.3 Determination of fluid composition after experiment

A conventional weight-loss procedure was employed for determination of the mole fractions of H₂O ($X^{\text{fl}}\text{H}_2\text{O}$) and CO₂ ($X^{\text{fl}}\text{CO}_2$) in the fluid phase after experiment. Capsules were weighed after the runs and cooled by putting them into liquid nitrogen to freeze H₂O in the fluid phase. Frozen capsules were punctured with a steel needle and warmed up to room temperature. By subsequent weighing, the mass of CO₂ in the fluid was determined. The capsules were then placed into an oven at 110°C for 2-3 minutes (500 MPa- runs were held at 60°C) and weighed to determine the mass of evaporated H₂O. Weighing was repeated until no loss of water was detected anymore. It can be noted that the technique to determine the mass of free CO₂ in the capsule does not discriminate between CO₂ and N₂. An entrapment of atmospheric nitrogen in the experimental charge during loading the capsules was estimated to be small (0.5 to 4 mol.%, Tamic et al., 2001). As a main source of errors for the determined mole fractions of H₂O and CO₂ in the fluid we considered the uncertainty in the weighing of the capsules before and after piercing (0.1 and 0.05 mg for CO₂ and H₂O, respectively). Additional uncertainty, induced by atmospheric nitrogen, was taken into account (0.007 mol.% for H₂O and 0.02 mol.% for CO₂, according to (Tamic et al., 2001).

In capsules for which the weight-loss procedure of determining the fluid composition failed, the mole fractions of H₂O and CO₂ in fluid were calculated by mass-balance using initial amounts of loaded volatiles and rock powder and measured concentrations of volatiles in run-product glasses (see Table 2-2). The data obtained by mass balance have a higher uncertainty, especially because the system is not closed for hydrogen during the experiments.

2.4 Water determination by Karl-Fischer Titration

The determination of H₂O dissolved in the glasses was made by Karl-Fischer titration (KFT, Behrens et al., 1996). The samples (composed of one or several glass pieces with a total weight of about 10-20 mg) were placed into an open platinum crucible and heated up with a high-frequency generator (Linn electronic HTG 1000/1,3) from room temperature to 1300°C. Extracted water was transported by an Ar-stream to the titration cell with an electrolytic solution. The amount of extracted H₂O was measured by a moisture meter (Mitsubishi CA-100) after quantitative reaction between H₂O and coulometrically generated I₂. The uncertainty in the water determination was estimated on the basis of the uncertainty of the titration rate which is 0.2 µg/s (Behrens et al., 1996).

Behrens et al. (1996) noted that there is always ~ 0.1 wt% unextracted water in the glasses after heating and corrected the water concentration in the glass by adding this value. However, this observation was made for feldspatic glasses. Considering that water diffusivity is higher in basaltic melts compared to that in more silicic melts (Behrens et al., 2004b), a more effective extraction can be expected in our glasses. Thus, instead of a correction of the KFT data, an additional uncertainty of ± 0.1 wt.% was considered in the error calculation. The results were also used for the calibration of IR absorption coefficients.

2.5 Determination of total dissolved carbon in reference glasses

For the calibration of IR absorption coefficients for carbon-related bands in glasses, the total carbon content in glasses needs to be analyzed. The total carbon concentration in the reference glasses was analyzed by combustion and subsequent IR spectroscopy using an ELTRA CS 800 analyzer. For each measurement about 100 mg of basaltic glass was loaded into a corundum crucible together with $\sim 1.5 \pm 0.05$ g W and 0.3 ± 0.03 g Fe. The mixture was fired in an oxygen stream at temperature up to 2200°C (according to the manufacturer). After combustion, the released CO_2 was measured in an IR cell. For calibration of the method, background measurements and analyses using metallic and glass standards with known carbon contents were performed. In the background measurements, a corundum crucible was loaded with W and Fe without any sample and an average value of 5.1 ± 0.4 $\mu\text{g C}$ was determined. The air-melted starting glass was analyzed and the average of three measurements yielded a carbon concentration of 8.2 ± 1.4 $\mu\text{g C}$ (about 0.009 wt.% CO_2). The concentrations of total carbon in the four glasses synthesized as reference materials were found to be 691 ± 11 (St-1), 1136 ± 74 (St-2), 1394 ± 125 (St-3) and 871 ± 16 (St-6) ppm CO_2 (water concentrations are 2.96 ± 0.09 , 2.84 ± 0.05 , 1.33 ± 0.04 and 1.58 ± 0.09 wt.%, respectively).

2.6 Fourier-transform infrared spectroscopy (FTIR)

Water and carbonate concentration in basaltic glasses were calculated using IR-spectra of absorption on the basis of the Beer-Lambert law:

$$C_i = 100 * M_i * A_j / (d * \rho * \epsilon_j) \quad (1)$$

where C_i is the concentration of species in wt.%, M_i is the molecular weight of the species, A_j is the absorbance (peak height) of band j , d is the thickness of the section, ρ is the density in g/L and ϵ_j is the absorption coefficient of band j in $\text{L}/(\text{mol} * \text{cm})$.

The concentrations of water- and carbon-bearing species dissolved in basaltic glass were determined from absorption spectra using a Bruker IFS88 FTIR spectrometer combined with an IR-ScopeII microscope (Institute of Mineralogy, Hannover). The bands of interest are in the mid-infrared (MIR) and near-infrared (NIR) range. The operating conditions for MIR were: global light source and KBr beamsplitter, spectral resolution 2 cm^{-1} ; for NIR – W-lamp and CaF_2 beamsplitter, spectral resolution 4 cm^{-1} . A MCT narrow range detector was used for both MIR and NIR. The microscope and the sample were flushed with dry air to minimize the effect of atmospheric carbon dioxide on CO_2 content of the glasses (Tamic et al., 2001). The glasses were prepared as both-side polished thin sections with a thickness of $\sim 100 \mu\text{m}$ for MIR and $\sim 250 \mu\text{m}$ for NIR. For each spectrum 50 to 100 scans were collected from spots with sizes of about $50 \times 50 \mu\text{m}$. For every sample 3 to 5 spectra were collected in different parts of the glass piece to check for homogeneity of volatile distribution.

The thickness of the polished pieces of glass was measured with a digital micrometer Mitutoyo (precision $\pm 2 \mu\text{m}$ (Behrens, 2009) in 5 points. It was not possible to measure the density of each experimental sample because of the small size of the glass pieces. Densities were calculated using the density of the water-free starting basaltic glass (composition given in Table 2-1) and assuming a partial molar volume of H_2O in the glass of $12.0 \pm 0.5 \text{ cm}^3/\text{mol}$ (Holtz et al., 1995; Richet et al., 2000). The density of the water-free glass was determined to be $2757 \pm 3 \text{ g/l}$ after weighing two glass pieces (640 and 1300 mg) in water and in air. The densities of hydrous glasses can be calculated using following equation:

$$\rho = (2757 - 22.1 * \text{H}_2\text{O}) \quad (2)$$

where H_2O is the water content in wt.%. The uncertainty on density values calculated following this procedure is estimated to be about $\pm 2 \text{ rel. } \%$ (Behrens et al., 2009). Density variations due to pressure can be neglected (Behrens et al., 2009) and were not taken into account.

2.7 Electron microprobe

Major-element composition of the air-melted starting glass and experimental products were analyzed by electron microprobe (Cameca SX100). Conditions of measurements were 15 keV accelerating voltage, 4 nA beam current, $20 \mu\text{m}$ diameter of electron beam. Sodium and potassium were analyzed first to minimize alkali-loss. Cameca standards were used for calibration. The composition of the starting glass is an average

value of 50 analyses (Table 2-1). For all other glasses, 5 to 10 different points were analyzed to check for the homogeneity of samples and to improve reproducibility.

2.8 Wet-chemical colorimetric method for determination of redox state of Fe

The analytical approach for the determination of ferrous Fe in experimental silicate glasses is based on the analytical technique of Wilson (1960) modified by Schuessler et al., (2008) to minimize the use of toxic materials. The analytical method was optimized to measure the Fe^{2+}/Fe -total ratio of milligram-sized samples. The accuracy and precision was tested with international reference materials and with standards analyzed by other methods. The replicate measurements for different rocks and minerals containing between 1 and 8 wt.% ferrous Fe showed that the precision of Fe^{2+}/Fe -total determination using this technique is within ± 0.03 (2σ). Based on the calibration, it was concluded that this method can be reliably applied for silicate glasses with Fe^{2+}/Fe -total ratios in the range from 0.4 to 0.9 (Schuessler et al., 2008). Three to six milligrams of glasses from our samples were measured, applying this technique. The errors of the Fe^{2+}/Fe -total determination include analytical uncertainty of the method (arise mainly from the spectroscopic measurements) (Table 2-2).

3. RESULTS

3.1 Experimental products and glass composition

The experimental conditions and the analytical results are reported in Table 2-2. The experiments were carried out at a temperature higher than the liquidus and most experimental products are composed of quenched brown bubble- and crystal-free glasses, coexisting with a fluid phase (as determined by weight-loss). In one sample (M22, run at 500 MPa and $X_{\text{H}_2\text{O in}}=1$) we observed some rare elongated needle-like crystals. This sample has the highest water content and the observed crystals may have formed during quench due to enhanced kinetics of crystallization in H_2O -rich melts. For this sample the water concentrations were not determined by IR spectroscopy since the presence of crystals in the glass may affect the quality of IR measurements.

In most cases, the major-element compositions of glasses do not differ significantly from the composition of the initial glass. Deviations from starting composition for SiO_2 , Al_2O_3 , MgO , CaO , TiO_2 are within ± 3 % relative (loss of Fe in some runs is discussed below) if normalized to volatile-free basis (Appendix, Table A-2-1), showing that the incongruent dissolution of melt components in the fluid can be neglected (the amount of

melt dominates over that of fluid). IR spectroscopic data demonstrate homogeneous distribution of H₂O and CO₂ in all glasses, indicating that run duration was long enough to reach equilibrium between fluid phase and melt.

Water was detected in all samples, even in experiments with initial $X_{H_2O_{in}} = 0$ (no H₂O was loaded in the capsule). This is related to the reduction of the melt in the high pressure experiments when compared to the starting melt composition (synthesized at oxidizing atmospheric conditions). In the presence of small amounts of hydrogen in the pressure vessel (hydrogen diffuses through the noble metal capsules at high temperature), the reduction of glasses results in the formation of water, presumably according to the reaction $Fe_2O_3 + H_2 = 2FeO + H_2O$. Thus, in the nominally dry samples, small amounts of water were generated in the capsules. The determination of the FeO/FeO_{total} ratios in the glasses confirm (1) that the glasses are more reduced after the experiments and (2) that there is an increasing amount of Fe³⁺ with increasing amount of added water (Table 2-2). The initial FeO/FeO_{total} ratio in the starting composition was ~0.45 (about 4 wt.% FeO and 5 wt.% Fe₂O₃), whereas after the experiments this ratio varied from 0.54 in the most oxidized glasses (samples with $X_{H_2O_{in}} = 1$) to 0.88 in the most reduced samples (samples with $X_{H_2O_{in}} = 0$).

In addition to a change of the redox state, a noticeable loss of Fe from the glass into Au₈₀Pd₂₀ capsules was observed in the six most reduced glasses performed with $X_{H_2O_{in}} = 0$ (Table 2-2). In those experiments, the relative loss of Fe (compared to the composition of the starting glass) was found to be 10 to 16% relative in four experiments and 27% relative in the experiment M37. For most glasses with $X_{H_2O_{in}} > 0$, the Fe loss is negligible (FeO is identical to that of the starting glass within the error of the electron microprobe measurements for hydrated silicate glasses) and always < 6.5% relative, except for experiment M9 (Table 2-2). Such change in the redox state of iron and in the melt composition (for nominally dry experiments) may potentially affect the concentrations of dissolved H₂O and CO₂.

3.2 Determination of IR absorption coefficients

Typical MIR and NIR spectra used to determine the CO₂ and H₂O concentrations are shown in Figure 2-1 (data at 500 MPa). It can be noted that carbon is dissolved as carbonate only, in agreement with previous observations made for basaltic compositions (e.g., Fine and Stolper, 1986; Blank and Brooker, 1994; Dixon 1995; Botcharnikov et al., 2005a). Using the data obtained from the bulk analysis (CS) of dissolved carbon in the four

reference glasses and using the KFT data obtained for the whole dataset, linear molar absorption coefficients (ϵ) were calculated for every IR band of interest by regression of absorbance (normalized by density and section thickness) against the total water or carbon concentrations in glasses determined with independent methods (Table 2-3). The absorbance for NIR bands was always determined using linear baselines (Fig. 2-1b). The intensity of carbonate bands and of the MIR water band was determined by first subtracting a spectrum of volatile-free glass (starting material) scaled to the same thickness and then drawing a linear baseline below the carbonate and the water bending vibration bands as shown in Fig. 1a (see also Behrens et al., 2009). In this work carbonate concentrations in the glasses were quantified using the peak height of the 1430 cm^{-1} band, because the band at 1520 cm^{-1} is partly superimposed with that of the molecular water at 1630 cm^{-1} . This effect results in increasing A_{1520}/A_{1430} value with increasing total water content in the glass, as already shown by Botcharnikov et al. (2006) and Behrens et al. (2009) for andesitic and phono-tephritic compositions, respectively.

Using the available dataset, the regression between the absorbances for bands at 4500 and at 5200 cm^{-1} (normalized by density, thickness and water content from KFT measurements), was evaluated in order to determine the absorption coefficients of water species in the glasses (see Fig. 2-2a). The absorption coefficients for the bands at 4500 cm^{-1} and at 5200 cm^{-1} are found to be equal to 0.69 ± 0.08 and $0.65\pm 0.08\text{ L/mol}\cdot\text{cm}$, respectively (Fig. 2-2a). These data are in a good agreement with observations on the effects of melt composition on the absorption coefficients (e.g. Ohlhorst et al., 2001; Mandeville et al., 2002; Behrens et al., 2009), indicating that approximately identical values should be expected for both the 4500 cm^{-1} and the 5200 cm^{-1} bands. In addition, our data are identical within error with those of MORB compositions determined by Dixon et al. (1995). The absorption coefficient for the band at 3550 cm^{-1} can be determined from an average of individual coefficients using each data point. In this case, the average absorption coefficient is $68\pm 10\text{ L/mol}\cdot\text{cm}$. The absorption coefficient can also be calculated using a regression of the absorbance (normalized by density and thickness) versus water concentration determined by KFT in experimental and standard glasses (Fig. 2-2b). In this case, a value of $65\pm 2\text{ L/mol}\cdot\text{cm}$ is obtained. Although both values are identical within uncertainty, the second value is in better agreement with the data published previously by Dixon et al. (1995; $63\pm 3\text{ L/mol}\cdot\text{cm}$). For carbonate, four samples could be used for the calibration of the absorption coefficient and a value of $316\pm 12\text{ L/mol}\cdot\text{cm}$ was determined with the slope of the normalized absorbance at 1430 cm^{-1} vs. $\text{CO}_2\text{ tot}$ (Fig. 2-3). A similar

value was obtained by averaging the ϵ_{1430} values determined for each section separately: 317 ± 23 L/mol*cm. This value is lower by 15 % relative than that proposed by Fine and Stolper (1986; 375 ± 20 L/mol*cm) for a tholeiitic composition. In this study we used the values of 317 ± 23 (ϵ_{1430}) and 68 ± 10 L/mol*cm (ϵ_{3550}) for the calculation of CO_2 and total water concentrations in the glasses, respectively.

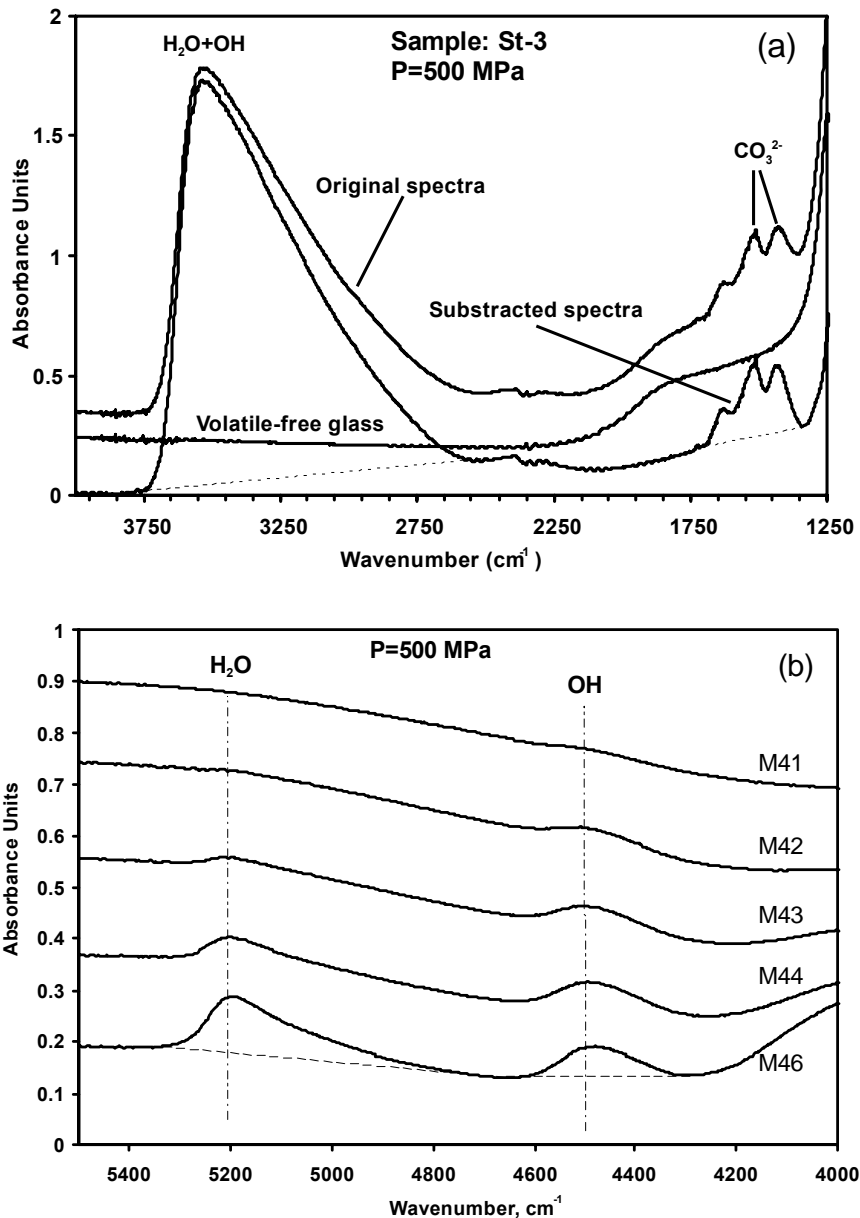


Fig. 2-1. Infrared spectra of experimental glasses. (a) Typical mid-infrared (MIR) spectrum of H_2O - and CO_2 -bearing glass (St-3, P=500 MPa; upper solid line), dry starting glass (thick solid line) and spectrum obtained by subtraction of a spectrum of volatile-free glass from that of the sample after normalization to the same thickness. Dashed lines are baselines that were used for measuring peaks heights for 3550 cm^{-1} and 1430 cm^{-1} bands. (b) Series of near-infrared (NIR) spectra (solid lines) of experimental glasses with different water concentrations after experiment at 500 MPa (see Table 2-2). Dashed-dotted lines show position of 4550 cm^{-1} (OH-group) and 5200 cm^{-1} (H_2O -molecular) bands. Dashed lines are baselines used for measuring band intensities.

Table 2-3. Linear molar absorption coefficients

	Species	ϵ [L/mol*cm] (linear regression)	ϵ [L/mol*cm] (average)	Range of H ₂ O ^{tot} (wt.%)
ϵ_{1430}	carbonate	316 ± 12	317 ± 23	1.33 - 2.96
ϵ_{3550}	OH, H ₂ O-m	65 ± 2	68 ± 10	0.28 - 2.26
ϵ_{4500}	OH	0.69 ± 0.08		0.28 - 6.75
ϵ_{5200}	H ₂ O-m	0.65 ± 0.08		0.28 - 6.75

Notes:

Molar absorption coefficients for carbonate band (1430 cm⁻¹) were calculated using standard glasses. For other bands the determination was performed by using dataset of experimental and standard glasses. Molar absorption coefficients for carbonate (1430 cm⁻¹) and water (3550 cm⁻¹) were calculated using two ways: 1) by averaging individual coefficients, calculated for each data point (average) and 2) by regression of absorbance normalized by density and section thickness against the total carbon or water concentrations in glasses determined by independent methods (linear regression). In this work, for calculations of CO₂ and H₂O concentrations in experimental glasses with 1430 cm⁻¹ and 3550 cm⁻¹ bands, respectively, linear molar absorption coefficients determined by averaging were used (see part 3.2). Errors for average values represent 1 standard deviation, for linear - 3 σ -deviations determined from linear regression.

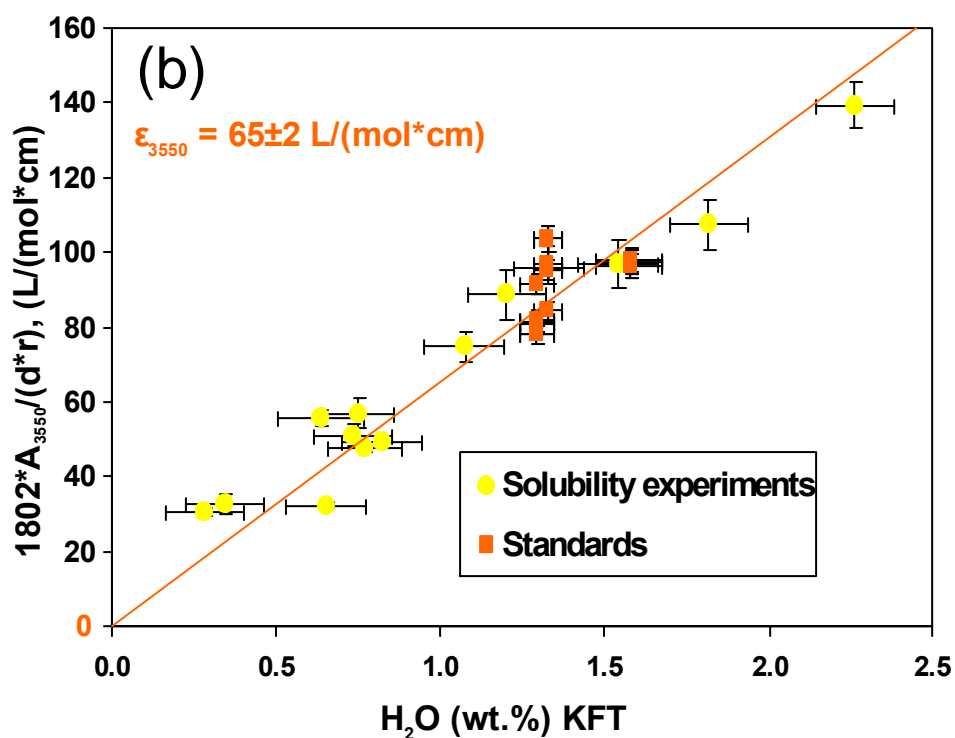
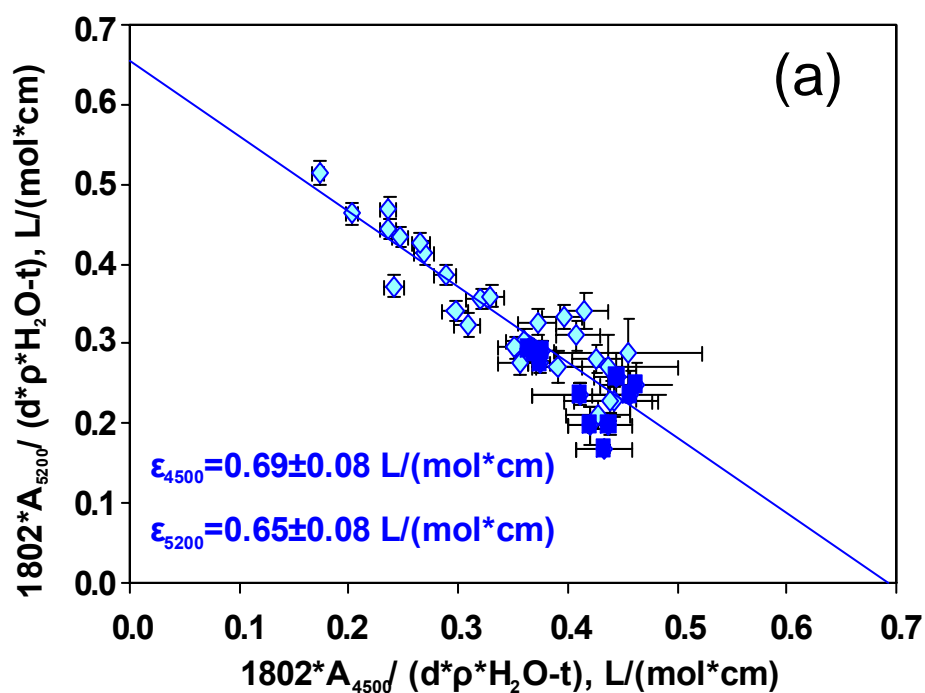


Fig. 2-2. (a) Calibration plot for the determination of the absorption coefficients for the 4550 cm^{-1} and 5200 cm^{-1} bands. (b) Plot of normalized absorbance of the 3550 cm^{-1} band vs. water concentration in the glasses determined by KFT (see part 3.2).

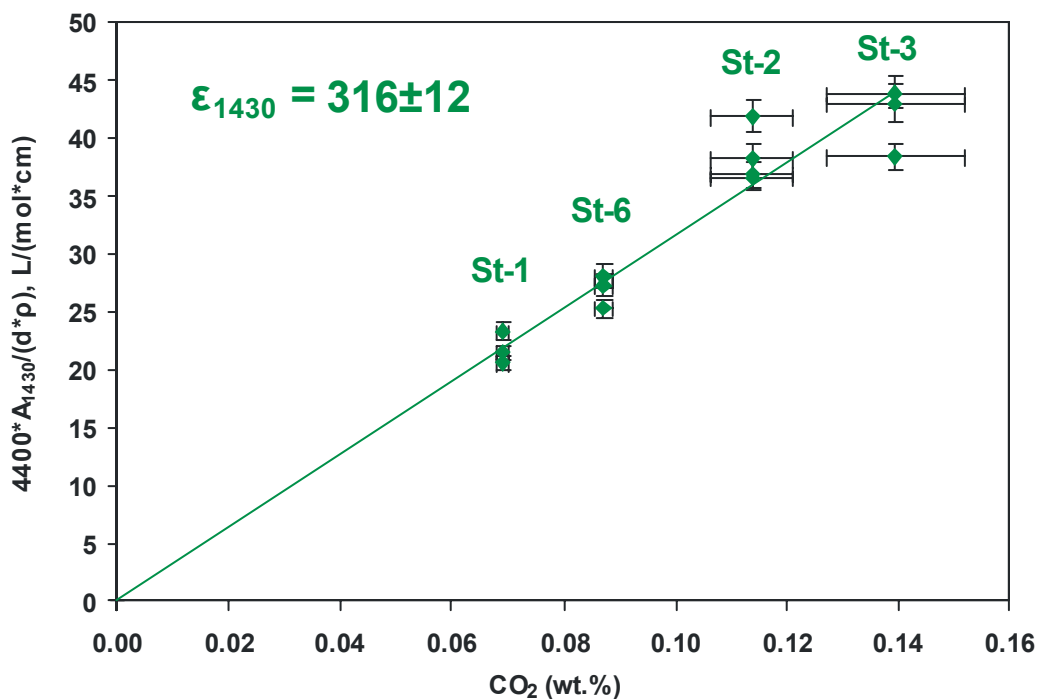


Fig. 2-3. Calibration plots for the determination of the absorption coefficient for the carbonate band at 1430 cm⁻¹: normalized absorbance of the 1430 cm⁻¹ band versus total carbon content determined by CS analyses (see parts 2.5 and 3.2).

3.3 Concentrations of water and CO₂ in coexisting fluids and glasses

The concentrations of H₂O and CO₂ dissolved in glasses as a function of the fluid phase composition are shown in Figure 2-4. In general, water and CO₂ concentrations increase non-linearly with increasing mole fraction of these components in the coexisting fluid (X^{fl}H₂O and X^{fl}CO₂, respectively).

In glasses which are in equilibrium with pure H₂O-bearing fluid, the amount of dissolved water increases from about 2.3 wt.% at 50 MPa to 8.8 wt.% at 500 MPa (Fig. 2-5a). At low pressures (<200 MPa), the dependence of water solubility on pressure can be generally described as a power function, and at higher pressures the trend becomes nearly linear. In the systems with H₂O-CO₂-fluids, a power law dependence of water solubility on X^{fl}H₂O is observed at X^{fl}H₂O < 0.3. At higher X^{fl}H₂O, the change of the H₂O concentration become less sensitive to changes in the fluid composition for experiments at pressures less than 300 MPa. At 300 and 400 MPa the dependence of H₂O solubility on X^{fl}H₂O is almost linear at X^{fl}H₂O > 0.3 (Fig. 2-4a). Moreover, at 500 MPa a point of inflexion in the trend is observed at X^{fl}H₂O ~ 0.5 (Fig. 2-4a).

The concentrations of CO₂ dissolved in the glass have an almost linear dependence on X^{fl}CO₂ at pressures of 50, 100 and 200 MPa (at least within the uncertainty of the data, Fig. 2-4b). The deviation from linearity increases with pressure. The maximum concentration of CO₂ in basaltic melt were analyzed in glasses coexisting with the most

CO₂-rich fluids (for different pressures maximum $X^f\text{CO}_2$ varies from 0.7 to 0.9). They vary from about 0.02 wt.% at 50 MPa to 0.33 wt.% at 500 MPa (Table 2-2). The dependence of CO₂ solubility on pressure can be described as a power function (Fig. 2-5b).

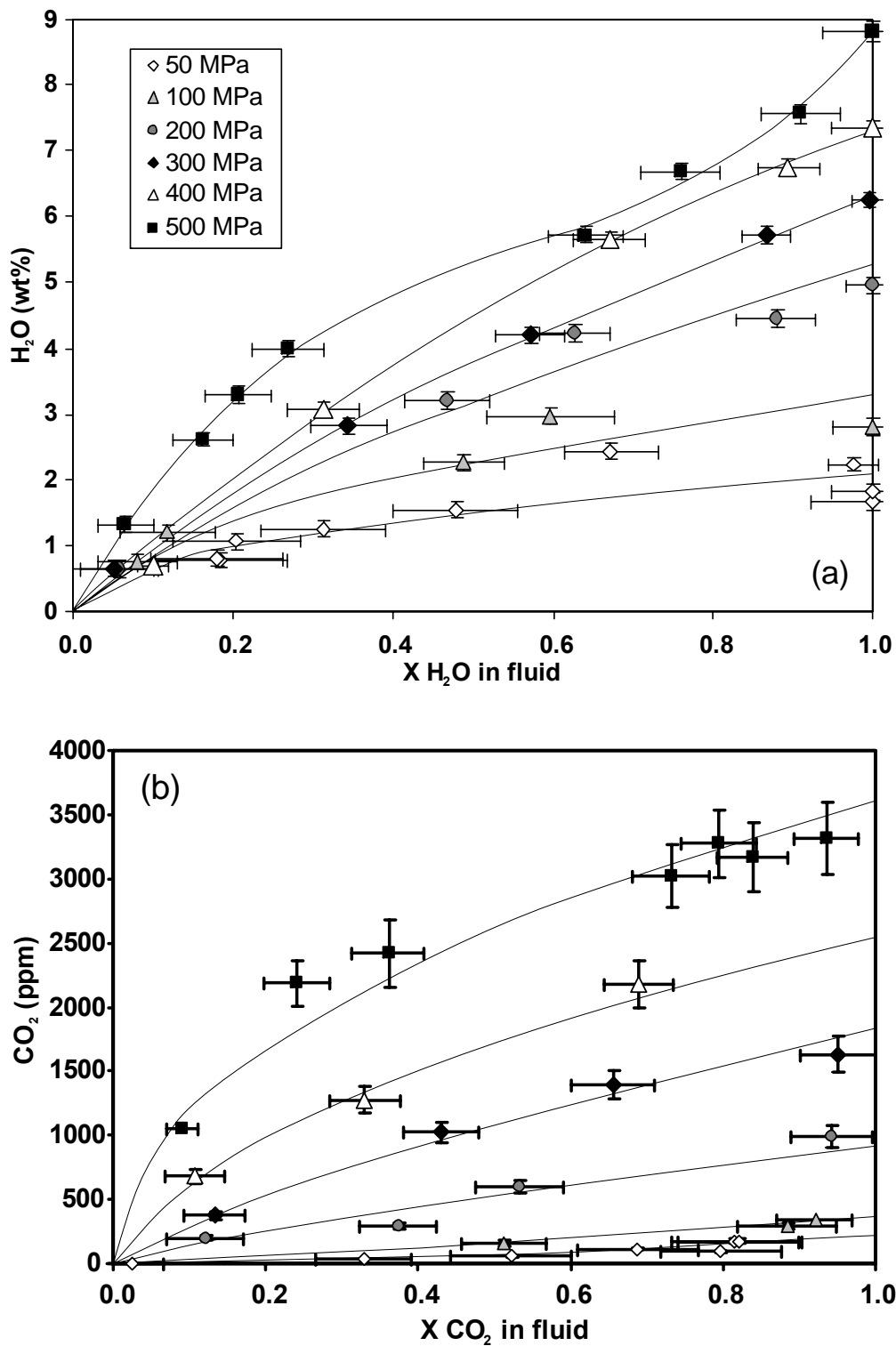


Fig. 2-4. Relationship between the mole fraction in the fluid phase and the total concentration in the melt for H₂O (a) and CO₂ (b). Dissolved H₂O data are from KFT, CO₂ data from MIR. Solid lines represent trends fitted by power-law for every studied pressure.

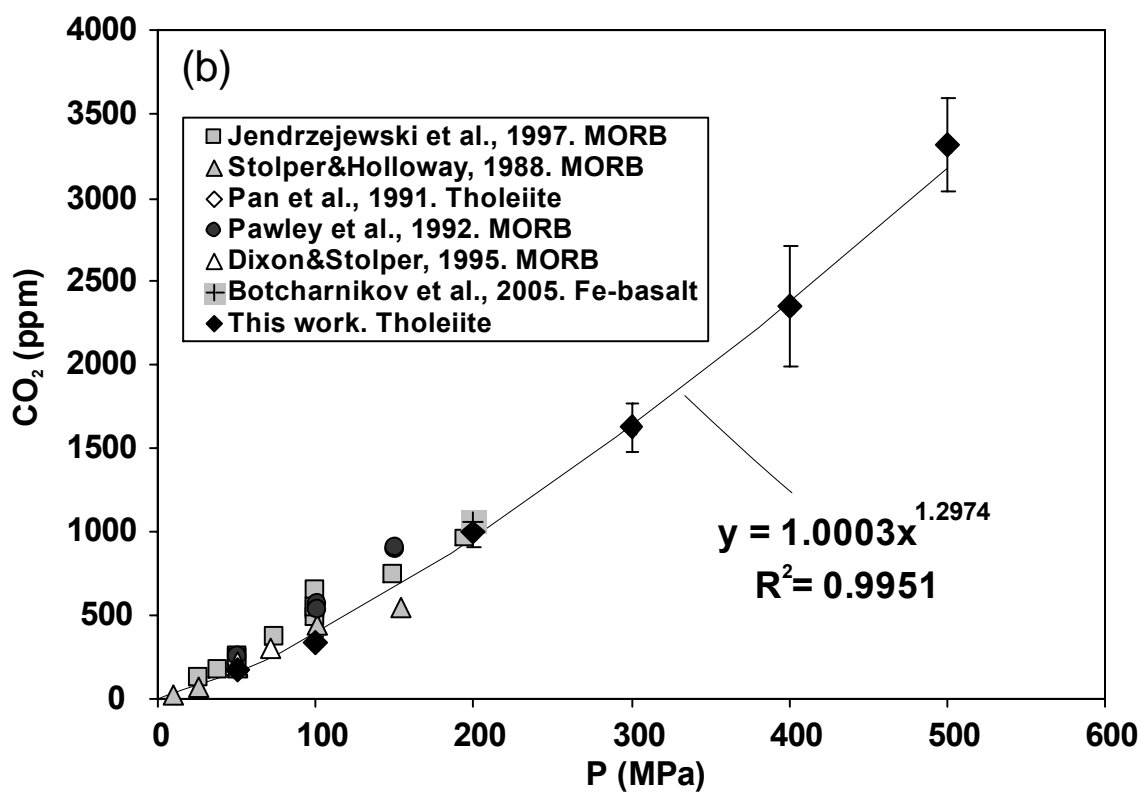
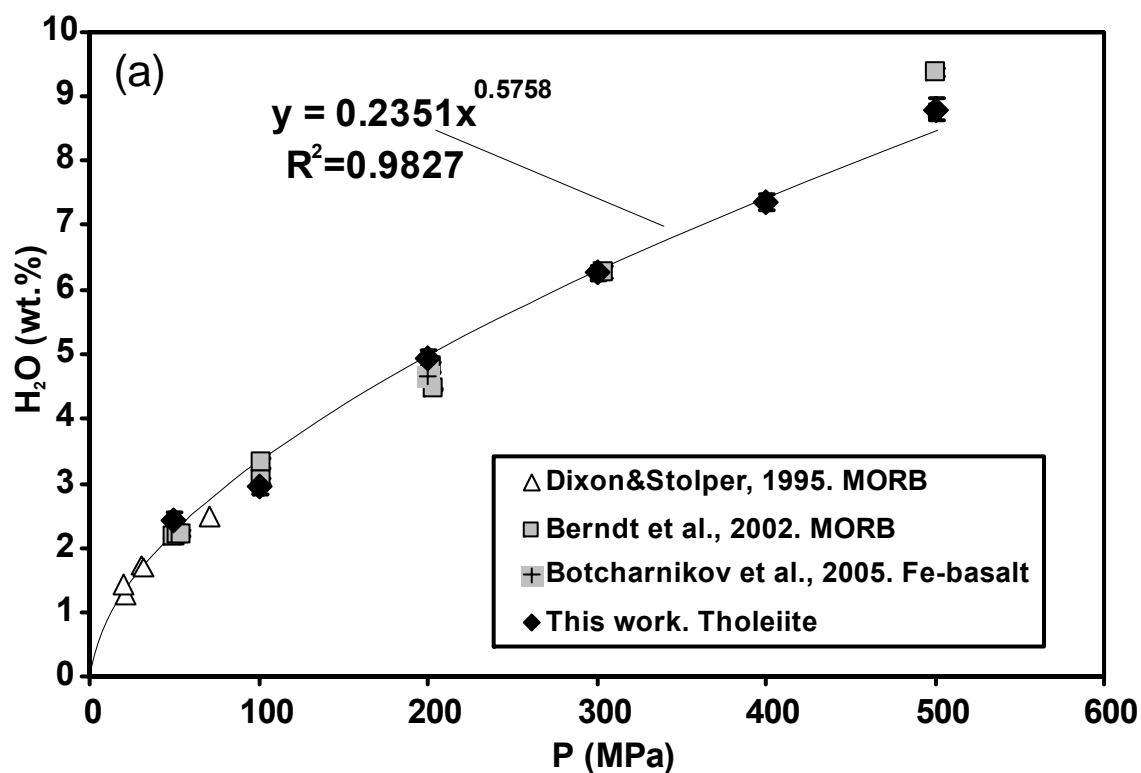


Fig. 2-5. Solubility of pure H₂O (a) and pure CO₂ (b) in basaltic melts as a function of pressure as determined in this work and from literature data. Power-law equations describe the solubility curves of pure H₂O or CO₂ as function of pressure.

4. DISCUSSION

4.1 Solubility curves in basaltic melts and composition of coexisting fluids

The increase in the concentration of water dissolved in tholeiitic basalt ($X^{\text{fl}}\text{H}_2\text{O} = 1$) with pressure is in a good agreement with recent literature data for other basaltic liquids (Fig. 2-5a). The plot of water solubility (expressed as wt% H_2O) as a function of pressure (expressed as MPa) is non-linear at pressures <200 MPa which may be attributed to the predominant solubility of OH groups in silicate melts at low water concentrations (see e.g., Stolper, 1982; Nowak and Behrens, 2001; Liu et al., 2005).

Since all samples contain water in the investigated system, the CO_2 solubility in melts coexisting with pure CO_2 -bearing fluids is estimated by the extrapolation of the experimental trends in Fig. 2-4b towards conditions with $X^{\text{fl}}\text{CO}_2 = 1$. The estimated solubility of CO_2 increases from 0.02 wt.% at 50 MPa to about 0.33 wt.% at 500 MPa. The trend of CO_2 solubility in the melts as a function of pressure is in a very good agreement with the solubility trends of CO_2 predicted by Holloway and Blank (1994) in basaltic tholeiites up to 500 MPa and with the experimental data for basalts obtained at $P < 200$ MPa (Fig.2-5b). The overall agreement with previous datasets indicates that small variations in melt composition (e.g., due to loss of Fe into the capsules observed in our study) do not significantly affect the solubility of CO_2 in basaltic melts.

The solubility of mixed fluids can be illustrated using a conventional diagram with isobaric solubility curves representing the maximum concentrations of CO_2 and H_2O in the silicate melt at a given pressure (solid lines in Fig. 2-6). The dashed lines in Fig. 2-6 are isopleths showing the composition of the first fluid that would be in equilibrium with the melt at the onset of degassing. The isobars were plotted by an empirical fit of the experimental data on the H_2O and CO_2 concentrations in the melt. Isopleths with given $X^{\text{fl}}\text{H}_2\text{O}$ were calculated by interpolating the fluid compositions measured in the experiments. It must be noted that these isopleths can not be extrapolated far beyond the investigated experimental range of pressures. The experimental data plotted in Fig.2-6 are helpful for estimating pressures at which magmas might become fluid-saturated and for evaluating the composition of fluids released from the magma, if the concentrations of H_2O and CO_2 in natural basaltic glasses are known. In the next section we compare our experimental results with predictions using the most popular models on H_2O and CO_2 solubility in silicate liquids.

regular solution model. This model takes into account important parameters such as temperature, pressure, melt composition and, in particular, the effect of the oxidation state of Fe on volatile solubility.

The comparison of experimental data on H₂O and CO₂ solubility in tholeiitic basalt with both the numerical models is illustrated in Figure 2-7. The diagrams in Figure 2-7 show the relationships between measured and predicted concentrations of H₂O (a) and CO₂ (b) in systems with H₂O- and CO₂-dominated fluids, respectively. The concentrations of dissolved H₂O predicted by the VolatileCalc model are in perfect agreement with the experimental data, whereas the model of Papale et al. (2006) slightly, but systematically, overestimates water solubility in basaltic melts at pressures above 100 MPa (Fig.2-7a). The model VolatileCalc reproduces correctly the experimental data on the solubility of CO₂ in basalts coexisting with CO₂-rich fluids (Fig.2-7b), but starts to underestimate CO₂ solubility at pressure of 500 MPa (by ~15 relative %). On the other hand, the model of Papale et al. (2006) shows a dramatic overestimation of the CO₂ solubility values. This comparison indicates that the simple approach of ideal behavior of water and carbon dioxide fluids, proposed by Dixon et al. (1995) and developed by Newman and Lowenstern (2002) is successful for basaltic systems coexisting with pure H₂O and pure CO₂ fluids, implying that the small variations in the compositional parameters of the melt (e.g., redox state of Fe) do not have considerable effect for such simple fluid compositions. The discrepancy observed for the second model will be discussed below.

Because the concentrations of dissolved H₂O and CO₂ in the melts equilibrated with mixed fluids depend on many different parameters, it is difficult to compare measured and calculated solubility values. Instead, one can calculate the pressures at which basaltic melts become fluid-saturated for given concentrations of dissolved volatiles and for a given melt composition. Figure 2-8 shows the comparison between pressures of the experiments and pressures of fluid saturation calculated using both models (assuming H₂O and CO₂ concentrations determined experimentally). The VolatileCalc model predicts higher pressures for the systems with mixed fluids at P>200 MPa, the difference increases with pressure and may reach about 40 rel.% at 500 MPa. On the contrary, the model of Papale et al. (2006) predicts significantly lower pressures over the entire investigated pressure range and even at 50 and 100 MPa. The observed discrepancy between the experiments and the predictions is presumably attributed to the influence of water on CO₂ solubility which is not properly calibrated in the models. The influence of water on CO₂ solubility in silicate melts has been documented in several studies (e.g., Jakobsson, 1997; Behrens et al., 2004a)

and is also illustrated in our dataset at high pressure. For example, at 500 MPa, the maximum CO₂ concentration decreases only slightly with increasing water concentration from 0 to 4 wt% H₂O. In this water concentration range, the CO₂ solubility is nearly constant within uncertainty with a value of ~ 3200 ppm (Fig. 2-6). The same observation was done by Jakobsson (1997) at 1 GPa for an andesitic composition. This behavior possibly results from the effect of dissolved OH groups on the incorporation of CO₂ as proposed in earlier studies (e.g., Mysen et al., 1975; Mysen, 1976; Botcharnikov et al., 2006; Behrens et al., 2009). Thus, the simple assumption of Henrian behavior for the incorporation of water and carbon dioxide in basaltic systems in equilibrium with mixed H₂O- and CO₂-bearing fluids is not valid at least at pressures >200 MPa.

The overestimation of the CO₂ concentrations in basaltic melts (by about 2-3 times for CO₂-rich compositions) using the model of Papale et al. (2006) is related to the limited database for the calibration of the model at pressures above 200 MPa. Moreover, Papale et al. (2006) used only 4 data points from the experiments at 500 MPa for an alkali basalt composition conducted by Freise (2004) and reported by Botcharnikov et al. (2005a). Recently, the basaltic composition studied by Freise (2004) has been re-investigated and we noted that the CO₂ concentrations (reported to be up to 0.7 wt.% CO₂ at 500 MPa) have been overestimated presumably due to a wrong correction factor for the thickness of the samples. The new estimated values for maximum CO₂ content in alkali basalt are in the range from 3500 to 4000 ppm (Botcharnikov et al., 2008) which is consistent with the CO₂ solubility data obtained in this study. Thus, the model of Papale et al. (2006) fails in predicting accurate solubilities at high pressure because no accurate database was available.

The dataset presented in this study is useful to extend the available quantitative models for predicting the degassing conditions of natural basaltic melts up to 500 MPa as it gives systematic information about H₂O-CO₂ solubilities, oxidation state of Fe and changes of the melt composition (Appendix, Table A-2-2).

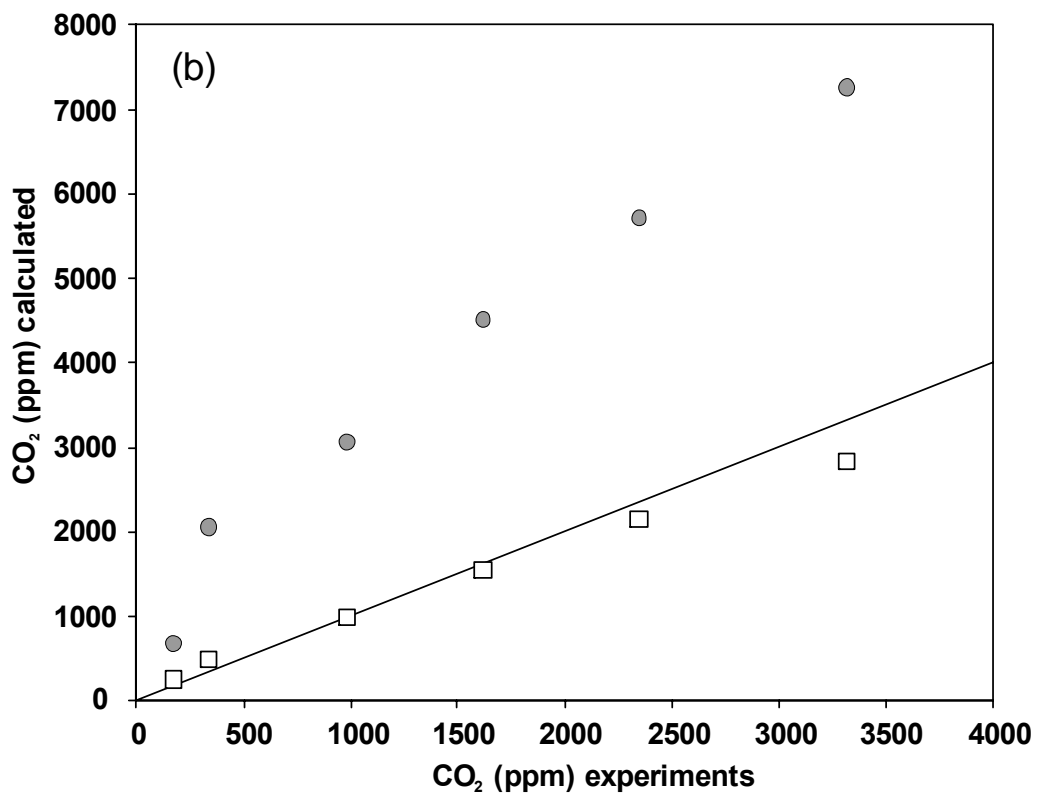
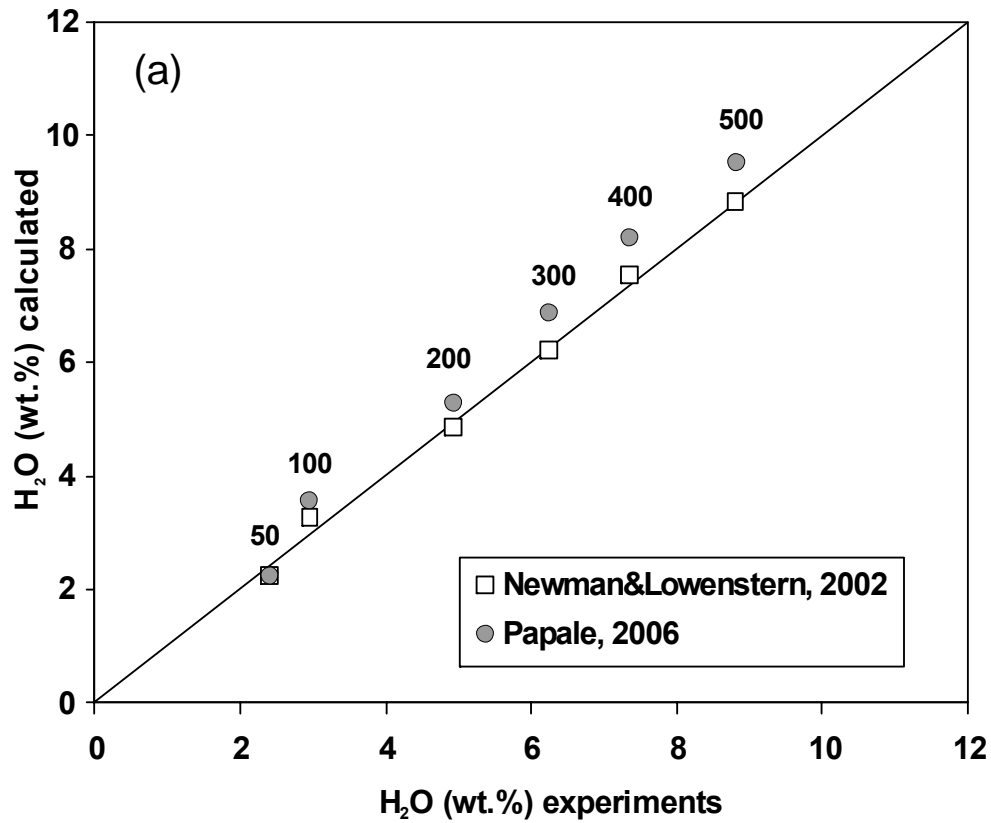


Fig. 2-7. Comparison of the experimental data on the solubility of pure H₂O (a) and CO₂ (b) in tholeiitic melt with solubilities predicted by numerical models. The solid lines are 1 : 1 relationships between the experimental and modeled data. Open squares are the data from the model of Newman and Lowenstern (2002), whereas grey circles are the results of the calculations using the model of Papale et al. (2006).

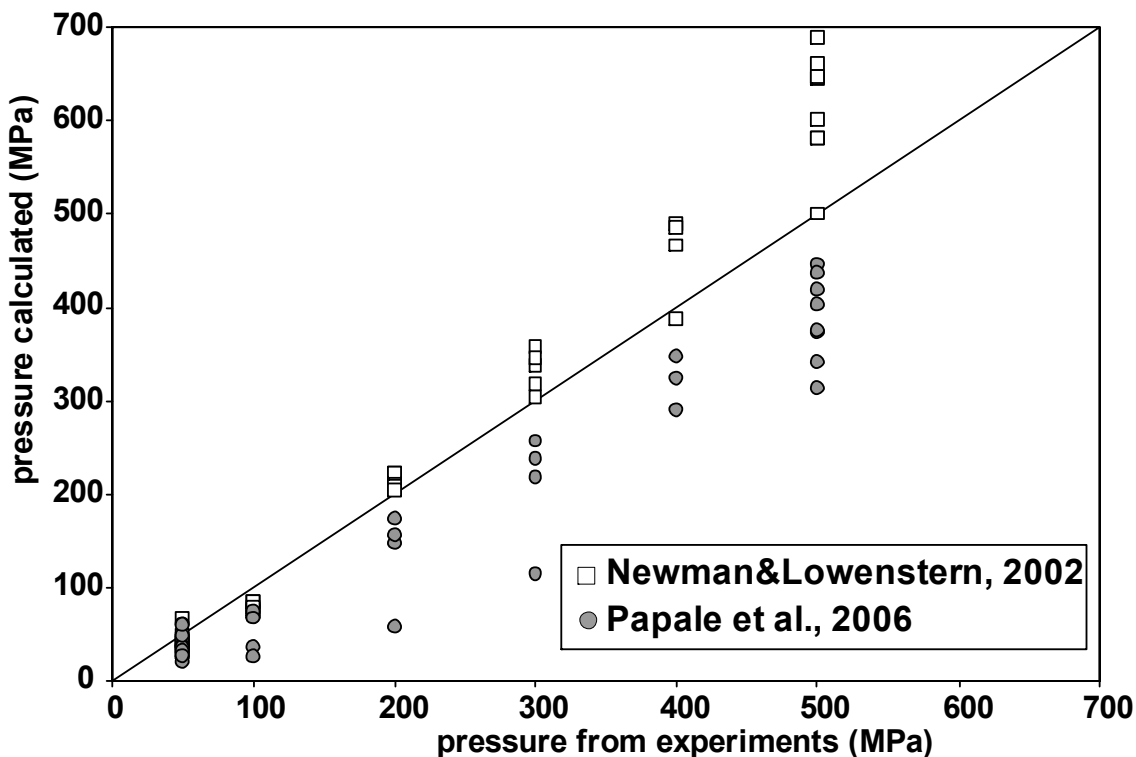


Fig. 2-8. Comparison between experimental and calculated pressures using the concentrations of dissolved H₂O and CO₂ in the melt. The model of Newman and Lowenstern (2002) significantly overestimates actual pressures at P>200 MPa, whereas the model of Papale et al. (2006) underestimates fluid-saturation pressures of the melt in the entire range of investigated pressures.

4.3. Implications for natural systems

As already mentioned above, the volatile solubility diagram shown in Figure 2-6 is a powerful tool for the interpretation of volatile concentrations obtained from the natural basaltic melts (quenched matrix glasses, melt inclusions) and especially for the determination of magma storage conditions. Our dataset, obtained only at 1250°C, needs to be extended to take the effect of temperature into account. However, the temperature effect on H₂O and CO₂ solubility is low in the temperature range from 1100 to 1300°C (see, for instance, solubility data for andesitic melts obtained by Botcharnikov et al., 2006). Furthermore, strong changes are not expected because tholeiitic melts are not stable at temperatures below 1100°C (partial crystallization is expected, leading to differentiation of the residual melt). With increasing temperature, the solubility of H₂O in melts coexisting with pure H₂O-bearing fluid decreases slightly at low pressures and increases slightly at high pressures (maximum variations are estimated to be 0.0025 wt% H₂O/°C in rhyolites; Holtz et al., 1995). Although there is no detailed study on the temperature effect of H₂O-solubility in basaltic melts, the pressure at which H₂O solubility is not dependent on

temperature is estimated to be in the range 200 – 400 MPa. The CO₂ solubility in mafic melts seems to be either independent (e.g., Holloway and Blank, 1994) or only slightly and negatively dependent on temperature (e.g., Botcharnikov et al., 2006 for andesites) indicating that significant temperature correction for the interpretation of melt inclusion or other natural data is not required. Another important aspect is the redox conditions of natural tholeiitic magmas which are typically more reduced than those investigated in this study. The reduction of the magma is expected to have a relatively small effect on the solubility of H₂O (e.g., Berndt et al., 2002; Botcharnikov et al., 2005b), but may presumably lead to changes in CO₂ solubility due to changes in carbon speciation and changes in the Fe redox state in the magma. Furthermore, the increasing proportion of CO over CO₂ in the fluid with reduction of the system will decrease the solubility of CO₂ (e.g., Pawley et al., 1992; Scaillet and Pichavant, 2004; Botcharnikov et al., 2005c). The effect of ferric/ferrous ratio on the solubility of the volatiles is complex and depends on the bulk composition and on the relative proportions of H₂O and CO₂ (according to the model of Papale et al., 2006). Hence, one may expect some deviations in the position of isobars and isopleths in Figs.2-6 and 2-9, but the exact changes remain experimentally unconstrained and require future efforts. It must be noted, however, that our CO₂-rich experiments simulated redox conditions that are relatively close to that of natural magmas (Table 2-2).

The data are also useful to discuss magmatic processes related with the dynamics of magma evolution and degassing in magma chambers and conduits beneath volcanoes. Figure 2-9 shows a compilation of data on volatile concentrations determined in melt inclusions in olivine from low- to mid-K basalts of several geographical and geological localities: Hawaii (Harris and Anderson, 1983; Anderson and Brown, 1993), Mariana arc (Newman et al., 2000; Shaw et al., 2008), Ryukyu arc (Saito et al., 2001), Izu arc (Nichols and Wysoczanski, 2007), La Réunion (Famin et al., 2009). The measured compositional values are compared with the experimental isobars and isopleths for basaltic melts saturated with respect to H₂O- and CO₂-bearing fluids. All reported values indicate that the melts were saturated with respect to fluids at pressures lower than 400 MPa. Assuming that melt inclusions did not exchange volatiles with the surrounding magma during magma evolution (no gain or loss), this observation indicates that most melt inclusions were trapped in olivines at relatively shallow levels in magmatic systems of the Mariana arc (<12-15km) and at very shallow levels for the other examples (< 5-6 km). The compositional trends for the different magmatic suites also clearly reflect different evolution and degassing histories of natural magmas, depending on their geodynamic

setting. As expected, the subduction-related magmas show systematically higher H₂O proportions, but the pressure at which the melt inclusions may become saturated with respect to fluids is in the same range for Hawaii, Ryukyu arc and Izu arc.

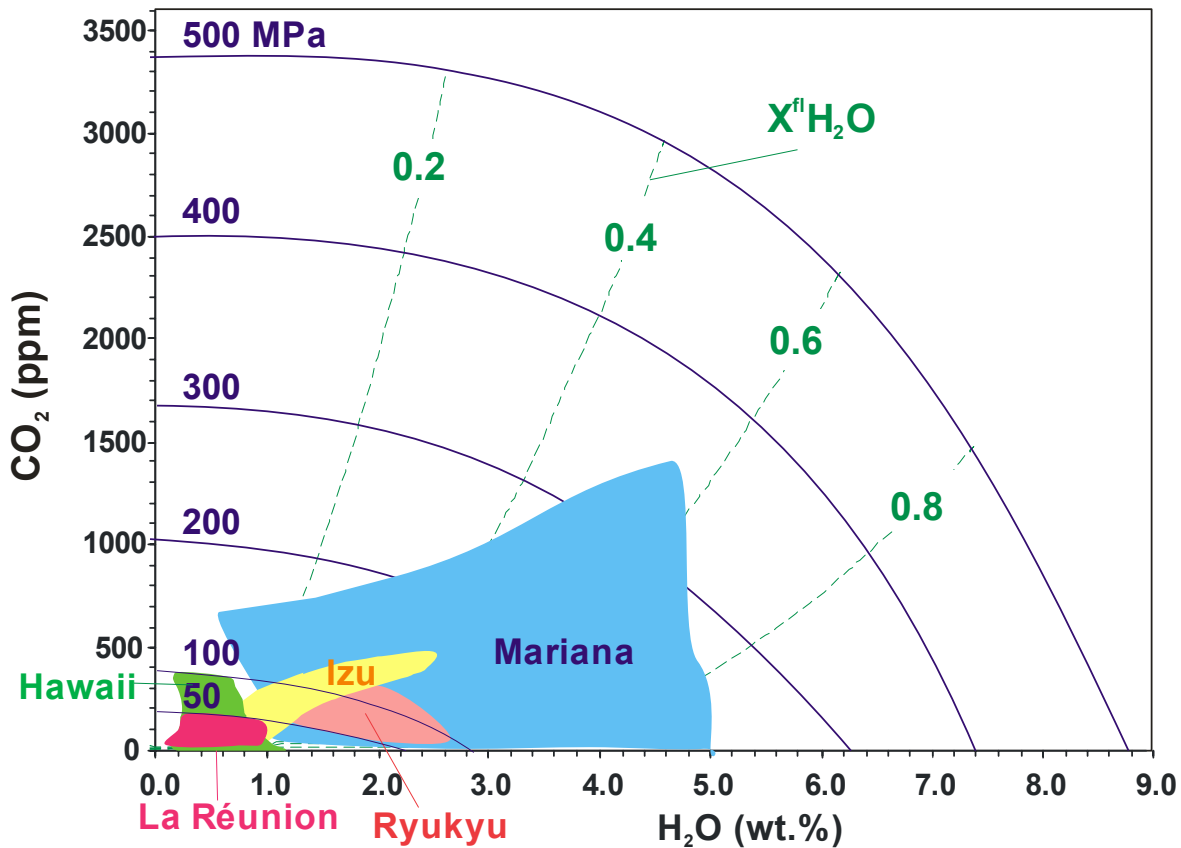


Fig. 2-9. Comparison of the experimental data with the concentrations of H₂O and CO₂ measured in melt inclusions hosted in olivines from low- to mid-K tholeiitic basalts from different localities: Mariana arc (Newman et al., 2000; Shaw et al., 2008), Ryukyu arc (Saito et al., 2001), Izu arc (Nichols and Wysoczanski, 2007), Hawaii (Harris and Anderson, 1983; Anderson, 1993), La Réunion (Famin et al., 2009).

5. CONCLUSION

Based on our experimental data combined with previous datasets, a quantitative evaluation of the storage conditions and degassing paths of tholeiitic magmas can be achieved up to 500 MPa. The experimental data on H₂O and CO₂ solubility in tholeiitic melts show that models neglecting the interactions between H₂O- and CO₂-bearing species (e.g., VolatileCalc; Newman and Lowenstern, 2002) are successful up to 200 MPa but that they do not predict accurately the volatile solubilities at pressures above 200 MPa. The deviation from such models increases with increasing pressure. Our dataset, obtained only at 1250 °C, needs to be extended to take the effect of temperature into account. The new experimental data can be used to improve the existing numerical models on H₂O-CO₂ solubility in basaltic melts and to provide more accurate constraints on the pressure conditions of magma storage, fractionation and degassing.

Acknowledgements

We thank H.Behrens for his advises, O.Diedrich for preparation of samples for infra-red spectroscopy and microprobe analyses, A.Wegorzewski for determinations of redox state of Fe. This research has been supported by the German Science Foundation (DFG project Ho1337/21) and by the Russian-German project KALMAR funded by BMBF.

References

- Anderson, A.T., Jr., Brown, G.G., 1993. CO₂ contents and formation pressures of some Kilauean melt inclusions. *American Mineralogist* 78, 794-803.
- Aranovich, L.Y., Newton, R.C., 1999. Experimental determination of CO₂-H₂O activity-concentration relations at 600–1000 C and 6–14 kbar by reversed decarbonation and dehydration reactions. *American Mineralogist* 84, 1319-1332.
- Behrens, H., Romano, C., Nowak, M., Holtz, F., Dingwell, D.B., 1996. Near-infrared spectroscopic determination of water species in glasses of system MAlSi₃O₈ (M=Li, Na, K): An interlaboratory study. *Chemical Geology* 128, 41-63.
- Behrens, H., Ohlhorst, S., Holtz, F., Champenois, M., 2004a. CO₂ solubility in dacitic melts equilibrated with H₂O–CO₂ fluids – implications for modelling the solubility of CO₂ in silicic melts. *Geochim. Cosmochim. Acta* 68, 4687-4703.
- Behrens, H., Zhang, Y., Xu, Z., 2004b. H₂O diffusion in dacitic and andesitic melts. *Geochim. Cosmochim. Acta* 68, 5139-5150.
- Behrens, H., Misiti V., Freda C., Vetere F., Botcharnikov, R.E., Scarlato, P., 2009. Solubility of H₂O and CO₂ in ultrapotassic melts at 1200 and 1250°C and pressure from 50 to 500 MPa. *American Mineralogist* 94, 105-120.
- Berndt, J., Liebske, C., Holtz, F., Freise, M., Nowak, M., Ziegenbein, D., Hurkuck, W., Koepke, J., 2002. A combined rapid-quench and H₂-membrane setup for internally heated pressure vessels: Description and application for water solubility in basaltic melts. *American Mineralogist* 87, 1717-1726.

- Blank, J.G., Stolper, E.M., Carrol, M.R., 1993. Solubilities of carbon dioxide and water in rhyolitic melt at 850C and 750 bars. *Earth and Planetary Science Letters* 119, 27-36.
- Blank, J.G., Brooker, R.A., 1994. Experimental studies of carbon dioxide in silicate melts: solubility, speciation, and stable carbon isotope behavior. In: Carrol, M.R., Holloway, J.R. (Ed.), *Reviews in Mineralogy* 30, 157-186.
- Botcharnikov, R.E., Freise, M., Holtz, F., Behrens, H., 2005a. Solubility of C-O-H mixtures in natural melts: new experimental data and application range of recent models. *Annals of Geophysics* 48, 633-646.
- Botcharnikov, R.E., Koepke, J., Holtz, F., McCammon, C., Wilke, M. 2005b. The effect of water activity on the oxidation and structural state of Fe in a ferro-basaltic melt. *Geochim. Cosmochim. Acta* 69, 5071-5085.
- Botcharnikov, R.E., Holtz, F., Behrens, H., Freise, M., 2005c. The effect of redox state on the solubility of C-O-H fluids in silicate melts: new experimental evidences. *Geophysical Research Abstracts* 7, 09237.
- Botcharnikov, R.E., Behrens, H., Holtz, F., 2006. Solubility and speciation of C-O-H fluids in andesitic melt at T = 1100-1300 °C and P = 200 and 500 MPa. *Chemical Geology* 229, 125-143.
- Botcharnikov, R.E., Almeev, R.R, Holtz, F., Behrens, H., 2008. Solubility of C-O-H fluids in mafic melts at 500 MPa. Abs. IAVCEI meeting 2008, General assembly, Reykjavik, Iceland.
- Dixon, E.J., Stolper, E.M., Holloway, J.R., 1995. An experimental study of water and carbon dioxide solubilities in mid-ocean ridge basaltic liquids. Part 1: Calibration and solubility models. *Journal of Petrology* 36, 1607-1631.
- Dixon, J.E., 1997. Degassing of alkali basalts. *American Mineralogist* 82, 368-378.
- Duggen, S., Portnyagin, M.V., Baker, J., Ulfbeck, D., Hoernle, K., Garbe-Schonberg, D., Grassineau, N., 2007. Drastic shift in lava geochemistry in the volcanic-front to rear-arc region of the Southern Kamchatkan subduction zone: Evidence for the transition from slab surface dehydration to sediment melting. *Geochim. Cosmochim. Acta* 71, 452-480.

- Famin, V., Welsch, B., Okumura, S., Bachelery P., Nakashima, S., 2009. Three differentiation stages of a single magma at Piton de la Fournaise volcano (Reunion hot spot). *Geochem. Geophys. Geosyst.* 10 (1).
- Fine, G., Stolper, E., 1986. Carbon dioxide in basaltic glasses: concentrations and speciation. *Earth and Planetary Science Letters* 76, 263-278.
- Fischer, T.P., Marty, B., 2005. Volatile abundances in the sub-arc mantle: Insights from volcanic and hydrothermal gas discharges. *Journal of Volcanology and Geothermal Research* 140, 205-216.
- Freise, M., 2004. Differenzierung von Basalten einer "Large Igneous Province" am Beispiel des Kerguelen Plateaus. Eine experimentelle Studie. PhD thesis, University of Hannover.
- Giggenbach, W.F., 1996. Chemical composition of volcanic gases. In: Scarpa, R., Tilling, R.I. (Eds.), *Monitoring and Mitigation of Volcanic Hazards*, Springer. Berlin, 221-256.
- Harris, D.M., Anderson A.T., Jr., 1983. Concentrations, sources, and losses of H₂O, CO₂, and S in Kilauean basalt. *Geochim. Cosmochim. Acta* 47, 1139-1150.
- Holloway, J.R., Blank, J.G., 1994. Application of experimental results to C-O-H species in natural melts. In: Carrol, M.R., Holloway, J.R. (Ed.), *Reviews in Mineralogy*. 30, 187-230.
- Holtz, F., Behrens, H., Dingwell, D.B., Johannes, W., 1995. Water solubility in haplogranitic melts. Compositional, pressure and temperature dependence. *American Mineralogist* 80, 94-108.
- Jakobsson, S., 1997. Solubility of water and carbon dioxide in an icelandite at 1400 °C and 10 kilobars. *Contributions to Mineralogy and Petrology* 127, 129-315.
- King, P.L., Holloway, J.R., 2002. CO₂ solubility and speciation in intermediate (andesitic) melts: the role of H₂O and composition. *Geochim. Cosmochim. Acta* 66, 1627-1640.
- Liu, Y., Zhang, Y., Behrens, H., 2005. Solubility of H₂O in rhyolitic melts at low pressures and a new empirical model for mixed H₂O-CO₂ solubility in rhyolitic melts. *Journal of Volcanology and Geothermal Research* 143, 219-235.

- Mandeville, C.W., Webster, J.D., Rutherford, M.J., Taylor, B.E., Timbal, A., Faure, K., 2002. Determination of molar absorptivities for infrared absorption bands of H₂O in andesitic glasses. *American Mineralogist* 87, 813-821.
- Martynov, Y.A., Chashchin, A., 1989. Rock-forming minerals of the mafic effusives of Mutnovsky geothermal field. New data on petrology of the magmatic and metamorphic rocks in Kamchatka. Vladivostok: FarEast Branch, USSR Academy of Science, 112-123 (in Russian).
- Martynov, Y.A., Perepelov, A.B., Chashchin, A., 1995. Geochemical typization of the basaltoids from Mutnovsky volcanic field (Southern Kamchatka). *Geology of the Pacific Ocean (Tikhookeanskaya Geologiya)* 5, 72-83 (in Russian).
- Moore, G., 2008. Interpreting H₂O and CO₂ Contents in Melt Inclusions: Constraints from Solubility Experiments and Modeling Reviews in *Mineralogy and Geochemistry* 69, 333-362.
- Mysen, B.O., Arculus, R.J., Eggler, D.H., 1975. Solubility of carbon dioxide in natural nephelinite, tholeiite, and andesite melt to 30 kbar pressure. *Contributions to Mineralogy and Petrology* 53, 227-239.
- Mysen, B.O., 1976. The role of volatiles in silicate melts; solubility of carbon dioxide and water in feldspar, pyroxene, and feldspathoid melts to 30 kb and 1625 degrees C. *American Journal of Science* 276, 969-996.
- Newman, S., Lowenstern, J. B., 2002. VolatileCalc: a silicate melt-H₂O-CO₂ solution model written in Visual Basic for Excel. *Computers & Geosciences* 28, 597-604.
- Newman, S., Stolper, Ed., Stern, R., 2000. H₂O and CO₂ in magmas from the Mariana arc and back arc systems. *Geochemistry, Geophysics, Geosystems* 1, 30 p.
- Nichols, A.R.L., Wysoczanski, R.J., 2007. Using micro-FTIR spectroscopy to measure volatile contents in small and unexposed inclusions hosted in olivine crystals. *Chemical Geology* 242, 371-384.
- Nowak, M., Behrens, H., 2001. Water in rhyolitic magmas: getting a grip on a slippery problem. *Earth Planetary Science Letters* 184, 515-522.
- Ohlhorst, S., Behrens, H., Holtz, F., 2001. Compositional dependence of molar absorptivities of near-infrared OH- and H₂O bands in rhyolitic to basaltic glasses. *Chemical Geology* 174, 5-20.

- Pan, V., Holloway, J.R., Hervig, R.L., 1991. The pressure and temperature dependence of carbon dioxide solubility in tholeiitic basalt melts. *Geochim. Cosmochim. Acta* 55, 1587-1595.
- Papale, P., 1999. Modeling of the solubility of a two-component H₂O + CO₂ fluid in silicate liquids. *American Mineralogist* 84, 477-492.
- Papale, P., Moretti, R., Barbato, D., 2006. The compositional dependence of the saturation surface of H₂O + CO₂ fluids in silicate melts. *Chemical Geology* 229, 78-95.
- Pawley, A.R., Holloway, J.R., McMillan, P.F., 1992. The effect of oxygen fugacity on the solubility of carbon-oxygen fluids in basaltic melt. *Earth and Planetary Science Letters*, 110 (1-4), 213-225.
- Pineau, F., Semet, M.P., Grassineau, N., Okrugin, V.M., Javoy, M., 1999. The genesis of the stable isotope (O, H) record in arc magmas: the Kamtchatka's case. *Chemical Geology* 153, 93-124.
- Pitzer, K.S., Sterner, S.M., 1994. Equation of state valid continuously from zero to extreme pressures for H₂O and CO₂. *Journal of Chemistry and Physics* 102, 3111-3116.
- Richet, P., Whittington, A., Holtz, F., Behrens, H., Ohlhorst, S., Wilke, M., 2000. Water and density of silicate glasses. *Contribution to Mineralogy and Petrology* 138, 337–347.
- Saito, G., Kazahaya, K., Shinohara, H., Stimac, J., Kawanabe, Y., 2001. Variation of volatile concentration in a magma system of Satsuma-Iwojima volcano deduced from melt inclusions analyses. *Journal of Volcanology and Geothermal Research* 108, 11–31.
- Scaillet, B., Pichavant, M., 2004. Role of fO_2 on fluid saturation in oceanic basalt. *Nature*, 430 (6999).
- Schuessler, J.A., Botcharnikov, R.E., Behrens, H., Misiti, V., Freda, C., 2008. Oxidation state of iron in hydrous phono-tephritic melts. *American Mineralogist* 93, 1493–1504.
- Shaw A.M., Hauri, E.H., Fischer, T.P., Hilton, D.R., Kelley, K.A., 2008. Hydrogen isotopes in Mariana arc melt inclusions: implications for subduction dehydration and the deep-Earth water cycle. *Earth Planetary Science Letters* 275, 138-145.

- Sisson, T.W., Layne, G.D., 1993. H₂O in basalt and basaltic andesite glass inclusions from four subduction-related volcanoes. *Earth and Planetary Science Letters* 117, 619-635.
- Stolper, E., 1982. The speciation of water in silicate melts. *Geochim. Cosmochim. Acta* 46, 2609-2620.
- Symonds, R.B., Rose, W.I., Bluth, G.J.S., Gerlach, T.M., 1994. Volcanic-gas studies; methods, results, and applications. In: Carroll, M.R., Holloway, J.R. (Ed.), *Reviews in Mineralogy* 30. Washington: Mineralogical Society of America, 1-66.
- Tamic, N., Behrens, H., Holtz, F., 2001. The solubility of H₂O and CO₂ in rhyolitic melts in equilibrium with a mixed CO₂-H₂O fluid phase. *Chemical Geology* 174, 333-347.
- Wallace, P.J., 2005. Volatiles in subduction zone magmas: concentrations and fluxes based on melt inclusion and volcanic gas data. *Journal of Volcanology and Geothermal Research* 140, 217-240.
- Wilson, A.D., 1960. The micro-determination of ferrous iron in silicate minerals by a volumetric and colorimetric method. *Analyst* 85, 823-827.

Chapter III.

Compositional and pressure effects on the solubility of H₂O and CO₂ in mafic melts

Results presented in Chapter III are modified after paper of Shishkina et al submitted to American Mineralogist:

Shishkina, T.A., Botcharnikov, R.E., Jazwa, A., Jakubiak, A., Holtz, F., Almeev, R., Wilke, M. Compositional and pressure effects on the solubility of H₂O-CO₂-bearing fluids in mafic melts, American Mineralogist (submitted in 2011).

ABSTRACT

The effect of the anhydrous composition on the solubilities of H₂O and CO₂ in mafic melts with different alkalinity varying from MORB to nephelinite was investigated experimentally at 100 and 500 MPa and at 1200 and 1250°C. Solubility experiments with an island arc tholeiitic composition were also conducted at 700 and 900 MPa for a better understanding of the effect of pressure. In all compositions, CO₂ is dissolved as carbonate species only. The concentrations of dissolved H₂O and CO₂ have been analyzed by KFT and FTIR and new values of the absorption coefficients for hydrogen- and carbon-bearing species were determined for different melt compositions. The Mid-Infrared (MIR) absorption coefficients for the H₂O band at 3500 cm⁻¹ are identical for the investigated melt compositions and equal to 58±2 L/(mol*cm). The absorption coefficients for carbonate bands at 1430 and 1530 cm⁻¹ vary from 306±32 to 360±22 L/(mol*cm) and a simple correlation with the melt composition could not be worked out.

The results confirm the strong effect of melt composition on the solubility of CO₂, whereas H₂O solubility changes are small or negligible at low pressure. For instance, at 500 MPa total pressure, mafic melts coexisting with nearly pure CO₂ fluids can dissolve from around 0.32 to more than 0.90 wt% CO₂ as melt composition changes from tholeiitic to nephelinitic. The solubility of H₂O in melts coexisting with nearly pure H₂O fluids varies from 8.8 to 9.5 wt.% for the same compositional range. The correlation between solubility of CO₂ and melt composition is best described by the compositional parameterization proposed by Dixon (1997; American Mineralogist, 82: 368-378) taking into account structural parameters and the Gibbs free energy of carbonation reactions for the different cations. The obtained relationship is used to propose an empirical model that predicts the solubility of CO₂ in silicate melts as a function of melt composition at pressures up to 900 MPa: $\ln(\text{CO}_2) = A \cdot \ln P + B \cdot \Pi^* + C$ [where CO₂ is carbon dioxide concentration in wt%; P is pressure in MPa, Π^* is a compositional parameter ($\text{Ca}^{2+} + 0.8\text{K}^+ + 0.7\text{Na}^+ + 0.4\text{Mg}^{2+} +$

$0.4 \text{ Fe}^{2+} / (\text{Si}^{4+} + \text{Al}^{3+})$ with cations expressed as cation fractions; A=1.014, B= 7.483 and C=-0.891 are multiple regression coefficients].

. The results at 700 and 900 MPa clearly indicate that H₂O may have a positive effect on the dissolution of carbonate species in mafic melts. The concentrations of CO₂ in melts saturated with pure CO₂ fluids were estimated to be about 0.40 and 0.50 wt% at 700 and 900 MPa, respectively. The highest concentration values for CO₂ (0.47 and 0.59 wt% CO₂ at 700 and 900 MPa, respectively) were determined in samples with mole fraction of CO₂ in the coexisting fluid close to 0.5-0.6 and with water concentration in the melt of about 4 to 7 wt% H₂O.

Key words: H₂O, CO₂, water, carbon dioxide, fluid, solubility, melt, alkali basalt, basanite, nephelinite, MORB, tholeiite

1. INTRODUCTION

Mafic magmas are the transport media of volatiles from depths of magma generation to the shallow levels of magma storage and differentiation. Tectonic setting, magma generation/storage conditions and magma degassing processes exert a major control on the volatile budget. However, the compositional variability of mafic magma is believed to be an additional important factor that can influence the efficiency of volatile transport. Early experimental studies showed that melt composition can significantly affect solubility of CO₂ in mafic melts, in contrast to a weak effect on H₂O solubility (e.g., Mysen 1988; Blank and Brooker 1994; Holloway and Blank 1994). It was found that the solubility of CO₂ is positively correlated with a degree of melt depolymerization, which can be expressed as NBO/Si or NBO/T parameter (e.g., Mysen et al. 1975; Mysen 1976). The most reliable dissolution mechanism was based on the reaction of CO₂ with non-bridging oxygens (or reaction oxygens) to form carbonate ion in the structure of mafic melts (e.g., Spera and Bergman 1980; Fine and Stolper 1985; Stolper and Holloway 1988; Blank and Brooker 1994; Kubicki and Stolper 1995). Later, Brooker et al. (2001a, 2001b) showed that CO₂ solubility can be described by a non-linear function of NBO/T. At the same time, Brooker et al. (2001a, 2001b) reported that melt compositions with high MgO contents dissolve much less CO₂ than other melts with the same NBO/T value. Brooker et al. (2001a) supposed that some proportion of Mg²⁺ cations can play a role of network-formers leading to the decrease in the amount of non-bridging oxygens in the melt and therefore reducing CO₂ solubility. These observations are in accord with the data of Holloway et al. (1976) who showed that in melts with the same degree of polymerization CO₂ solubility decreases along the CaO-MgO join. Moore (2008) reported a strong positive correlation of CO₂ solubility with CaO content in basaltic melts. Behrens et al. (2009) found that K₂O-rich phonotephritic melts dissolve significantly more CO₂ than K₂O-poor tholeiitic basalts and suggested that K can stabilize carbonate-bearing species in the silicate melt. Recently, Lesne et al. (2011b) also reported a positive effect of alkalis on the concentrations of CO₂ dissolved in basaltic melts. The effect of the melt composition on H₂O solubility is not strong in mafic systems and, moreover, there is no large difference between H₂O solubilities in mafic, intermediate and silicic melts at given conditions. However, despite the large experimental database on H₂O and CO₂ solubilities produced up to now (see review of Moore (2008) and more recent studies of Iacono-Marziano et al. 2008; Behrens et al. 2009; Morizet et al. 2010; Shishkina et al. 2010; Lesne et al. 2011a, 2011b; Vetere et

al. 2011), a systematic analysis of the compositional effect of mafic melts on H₂O and CO₂ solubilities is still missing. In particular, the effect of alkalis should be investigated more precisely.

In this work we present new experimental data on the solubility of mixed H₂O-CO₂ fluids in mafic melts and analyze the compositional effect of the melt on volatile behavior at pressures up to 500 MPa. In addition, two experimental series with island arc tholeiitic melt at 700 and 900 MPa extend the existing database at 50-500 MPa (Shishkina et al. 2010) to better understand the effect of pressure. It is emphasized that the C-bearing species dissolved in all the compositions investigated and discussed in this study are carbonates only. Data obtained in melts containing both carbonate species and molecular CO₂ (e.g., dacite) or molecular CO₂ only (such as rhyolite) have been excluded from the discussion.

2. EXPERIMENTAL AND ANALYTICAL METHODS

2.1 Preparation of starting materials and capsules for solubility experiments

2.1.1 Starting compositions

Nine compositions of mafic magmas have been used in this study as listed in Table 3-1. The investigated silicate melts represent a relatively wide range of mafic compositions with a strong variation of the alkali concentrations. Experiments at 100 and 500 MPa were performed with four natural alkali-rich mafic compositions sampled in two active quarries in Lower and Opole Silesia regions (SW Poland) which belong to the Tertiary Central European Volcanic Province, extending from the Eifel Mountains in Germany through the Czech Republic to Lower Silesia: basanite (B2518) and basalt (B2507) from Męcinka quarry, basanite (A2549) from Rutki-Ligota and nephelinite (E2624) from Gracze. All these rocks consist of olivine and clinopyroxene phenocrysts dispersed in a groundmass of olivine, clinopyroxene, plagioclase, spinel, nepheline, apatite and glass.

These four natural samples were powdered, melted for 2 h in platinum crucible in an oven at 1600°C and 1 atm, and rapidly quenched to a glass by placing the crucible into a water bath. The quenched glass was crushed in a rotary mortar and remelted for 2 h to improve homogeneity of the batch. Finally, the glass was crushed to a grain size of <200 μm.

The other mafic compositions consisted in a ferrobasalt (SC1), two alkali basalts (OB93 and Etna), a typical Mid-Oceanic Ridge basalt (169oxi), and an island arc tholeiitic

basalt (N72). The ferrobasalt SC1 (synthetic analogue of a ferrobasalt from Skaergaard intrusion, Toplis and Carroll 1995; Botcharnikov et al. 2005a, 2008) and alkali basalt OB93 (natural sample from the Mont Crozier on the Courbet Peninsula of the Kerguelen Island, Freise et al. 2009) were already used in the study on volatile solubility by Botcharnikov et al. (2005b) who provided a description of the starting material preparation. The alkali basalt from Etna volcano (Etna) is a natural trachybasaltic sample taken at Rifugio Sapienza (S-side of Mt. Etna, 1892 m above sea level) from a lava flow of the 2001 eruption. The sample was melted and prepared for experiments in a similar way as described above for the other samples (see also Stelling et al. 2008). The starting composition 169oxi is a fused glass of the natural MORB whole rock powder left after separation of olivine phenocrysts (sample 169DS2 collected from the Mid-Atlantic ridge 7-11°S near Ascension Island as described by Almeev et al. 2008). The experiments with these four samples were conducted at 1250°C and 500 MPa.

In addition, a natural sample of typical alumina-rich island-arc tholeiitic basalt (N72) from Mutnovsky volcano (Kamchatka, Russia) was investigated at pressures of 700 and 900 MPa to extend the existing dataset for H₂O-CO₂-solubility at 50 to 500 MPa (Shishkina et al., 2010) to higher pressures. The preparation of the starting material is described by Shishkina et al. (2010).

Table 3-1. Starting compositions and molar absorption coefficients for FTIR bands.

Composition	Alkali Basalt	Basanite	Basanite	Nephelinite	Ferro-basalt	Alkali basalt	Alkali basalt	MORB	Tholeiite
Sample	B2507	B2518	A2549	E2624	SC1	OB93	Etna	169oxi	N72
SiO ₂	47.30	46.21	43.64	42.32	48.88	49.03	48.34	50.69	50.17
TiO ₂	2.35	2.70	2.64	2.26	2.89	2.76	1.77	1.46	0.92
Al ₂ O ₃	14.17	14.65	12.65	11.80	14.77	16.20	16.40	16.95	18.28
FeO-t	10.82	11.74	11.54	11.00	13.05	11.90	10.48	8.51	9.37
MnO	0.17	0.16	0.19	0.19	0.00	0.17	0.20	0.13	0.17
MgO	10.36	8.71	12.07	13.31	6.47	5.88	5.97	7.48	7.00
CaO	9.94	10.63	11.82	13.23	10.99	9.80	10.83	12.03	11.37
Na ₂ O	3.52	3.51	3.68	3.72	2.63	3.13	3.46	2.52	2.33
K ₂ O	0.83	1.06	1.01	0.96	0.30	1.12	1.96	0.22	0.23
P ₂ O ₅	0.47	0.56	0.70	1.13	0.00	0.00	0.59	0.00	0.15
Cr ₂ O ₃	0.06	0.06	0.06	0.08	n.a.	n.a.	n.a.	n.a.	n.a.
Total	100	100	100	100	100	100	100	100	100
Density (g/L)	2828	2911	2911	2889	n.d.	n.d.	n.d.	n.d.	2757
CIPW norms:									
Quartz									
Orthoclase	4.93	6.27	5.94		1.79	6.64	11.60	1.32	1.36
Albite	18.89	14.61	1.30		22.25	25.35	15.70	21.35	19.72
Anorthite	20.39	21.07	15.02	12.63	27.61	26.83	23.43	34.27	38.74
Nepheline	5.91	8.19	16.18	17.07		0.62	7.34		
Diopside	21.09	23.05	31.80	31.97	22.42	18.15	21.97	20.81	13.78
Hypersthene					9.93			12.96	17.87
Olivine	23.19	20.36	23.12	25.01	10.52	17.18	15.24	6.55	6.44
Magnetite									
Ilmenite	4.47	5.13	5.01	4.29	5.49	5.24	3.37	2.78	1.75
Apatite	1.09	1.29	1.62	2.62			1.37		0.35
Π (Dixon, 1997)	1.03	1.13	2.05	2.56	0.49	0.28	0.68	0.20	-0.04
Π*	0.41	0.42	0.51	0.57	0.36	0.34	0.37	0.34	0.32
e1430 (CO ₃ ²⁻)	311±41	n.d.	306±32	n.d.	329±14	341±15	360±22	307±27	317±23
e1520 (CO ₃ ²⁻)	380±30	n.d.	349±25	n.d.	353±16	384±16	358±24	359±33	361±43
e1430* (CO ₃ ²⁻)	308±35	308±35	308±35	308±35	329±14	341±15	360±22	307±27	317±23
e3550* (H ₂ O-t)	60±8	60±8	60±8	60±8	n.d.	n.d.	n.d.	n.d.	68±10

Table 3-1. Notes:

Every starting composition represents an average of about 50 electron microprobe analyses of glasses normalized to 100%.

Major elements in wt.%.

N.a. - was not analyzed, n.d. - was not determined.

Π - compositional factor derived by Dixon (1997) $\Pi = -6.5*(Si^{+4} + Al^{+3}) + 20.17*(Ca^{+2} + 0.8K^{+1} + 0.7Na^{+1} + 0.4Mg^{+2} + 0.4Fe^{+2})$.

Π* - compositional factor calculated as $(Ca^{+2} + 0.8K^{+1} + 0.7Na^{+1} + 0.4Mg^{+2} + 0.4Fe^{+2}) / (Si^{+4} + Al^{+3})$.

e1430 (CO₃²⁻) and e1520 (CO₃²⁻) - molar absorption coefficients for carbonate IR bands derived from an averaging of the individual determinations for every standard (see text). e1430* (CO₃²⁻), e3550* (H₂O-t) - values of molar absorption coefficients that were used for calculations of CO₂ or H₂O concentrations in glasses in this study.

2.1.2 Capsule preparation

The solubility experiments were prepared by loading about 50 mg of glass powder in Au₈₀Pd₂₀ capsules (15 – 20 mm long and 2.6 – 3.4 mm in diameter). Distilled water and silver oxalate (Ag₂C₂O₄) were used as sources of H₂O and CO₂, respectively. Different proportions of water and silver oxalate were loaded into the capsules to establish different mole fraction of water in the added fluid phase (X_{H_2O}) as reported in Table 3-2). Capsules were weighted after loading of each component, closed with pliers and welded shut.

The concentrations of water- and carbon- bearing species in the quenched glasses were determined by infrared spectroscopy (IR). Since the absorptivity of the bands assigned to water and carbonate species depends on the glass composition, reference materials were synthesized for each composition (H₂O and CO₂ analyses in reference samples were done using independent analytical techniques as described below). These standards were used for the calibration of IR molar absorption coefficients. For the synthesis of standards for carbon, 500 mg of glass powder, distilled water and CaCO₃ or Ag₂C₂O₄ were loaded in large Au₈₀Pd₂₀ capsules (35 mm long and 5 mm diameter). The amounts of added volatile components were kept lower than the expected solubility values to ensure complete dissolution of the volatiles in the melt. Calcium carbonate powder was mixed with basalt glass powder before loading. The capsules were filled with powder and water in several steps to force homogenous distribution of the components. In total, 8 standards for bulk carbon determinations were synthesized. Two of them were prepared from basanite A2549 (St-1 and St-2) and two from alkali basalt B2507 (St-3 and St-4). Individual single standards were also prepared for the ferrobasalt (SC1), the two alkali basalts (OB93 and Etna), and the MORB (169oxi) compositions.

2.2 Experimental technique

The experiments at 100 and 500 MPa and the synthesis of the standards were performed in a vertically oriented internally heated pressure vessel (IHPV) at the Institut für Mineralogie, Leibniz Universität Hannover (see also Shishkina et al. 2010). Experiments at 700 and 900 MPa were conducted in an IHPV at the Helmholtzzentrum Potsdam (GFZ). Usually, five capsules containing the same starting composition and different H₂O-CO₂ proportions (X_{H_2O} from 0 to 1, Table 3-2) were run simultaneously. Standards for carbon determination were prepared at 300 or 500 MPa and 1250°. Single large standard capsules were run individually. The experimental duration varied from 24 to

72 hours. This experimental duration is expected to be sufficient to reach homogeneous distribution of volatiles between the low-viscosity silicate melts and fluids. Experimental temperatures were 1200 and 1250°C as reported in Table 3-2. Four Pt – Pt₉₀Rh₁₀ (S-type) thermocouples were used for the recording of the temperature in the IHPV during the experiments. Typically, the temperature gradient along the sample was in the range of ±3°C. The variations of the temperature during the experiments were within the range of ±2°C at 100 MPa and of ±10°C at 500 MPa. Total pressure was recorded continuously with a calibrated Burster Type 8221 digital pressure transducer (pressure uncertainty ±1 MPa). The variation of pressure during the experiments was less than 5 MPa. The capsules were quenched isobarically using a rapid-quench technique described by Berndt et al. (2002). The quench rate was about 150°C/sec.

The intrinsic redox conditions in the IHPV used at Hannover ($\log fO_2^{\text{intrinsic}}$) are close to NNO+2.6 (i.e., fO_2 is 2.6 log units higher than that buffered by the Ni-NiO solid oxygen buffer) in systems with water activity (aH_2O) close to 1 (Schuessler et al. 2008). The redox conditions of the IHPV in Potsdam have not been measured but are expected to be close to that in Hannover, because similar vessel materials and pressurizing medium (Ar gas) are used in both laboratories. The oxygen fugacity for every single run ($\log fO_2^{\text{capsule}}$) was calculated as $\log fO_2^{\text{capsule}} = \log fO_2^{\text{intrinsic}} + 2\log (aH_2O)$ (Appendix, Table A-3-1). Water activities (aH_2O) for every run were calculated following two different ways. As a first approach water activity (aH_2O^{fluid}) was calculated from the composition of the fluid phase ($X^{\text{fl}}H_2O$) using activity coefficients after Aranovich and Newton (1999) and molar volumes of pure H₂O after Pitzer and Sterner (1994). Since the determination of fluid composition failed in a number of runs or determined values of $X^{\text{fl}}H_2O$ do not look realistic, we calculated aH_2O and fO_2 using the concentration of H₂O in the glass according to the model of Burnham (1979). The fO_2 values determined with these both approaches range from about NNO to about NNO+2.7 in most of the runs (Appendix, Table A-3-1).

Table 3-2. Experimental conditions, results of Karl-Fischer titration and infrared spectroscopy.

	Sample	NN	P (MPa)	T (C°)	X H ₂ O in	X (H ₂ O) fluid	KFT H ₂ O (wt%)	KFT Error H ₂ O	CO ₂ (ppm)	Error CO ₂ (ppm)	MIR H ₂ O (wt.%)	Error H ₂ O (wt%)	Comments for run products
basanite	B2518	1	100	1250	0.95	0.85	3.10	0.12	0		2.34	0.33	
basanite	B2518	2	100	1250	1.00	0.99	3.38	0.13	0		2.39	0.23	
basanite	B2518	3	100	1250	0.76	0.56	2.29	0.12	284	33	2.09	0.20	
basanite	B2518	4	100	1250	0.41	0.2*	2.21	0.12	648	76	1.31§	0.13	
basanite	B2518	50	100	1250	0.00	0.11	0.85	0.11	518	69	0.93	0.10	
basanite	B2518	54	100	1250	0.00	0.11	0.88	0.11	706	82	0.91	0.10	
basanite	B2518	9	500	1250	0.64	0.24	3.34	0.12	4517	526	2.70	0.26	
basanite	A2549	11	100	1250	1.00	1.00	3.13	0.14	0				
basanite	A2549	12	100	1250	0.94	0.91*	3.17	0.12	127	15			
basanite	A2549	13	100	1250	0.77	0.76*	1.09	0.12	1411	168	0.50§	0.06	
basanite	A2549	14	100	1250	0.37	0.07*	1.29	0.12	1771	209	0.97§	0.10	
basanite	A2549	51	100	1250	0.00	0.03	0.86	0.12	1500	178	0.85	0.10	
basanite	A2549	18	500	1250	0.87	0.64	5.82	0.12	6716	795			rare QC
basanite	A2549	19	500	1250	0.62	0.66*	0.50	0.12	7654	895	0.49	0.08	
basanite	A2549	47	500	1250	0.00	0.00*	0.27	0.12	7159	844	0.40	0.10	Ol (<1%)
basanite	A2549	48	500	1250	0.64	0.27	3.48	0.13	7368	885			
Alkali basalt	B2507	21	100	1250	1.00	0.92	3.31	0.13	0		2.46	0.24	
Alkali basalt	B2507	22	100	1250	0.94	0.84	3.15	0.12	0		2.61	0.25	
Alkali basalt	B2507	23	100	1250	0.79	0.65	2.45	0.13	219	26	2.30	0.23	
Alkali basalt	B2507	24	100	1250	0.38	0.20	1.24	0.11	638	77	1.25	0.13	
Alkali basalt	B2507	25	100	1250	0.00	0.19	0.85	0.12	750	88	0.88	0.11	
Alkali basalt	B2507	29	500	1250	0.64	0.31	3.44	0.12	5440	748	2.86	0.28	
Alkali basalt	B2507	30	500	1250	0.00	0.00	0.65	0.12	5413	809	0.69	0.10	
Alkali basalt	B2507	52	500	1250	0.00	0.00*	0.26	0.12	4852	567	0.29	0.08	
nephelinite	E2624	31	100	1250	1.00	0.99	3.19	0.13	0				
nephelinite	E2624	33	100	1250	0.77	0.60	2.69	0.12	1090	133	2.32	0.23	

Table 3-2 continued.

	Sample	NN	P (MPa)	T (C°)	X H ₂ O in	X (H ₂ O) fluid	KFT H ₂ O (wt%)	KFT Error H ₂ O	CO ₂ (ppm)	Error CO ₂ (ppm)	MIR H ₂ O (wt.%)	Error H ₂ O (wt%)	Comments for run products
nephelinite	E2624	35	100	1250	0.00	0.00	0.54	0.11	2868	364	0.57	0.07	Ol (<3%)
nephelinite	E2624	38	500	1250	0.87	0.55	5.86	0.14	8549	992			
nephelinite	E2624	40	500	1250	0.00	0.00*	1.12	0.12	8993#		0.96	0.10	Ol (<3%)
Ferrobasalt	SC1	B160	500	1200	0.00	0.04	1.18	0.10	4163	217			
Ferrobasalt	SC1	B159	500	1200	0.56	0.21	2.82	0.10	3946	293			
Ferrobasalt	SC1	B158	500	1200	0.85	0.55	5.54	0.14	2608	196			
Ferrobasalt	SC1	B157	500	1200	0.97	0.76	8.18	0.11	1194	111			
Ferrobasalt	SC1	B156	500	1200	1.00	0.94	9.02	0.11	0				
Alkali basalt	OB93	OB93-1	500	1200	0.00	0.02	1.07	0.10	3130	200			
Alkali basalt	OB93	OB93-2	500	1200	0.59	0.21	3.15	0.10	3233	204			
Alkali basalt	OB93	OB93-3	500	1200	0.85	0.57	5.44	0.10	2487	101			
Alkali basalt	OB93	OB93-4	500	1200	0.97	0.51	7.45	0.10	1334	124			
Alkali basalt	OB93	OB93-5	500	1200	0.99	0.86	7.96	0.10	727	36			
Alkali basalt	OB93	M148 \$	500	1150	1.00	1	9.54	0.48	0				
Alkali basalt	Etna	Etna-11	500	1200	1.00	1.00	8.78	0.12	0				
Alkali basalt	Etna	Etna-12	500	1200	0.00	0.06	0.81	0.08	4356	193			
Alkali basalt	Etna	Etna-13	500	1200	0.63	0.27	2.22	0.12	4196	176			
Alkali basalt	Etna	Etna-14	500	1200	0.84	0.50	4.61	0.11	3337	158			
Alkali basalt	Etna	Etna-15	500	1200	0.96	0.82	7.19	0.08	1963	82			
MORB	169oxi	169oxi-17	500	1200	0.57	0.18	2.57	0.10	4368	247			
MORB	169oxi	169oxi-18	500	1200	0.84	0.46	5.99	0.09	2886	183			
MORB	169oxi	169oxi-19	500	1200	0.97	0.55	7.36	0.07	1186	74			
MORB	169oxi	169oxi-20	500	1200	1.00	1.00	8.85	0.10	0	0			
Tholeiite	N72	M52	700	1250	1.00	1.00*	11.21	0.13	0				Clayey mass
Tholeiite	N72	M55	700	1250	0.83	0.50*	6.32	0.14	4233	357			

Table 3-2 continued.

Sample	NN	P (MPa)	T (C°)	X H ₂ O in	X (H ₂ O) fluid	KFT H ₂ O (wt%)	KFT Error H ₂ O	CO ₂ (ppm)	Error CO ₂ (ppm)	MIR H ₂ O (wt.%)	Error H ₂ O (wt%)	Comments for run products	
Tholeiite	N72	M56	700	1250	0.00	0.00*	0.79	0.13	4363	363	0.73	0.10	
Tholeiite	N72	M63	700	1250	0.89	0.67*	7.31	0.15	3679	292			
Tholeiite	N72	M64	700	1250	0.85	0.52*	6.07	0.15	4478	356			
Tholeiite	N72	M65	700	1250	0.52	0.06*	2.27	0.13	4788	381			
Tholeiite	N72	M57	900	1250	1.00	1.00*	12.78	0.18	0				Clayey mass
Tholeiite	N72	M60	900	1250	0.77	0.35*	5.89	0.15	5952	487			
Tholeiite	N72	M61	900	1250	0.00	0.00*	1.51	0.13	5193	425	0.64	0.07	
Tholeiite	N72	M67	900	1250	0.90	0.61*	9.53	0.16	5129	407			
Tholeiite	N72	M68	900	1250	0.90	0.59*	8.62	0.15	5252	417			
Tholeiite	N72	M69	900	1250	0.85	0.55*	7.01	0.14	5976	475			
Tholeiite	N72	M70	900	1250	0.56	0.13*	2.65	0.13	5943	477			
Tholeiite	N72	M71	900	1250	0.00	0.00*	1.25	0.12	5320	426	1.18	0.13	

Table 3-2. Notes:

Analytical errors and uncertainties, if not specified in the text, were calculated as described in Shishkina et al. (2010).

* - mole fraction of H₂O in the fluid determined by mass-balance, in all other runs - by gravimetry.

§ - for these samples H₂O values determined by MIR were used for constructing of diagrams and calculations, for all other samples KFT determinations of H₂O content were used.

- minimum CO₂-content that could be estimated from MIR spectra. Correct value was not possible to determine because of saturation of IR detector.

\$ - sample from Bocharnikov et al., 2005

QC - quench crystals, Ol - olivine.

2.3 Analytical methods

2.3.1 Major element glass composition

Major-element compositions of the starting materials and experimental products were analyzed by electron microprobe (Cameca SX100) using glass and mineral standards for calibration. Samples of experimental glasses were analyzed in 5 to 10 different points using 15 keV accelerating voltage, 4 nA beam current, 20 μm diameter of electron beam. Sodium and potassium were analyzed first to minimize alkali-loss.

The $\text{Fe}^{2+}/\text{Fe}_{\text{total}}$ ratio was determined in several glass samples using the wet-chemical colorimetric analytical technique of Wilson (1960) modified by Schuessler et al. (2008). Four to ten milligrams of glass chips from run products were taken for analyses and results are reported in (Appendix, Table A-3-1).

2.3.2 Fluid composition after the experiments

The weight-loss procedure was used for the determination of the fluid composition (mole fractions of H_2O ($X^{\text{fl}}\text{H}_2\text{O}$) and CO_2 ($X^{\text{fl}}\text{CO}_2$) in the fluid phase). The capsules were weighed after the run and weighing was repeated after freezing the capsule in liquid nitrogen with subsequent piercing of the capsule (determination of the CO_2 mass in the fluid) and after holding the capsule in an oven at 110°C for 2-3 minutes (determination of the mass of evaporated H_2O). If the weight-loss procedure failed, we have calculated the mole fractions of H_2O and CO_2 in the fluid by mass-balance using known amounts of loaded volatiles and rock powder and measured concentrations of volatiles in run-product glasses (Table 3-2).

2.3.3 Determination of bulk concentrations of volatiles in glasses

The concentration of H_2O dissolved in the glasses was measured by Karl-Fischer titration (KFT, Behrens et al. 1996). Ten to twenty mg of the sample was heated from room temperature to 1300°C using a high-frequency generator (Linn electronic HTG 1000/1.3). Extracted water was transported by an Ar-stream to the titration cell with an electrolytic solution and the amount of extracted H_2O was detected by a moisture meter (Mitsubishi CA-100).

The total carbon content in the reference glass standards was determined by combustion and subsequent IR spectroscopy using an ELTRA CS 800 analyzer. For a single measurement, about 100 mg of glass was loaded into a corundum crucible together

with 1.5 ± 0.05 g W and 0.3 ± 0.03 g Fe. The mixture was burn in an oxygen stream at temperature up to 2200°C . The released CO_2 was measured in an IR cell. Accuracy and reproducibility of the measurements were checked by analyses of metallic and glass standards with known carbon concentrations (from 0.0018 to 0.75 wt. % C). For every standard three bulk carbon measurements of the glass material from the top (U), central (M) and bottom (D) parts of a capsule were made to perform the calibration of FTIR spectra. Glass pieces from these 3 zones were also analyzed by FTIR and KFT.

2.3.4 Determination of H_2O and CO_2 concentrations in glasses by Fourier-transform infrared spectroscopy (FTIR)

The IR spectra were taken from doubly polished glass chips with a thickness of ~ 80 to $110 \mu\text{m}$. The thickness was measured with a digital micrometer Mitutoyo (precision $\pm 2 \mu\text{m}$ (Behrens, 2009) in 5 points for every polished glass chip. Absorption spectra in the mid-infrared (MIR) range were collected with a Bruker IFS88 FTIR spectrometer combined with an IR-ScopeII microscope (Institut für Mineralogie, Hannover) and were used for the determination of the concentrations of water- and carbon-bearing species dissolved in the glasses. The operating conditions for MIR were: globar light source and KBr beamsplitter, spectral resolution of 2 cm^{-1} . A MCT narrow range detector was used. For each spectrum 50 to 100 scans were collected from spots with sizes of about $50 \times 50 \mu\text{m}$. Homogeneity of volatile distribution was checked collecting the spectra in 3 to 5 spots in different parts of the glass chips.

The densities of the water-free glasses from samples B2518, B2507, A2549, and E2624 were determined using the Archimedean method by weighing large pieces of glass (200 to 1700 mg) in water and in air (Table 3-1). Densities of volatile-bearing glasses (ρ in g/L) in every run were calculated using the densities of the water-free starting glasses and assuming a partial molar volume of H_2O in the glass of $12.0 \pm 0.5 \text{ cm}^3/\text{mol}$ (Holtz et al. 1995; Richet et al. 2000):

$$\text{B2518: } \rho = 2910.4 - 26.1 * \text{CH}_2\text{Ot} \quad (1)$$

$$\text{B2507: } \rho = 2826.7 - 23.9 * \text{CH}_2\text{Ot} \quad (2)$$

$$\text{A2549: } \rho = 2910.1 - 26.1 * \text{CH}_2\text{Ot} \quad (3)$$

$$\text{E2624: } \rho = 2887.5 - 25.4 * \text{CH}_2\text{Ot} \quad (4)$$

where CH_2Ot is the water content in wt.%.

The density of the tholeiitic sample N72 was determined as $\rho = (2757 - 22.1 * \text{H}_2\text{O})$ (Shishkina et al., 2010). Determination of densities for ferrobasalt (SC1), alkali basalts

(OB93 and Etna) and MORB (169oxi) were not performed in this study. Glass densities were calculated using the equation of Yamashita et al. (1997) for basaltic compositions: $\rho = 2819 - 20.8 \cdot \text{CH}_2\text{O}_t$.

3. RESULTS

3.1 Experimental products and glass composition

The experimental conditions, description of the run products (presence of olivine crystals in some cases, quench crystals), fluid compositions, H₂O and CO₂ contents in glasses determined by the different methods are presented in Table 3-2. Small amounts (less than 3 vol.%) of olivine crystals (Fo 88.5 – 92) were found in several runs with basanite A2549 (run 47 at 500 MPa) and nephelinite E2624 (run 35 at 100 MPa and run 40 at 500 MPa). These runs have low XH₂O_{in} (Table 3-2), resulting in high liquidus temperatures (higher than 1250°C). However, since the proportion of olivine is low (<3%), its presence is not expected to affect significantly the glass composition and the volatile solubility data. On the other hand, in experiments with high XH₂O_{in} (XH₂O_{in} 0.87-1) at 500 MPa, the run products of the starting compositions B2518, A2549, B2507 and E2624 were represented by black non-transparent masses composed of aggregates of chaotically oriented needle-like crystals, which sometimes form spherulitic textures with small amounts of interstitial residual glass. Such textures of run products indicate that the quench rate was not sufficient for these H₂O-rich melts leading to the formation of quench phases. Previous experimental studies with mafic melts at 500 MPa and XH₂O_{in} = 1 report about 9 to 10 wt.% H₂O dissolved in the glasses (e.g., Berndt et al. 2002; Botcharnikov et al. 2005b; Behrens et al. 2009; Shishkina et al. 2010). The quenched MORB glasses of Berndt et al. (2002) at 500 MPa and 1200°C were bubble- and crystal-free, whereas Shishkina et al. (2010) reported that rare elongated needle-like crystals were observed within the quenched glass of tholeiitic basalt (their run M22 at 1250°C, 500 MPa, XH₂O_{in}=1). Behrens et al. (2009) reported that quenched glasses from alkali-rich phonotephritic melts with more than 6 wt.% H₂O were very dark and contained homogeneously distributed fibrous crystals (micas). These observations indicate that the melt composition may have a considerable control on the kinetics of crystallization during quench in low-silica melts containing high amounts of dissolved H₂O. Similarly, the experimental products obtained with composition N72 at 700 and 900 MPa and with XH₂O_{in} = 1 (M52 and M57, Table 3-2) are composed of a greenish-grey «gel-like» mass and H₂O-bearing fluid. In these cases,

the very high amount of dissolved H₂O (in molar proportions) probably prevented quenching of those melts to a glass. The samples containing quench crystals were not used for the determination of volatile concentrations, whereas the gel-like H₂O-rich experimental products were analyzed and used in the interpretation of experimental results (assuming that quench products represent the bulk composition of the water-rich silicate melt at the experimental conditions).

Major-element compositions of the quenched glasses with more than 1 wt.% H₂O do not differ significantly from the composition of starting materials, i.e., the differences in the concentrations of SiO₂, TiO₂, Al₂O₃, MgO, CaO, K₂O, Na₂O are within ± 5 rel.%. In most cases Fe-loss in these glasses is < 10 rel.%. In H₂O-poor glasses (with less than 1 wt.% H₂O) strong Fe-loss (to capsule or olivine) was observed at both pressures: from 13 to 52 rel.% (Appendix, Table A-3-1) and therefore the concentration of other major-elements is higher by up to 10-15% rel. than in the starting materials (only MgO is up to 15% rel. lower, which coincides with crystallization of olivine in several runs). The Fe-loss effect is usually explained by a reduction of part of ferric iron to ferrous iron during the experiments which are performed at conditions more reduced than those of the synthesis of starting glass (at oxidizing atmospheric conditions).

Experimental glasses have homogeneous compositions as confirmed by electron microprobe analyses of major-elements and IR determinations of H₂O and CO₂ in several different points for every run. These observations indicate that run duration was long enough to reach homogeneous distribution of elements and equilibration between coexisting melts and fluids.

The experimental products from the high-pressure (700 and 900 MPa) experiments with island arc tholeiitic composition are composed of crystal- and bubble-free glasses and co-existing H₂O-CO₂-bearing fluid in the runs with $X_{\text{H}_2\text{O}}^{\text{fluid}} \leq 0.6$. The major-element compositions of most of the glasses do not differ significantly from the starting composition: deviations of SiO₂, Al₂O₃, TiO₂, FeO-t, CaO, MgO contents from the starting composition are within ± 5 rel.%. But in 3 runs (M65, M70 and M71) with low H₂O and high CO₂ contents the significant Fe-loss is observed: 6.7; 8.3 and 24 rel.% respectively.

3.2 Infrared spectroscopy and determination of IR absorption coefficients

Experimental glasses were analyzed by mid-infrared spectroscopy (MIR) for determination of H₂O and CO₂ contents. MIR spectra were used for the calculation of CO₂ concentrations in all glasses and H₂O concentrations in glasses with less than 2.7 wt.%

H₂O. Water concentrations were evaluated using a broad peak with a center at about 3550 cm⁻¹. From the MIR spectra, it is evident that in the studied mafic melts CO₂ dissolves as carbonate species (CO₃²⁻) only, which appears as a double-peak at 1430 and 1520 cm⁻¹. The characteristic peak of molecular CO₂ at 2200 cm⁻¹ was not detected in any sample. This observation is in agreement with previous IR studies of basaltic glasses (e.g., Fine and Stolper 1986; Blank and Brooker 1994; Dixon et al. 1995; Botcharnikov et al. 2005a; Shishkina et al. 2010).

Water and carbonate concentrations in basaltic glasses were calculated using IR absorption spectra on the basis of the Beer-Lambert law:

$$C_i = 100 * M_i * A_j / (d * \rho * \epsilon_j) \quad (5)$$

where C_i is the concentration of species in wt.%, M_i is the molecular weight of the species, A_j is the absorbance (peak height) of band j, d is the thickness of the section, ρ is the density in g/L and ε_j is the absorption coefficient of band j in L/(mol*cm).

Absorbances of the carbonate and water bands in MIR spectra were measured as scaled peak heights after subtraction of MIR spectra of the volatile-free glass with the same composition scaled to the same thickness. Linear tangential baselines below the carbonate and the water bands were used for the peak height determination (same procedure as in Behrens et al. 2009; Shishkina et al. 2010).

The calibration of the molar absorption coefficients (ε₁₄₃₀ and ε₁₅₂₀) for the carbonate bands at 1430 cm⁻¹ and 1520 cm⁻¹ was made using the data of bulk carbon analyses of the reference glasses. The evaluation was performed in two ways. As a first approach, individual ε₁₄₃₀ and ε₁₅₂₀ values for each standard were determined based on the known CO₂-content (from bulk C analysis), absorbance of IR band, density and thickness of the glass sample. The average values of ε₁₄₃₀ and ε₁₅₂₀ calculated from these individual determinations for every composition are listed in Table 3-1. The second way of evaluation was a determination of the slope of the linear regression of normalized absorbance at 1430 cm⁻¹ (or 1520 cm⁻¹) vs. bulk CO₂ concentration (CO₂-tot) (Fig. 3-1a). This method was applied for two compositions and values of ε₁₄₃₀ were found to be 310±20 L/(mol*cm) for the composition A2549 and 322±20 L/(mol*cm) for B2507. For these samples, both methods give ε₁₄₃₀ values which are identical within the uncertainty of the calculation. Moreover, they are identical within an error between the two samples A2549 and B2507. Therefore, the same value of ε₁₄₃₀ was used for the calculation of CO₂ content in four samples: B2518, B2507, A2549 and E2624. It was derived by averaging individual determinations from the first method, i.e., 308±35 L/(mol*cm) shown as ε₁₄₃₀* in Table 3-

1. Use of the 1430 cm^{-1} band is preferred due to the fact that the band at 1520 cm^{-1} is strongly affected by the H_2O -band at 1630 cm^{-1} as discussed in previous studies (e.g., Botcharnikov et al. 2006; Behrens et al. 2009).

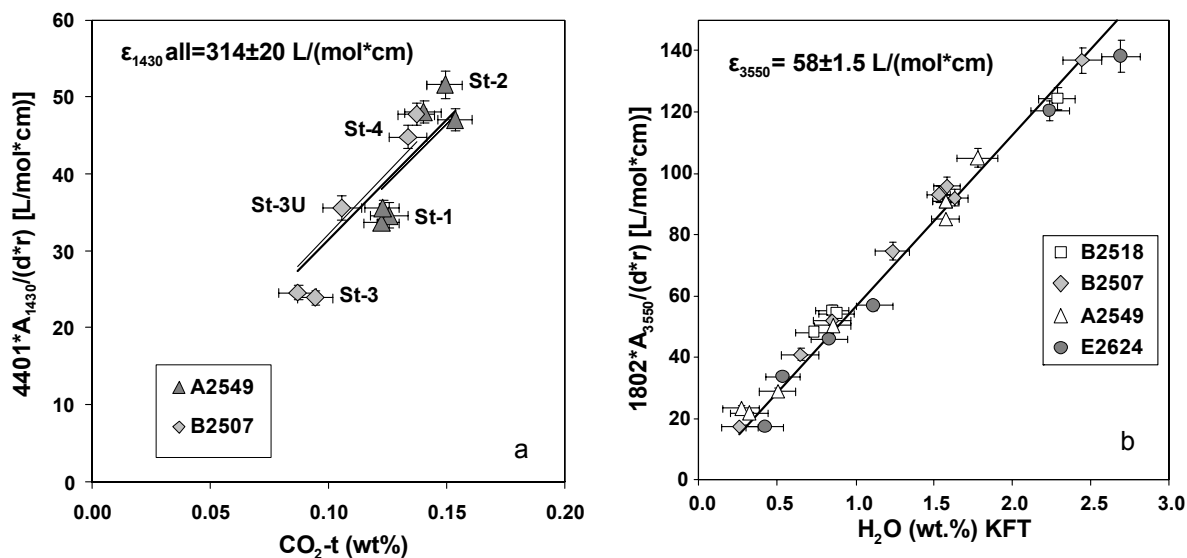


Figure 3-1. (a) Calibration plot for determination of the absorption coefficient for carbonate band at 1430 cm^{-1} for compositions A2549 and B2507: normalized absorbance of the 1430 cm^{-1} band versus total carbon content measured by CS analyses in standard glasses. The fit was forced through the origin (see text for description and values). (b) Plot of normalized absorbance of the 3550 cm^{-1} band vs. water concentration in glasses determined by KFT. ϵ_{3550} of $58 \pm 1.5 \text{ L}/(\text{mol} \cdot \text{cm})$ is derived from the slope of the regression of data for experimental and standard glasses. The fit was forced through the origin.

The values of ϵ_{1430} and ϵ_{1520} from this study are identical within the error with most of the previously reported determinations for mafic melts [ϵ_{1430} : $375 \pm 20 \text{ L}/(\text{mol} \cdot \text{cm})$ for tholeiite (Fine and Stolper 1986); 281 ± 6 for basanite (Dixon and Pan 1995); $308 \pm 110 \text{ L}/(\text{mol} \cdot \text{cm})$ for phonotephrite (Behrens et al. 2009); $356 \pm 18 \text{ L}/(\text{mol} \cdot \text{cm})$ for shoshonite (Vetere et al. 2011); ϵ_{1520} : $375 \pm 20 \text{ L}/(\text{mol} \cdot \text{cm})$ for tholeiite (Fine and Stolper 1986); $340 \pm 20 \text{ L}/(\text{mol} \cdot \text{cm})$ for leucitite (Thibault and Holloway 1994); $284 \pm 5 \text{ L}/(\text{mol} \cdot \text{cm})$ for basanite (Dixon and Pan 1995); $398 \pm 10 \text{ L}/(\text{mol} \cdot \text{cm})$ for MORB (Jendzejewsky et al. 1997)] as illustrated in Fig. 3-2.

Dixon and Pan (1995) proposed that the value of the molar absorption coefficient for carbonate species is a function of the glass composition. Using several values of ϵ_{1520} [basanite from Dixon and Pan (1995); tholeiite and diopside from Fine and Stolper (1986); albite and jadeite from Fine and Stolper (1985); leucitite from Thibault and Holloway (1994)] they derived an equation: $\epsilon_{1525} = 451 - 342 \cdot (\text{Na}/(\text{Na} + \text{Ca}))$. The dataset for ϵ_{1520} obtained in this work shows that the simple linear correlation of ϵ_{1525} with $\text{Na}/(\text{Na} + \text{Ca})$ is

not valid for a wide range of compositions and the ϵ_{1525} values can not be adequately predicted by the equation of Dixon and Pan (1995) as evident from Fig. 3-2a, b. Values of ϵ_{1430} also do not show a clear correlation with $\text{Na}/(\text{Na}+\text{Ca})$ or any other combination of cations and can not be evaluated in a simple way (Fig. 3-2c, d).

The molar absorption coefficient for the water band at 3550 cm^{-1} was calculated for four compositions (B2518, B2507, A2549, E2624) in two ways, similar to the approach applied for CO_2 . First, it was determined using a regression between the normalized IR absorbance and the H_2O content in glasses measured by KFT (for glasses with less than 2.7 wt.% H_2O). The linear regressions for all four studied compositions yield an identical slope (Fig. 3-1b) and a value of $58 \pm 1.5\text{ L}/(\text{mol} \cdot \text{cm})$ was derived for ϵ_{3550} from the slope of the linear regression. Averaging the individual ϵ_{3550} determinations gives a value of $59.5 \pm 8.1\text{ L}/(\text{mol} \cdot \text{cm})$. Both values are identical within error to those determined for basalts in previous works [$67.1 \pm 6\text{ L}/(\text{mol} \cdot \text{cm})$ after Stolper (1982); $61.0 \pm 1.0\text{ L}/(\text{mol} \cdot \text{cm})$ after Pandya et al. (1992); $63.0 \pm 3.0\text{ L}/(\text{mol} \cdot \text{cm})$ after Dixon et al. (1995); $64.0 \pm 1.0\text{ L}/(\text{mol} \cdot \text{cm})$ after Yamashita et al. (1997); $60 \pm 2\text{ L}/(\text{mol} \cdot \text{cm})$ after Di Matteo et al. (2006); $63.9 \pm 5.4\text{ L}/(\text{mol} \cdot \text{cm})$ after Behrens et al. (2009) and $68 \pm 10\text{ L}/(\text{mol} \cdot \text{cm})$ after Shishkina et al. (2010)]. The value of $59.5 \pm 8.1\text{ L}/(\text{mol} \cdot \text{cm})$ was used for those four samples..

For basalt N72, the value of $\epsilon_{3550} = 68 \pm 10\text{ L}/(\text{mol} \cdot \text{cm})$ after Shishkina et al. (2010) was used. Water concentration in the other samples (SC1, OB93, Etna, and 169oxi) was determined by KFT only.

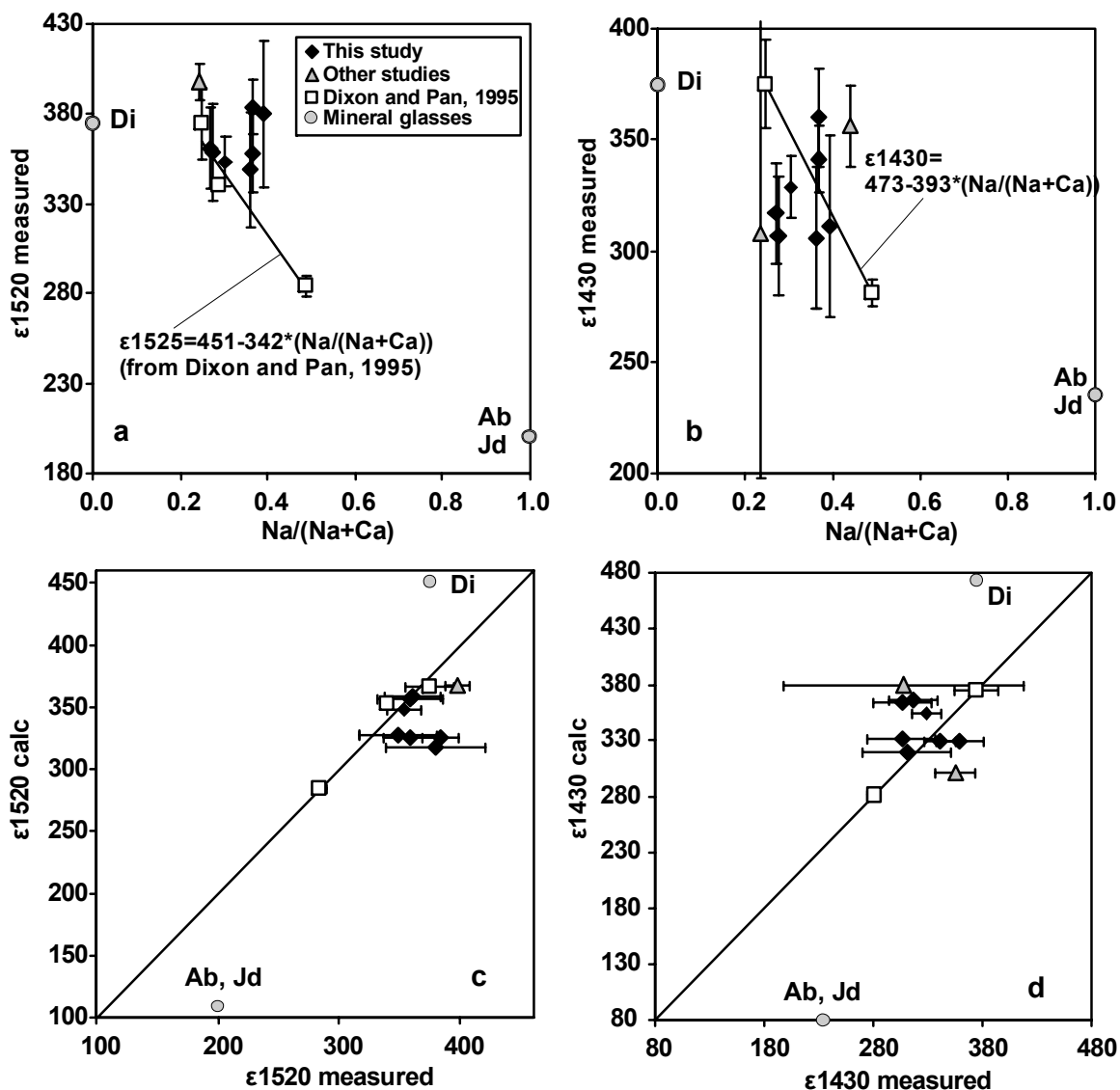


Figure 3-2. Molar absorption coefficients for carbonate bands at 1520 cm^{-1} and 1430 cm^{-1} for mafic glass compositions from this study and from previous works (Fine and Stolper 1986; Thibault and Holloway 1994; Dixon and Pan 1995; Jendrzewsky et al. 1997; Behrens et al. 2009; Shishkina et al. 2010; Vetere et al. 2011) and for mineral glasses of albitic and jadeitic (Fine and Stolper 1985), and diopsidic (Fine and Stolper 1986) compositions. Measured values of absorption coefficients vs. $\text{Na}/(\text{Na}+\text{Ca})$ molar ratio in the glasses: (a) ϵ_{1520} , (b) ϵ_{1430} . (c) Measured values of absorption coefficients ϵ_{1520} vs. values calculated for the same melt compositions as a function of $\text{Na}/(\text{Na}+\text{Ca})$ using the equation of Dixon and Pan (1995). (d) Measured values of absorption coefficients ϵ_{1430} vs. values calculated for the same melt compositions as a function of $\text{Na}/(\text{Na}+\text{Ca})$ using the linear equation derived from fitting only two datapoints of Dixon and Pan (1995).

3.3 Concentrations of H₂O and CO₂ in coexisting fluids and glasses

3.3.1 H₂O and CO₂ concentrations in mafic melts at 100 and 500 MPa

Because of difficulties with the determination of fluid composition in several runs, it is not possible to discuss the dependences between fluid and melt compositions in detail. In general, for all studied samples a positive correlation between the amounts of dissolved volatile and its molar fraction in the coexisting fluid is detected at both. It should be noted that such correlations for H₂O and CO₂ are close to linear at 100 and 200 MPa but they are significantly non-linear at 500 MPa in general agreement with previous experimental data. As expected, the solubility of each of the studied volatiles increases significantly with an increase in total pressure from 100 to 500 MPa (Fig. 3-3).

At both pressures, the melt composition has a very pronounced effect on the CO₂ solubility whereas it has an almost negligible effect on the solubility of H₂O. At 100 MPa, about 3.1-3.4 wt.% H₂O can be dissolved in the compositions B2518, B2507, A2549 and E2426 in runs with $X_{H_2O}^{in} = 1$ (Table 3-2). This is consistent with the available data on H₂O solubility in a variety of basaltic compositions at 100 MPa (Dixon et al. 1995; Pineau et al. 1998; Berndt et al. 2002; Shishkina et al. 2010; Lesne et al. 2011a; Vetere et al. 2011) which report similar values of about 3 wt.% H₂O.

At 500 MPa, the H₂O content in glasses saturated with pure H₂O ($X_{H_2O}^{in} = 1$) was determined only in four of eight studied melts (SC1, OB93, Etna and 169oxi). The solubility values for H₂O in glasses for samples B2518, B2507, A2549 and E2426 could not be determined at 500 MPa because of quench crystals. In the analyzed SC1, OB93, Etna and 169oxi samples, H₂O solubility varies in a quite narrow range from 8.8 to 9.5 wt% H₂O. Previous determinations of H₂O solubility in mafic melts at 500 MPa show similar H₂O-concentrations: 8.8 to 10.3 wt.% H₂O (Berndt et al. 2002; Botcharnikov et al. 2005; Behrens et al. 2009; Shishkina et al. 2010) as illustrated in Fig.3-4.

The solubility of CO₂ was determined in four melt compositions at 100 MPa and in seven melt compositions at 500 MPa (Table 3-2). Since water was present in all runs, even in runs with $X_{H_2O}^{in}=0$, the values of CO₂ contents in melts coexisting with pure CO₂ fluid were evaluated by extrapolating the trends to zero H₂O values as shown in Figs. 3-3 and 3-4. The resulting CO₂ solubility values vary significantly between different melt compositions at both pressures (Fig. 3-3, 3-4). At 100 MPa, the solubility values of CO₂ nearly coincide for alkali basalt B2507 and basanite B2518 and reach approximately 850 ppm. On the other hand, basanite A2549 can dissolve almost 2 times more (around 1800

ppm) and nephelinite (E2624) almost 3 times more (around 3000 ppm) CO₂ at the same pressure (Fig. 3-3).

At 500 MPa, the solubilities of CO₂ (extrapolated to $X_{H_2O}^{in}=0$) in the studied melt compositions are as follows: alkali basalt (OB93) has 3250 ppm, ferrobasalt (SC1) has 4250 ppm, alkali basalt (Etna) has 4400 ppm, MORB (169oxi) has 4500 ppm, alkali basalt (B2507) and basanite (B2518) have 5300 ppm each, and basanite (A2549) has 7500 ppm (Fig. 3-3, 3-4). The maximum concentration of CO₂ in nephelinite (E2624) could not be determined due to saturation of the IR detector using a 70 μm thin section. However, the minimum measured value is at least 9100 ppm (as reported in Table 3-2) which is significantly higher than the values for other compositions.

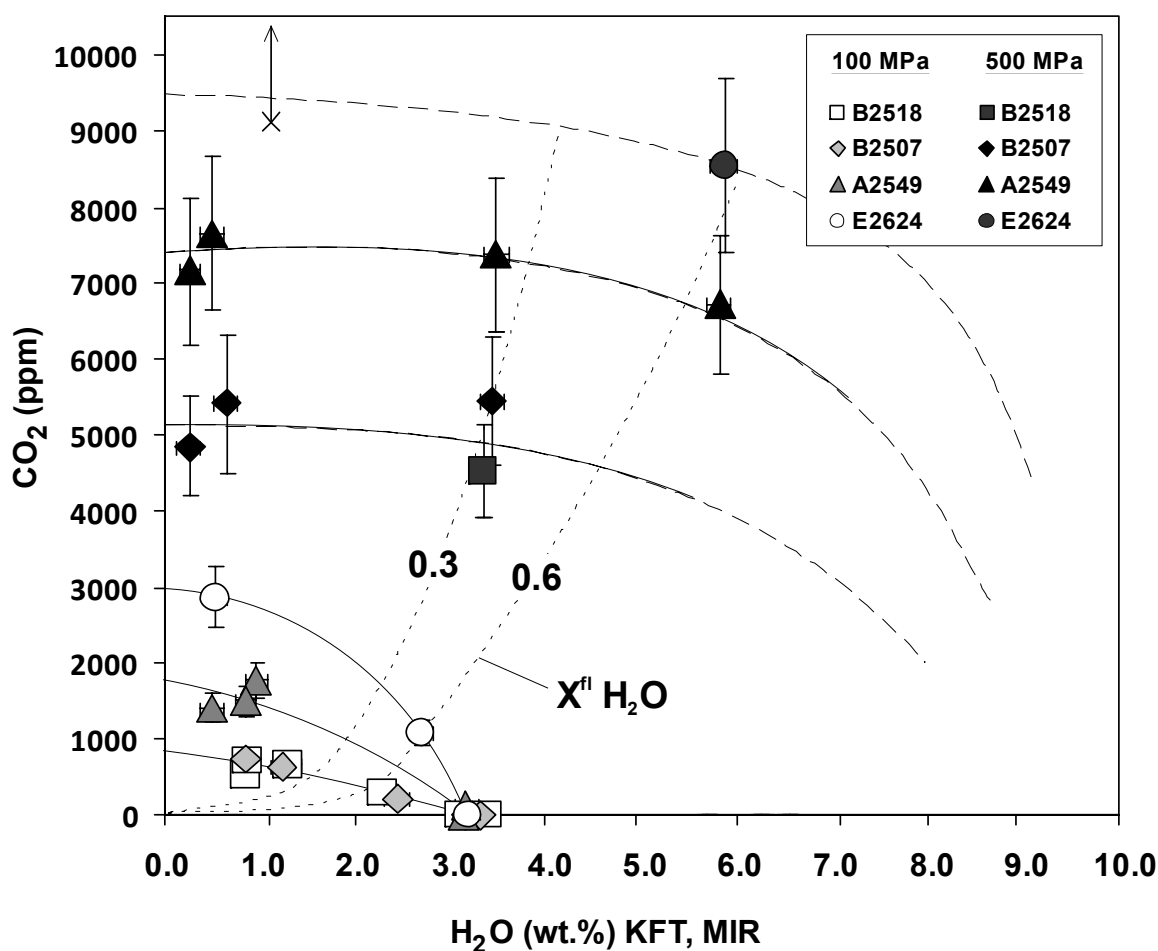


Figure 3-3. Solubility of H₂O and CO₂ coexisting with H₂O-CO₂ mixed fluids in alkali-rich mafic melts at 100 (light symbols) and 500 MPa (dark symbols): basanite (B2518), alkali basalt (B2507), basanite (A2549) and nephelinite (E2624). The solid lines represent isobars fitted to experimental data. Dashed lines show extrapolated solubility curves at 500 MPa to higher water contents in the melts (see text). The cross with arrow shows the minimum concentration of CO₂ in E2624 as measured by MIR (see table 3-2 and text for details). Basanite (B2518) and basalt (B2507) show identical solubility isobars for both pressures. Only two isopleths for the composition of coexisting fluid could be constrained from our data ($X_{H_2O}^{fluid}$ of 0.3 and 0.6).

3.3.2 Solubility of mixed H₂O-CO₂ fluids in mafic melts at 100 and 500 MPa

Isobaric solubility curves (isobars) at 100 and 500 MPa for mixed H₂O-CO₂ fluid in alkali basalt (B2507), basanite (B2518), basanite (A2549) and nephelinite (E2624) are shown in Fig. 3-3 (note that the isobar for nephelinite is an estimation by analogy with the other compositions). Due to the limited number of data on fluid composition for these samples, only isopleths for $X^{\text{H}_2\text{O}}=0.3$ and 0.6 are plotted. This plot demonstrates a large variation in the concentrations of dissolved CO₂ in melts of different composition and only weak or no compositional dependence for H₂O at 100 MPa.

The 500 MPa isobars obtained for other melt compositions are illustrated in Fig. 3-4. The SC1, Etna and 169oxi compositions show similar trends, whereas OB93 composition has slightly lower CO₂ concentrations in CO₂-rich samples. It must be noted that these four compositions are significantly depleted in CO₂ relative to other alkali-rich melts (basanites and nephelinite from this study and phonotephrite from Behrens et al. (2009) shown as lines in Fig. 3-4, but have comparable volatile concentrations to the island arc tholeiitic melt from Shishkina et al. (2010).

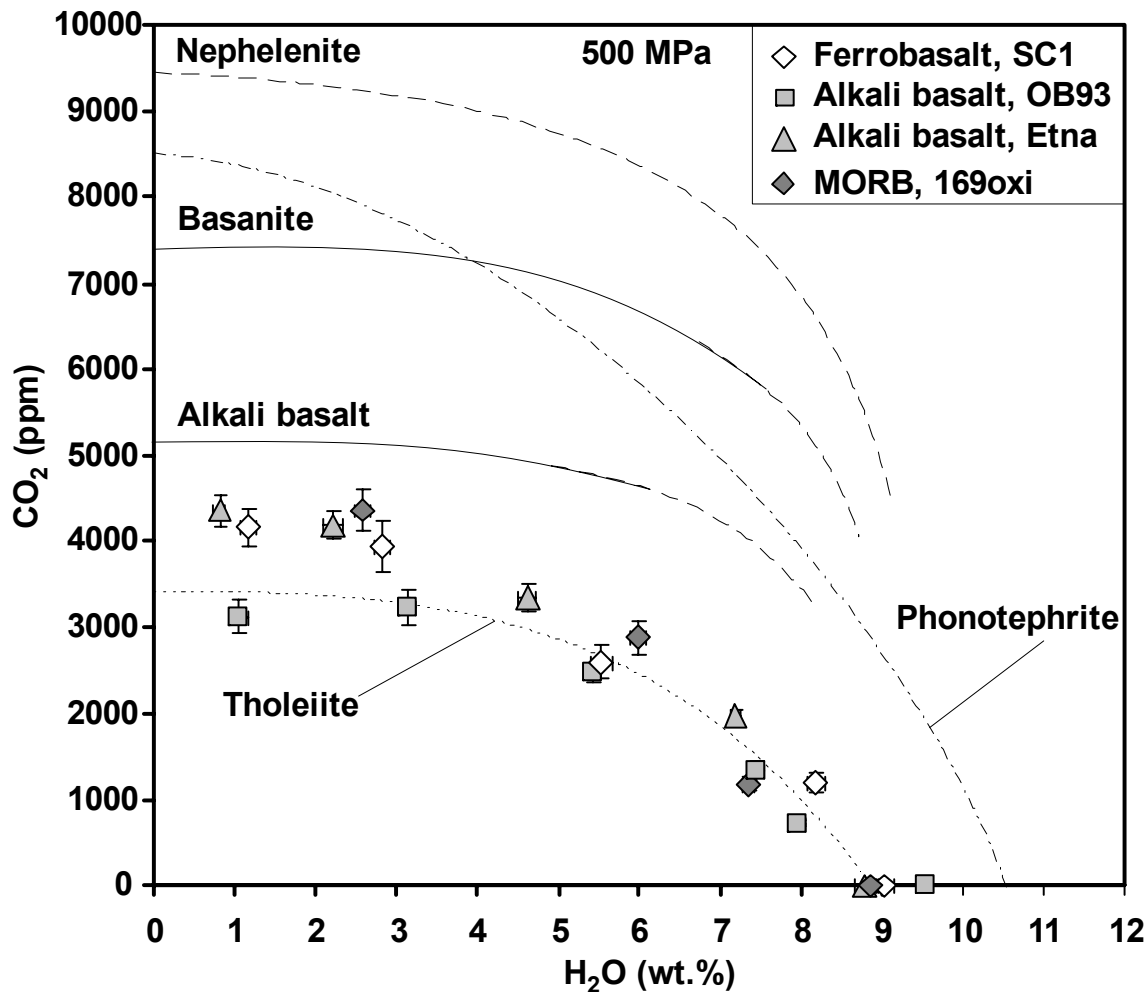


Figure 3-4. Solubility of H₂O and CO₂ coexisting with H₂O-CO₂-bearing fluids in mafic melts at 500 MPa.

Experimental data for ferrobasalt SC1, alkali basalt OB93, alkali basalt Etna and MORB 169oxi are shown with different symbols (see legend) and error bars. Solid lines represent 500 MPa isobars for nephelinite E2624, basanite A2549, basanite B2518 and alkali basalt B2507 (this study, see Fig. 3-3). Dashed-dotted line shows the solubility isobar for phonotephrite at 500 MPa and 1250°C by Behrens et al. (2009). Dotted line represents solubility isobar for tholeiite at 500 MPa and 1250°C of Shishkina et al. (2010).

Note: The concentrations of CO₂ in alkali basalt OB93 equilibrated with CO₂-rich fluids are modified after Botcharnikov et al. (2005b). They are about 2-2.5 times lower than those reported by Botcharnikov et al. (2005b). This discrepancy is attributed to an erroneous subtraction procedure for IR spectra applied for OB93 samples (conducted by Freise 2004 and reported in the work of Botcharnikov et al. 2005b). The spectra were normalized to a wrong thickness of the volatile-free reference material used for the calculations. Hence, the results for OB93 composition at 500 MPa published previously should not be used in the future and should be replaced with the data reported in this study.

3.3.3 Volatile solubility in tholeiite at 700 and 900 MPa

At both high pressures, the concentration of dissolved H₂O increases non-linearly with increasing $X_{H_2O}^{fluid}$ from 0 to 1 (Fig. 3-5a). In the range of $X_{H_2O}^{fluid}$ from 0.0 to 0.2, it increases quite rapidly becoming flatter up to $X_{H_2O}^{fluid}$ of about 0.8. At higher $X_{H_2O}^{fluid}$,

the concentration of H₂O increases faster. The inflexion of this trend was also observed in experimental products of previous studies at 500 MPa with tholeiite (Shishkina et al. 2010), rhyolite (Tamic et al. 2001) and phonotephrite (Behrens et al. 2009).

The concentration of CO₂ shows a strongly non-linear dependence on the fluid composition (Fig. 3-5b). At both pressures, an increase in CO₂ content can be observed with decreasing XCO₂^{fluid} from 1 to around 0.8, probably indicating a positive effect of H₂O on the CO₂ dissolution (see Discussion). In the range of XCO₂^{fluid} from 0.8 to 0.4, the concentration of CO₂ is constant within the error at both 700 and 900 MPa.

The solubility of H₂O in tholeiitic melt could not be determined accurately at these pressures since it was not possible to properly quench melts with such high water contents to a glass. Nevertheless, since quenched products represented hydrous silicate gels, it was assumed that they do retain most of water. These H₂O-rich samples were analyzed by KFT directly after opening the capsules to minimize dehydration or evaporation. The measured concentrations of H₂O are 11.21 wt.% at 700 MPa and 12.78 wt.% H₂O 900 MPa, which are more or less consistent with the general trend of H₂O solubility with pressure (Fig. 3-5a).

Surprisingly, the maximum CO₂ concentrations of about 4700 ppm and 5900 ppm at 700 and 900 MPa, respectively, are observed in glasses which are in equilibrium with fluid having XCO₂^{fluid} of about 0.6-0.8. The systems saturated with pure CO₂ fluid have significantly lower CO₂ concentrations of 4200 and 5100 ppm, respectively (Fig. 3-6).

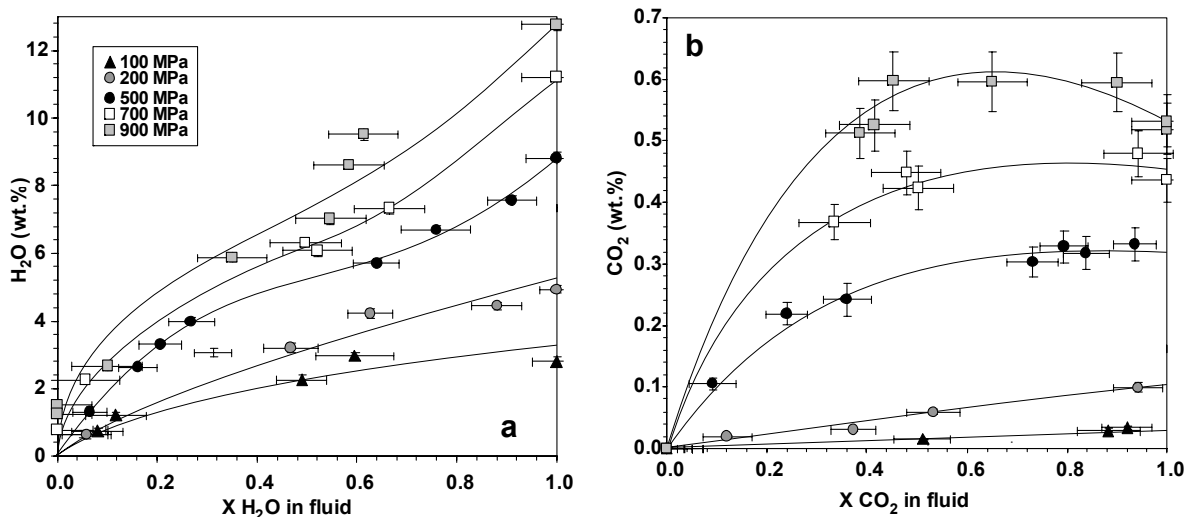


Figure 3-5. Relationship between the concentrations of volatile components in the melt and their mole fraction in the coexisting fluid: (a) H₂O, (b) CO₂. The data at 100-500 MPa are after Shishkina et al. (2010).

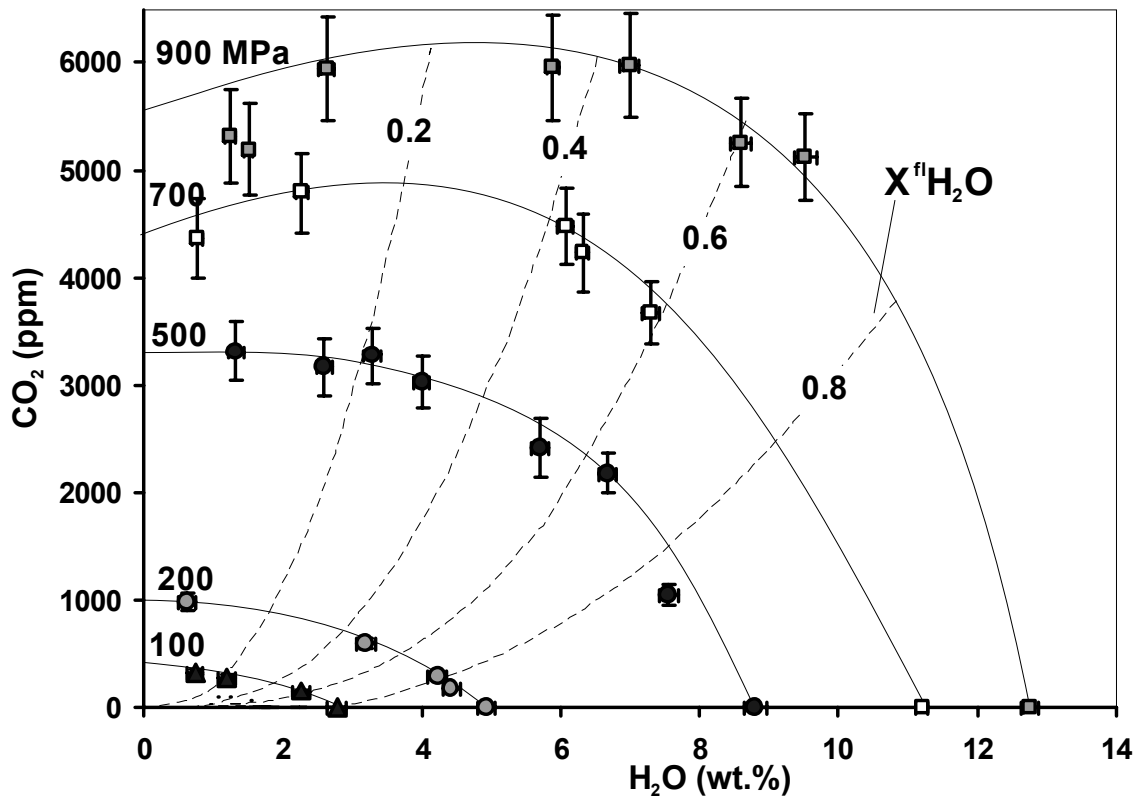


Figure 3-6. Solubility of H₂O and CO₂ coexisting with H₂O-CO₂-bearing fluids in tholeiitic basalt N72 (Mutnovsky volcano). Data at 100, 200 and 500 MPa are from Shishkina et al. (2010), whereas those at 700 and 900 MPa are from this study. Solid lines represent isobars, dashed lines – isopleths for fluid composition.

4. DISCUSSION

4.1 Pressure effect on the solubility of mixed CO₂-H₂O-bearing fluids in basaltic melts

Solubility of mixed H₂O-CO₂ fluids in low-alkali high-Al tholeiitic melt was studied in the pressure range of 50-500 MPa (Shishkina et al. 2010) and at 700 and 900 MPa (this study). At low pressures, almost ideal solubility behavior is observed for both CO₂ and H₂O (Fig.3-5, only data at 100 and 200 MPa are shown for clarity). At pressures > 200 MPa, the distribution of volatiles between melt and fluid shows significant deviation from ideal behavior. In particular, the CO₂ content in the glasses becomes less sensitive to the concentration of CO₂ in the coexisting fluid and a maximum is even detected as $X_{\text{CO}_2}^{\text{fl}}$ decreases from 1 to 0.6 at 700 and 900 MPa (Figs.3-5b and 3-6).

The observed behavior of CO₂ can be attributed to the effect of H₂O on the CO₂ dissolution mechanisms in the melt. A positive effect of H₂O on CO₂ solubility at relatively high pressures (≥ 500 MPa) was reported in a number of works on solubility of mixed

fluids in silicate melts of different compositions [e.g.,: icelandite, Jakobsson (1997); dacite, Behrens et al. (2004); andesite, Botcharnikov et al. (2006); phonotephrite, Behrens et al. (2009); tholeiite, Shishkina et al., 2010; shoshonite, Vetere et al., 2011)]. It was already proposed in earlier studies that increasing concentration of water in silicate melts may cause substitution of some bridging oxygens by non-bridging OH-groups (e.g.: Burnham, 1975; Mysen et al., 1980), resulting in a depolymerization of the melt structure which could potentially favor an increase in CO₂ concentration. This effect seems to be enhanced with increasing pressure. The data at 700 and 900 MPa clearly indicate that the effect of melt depolymerization due to incorporation of high amounts of water (leading to an increase of CO₂ concentration) dominates over that of decreasing fugacity of CO₂ (leading to a decrease of CO₂ concentration). Alternatively, it can be argued that the observed maximum is caused by changes in the redox conditions in the system due to low activity of water and hence, due to increased proportion of reduced carbon species (e.g., CO, CH₄) in the fluid phase in expense of CO₂. This can lead to a potential decrease in CO₂ concentration in the melt due to low solubility of CO and CH₄ and reduced fugacity of CO₂ (e.g., Pawley et al. 1992; Scaillet and Pichavant 2004; Behrens et al. 2009; Morizet et al. 2010). However, intrinsic redox conditions and hence, redox conditions in the experimental capsules are expected to be similar at different pressures (relative to a given redox buffer). Thus, the reduction of CO₂ in the fluid can not explain the observed maximum in CO₂ concentration at 700 and 900 MPa (Figs.3-5b and 3-6). Note also that the maximum value relative to the expected solubility of pure CO₂ increases with pressure (Figs.3-5b and 3-6).

4.2 Compositional effect on the solubility of H₂O in basaltic melts

The effect of anhydrous melt composition on H₂O solubility is relatively weak and the H₂O solubility increases in general with the change from mafic to silicic composition. Systematic studies of the compositional effects on H₂O solubility have been done mostly with silicic systems (e.g., Holtz et al. 1992, 1995, 2000; Dingwell et al. 1997; Behrens et al. 2001; Behrens and Jantos 2001), pointing that increasing Na/K ratio, peralkalinity, (MCLNK-Al)/O and decreasing SiO₂ content have a positive effect on H₂O solubility. Systematic studies for mafic melts are scarce. Benne and Behrens (2003) studied the haplobasaltic system Ab-An-Di at 50, 200 and 500 MPa and found that the compositional effect is not pronounced at low pressures (below 200 MPa), but increases at higher pressure of 500 MPa. According to their observations, a decrease in H₂O solubility is observed with an increase in the proportion of Di component and An/Ab ratio.

Dixon (1997) found that H₂O solubility in basaltic melt is about 20% lower than that in tholeiitic melt and proposed a simple linear positive correlation between H₂O solubility and SiO₂ content of the melt (empirically calibrated for a SiO₂ range of 40-49 wt.%). Recently, Lesne et al. (2011a) investigated three alkali-rich basalts and found a positive correlation between H₂O solubility and Na₂O+K₂O (wt.%). This correlation, which takes into account also the positive effect of oxygen fugacity noted by Berndt et al. (2002), was expressed in the form:

$$\text{H}_2\text{O (wt.\%)} = \text{H}_2\text{O}_{\text{MORB}} \text{ (wt.\%)} + (\alpha * P \text{ (bar)} + \beta) * (\text{Na}_2\text{O} + \text{K}_2\text{O}) \text{ (wt.\%)} + \gamma * \Delta\text{NNO} + \delta \quad (6)$$

where H₂O_{MORB} is the solubility of water in the MORB determined by the model of Dixon et al. (1995), ΔNNO is the oxygen fugacity relative to NNO buffer and $\alpha = 5.84 * 10^{-5}$, $\beta = -2.04 * 10^{-2}$, $\gamma = 4.67 * 10^{-2}$, and $\delta = -2.29 * 10^{-1}$ are empirical parameters derived from fitting of the experimental data (Lesne et al., 2011b).

Figure 3-7 illustrates the compilation of the experimental data on H₂O solubility in melts with mafic to intermediate compositions at pressures from 50 to 500. The positive effect of Na+K and the negative effect of SiO₂ become more pronounced with increasing pressure, keeping, however, almost linear relationships. It must be taken into account that experimental conditions in different studies may vary in terms of temperature and redox conditions at the given pressure, which may have an additional effect on H₂O solubility.

It should be noted that empirical parameterizations proposed by Dixon (1997) and Lesne (2011a) (Fig. 3-7) as well as those from earlier studies for specific compositions (e.g., Stolper et al. 1982; Holloway and Blank 1994; Moore et al. 1998) are able to predict H₂O solubility within the uncertainty of determinations for many experiments, especially at pressures below 200 MPa, which is not surprising owing to the relatively small compositional effect. Nevertheless, linear regression equations are reported for the data at all studied pressures in Figure 3-8 for consistency.

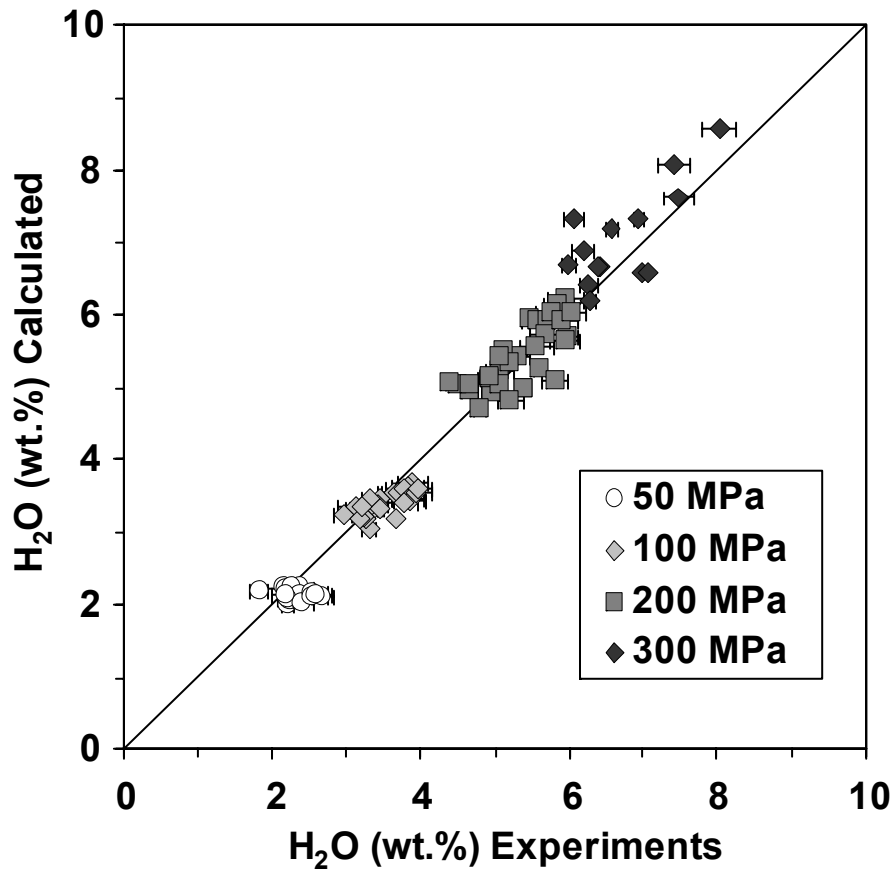


Figure 3-7. H₂O solubility in mafic and intermediate melts calculated with empirical equation of Lesne et al. (2011a) (see text eq. 6) vs. experimentally determined values at pressures of 50, 100, 200 and 300 MPa for data from this study and other works studies (Dixon et al., 1995; Moore et al. 1995, 1998; Pineau et al. 1998; Webster et al. 1999; Berndt et al. 2002; Benne and Behrens 2003; Botcharnikov et al. 2005b; Di Matteo et al. 2006; Iacono-Marziano et al. 2007; Stelling et al. 2008; Schmidt and Behrens 2008; Behrens et al. 2009; Shishkina et al. 2010; Vetere et al. 2011; Lesne et al. 2011a).

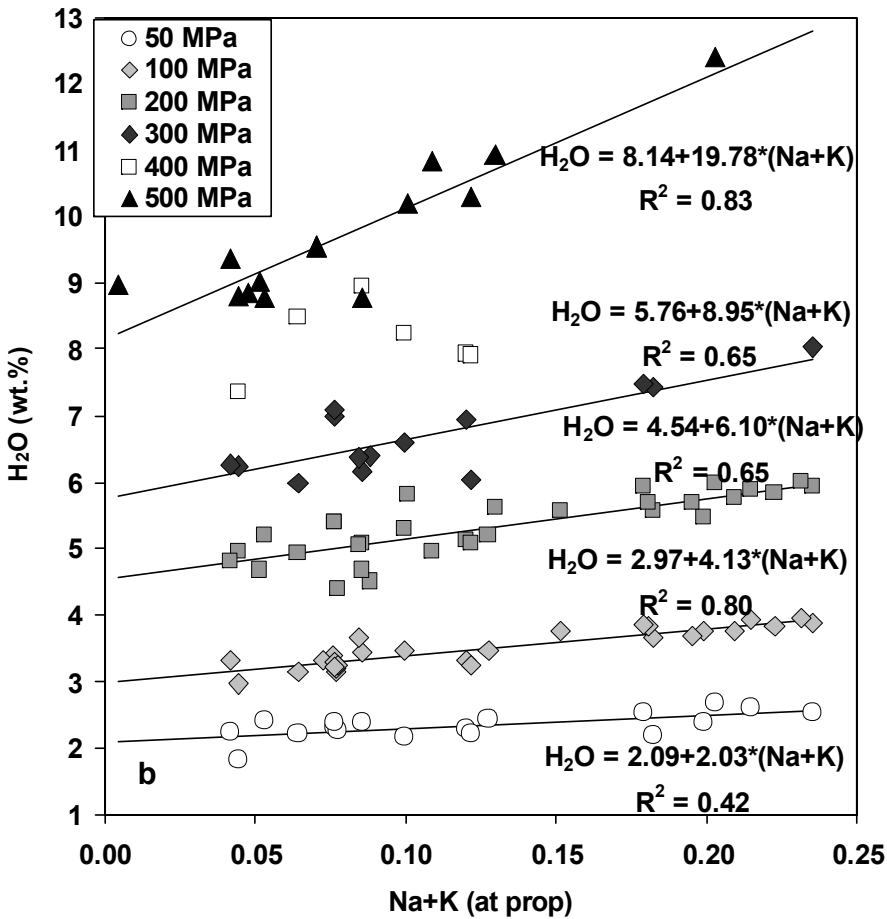
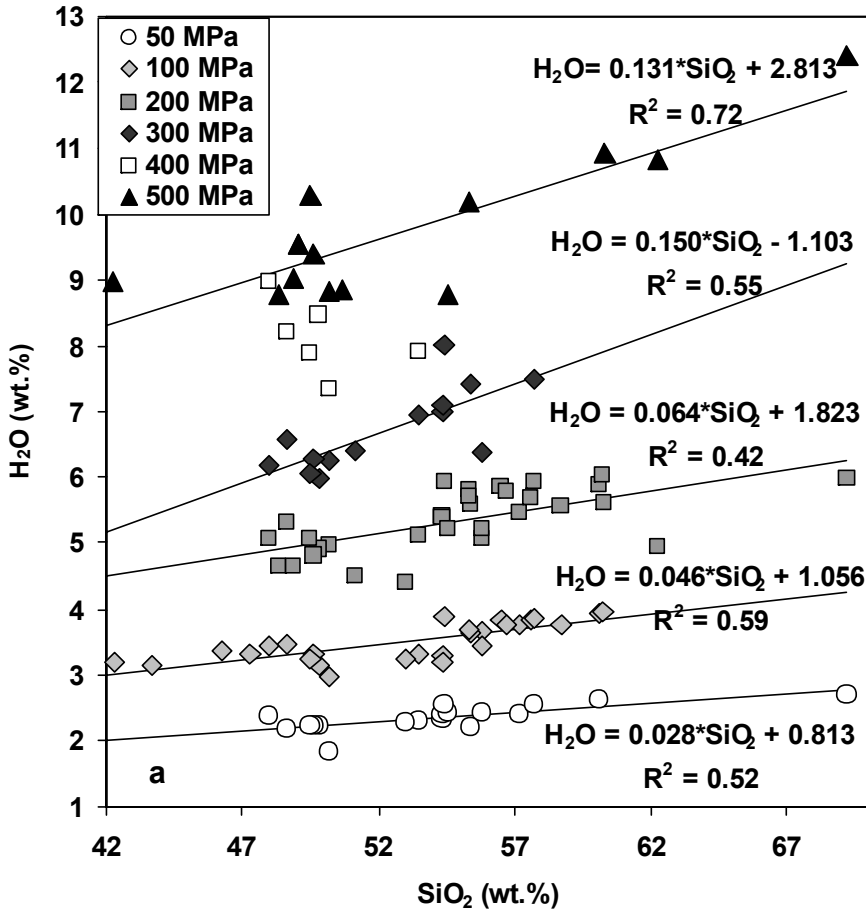


Figure 3-8. H₂O solubility in mafic and intermediate melts versus (a) SiO₂ (wt.%) and (b) Na+K (atomic fraction) at pressures from 50 to 500 MPa. Data from this study and other studies (see references in caption of Fig. 3-7).

4.3 Compositional effect on CO₂ solubility in basaltic melts

A strong effect of the silicate melt composition on CO₂ solubility, even within the range of mafic compositions (42-51 wt.% SiO₂), was noticed already in many previous studies and a number of explanations, interpretations and attempts of empirical compositional parameterizations for this dependence were conducted (e.g., Blank and Brooker 1994; Holloway and Blank 1994; Dixon et al. 1995; Dixon 1997; Brooker et al. 2001a, 2001b; Lesne et al., 2011b). A thermodynamic parameterization calibrated against experimental data was developed in the models of Papale (1999) and Papale et al. (2006).

It is suggested that the main compositional factors controlling dissolution mechanism of CO₂ are related to the structural parameters of the silicate melt. Spectroscopic studies (e.g., Blank and Brooker 1994; Dixon et al. 1995) showed that CO₂ dissolves in mafic melts mainly as carbonate ion CO₃²⁻, though recent studies of Nowak et al. (2003, 2004) indicated that proportion of CO₂ dissolved in molecular form can be considerably high in depolymerized melts. Moreover, even in melts with the same depolymerization degree, the solubility of CO₂ can vary in a wide range (Brooker et al. 2001 a, b) and may depend on the proportions of different cations which act as network modifiers in the melt structure (e.g., Holloway 1976; Brooker et al. 2001a; Moore 2008). Figure 3-9 shows the relationship between CO₂ solubility and major element composition of mafic silicate melts for the experiments at 100 MPa. Most cations do not show any clear correlation with the amounts of dissolved CO₂. General negative trends in Figure 3-9 are observed for SiO₂ (a) and Al₂O₃ (b), whereas general positive trends are related with increasing concentrations of MgO (d) and CaO (e). Surprisingly, neither Na₂O (g) nor K₂O (h) concentrations have a pronounced and clear effect on CO₂. If melt composition is expressed as a structural parameter NBO/T (e.g.: following the approach of Brooker et al. (2001a) when all Si, Ti, Al³⁺, Fe³⁺ and Fe²⁺ are considered as tetrahedral cations (T) and all Mg²⁺, Ca²⁺, Na⁺ and K⁺ in excess are net-work modifiers corresponding to NBO) as illustrated in Figure 3-10, it shows a positive non-linear correlation with CO₂ solubility and emphasizes the important role of melt depolymerization, although the scattering of the data is quite significant. Furthermore, it is expected that the ability of different network modifiers to form complexes with carbonate ion should decrease in a row Ca>K>Na>Li>Mg>Fe ≈Mn as suggested by Spera and Bergman (1980) based on the values of Gibbs free energies for carbonation reactions for these cations. Taking this approach into account, Dixon (1997) proposed a compositional parameter *I* which reflects

both the degree of melt depolymerization and the “energetic” input of different network modifiers in the carbonate dissolution capacity of the melt. This parameter resulted from linear fitting of the relationship between the CO₂ content (solubility) and the compositions of four mafic melts (MORB, tholeiite, basanite and leucitite). The *II* parameter was normalized to the carbonate concentration in the melt at 100 MPa, resulting in a linear regression with corresponding regression coefficients (see Dixon 1997 for details):

$$II = -6.50*(Si^{4+} + Al^{3+}) + 20.17*(Ca^{2+} + 0.8K^{+} + 0.7Na^{+} + 0.4 Mg^{2+} + 0.4 Fe^{2+}) \quad (7)$$

where (Si⁴⁺ + Al³⁺) term represents the degree of melt polymerization, whereas the (Ca²⁺ + 0.8K⁺ + 0.7Na⁺ + 0.4 Mg²⁺ + 0.4 Fe²⁺) term reflects the “energetic” effect of the carbonation reactions. All cations are in cation fractions. The coefficients for each cation in the last term correspond to the contribution of each cation to the Gibbs free energy of carbonation reactions relative to that of Ca (as proposed by Dixon 1997 using the approach of Spera and Bergman 1980). Furthermore, using the dataset on natural glasses from the North Arch seafloor eruptions of alkalic lavas, Dixon (1997) found a linear correlation between *II* and SiO₂ content of the glasses and proposed that even simplified compositional parameterization (only via SiO₂ content) can be applied. Despite the empirical nature of this parameter, it showed in general a good correlation with the solubility of CO₂ in mafic melts investigated so far. The simplified parameterization was included as a basis for the widely-used VolatileCalc model (Newman and Lowenstern 2002), whereas the 7-parameter approach was incorporated in the new SolEx model for mixed fluids (Witham et al. in press). Recently, the *II* parameter was recalibrated by Lesne et al. (2011b) using 3 new data points for alkali basalts from experiments at 100 MPa, still resulting in similar linear relation between *II* and CO₂ solubility as reported by Dixon (1997).

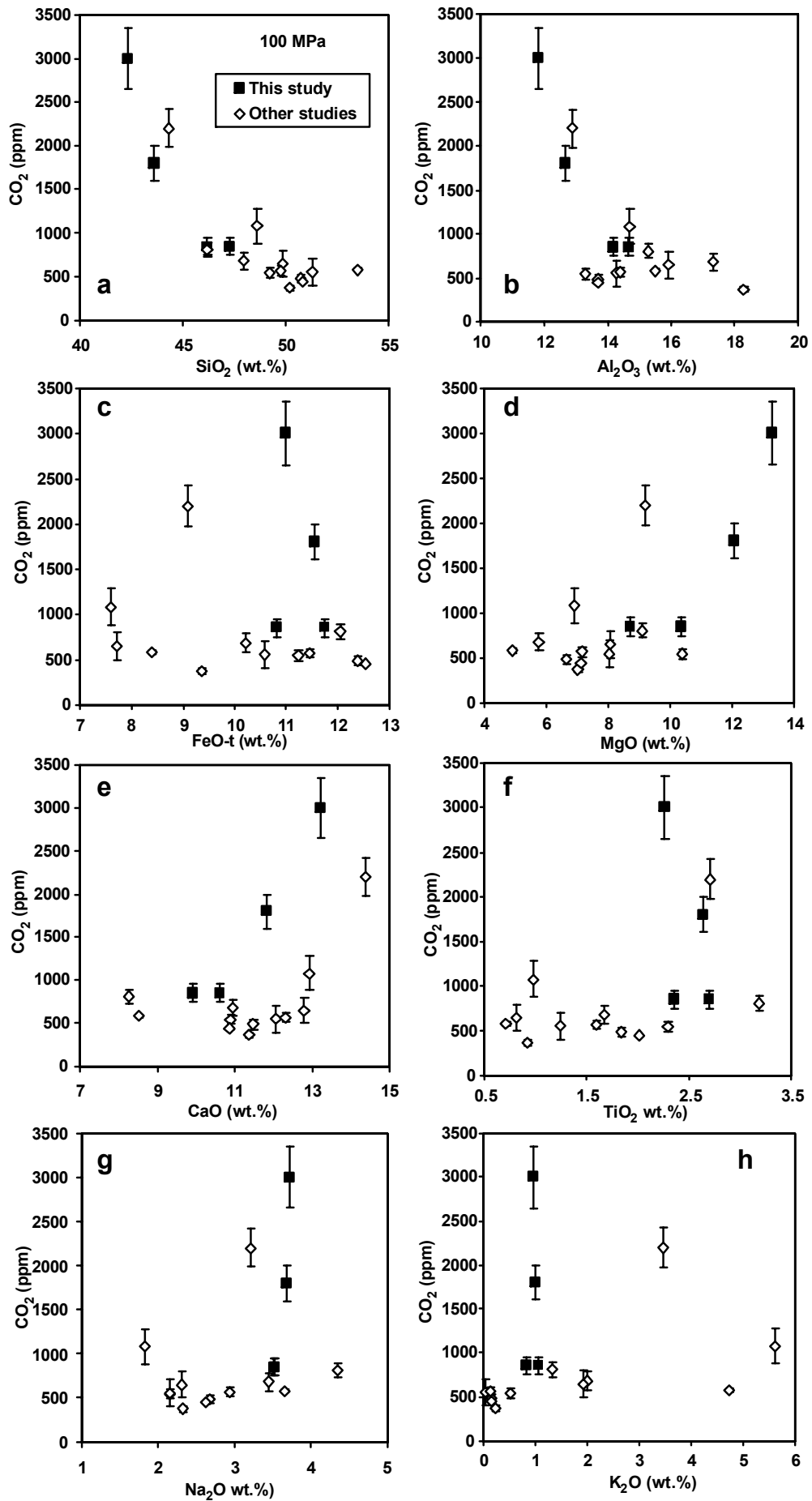


Figure 3-9 (Previous page). Dependence of CO₂ solubility on concentrations of major oxide components in mafic glasses at 100 MPa: a – SiO₂, b – Al₂O₃, c – FeO-t, d – MgO, e – CaO, f – TiO₂, g – Na₂O, h – K₂O. Data for this study (black squares) together with data from other sources (Stolper and Holloway 1988; Pan et al. 1991; Pawley et al. 1992; Holloway and Blank 1994; Thibault and Holloway 1994; Dixon et al. 1995; Jendrzewski et al. 1997; Botcharnikov et al. 2005b; Behrens et al. 2009; Shishkina et al. 2010; Lesne et al. 2011b; Vetere et al. 2011) (white diamonds) are shown (experimental data at 1200-1300°C).

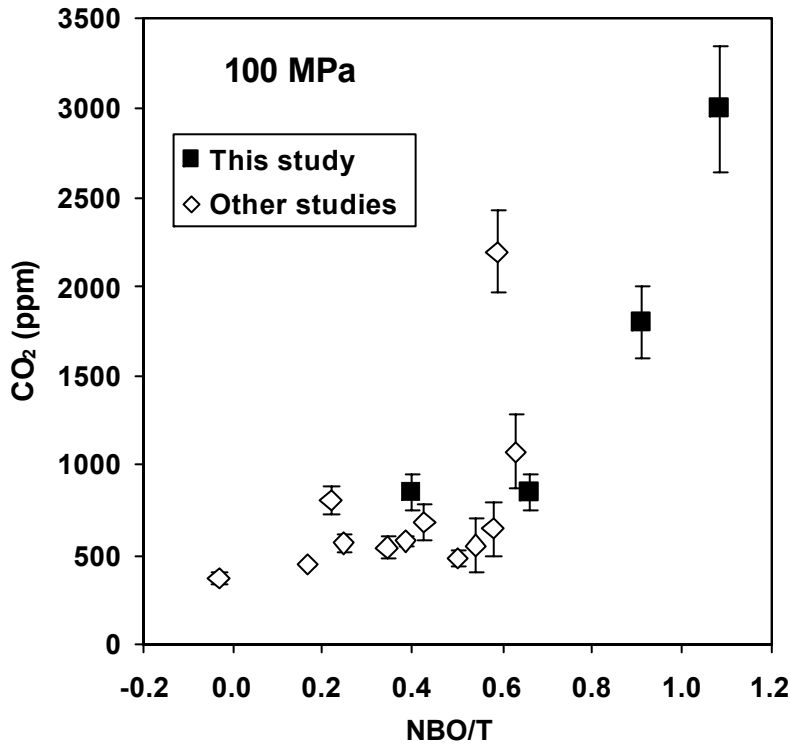


Figure 3-10. Dependence of CO₂ solubility in mafic melts on the NBO/T parameter (calculated following Brooker et al. 2001a, see text) at 100 MPa. The data are from this study (black squares) and from other sources (same as for Fig. 3-9).

A serious disadvantage of the H -parameterization approach is that it is limited to the narrow range of SiO₂ concentrations from 40 to 49 wt% as discussed also by Moore (2008). New experimental data (Botcharnikov et al. 2005b; Behrens et al. 2009; Shishkina et al. 2010; Lesne et al. 2011b; Vetere et al. 2011; this study), combined with the data from previous studies, are plotted in Figure 3-11 as a function of H . Since for most compositions no data on Fe²⁺/Fe³⁺ ratio is available, the concentration of total iron (Fe_{total}) was used instead of Fe²⁺ in the equation (2) (assuming that experiments with pure CO₂ fluid are relatively reduced and the large proportion of Fe is present in the reduced form). The contribution of Fe to the eq.(2) is relatively minor and this assumption is not expected to change the results significantly. Experimental data are plotted in Figure 3-11 as a series at pressures of 50, 100, 200, and 500 MPa. The data clearly demonstrate that the relationship

between CO₂ solubility and the melt compositional parameter Π is actually not linear (Fig. 3-11). The dashed lines in Figure 3-11 denote linear relationships between CO₂ solubility and Π as calculated using VolatileCalc model (Newman and Lowenstern 2002). The solid lines in Figure 3-11 are the exponential trends through the experimental data points (similar form of exponential equations was chosen based on the best fit for the 100 MPa data as shown in panels). The phonotephritic composition investigated by Behrens et al. (2009) at 200 and 500 MPa is shown in Figure 3-11c,d, but not included in the regression due to significant deviation from the trends. The reason for this deviation is not clear. The concentration of CO₂ in nephelinite composition E2624 at 500 MPa was estimated as a minimum value due to analytical problems (see Results) and thus, it was not included in the fitting. It is obvious that from the linear regressions used in the VolatileCalc model it is not possible to predict CO₂ solubility in melts with negative Π values (trend ends at $\Pi=0$).

In order to adapt the the Π -parameterization for the extrapolation to other compositions, the relationship between depolymerization ($\text{Si}^{+4} + \text{Al}^{+3}$) and carbonation ($\text{Ca}^{2+} + 0.8\text{K}^{+} + 0.7\text{Na}^{+} + 0.4 \text{Mg}^{2+} + 0.4 \text{Fe}^{2+}$) terms can be considered as a ratio instead of difference (as proposed by Dixon, 1997). The $(\text{Ca}^{2+} + 0.8\text{K}^{+} + 0.7\text{Na}^{+} + 0.4 \text{Mg}^{2+} + 0.4 \text{Fe}^{2+}) / (\text{Si}^{+4} + \text{Al}^{+3})$ ratio is defined here as a new parameter, Π^* and the CO₂ solubility values are plotted in Figure 3-12 versus Π^* . The obtained trends of the experimental data have non-linear shapes similar to those in Figure 3-11, and they can be fitted also by exponential equations. The form of exponential equations at different pressures was selected to be in agreement with that established for the data at 100 MPa (which has the best regression correlation coefficient). Identical form of the exponential equations and systematic shift of these equations with pressure allowed multiple linear regression of the data in terms of $\ln(\text{CO}_2)$ vs. Π^* and $\ln P$. The regression equation can be expressed as:

$$\ln(\text{CO}_2) = A \cdot \ln P + B \cdot \Pi^* + C \quad (8)$$

where CO_2 is carbon dioxide concentration in wt%; P is pressure in MPa, Π^* is compositional parameter $(\text{Ca}^{2+} + 0.8\text{K}^{+} + 0.7\text{Na}^{+} + 0.4 \text{Mg}^{2+} + 0.4 \text{Fe}^{2+}) / (\text{Si}^{+4} + \text{Al}^{+3})$ with cations in cation fractions; $A=1.014$, $B= 7.483$ and $C=-0.891$ are the multiple regression coefficients. This empirical expression can be used to predict the solubility of CO₂ in mafic melts at pressures at least up to 500 MPa. Figure 3-13 illustrates the comparison between the experimental and predicted CO₂ solubilities. In addition to the data used for calibration (see Fig.3-12), the experimental results obtained at other pressures (e.g., 300, 400 MPa) were included in the calculation. Most of the experimental data can be predicted within the uncertainty (Fig. 3-13a,b). The model shows also quite good results for the data at 700 and

900 MPa, although it tends to slightly underestimate the experimental data (Fig.3-13a). The prediction by VolatileCalc model is also shown in Figure 3-13c,d. Clearly, the prediction of CO₂ solubility is more accurate using equation (8) and the H^* parameter.

The exponential dependence of CO₂ solubility on compositional parameter H^* indicates that the contribution of an “energetic” term, i.e., contribution of cation carbonation reactions, becomes more and more dominant with increasing degree of depolymerization or with the proportion of such cations. Furthermore, it must be noted that the representation a parameter such as the NBO/T does not seem to be an appropriate choice for modeling the ability of melt to dissolve CO₂ (Fig. 3-10). A poor correlation between NBO/T and CO₂ solubility was also reported by Brooker et al. (2001b) for melts with different MgO concentrations at 2 GPa. These findings emphasize that the “energetic” approach of Spera and Bergman (1980) and Dixon (1997) is better suited to describe the dissolution mechanism of CO₂ in mafic melts than simple structural parameters. However, this energetic effect should diminish with the evolution of magma composition to intermediate and more silicic compositions, because CO₂ dissolved as carbonate will be progressively replaced by molecular CO₂ (e.g., Nowak et al. 2004). Since molecular CO₂ solubility is dependent on the so called ionic porosity in the melt, it should be more dependent on the network structure of the melt than on the energy of cation – carbonate interaction.

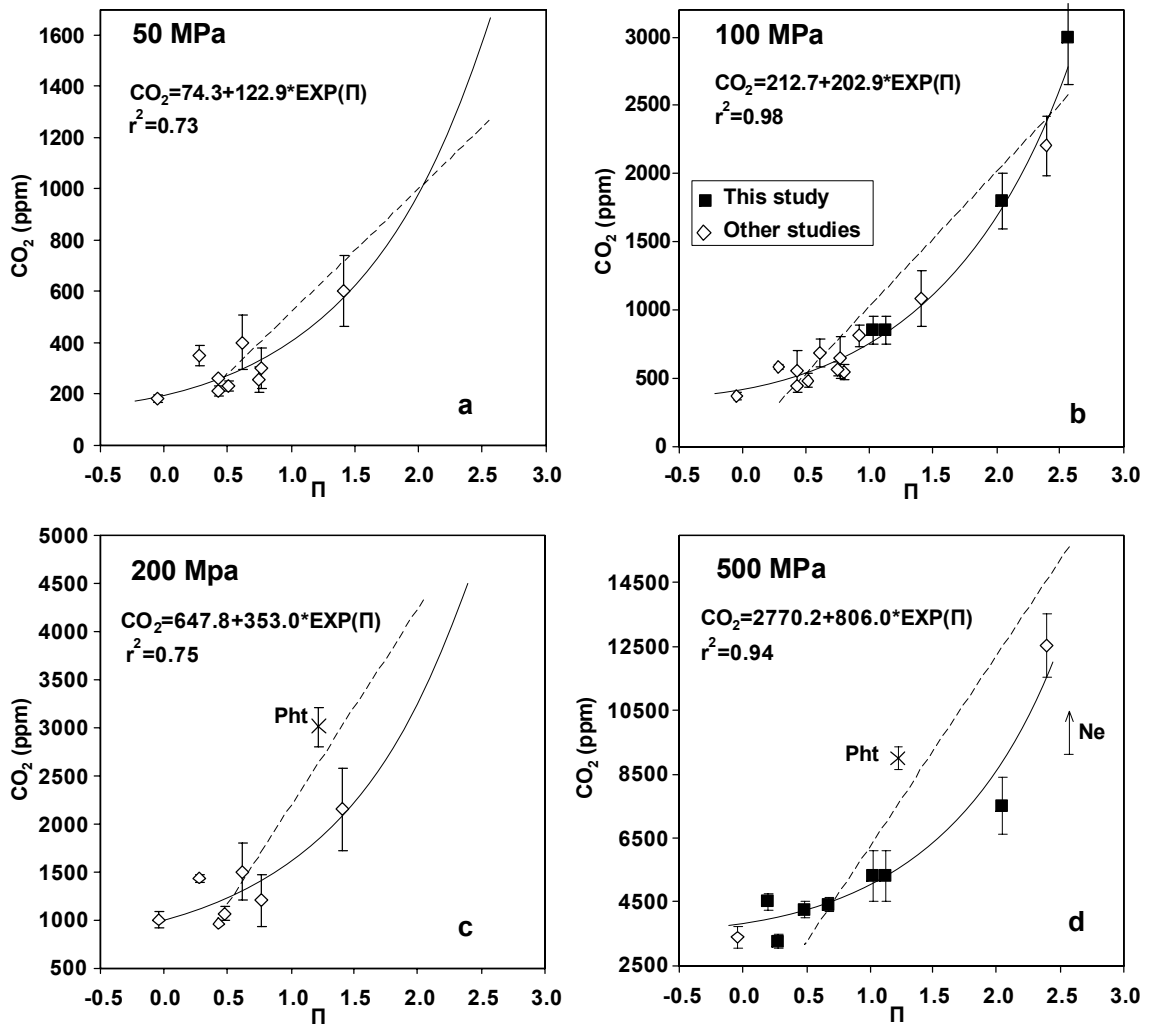


Figure 3-11. Dependence of CO₂ solubility on the parameter Π derived by Dixon (1997) (see text eq.7) at different pressures: 50 MPa (a), 100 MPa (b), 200 MPa (c), 500 MPa (d). The data are from this study (black squares) and from other sources (same as for Fig. 3-9). The solid lines represent an exponential fit of experimental results. Dashed lines represent calculations with the model of Dixon (1997).

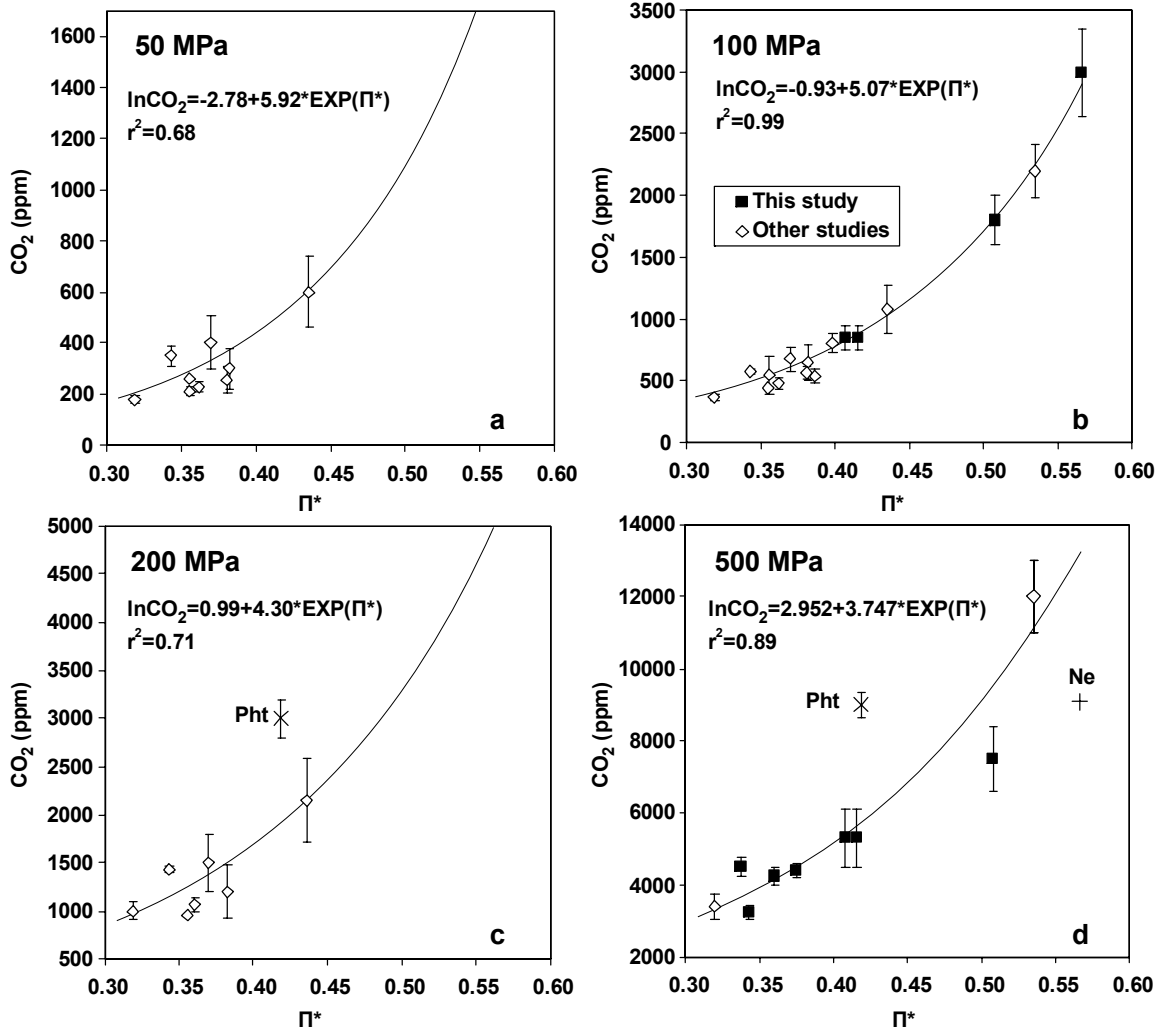


Figure 3-12. Dependence of CO₂ solubility on parameter Π* (see text) at different pressures: 50 MPa (a), 100 MPa (b), 200 MPa (c), 500 MPa (d). Results of this study (black squares) together with data from other sources (same as for Fig. 3-9) (white diamonds) are shown. Solid lines represent exponential trends of compositional dependence drawn through experimental results.

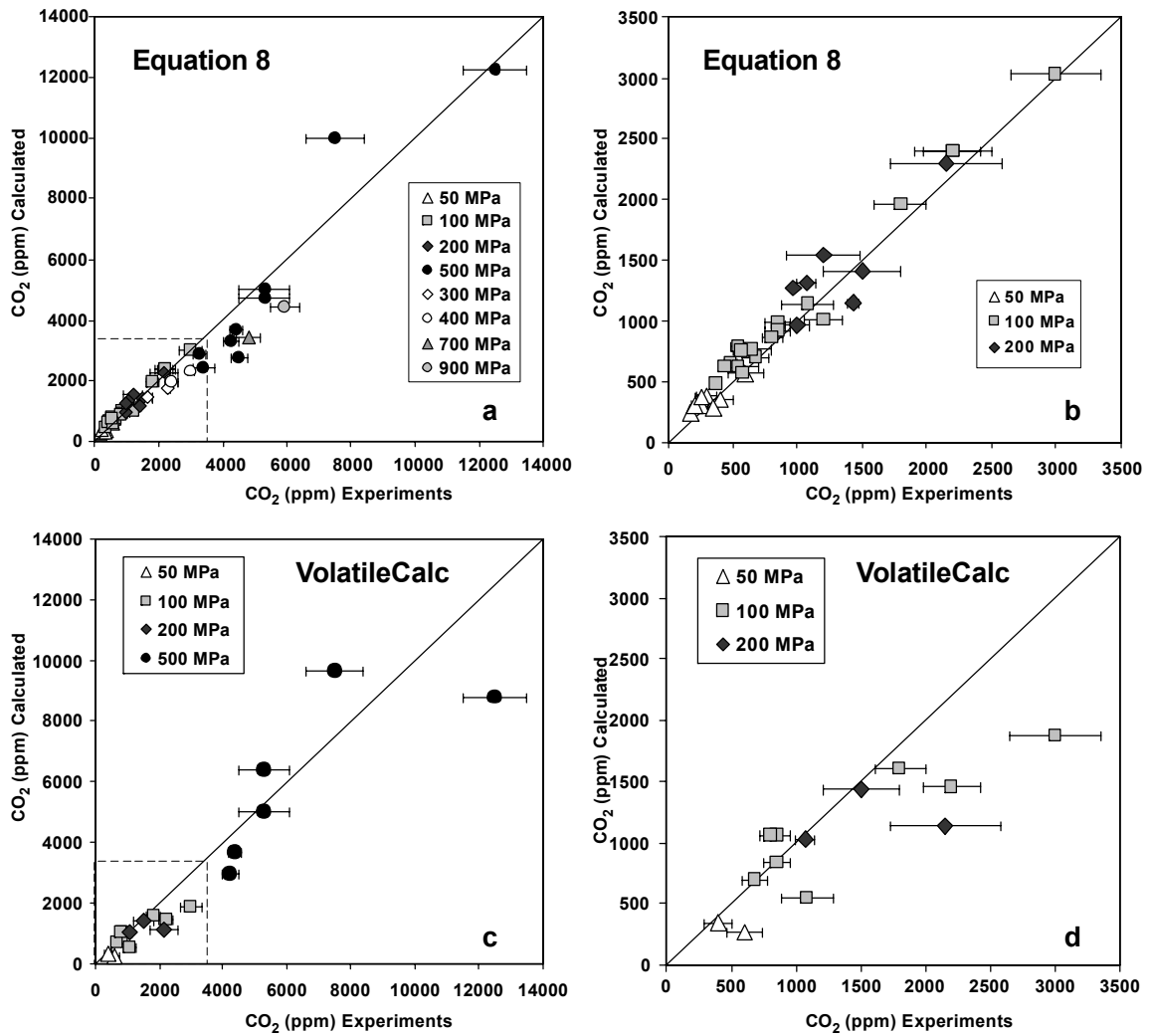


Figure 3-13. Comparison of calculated with experimentally determined CO₂ solubilities. a, b - CO₂ concentrations were calculated using an empirical equation (see text eq. 8) derived from the multiple linear regression of the experimental data on CO₂ solubility in mafic melts at 50, 100, 200 and 500 MPa (see text). a – data for 50 – 900 MPa, b – data for 50, 100 and 200 MPa (enlargement of Fig. 3-3a). c, d - CO₂ concentrations calculated by VolatileCalc (Newman&Lowenstern, 2002).

5. CONCLUDING REMARKS

New experimental data on the solubility of H₂O and CO₂ in mafic melts in combination with the data from previous studies are used to quantify the effects of pressure and melt composition, which are the two most important parameters that control H₂O and CO₂ degassing from basaltic magmas. The effect of pressure is illustrated on the example of tholeiitic magma indicating that such magmas can dissolve up to 12 wt% H₂O and up to 0.5 wt% CO₂ as pressure progressively increases to 900 MPa. The influence of anhydrous melt composition on volatile solubilities is complex with a strong effect on CO₂ and very

small effect on H₂O solubility (relative variations). The compositional dependence of CO₂ solubility in mafic melts coexisting with pure CO₂ fluids can best be interpreted in terms of structural and “energetic” parameters of silicate melts, attributed to the individual effects of carbonation reactions for different cations of the silicate melt Spera and Bergman (1980) and Dixon (1997).. The observed correlations between melt composition, CO₂ solubility and pressure are used for the development of an empirical model predicting CO₂ solubility as a function of mafic melt composition and pressure up to 900 MPa.

Acknowledgements

The authors thank H. Behrens for consultations, S. Cichy for the help with performing the experiments, O. Diedrich for preparation of samples for infra-red spectroscopy and microprobe analyses, F. Adams and L. Crede for determinations of redox state of Fe of part of the samples. This research has been supported by the German Science Foundation (DFG projects Ho1337/21 and Ho1337/19-1, DAAD scholarship A/08/79422, Europlanet Ri TNA program, grant 228319.

References

- Almeev, R. R., Holtz, F., Koepke, J., Haase, K. M. & Devey, C. W. (2008) Depths of Partial Crystallization of H₂O-bearing MORB: Phase Equilibria Simulations of Basalts at the MAR near Ascension Island (7°-11°S). *Journal of Petrology*, 49, 25-45.
- Aranovich, L.Y., Newton, R.C. (1999) Experimental determination of CO₂-H₂O activity-concentration relations at 600–1000 C and 6–14 kbar by reversed decarbonation and dehydration reactions. *American Mineralogist*, 84, 1319-1332.
- Behrens, H., Jantos, N. (2001) The effects of anhydrous composition on water solubility in granitic melts. *American Mineralogist*, 86, 14-20.
- Behrens, H., Meyer, M., Holtz, F., Benne, D., Nowak, M. (2001) The effect of alkali ionic radius, temperature and pressure on the solubility of water in MAISi₃O₈ melts (M = Li, Na, K, Rb). *Chemical Geology*, 174, 275–289.
- Behrens, H., Romano, C., Nowak, M., Holtz, F., Dingwell, D.B. (1996) Near-infrared spectroscopic determination of water species in glasses of system MAISi₃O₈ (M=Li, Na, K): An interlaboratory study. *Chemical Geology*, 128, 41-63.

- Behrens, H., Ohlhorst, S., Holtz, F., Champenois, M. (2004) CO₂ solubility in dacitic melts equilibrated with H₂O–CO₂ fluids – implications for modelling the solubility of CO₂ in silicic melts. *Geochim. Cosmochim. Acta*, 68, 4687-4703.
- Behrens, H., Misiti V., Freda C., Vetere F., Botcharnikov, R.E., Scarlato, P. (2009) Solubility of H₂O and CO₂ in ultrapotassic melts at 1200 and 1250°C and pressure from 50 to 500 MPa. *American Mineralogist*, 94, 105-120.
- Benne, D., Behrens, H. (2003) Water solubility in haplobasaltic melts. *European Journal of Mineralogy*, 15, 803–814.
- Berndt, J., Liebske, C., Holtz, F., Freise, M., Nowak, M., Ziegenbein, D., Hurkuck, W., Koepke, J. (2002) A combined rapid-quench and H₂-membrane setup for internally heated pressure vessels: Description and application for water solubility in basaltic melts. *American Mineralogist*, 87, 1717-1726.
- Blank, J.G., Brooker, R.A. (1994) Experimental studies of carbon dioxide in silicate melts: solubility, speciation, and stable carbon isotope behavior. In: Carrol, M.R., Holloway, J.R. (Ed.), *Reviews in Mineralogy*, 30, 157-186.
- Botcharnikov, R.E., Koepke, J., Holtz, F., McCammon, C. and Wilke, M. (2005a) The effect of water activity on the oxidation and structural state of Fe in a ferro-basaltic melt. *Geochimica et Cosmochimica Acta*, 69 (21), 5071-5085.
- Botcharnikov, R., Freise, M., Holtz, F. and Behrens, H. (2005b) Solubility of C-O-H mixtures in natural melts: new experimental data and application range of recent models. *Annals of Geophysics*, 48 (4-5), 633-646.
- Botcharnikov, R.E., Behrens, H., Holtz, F. (2006) Solubility and speciation of C-O-H fluids in andesitic melt at T = 1100-1300 °C and P = 200 and 500 MPa. *Chemical Geology*, 229, 125-143.
- Botcharnikov, R.E., Almeev, R.R., Koepke, J. and Holtz, F. (2008) Phase relations and liquid lines of descent in hydrous ferrobasalt - Implications for the Skaergaard Intrusion and Columbia River flood basalts. *Journal of Petrology*, 49(9), 1687-1727.
- Brooker, R.A., Kohn, S.C., Holloway, J.R., McMillan, P.F. (2001a) Structural controls on the solubility of CO₂ in silicate melts. Part I: bulk solubility data. *Chemical Geology*, 174, 225–239.

- Brooker, R.A., Kohn, S.C., Holloway, J.R., McMillan, P.F. (2001b) Structural controls on the solubility of CO₂ in silicate melts. Part II: IR characteristics of carbonate groups in silicate glasses. *Chemical Geology*, 174, 241–254.
- Burnham, C.W. (1975) Water and magmas; a mixing model. *Geochimica et Cosmochimica Acta*, 39, 1077-1084.
- Burnham, C.W. (1979) The importance of volatile constituents. In: Yoder, H.S. (Ed.), *The Evolution of the Igneous Rocks*. Princeton University Press, Princeton, NJ, pp. 439–482.
- Di Matteo, V., Mangiacapra, A., Dingwell, D.B., Orsi, G. (2006) Water solubility and speciation in shoshonitic and latitic melt composition from Campi Flegrei Caldera (Italy). *Chemical Geology*, 229, 113–124
- Dingwell, D.B., Holtz, F., Behrens, H. (1997) The solubility of H₂O in peralkaline and peraluminous melts. *American Mineralogist*, 82, 434–437
- Dixon, E.J., Stolper, E.M., Holloway, J.R. (1995) An experimental study of water and carbon dioxide solubilities in mid-ocean ridge basaltic liquids. Part 1: Calibration and solubility models. *Journal of Petrology*, 36, 1607-1631.
- Dixon, J.E., Pan, V. (1995) Determination of the molar absorptivity of dissolved carbonate in basaltic glass. *American Mineralogist*, 80, 1339–1342.
- Dixon, J.E. (1997) Degassing of alkali basalts. *American Mineralogist*, 82, 368-378.
- Fine, G., Stolper, E. (1985) The speciation of carbon-dioxide in sodium aluminosilicate glasses. *Contributions to Mineralogy and Petrology*, 91(2), 105–121.
- Fine, G., Stolper, E. (1986) Carbon dioxide in basaltic glasses: concentrations and speciation. *Earth and Planetary Science Letters*, 76, 263-278.
- Freise, M. (2004) Differenzierung von Basalten einer “Large Igneous Province” am Beispiel des Kerguelen Plateaus. Eine experimentelle Studie. PhD thesis, University of Hannover.
- Freise, M., Holtz, F., Nowak, M., Scoates, J., Strauss, H. (2009) Differentiation and crystallization conditions of basalts from the Kerguelen large igneous province: an experimental study. *Contributions to Mineralogy and Petrology*, 158(4): 505-527.

- Holloway, J.R., Blank, J.G. (1994) Application of experimental results to C-O-H species in natural melts. In: Carrol, M.R., Holloway, J.R. (Ed.), *Reviews in Mineralogy*, 30, 187-230.
- Holloway, J.R., Mysen, B.O., Eggler, D.H. (1976) The solubility of CO₂ in liquids on the join CaO-MgO-SiO₂-CO₂. *Carnegie Institute of Washington Yearbook*, 75, 626–631.
- Holtz, F., Behrens, H., Dingwell, D.B., Taylor, R.P. (1992) Water solubility in aluminosilicate melts of haplogranite composition at 2 kbar. *Chemical Geology*, 96, 289–302.
- Holtz, F., Behrens, H., Dingwell, D.B., Johannes, W. (1995) Water solubility in haplogranitic melts. Compositional, pressure and temperature dependence. *American Mineralogist*, 80, 94-108.
- Holtz, F., Roux, J., Behrens, H., Pichavant, M. (2000) Water solubility in silica and quartzofeldspathic melts. *American Mineralogist*, 85, 682–686.
- Iacono-Marziano, G., Schmidt, B.C., Dolfi, D. (2007) Equilibrium and disequilibrium degassing of a phonolitic melt (Vesuvius A.D. 79 “White Pumice”) simulated by decompression experiments. *Journal of Volcanology and Geothermal Research*, 161, 151–164.
- Iacono Marziano, G., Gaillard, F. and Pichavant, M. (2008) Limestone assimilation by basaltic magmas: an experimental re-assessment and application to Italian volcanoes. *Contributions to Mineralogy and Petrology*, 155(6): 719-738.
- Jakobsson, S. (1997) Solubility of water and carbon dioxide in an icelandite at 1400 °C and 10 kilobars. *Contributions to Mineralogy and Petrology*, 127, 129-315
- Jendrzewski, N., Trull, T.W., Pineau, F., Javoy, M. (1997) Carbon solubility in Mid-Ocean Ridge basaltic melt at low pressures (250–1950 bar). *Chemical Geology*, 138, 81–92.
- King, P.L., Holloway, J.R. (2002) CO₂ solubility and speciation in intermediate (andesitic) melts: the role of H₂O and composition. *Geochimica et Cosmochimica Acta*, 66, 1627-1640.

- Kubicki, J.D., Stolper, E.M. (1995) Structural roles of CO₂ and [CO₃]²⁻ in fully polymerized, sodium aluminosilicate melts and glasses. *Geochimica et Cosmochimica Acta*, 59, 683–698.
- Lesne, P., Scaillet, B., Pichavant, M., Iacono-Marziano, G., Beny, J. M. (2011a) The H₂O solubility of alkali basaltic melts: an experimental study. *Contributions to Mineralogy and Petrology*, 162, 133-151.
- Lesne, P., Scaillet, B., Pichavant, M., Beny, J.M. (2011b) The carbon dioxide solubility in alkali basalts: an experimental study. *Contributions to Mineralogy and Petrology*, 162, 153-168.
- Moore, G., Vennemann, T., Carmichael, I.S.E. (1995) Solubility of water in magmas to 2 kbar. *Geology*, 23, 1099–1102.
- Moore, G., Vennemann, T., Carmichael, I.S.E. (1998) An empirical model for the solubility of H₂O in magmas to 3 kilobars. *American Mineralogist*, 83, 36–42.
- Moore, G. (2008) Interpreting H₂O and CO₂ Contents in Melt Inclusions: Constraints from Solubility Experiments and Modeling Reviews in *Mineralogy and Geochemistry*, 69, 333-362.
- Morizet, Y., Paris, M., Gaillard, F. and Scaillet, B. (2010) C-O-H fluid solubility in haplobasalt under reducing conditions: An experimental study. *Chemical Geology*, 279(1-2): 1-16.
- Mysen, B.O. (1988) Structure and properties of silicate melts (Developments in geochemistry, 4). 354 p. Elsevier, Amsterdam.
- Mysen, B.O., Virgo, D., Harrison, W.J. and Scarfe, C.M. (1980) Solubility mechanisms of H₂O in silicate melts at high pressures and temperatures: a Raman spectroscopic study. *American Mineralogist*, 65, 900-914.
- Mysen, B.O., Arculus, R.J., Eggler, D.H. (1975) Solubility of carbon dioxide in melts of andesite, tholeiite, and olivine nephelinite composition to 30 kbar pressure. *Contribution to Mineralogy and Petrology*, 53, 227-239.
- Mysen, B.O. (1976) The role of volatiles in silicate melts; solubility of carbon dioxide and water in feldspar, pyroxene, and feldspathoid melts to 30 kb and 1625 degrees C. *American Journal of Science*, 276, 969-996.

- Newman, S. Lowenstern, J. B. (2002) VolatileCalc: a silicate melt-H₂O-CO₂ solution model written in Visual Basic for Excel. *Computers & Geosciences*, 28, 597-604.
- Nowak, M., Porbatzki, D., Spickenbom, K., Diedrich, O. (2003) Carbon dioxide speciation in silicate melts: A restart. *Earth Planetary Science Letters*, 207, 131-139.
- Nowak, M., Schreen, D., Spickenbom, K. (2004) Argon and CO₂ on the race track in silicate melts: a tool for the development of a CO₂ speciation and diffusion model. *Geochimica et Cosmochim Acta*, 64, 5127–5138.
- O'Neill, H.St.C. (1987b) The free energies of formation of NiO, CoO, Ni₂SiO₄. *American Mineralogist*, 72, 280-291.
- Pan, V., Holloway, J.R., Hervig, R.L. (1991) The pressure and temperature dependence of carbon dioxide solubility in tholeiitic basalt melts. *Geochimica et Cosmochimica Acta*, 55, 1587-1595.
- Pandya, N., Muenow, D.W, Sharma, S.K. (1992) The effect of bulk composition on the speciation of water in submarine volcanic glasses. *Geochimica et Cosmochimica Acta*, 56, 1875–1883.
- Papale, P. (1999) Modeling of the solubility of a two-component H₂O + CO₂ fluid in silicate liquids. *American Mineralogist*, 84, 477-492.
- Papale, P., Moretti, R., Barbato, D. (2006) The compositional dependence of the saturation surface of H₂O + CO₂ fluids in silicate melts. *Chemical Geology*, 229, 78-95.
- Pawley, A.R., Holloway, J.R., McMillan, P.F. (1992) The effect of oxygen fugacity on the solubility of carbon-oxygen fluids in basaltic melt. *Earth and Planetary Science Letters*, 110 (1-4), 213-225.
- Pineau, F., Shilobreeva, S., Kadik A., Javoy M. (1998) Water solubility and D/H fractionation in the system basaltic andesite-H₂O at 1250°C and between 0.5 and 3 kbars. *Chemical Geology*, 147 (1), 173-184.
- Pitzer, K.S., Sterner, S.M. (1994) Equation of state valid continuously from zero to extreme pressures for H₂O and CO₂. *Journal of Chemistry and Physics*, 102, 3111-3116.
- Richet, P., Whittington, A., Holtz, F., Behrens, H., Ohlhorst, S., Wilke, M. (2000) Water and density of silicate glasses. *Contribution to Mineralogy and Petrology*, 138, 337–347.

- Scaillet, B. and Pichavant, M. (2004) Role of fO_2 on fluid saturation in oceanic basalt. *Nature*, 430 (6999).
- Schmidt, B.C., Behrens, H., Riemer, T., Kappes, R., Dupree, R. (2001) Quantitative determination of water speciation in aluminosilicate glasses: a comparative NMR and IR spectroscopic study. *Chemical Geology*, 174, 195–208.
- Schuessler, J.A., Botcharnikov, R.E., Behrens, H., Misiti, V., Freda, C. (2008) Oxidation state of iron in hydrous phono-tephritic melts. *American Mineralogist*, 93, 1493–1504.
- Shishkina, T.A., Botcharnikov, R.E., Holtz, F., Almeev, R.R., Portnyagin, M.V. (2010) Solubility of H₂O- and CO₂-bearing fluids in tholeiitic basalts at pressures up to 500 MPa. *Chemical Geology*, 277, 115–125.
- Spera, F.J., Bergman, S.C. (1980) Carbon-dioxide in igneous petrogenesis: I. Aspects of the dissolution of CO₂ in silicate liquids. *Contributions to Mineralogy and Petrology*, 74(1), 55–66.
- Stelling, J., Botcharnikov, R.E., Beermann, O., Nowak, M. (2008) Solubility of H₂O- and chlorine-bearing fluids in basaltic melt of Mount Etna at T = 1050-1250 °C and P = 200 MPa. *Chemical Geology*, 256(3-4): 102-110.
- Stolper, E. (1982) The speciation of water in silicate melts. *Geochimica et Cosmochimica Acta*, 46, 2609–2620.
- Stolper, E., Holloway, J.R. (1988) Experimental-determination of the solubility of carbon-dioxide in molten basalt at low-pressure. *Earth Planetary Science Letters*, 87, 397–408.
- Tamic, N., Behrens, H., Holtz, F. (2001) The solubility of H₂O and CO₂ in rhyolitic melts in equilibrium with a mixed CO₂-H₂O fluid phase. *Chemical Geology*, 174, 333-347.
- Thibault, Y., Holloway, J.R. (1994) Solubility of CO₂ in a Ca-rich leucitite: effects of pressure, temperature and oxygen fugacity. *Contributions to Mineralogy and Petrology*, 116, 216–224.
- Toplis, M.J., Carroll, M.R. (1995) An experimental study of the influence of oxygen fugacity of Fe-Ti oxide stability, phase relations, and mineral-melt equilibria in ferro-basaltic systems. *Journal of Petrology*, 36, 1137–1170.

- Vetere, F., Botcharnikov, R. E., Holtz, F., Behrens, H., De Rosa, R. (2011) Solubility of H₂O and CO₂ in shoshonitic melts at 1250°C and pressures from 50 to 400 MPa: implications for Campi Flegrei magmatic systems. *Journal of Volcanology and Geothermal Research*, 202, 251–261
- Webster, J. D., Kinzler, R. J., Mathez, E. A. (1999) Chloride and water solubility in basalt and andesite melts and implications for magmatic degassing. *Geochimica et Cosmochimica Acta*, 63, 729-738.
- Wilson, A. D. (1960) The micro-determination of ferrous iron in silicate minerals by a volumetric and colorimetric method. *Analyst*, 85, 823–827.
- Witham, F., Blundy, J., Kohn, S. C., Lesne, P., Dixon, J., Churakov, S., and Botcharnikov, R. (in press) SolEx: A model for mixed COHSCl-fluid solubilities and exsolved gas compositions in basalt. *Computers and Geosciences*, doi:10.1016/j.cageo.2011.09.021.
- Yamashita, S., Kitamura, T. & Kusakabe, M. (1997) Infrared spectroscopy of hydrous glasses of arc magma compositions. *Geochemical Journal*, 31, 169–174.

APPENDIX

List of tables

CHAPTER I

Table A-1-1 Compositions of melt inclusions in olivines from Mutnovsky tephra (Electron microprobe analyses)-----	184
Table A-1-2. Compositions of melt inclusions recalculated with Petrolog3 to equilibrium with Ol-host (normalized to 100%)-----	186
Table A-1-3. Volatiles in melt inclusions-----	188
Table A-1-4. Experimental conditions of phase relations experiments--	189
Table A-1-5. Compositions of experimental glasses-----	193
Table A-1-6. Compositions of experimental olivines-----	196
Table A-1-7. Compositions of experimental plagioclases-----	198
Table A-1-8. Compositions of experimental clinopyroxenes-----	201
Table A-1-9. Compositions of experimental orthopyroxenes-----	203
Table A-1-10. Compositions of experimental amphiboles-----	204
Table A-1-11. Compositions of experimental magnetites-----	205

CHAPTER II

Table A-2-1. Major-element compositions of experimental glasses (wt.%) determined by electron microprobe-----	207
Table A-2-2. Major-element compositions of experimental glasses (wt.%) determined by electron microprobe, recalculated to 100% using Fe ²⁺ /Fe-total ratio determined by colorimetry. -----	209

CHAPTER III

Table A-3-1. Experimental conditions, results of Karl-Fischer titration, determinations of redox state of Fe and infrared spectroscopy-----	211
---	-----

APPENDIX

CHAPTER I

Table A-1-1 Compositions of melt inclusions in olivines from Mutnovsky tephra (Electron microprobe analyses)

NN	Size, µm	Sample	Fo-host	SiO ₂	TiO ₂	Al ₂ O ₃	FeO-t	MnO	MgO	CaO	Na ₂ O	K ₂ O	P ₂ O ₅	S	Cl	Total
Naturally quenched melt inclusions in olivines																
KM9-10-29-1	110	KM9-10	77.9	52.84	1.22	17.31	8.05	0.17	3.91	8.53	3.99	0.80	0.29	0.11	0.07	97.27
KM9-10-29-2a	45	KM9-10	77.9	52.51	1.07	17.91	7.85	0.29	3.40	8.48	3.51	0.80	0.14	0.08	0.06	96.10
KM9-10-32-1	55	KM9-10	78.3	53.37	1.12	15.70	7.31	0.22	3.15	9.18	3.49	1.01	0.20	0.09	0.07	94.91
KM9-10-32-2	75	KM9-10	78.3	50.41	1.24	17.23	8.77	0.21	3.33	10.31	3.47	0.51	0.26	0.13	0.07	95.94
KM9-10-32-3	140	KM9-10	78.3	49.98	1.07	17.08	8.63	0.19	3.99	10.68	3.39	0.47	0.21	0.12	0.06	95.88
KM9-10-34-2	45	KM9-10	78.3	51.21	1.15	16.73	8.84	0.25	3.39	10.64	3.66	0.56	0.18	0.12	0.06	96.79
KM9-10-35-1a	25	KM9-10	78.0	53.92	0.96	17.36	7.12	0.00	2.72	9.56	3.87	0.87	0.07	0.07	0.07	96.58
KM9-10-37-1	100	KM9-10	77.9	51.63	1.24	17.26	9.39	0.13	3.45	9.35	3.41	0.64	0.15	0.15	0.07	96.87
KM9-10-40-1	130*65	KM9-10	78.1	53.20	1.73	16.32	8.10	0.18	3.81	8.65	3.69	1.19	0.46	0.08	0.07	97.48
KM9-11-42-1	100	KM9-11	78.0	51.74	1.21	16.97	9.60	0.18	3.61	9.46	2.72	0.55	0.19	0.15	0.07	96.44
KM9-11-43-1	180*75	KM9-11	77.4	50.01	1.11	17.11	9.49	0.18	4.15	10.45	3.17	0.51	0.25	0.13	0.06	96.62
KM9-11-43-2	75	KM9-11	77.6	52.20	1.14	17.60	8.78	0.27	3.65	8.78	3.62	0.73	0.24	0.13	0.07	97.21
KM9-11-48-1	30	KM9-11	77.8	53.30	1.11	17.06	8.54	0.11	3.27	9.65	3.91	0.94	0.09	0.05	0.06	98.08
KM9-11-50-1	75*50	KM9-11	78.1	50.31	1.31	17.22	9.37	0.09	3.78	9.92	3.38	0.54	0.25	0.12	0.07	96.37
Re-homogenized melt inclusions																
KM9-10-52-1		KM9-10	78.4	51.09	0.97	18.26	8.15	0.15	7.62	9.79	2.71	0.51	0.04	0.12	0.04	99.45
KM9-10-53-2		KM9-10	78.2	49.66	1.18	15.93	11.38	0.20	7.89	9.24	2.72	0.63	0.22	0.12	0.05	99.24
KM9-10-53-3		KM9-10	78.2	50.73	1.14	15.83	11.06	0.15	7.67	9.22	3.20	0.54	0.07	0.12	0.06	99.79
KM9-10-54-1-1		KM9-10	79.2	51.25	0.99	15.13	8.89	0.25	7.41	10.25	2.84	0.90	0.34	0.14	0.05	98.43
KM9-10-57-1-1		KM9-10	78.3	49.12	1.06	16.07	10.39	0.25	7.91	9.05	2.90	0.53	0.13	0.14	0.05	97.60
KM9-10-57-2-1		KM9-10	78.6	52.55	0.95	14.80	8.08	0.15	6.92	10.18	3.08	0.92	0.07	0.07	0.05	97.85
KM9-10-58-1-1		KM9-10	77.9	52.07	0.96	18.18	8.43	0.19	7.09	9.41	3.19	0.56	0.19	0.11	0.05	100.43
KM9-10-59-1-1		KM9-10	78.0	50.34	1.10	16.03	9.81	0.11	7.89	8.95	3.25	0.58	0.21	0.15	0.05	98.47
KM9-10-59-2-2		KM9-10	78.0	50.64	1.02	15.77	10.06	0.25	7.81	8.61	2.92	0.66	0.41	0.12	0.06	98.31
KM9-10-59-3-3		KM9-10	78.4	51.40	1.04	16.11	10.32	0.17	8.06	8.92	3.31	0.57	0.34	0.11	0.06	100.40
KM9-10-59-4-4a		KM9-10	78.8	52.99	0.97	15.43	9.38	0.12	7.16	7.27	3.65	1.05	0.38	0.06	0.06	98.52

Table A-1-1 continued

NN	Size, μm	Sample	Fo-host	SiO ₂	TiO ₂	Al ₂ O ₃	FeO-t	MnO	MgO	CaO	Na ₂ O	K ₂ O	P ₂ O ₅	S	Cl	Total
KM9-11-60-1-1		KM9-11	78.5	51.82	0.65	18.11	8.05	0.24	6.49	10.18	2.75	0.46	0.04	0.08	0.03	98.89
KM9-11-60-2-1		KM9-11	78.4	52.61	0.78	18.77	8.27	0.10	6.67	9.26	2.86	0.49	0.08	0.07	0.02	99.97
KM9-11-60-3		KM9-11	78.1	51.12	1.00	15.13	9.61	0.41	7.71	10.80	3.18	0.56	0.19	0.05	0.05	99.80
KM9-11-62-1-1		KM9-11	78.8	49.06	1.08	16.15	10.70	0.14	8.53	9.58	3.08	0.42	0.28	0.13	0.05	99.20
KM9-11-63-1-1		KM9-11	78.4	51.78	0.93	16.12	10.02	0.29	8.10	9.32	3.19	0.65	0.17	0.11	0.05	100.73
KM9-11-65-1-1		KM9-11	78.5	49.64	0.95	16.17	10.89	0.24	8.57	9.49	2.92	0.44	0.22	0.12	0.05	99.71
KM9-11-66-1a		KM9-11	78.8	49.13	0.98	15.51	10.96	0.25	7.59	8.98	2.44	0.50	0.24	0.23	0.05	96.85
KM9-11-68-1-1a		KM9-11	78.6	50.46	1.09	15.83	10.62	0.19	8.36	8.86	2.52	0.60	0.21	0.13	0.06	98.92
KM9-11-68-2		KM9-11	80.6	47.56	0.98	15.74	8.88	0.26	7.70	8.15	4.17	0.43	0.19	0.10	0.05	94.21
KM9-11-69-1		KM9-11	78.4	50.71	1.05	16.91	9.98	0.14	7.50	9.59	3.50	0.45	0.19	0.11	0.05	100.18
KM9-11-71-1-1		KM9-11	78.6	50.73	0.97	15.74	10.47	0.21	8.14	8.90	3.06	0.58	0.24	0.15	0.05	99.23
KM9-11-72-2-2a		KM9-11	78.4	54.51	1.36	16.80	7.76	0.19	5.35	8.05	4.63	0.96	0.49	0.11	0.07	100.28
KM9-11-72-3-3a		KM9-11	78.2	52.64	0.76	18.05	8.20	0.15	6.67	9.51	2.49	0.50	0.04	0.06	0.03	99.10
KM9-11-73-1-1		KM9-11	78.0	49.85	1.04	15.60	10.74	0.12	7.67	8.88	3.14	0.47	0.10	0.25	0.05	97.92
KM9-11-73-2-2		KM9-11	78.8	50.03	1.06	15.39	10.52	0.17	7.81	9.22	2.86	0.47	0.22	0.27	0.05	98.07
KM9-11-75-1-1a		KM9-11	79.3	49.56	1.05	15.05	9.67	0.20	7.73	8.38	0.34	0.59	0.19	0.23	0.06	93.04
KM9-11-75-2-2		KM9-11	79.4	49.14	1.73	15.01	10.27	0.31	7.42	7.71	3.36	0.81	0.07	0.21	0.06	96.08
KM9-11-76-1-1		KM9-11	77.3	48.72	0.94	16.21	9.56	0.12	7.84	9.54	2.64	0.46	0.32	0.31	0.05	96.69
KM9-11-82-1-1		KM9-11	78.7	49.01	0.96	15.94	10.86	0.09	8.04	9.25	2.77	0.52	0.20	0.30	0.05	98.00

Fo-host – magnesium number of olivine-host for the melt inclusions.

Table A-1-2. Compositions of melt inclusions recalculated with Petrolog3 to equilibrium with Ol-host (normalized to100%)

NN	Fo-host	SiO ₂	TiO ₂	Al ₂ O ₃	FeO-t	MnO	MgO	CaO	Na ₂ O	K ₂ O	P ₂ O ₅	H ₂ O	CaO/Al ₂ O ₃	Mg#	FeO-t/ MgO
Naturally quenched melt inclusions in olivines															
KM9-10-29-1	77.9	54.13	1.23	17.50	8.52	0.17	4.67	8.63	4.03	0.81	0.30	2.01	0.49	49.4	1.82
KM9-10-29-2a	77.9	54.07	1.07	17.92	8.75	0.30	4.95	8.49	3.51	0.80	0.14	1.49	0.47	50.2	1.77
KM9-10-32-1	78.3	55.62	1.14	15.92	8.29	0.24	4.71	9.31	3.54	1.02	0.20	1.93	0.58	50.3	1.76
KM9-10-32-2	78.3	51.78	1.21	16.90	10.00	0.23	5.59	10.13	3.41	0.50	0.25	1.43	0.60	49.9	1.79
KM9-10-32-3	78.3	51.79	1.09	17.27	9.42	0.21	5.29	10.81	3.43	0.48	0.21	1.73	0.63	50.0	1.78
KM9-10-34-2	78.3	52.14	1.12	16.30	9.97	0.27	5.54	10.37	3.57	0.55	0.18	2.03	0.64	49.8	1.80
KM9-10-35-1a	78.0	55.03	0.94	17.10	8.19	0.00	4.59	9.42	3.81	0.86	0.07	1.90	0.55	50.0	1.78
KM9-10-37-1	77.9	52.34	1.19	16.58	10.69	0.15	6.02	8.99	3.28	0.61	0.15	1.35	0.54	50.1	1.78
KM9-10-40-1	78.1	54.33	1.75	16.42	8.59	0.18	4.65	8.70	3.71	1.21	0.46	1.73	0.53	49.1	1.85
KM9-11-42-1	78.0	52.48	1.16	16.19	11.09	0.21	6.54	9.03	2.59	0.52	0.18	1.66	0.56	51.2	1.70
KM9-11-43-1	77.4	51.25	1.10	16.94	10.40	0.20	5.87	10.35	3.14	0.50	0.25	1.71	0.61	50.2	1.77
KM9-11-43-2	77.6	53.07	1.12	17.26	9.71	0.28	5.45	8.62	3.55	0.72	0.23	1.66	0.50	50.0	1.78
KM9-11-48-1	77.8	53.54	1.07	16.47	9.48	0.13	5.21	9.33	3.78	0.91	0.09	1.89	0.57	49.5	1.82
KM9-11-50-1	78.1	51.54	1.29	16.91	10.45	0.11	5.83	9.76	3.32	0.53	0.25	1.89	0.58	49.9	1.79
Re-homogenized melt inclusions															
KM9-10-52-1	78.4	52.57	1.07	20.11	7.42	0.14	4.35	10.75	2.99	0.56	0.04	2.19	0.53	51.1	1.71
KM9-10-53-2	78.2	50.68	1.25	16.89	11.12	0.20	6.27	9.78	2.89	0.67	0.24	2.10	0.58	50.1	1.77
KM9-10-53-3	78.2	51.55	1.20	16.71	10.71	0.14	5.95	9.72	3.37	0.57	0.07	2.11	0.58	49.7	1.80
KM9-10-54-1-1	79.2	53.17	1.08	16.60	8.40	0.26	4.82	11.22	3.11	0.98	0.37	2.16	0.68	50.5	1.74
KM9-10-57-1-1	78.3	51.21	1.16	17.67	10.15	0.26	5.71	9.93	3.19	0.59	0.14	2.36	0.56	50.0	1.78
KM9-10-57-2-1	78.6	54.88	1.05	16.30	7.59	0.15	4.35	11.19	3.39	1.01	0.09	2.05	0.69	50.5	1.74
KM9-10-58-1-1	77.9	52.85	1.03	19.46	7.75	0.18	4.45	10.05	3.42	0.60	0.20	2.15	0.52	50.5	1.74
KM9-10-59-1-1	78.0	52.21	1.21	17.65	9.36	0.09	5.19	9.83	3.58	0.64	0.23	2.28	0.56	49.7	1.80
KM9-10-59-2-2	78.0	52.46	1.11	17.20	9.70	0.25	5.56	9.37	3.18	0.72	0.45	2.57	0.55	50.5	1.75
KM9-10-59-3-3	78.4	52.18	1.12	17.28	9.73	0.16	5.44	9.56	3.56	0.61	0.37	2.15	0.55	49.9	1.79
KM9-10-59-4-4a	78.8	54.83	1.06	16.74	8.97	0.11	4.91	7.87	3.96	1.14	0.41	2.46	0.47	49.4	1.82
KM9-11-60-1-1	78.5	53.21	0.70	19.37	7.59	0.24	4.54	10.87	2.94	0.50	0.04	2.12	0.56	51.6	1.67
KM9-11-60-2-1	78.4	53.47	0.83	19.91	7.71	0.09	4.56	9.80	3.03	0.52	0.08	2.12	0.49	51.3	1.69
KM9-11-60-3	78.1	52.18	1.08	16.33	9.04	0.42	5.08	11.64	3.44	0.60	0.20	2.15	0.71	50.0	1.78

Table A-1-2. Continued

NN	Fo-host	SiO ₂	TiO ₂	Al ₂ O ₃	FeO-t	MnO	MgO	CaO	Na ₂ O	K ₂ O	P ₂ O ₅	H ₂ O	CaO/Al ₂ O ₃	Mg#	FeO-t/ MgO
KM9-11-62-1-1	78.8	50.44	1.18	17.73	10.22	0.14	5.66	10.50	3.38	0.46	0.30	2.72	0.59	49.7	1.80
KM9-11-63-1-1	78.4	52.47	1.00	17.33	9.35	0.29	5.28	9.99	3.42	0.70	0.18	2.16	0.58	50.1	1.77
KM9-11-65-1-1	78.5	50.74	1.03	17.57	10.38	0.23	5.86	10.28	3.18	0.49	0.24	2.82	0.59	50.1	1.77
KM9-11-66-1a	78.8	51.38	1.06	16.75	11.03	0.25	6.43	9.68	2.63	0.53	0.26	2.20	0.58	51.0	1.71
KM9-11-68-1-1a	78.6	52.01	1.19	17.24	10.20	0.18	5.92	9.64	2.75	0.65	0.23	2.26	0.56	50.8	1.72
KM9-11-68-2	80.6	51.72	1.15	18.49	8.71	0.27	4.51	9.54	4.90	0.50	0.22	2.21	0.52	48.0	1.93
KM9-11-69-1	78.4	51.46	1.12	18.03	9.45	0.13	5.19	10.20	3.73	0.48	0.20	1.82	0.57	49.5	1.82
KM9-11-71-1-1	78.6	52.13	1.04	17.08	10.02	0.20	5.68	9.63	3.32	0.62	0.27	2.37	0.56	50.2	1.77
KM9-11-72-2-2a	78.4	55.10	1.42	17.49	7.30	0.19	3.81	8.37	4.81	1.00	0.51	2.09	0.48	48.2	1.92
KM9-11-72-3-3a	78.2	53.98	0.82	19.29	7.71	0.14	4.68	10.15	2.66	0.53	0.04	2.12	0.53	51.9	1.65
KM9-11-73-1-1	78.0	51.74	1.12	16.90	10.57	0.12	5.91	9.60	3.40	0.51	0.11	2.33	0.57	49.9	1.79
KM9-11-73-2-2	78.8	51.94	1.15	16.73	10.28	0.16	5.86	10.01	3.11	0.50	0.25	2.13	0.60	50.4	1.75
KM9-11-75-1-1a	79.3	54.14	1.19	17.03	10.00	0.20	6.70	9.47	0.39	0.66	0.21	2.32	0.56	54.4	1.49
KM9-11-75-2-2	79.4	52.09	1.93	16.72	10.22	0.33	5.43	8.58	3.73	0.90	0.09	2.57	0.51	48.6	1.88
KM9-11-76-1-1	77.3	51.48	1.05	18.18	9.30	0.11	5.36	10.68	2.96	0.51	0.36	2.28	0.59	50.7	1.73
KM9-11-82-1-1	78.7	50.90	1.05	17.40	10.65	0.08	6.03	10.08	3.03	0.57	0.22	2.46	0.58	50.2	1.77

Compositions of melt inclusions were recalculated using the software for crystallization modeling Petrolog3 (Danyushevsky&Plechov, 2011). Not-heated (naturally quenched) inclusions were recalculated using option „Reverse crystallization“, whereas re-heated inclusions with option “Fractional crystallization”. In both cases calculation conditions were set as pressure equal to 100 MPa, oxygen fugacity on the level of QFM+1. Fo-number of the host-olivine was used as a parameter for stop calculations; model of Danyushevsky (2001) was applied for olivine (Chapter I, paragraph 3.1.3).

Table A-1-3. Volatiles in melt inclusions

	H ₂ O (wt.%) SIMS, Yaroslavl	S ⁶⁺ /S-total XANES	d QFM Jugo et al., 2010	H ₂ O (wt.%) Ion Probe Nancy	CO ₂ (ppm)
Naturally quenched melt inclusions in olivines					
KM9-10-29-1	2.04				
KM9-10-29-2a	1.55	0.49	1.04		
KM9-10-32-2	1.52	1.11	2.00		
KM9-10-32-3	1.78	1.11	2.00		
KM9-10-34-2	2.15	1.11	2.00		
KM9-10-37-1	1.45				
KM9-10-40-1	1.76	0.38	0.94		
KM9-11-42-1	1.80				
KM9-11-43-1	1.79	0.61	1.15		
KM9-11-43-2	1.74	0.73	1.27		
Re-homogenized melt inclusions					
KM9-10-52-1					
KM9-10-53-2					
KM9-10-53-3					
KM9-10-54-1-1				2.0	178
KM9-10-57-1-1				2.2	b.d.
KM9-10-57-2-1				1.9	b.d.
KM9-10-59-1-1				2.1	b.d.
KM9-10-59-2-2				2.4	b.d.
KM9-10-59-4-4a				2.3	b.d.
KM9-11-62-1-1				2.5	b.d.
KM9-11-63-1-1				2.0	b.d.
KM9-11-65-1-1				2.6	
KM9-11-66-1a				2.1	b.d.
KM9-11-68-1-1a				2.1	b.d.
KM9-11-69-1				1.7	102
KM9-11-71-1-1				2.2	
KM9-11-73-2-2					
KM9-11-75-1-1a				2.2	b.d.
KM9-11-75-2-2				2.4	b.d.
KM9-11-76-1-1				2.1	b.d.
KM9-11-82-1-1				2.3	
KM9-11-86-1b				2.27	51
KM9-11-88-1a				2.44	b.d.
KM9-11-88-1b				2.73	b.d.
KM9-11-89-1b				2.66	181
KM9-11-89-1				2.46	52
KM9-11-111-1b				2.63	b.d.
KM9-11-113				2.06	22
KM9-11-117-1-nh				2.34	b.d.

For description of applied methods see Chapter I, paragraph 2.4.

Table A-1-4. Experimental conditions of phase relations experiments

Experiments performed at 300 MPa

N	T, C	Dur (h)	X H ₂ O ini	H ₂ O in glass	a H ₂ O Burnham	a H ₂ O fluid	lg fO ₂ Burnham	Fe ²⁺ /Fe-tot K&C	Phase proportions											Kd (Fe ²⁺ -Mg) Ol-L					
									Ol	Cpx	Opx	Pl	Mt	Am	Gl	Bulk	R ²								
N72-Cr3-6	1000	48	1.00	7.6	1.2	0.93	-7.2	0.51			Cpx	9.0			Mt	3.8	Am	3.2	Gl	84.2	100.1	0.08			
N72-Cr3-7	1000	48	0.95	0.0		0.65					Cpx	17.7	Opx	16.7	Pl	61.7	Mt	5.6				101.7	2.29		
N72-Cr3-8	1000	48	0.83	0.0		0.42					Cpx	17.9	Opx	16.7	Pl	61.0	Mt	5.6				101.2	1.41		
N72-Cr3-9	1000	48	0.74	0.0		0.25																			
N72-Cr3-10	1000	48	0.00	0.0		0.07																			
N72-Cr3-11	1050	72	1.00	7.2	1.2	0.98	-6.49	0.52							Mt	1.4			Gl	98.8	100.2	0.38			
N72-Cr3-12	1050	72	0.95	5.9	1.0	0.91	-6.67	0.55							Mt	1.6			Gl	98.2	99.7	0.52			
N72-Cr3-13	1050	72	0.87	4.8	0.8	0.56	-7.99	0.69			Cpx	8.5		Pl	5.1	Mt	2.0		Gl	84.3	99.9	0.37			
N72-Cr3-14	1050	72	0.73	2.2	0.3	0.36	-7.82	0.67											Gl	62.6	100.3	0.22	0.3		
N72-Cr3-16	1100	3	1.00	6.9	1.2	1.00	-5.85	0.54																	
N72-Cr3-17	1100	3	0.96	6.0	1.0	0.82	-5.97	0.55																	
N72-Cr3-18	1100	3	0.84	4.6	0.8	0.60	-6.23	0.58																	
N72-Cr3-19	1100	3	0.72	3.6	0.6	0.36	-6.49	0.61						Pl	1.7				Gl	97.8	99.5	0.46			
N72-Cr3-1	1150	3	1.00	6.8	1.2	1	-5.23	0.55																	
N72-Cr3-2	1150	3	0.95	5.9	1.0	0.87	-5.36	0.57																	
N72-Cr3-3	1150	3	0.85	4.4	0.7	0.63	-5.64	0.6																	
N72-Cr3-4	1150	3	0.71	3.3	0.5	0.38	-5.98	0.63																	
N72-Cr3-5	1150	3	0.00	0.27		0.13									Ol	2.8			Pl	26.6		Gl	70.8	100.2	0.25
N72-Cr3-23	1200	2	1.00	7.1	1.3	1.00	-4.6	0.55																	
N72-Cr3-24	1200	2	0.95	5.6	1.0	0.90	-4.83	0.58																	
N72-Cr3-25	1200	2	0.84	4.4	0.7	0.59	-5.07	0.6																	
N72-Cr3-26	1200	2	0.72	3.2	0.5	0.47	-5.42	0.64																	
N72-Cr3-27	1200	2	0.00	0.90	0.1	0.02	-7.19	0.79																	
N72-Cr3-28	950	168	1.00	6.48	1.0	1.00	-8.14	0.52			Cpx	6.5		Pl	19.2	Mt	4.8	Am	25.9	Gl	43.6	99.9	0.16		
N72-Cr3-29	950	168	0.88	6.00		0.82							Opx	21.2	Pl	57.3	Mt	4.8	Am	19.7		103.1	4.17		
N72-Cr3-30	950	168	0.90	5.75	0.9	0.76	-8.25	0.53					Opx	-6.1	Pl	21.0	Mt	4.3	Am	44.3	Gl	37.2	100.8	0.64	
N72-Cr3-31	950	168	0.76	5.00		0.47							Opx	24.1	Pl	59.7	Mt	4.8	Am	13.8		102.4	4.03		
N72-Cr3-32	950	168	0.00	0.00	0.0	0.21																			

Table A-1-4. Continued (experiments at 300 MPa)									Phase proportions															
N	T, C	Dur (h)	X H ₂ O ini	H ₂ O in glass	a H ₂ O Burnham	a H ₂ O fluid	lg fO ₂ Burnham	Fe ²⁺ /Fe-tot K&C	Ol	Cpx	Opx	Pl	Mt	Amph	Gl	Bulk	R ²	Kd (Fe ²⁺ -Mg) Ol-L						
N72-Cr3-33	1150	15	0.00	0.73	0.1	0.10	-8.04	0.81	Ol	5.4	Cpx	-1.0			Pl	21.4			Gl	73.9	99.7	0.53	0.3	
N72-Cr3-34	1150	15	0.00	0.76	0.1	0.69	-7.98	0.81	Ol	6.1	Cpx	-3.7			Pl	23.5			Gl	73.7	99.6	0.59	0.3	
N72-Cr3-35	1150	15	0.61	1.45	0.2	0.55	-7.04	0.73							Pl	7.9			Gl	91.3	99.2	0.83		
N72-Cr3-36	1150	15	0.45	1.47	0.2	0.35	-7.01	0.73							Pl	7.9			Gl	91.4	99.3	0.61		
N72-Cr3-38	1050	23	0.00	0.00																				
N72-Cr3-39	1050	23	0.00	0.00							Cpx	34.8			Pl	62.0	Mt	4.9				101.7	2.00	
N72-Cr3-40	1050	23	0.55	0.96	0.1	0.14	-8.98	0.77			Cpx	12.4	Opx	9.4	Pl	29.1	Mt	3.5	Gl	46.0	100.4	0.26		
N72-Cr3-41	1050	23	0.35	0.00							Cpx	16.4	Opx	15.1	Pl	65.7	Mt	3.8				101.1	0.77	
N72-Cr3-42	1100	15	0.00	0.61	0.0	0.00	-8.95	0.84	Ol	7.1	Cpx	12.0	Opx	-1.2	Pl	36.5			Gl	45.7	100.1	0.09	0.3	
N72-Cr3-43	1100	15	0.00	0.90	0.1	0.00	-8.32	0.79	Ol	4.4	Cpx	15.6			Pl	39.5			Gl	40.1	99.6	0.49	0.4	
N72-Cr3-44	1100	15	0.38	1.30	0.1	0.17	-7.82	0.75	Ol	4.8	Cpx	7.0			Pl	22.2			Gl	65.1	99.2	0.62	0.4	
N72-Cr3-45	1100	15	0.59	2.11	0.3	0.55	-7.14	0.68	Ol	2.1					Pl	10.0			Gl	87.0	99.0	0.68	0.4	
N72-Cr3-47	1125	20	0.00	0.55	0.0	0.74	-8.78	0.84	Ol	6.3	Cpx	8.5	Opx	-2.2	Pl	33.8			Gl	53.8	100.2	0.19	0.4	
N72-Cr3-48	1125	20	0.00	0.44	0.0	0.26	-9.13	0.86	Ol	5.9	Cpx	10.4			Pl	40.5			Gl	43.2	100.1	0.34	0.3	
N72-Cr3-49	1125	20	0.43	1.24	0.1	0.48	-7.56	0.75	Ol	3.2					Pl	18.8	Mt	0.1	Gl	77.9	100.0	0.31	0.3	
N72-Cr3-50	1125	20	0.60	1.86	0.2	0.64	-7	0.7							Pl	7.4	Mt	0.2	Gl	92.5	100.1	0.25		
N72-Cr3-51	1125	20	0.71	2.47	0.3	0.82	-6.63	0.66																
N72-Cr3-52	1075	20	0.00	0.00							Cpx	21.6	Opx	11.4	Pl	62.1	Mt	5.4				100.6	0.55	
N72-Cr3-53	1075	20	0.00	0.00							Cpx	38.6			Pl	58.7	Mt	3.7				101.0	1.10	
N72-Cr3-54	1075	20	0.42	0.00							Cpx	17.7	Opx	19.4	Pl	60.2	Mt	4.4				101.8	2.43	
N72-Cr3-55	1075	20	0.58	0.00					Ol	15.0	Cpx	27.7			Pl	58.8						101.5	6.88	0.3
N72-Cr3-56	1075	20	0.71	2.29	0.3	0.82	-7.37	0.66	Ol	2.8	Cpx	1.9			Pl	9.6	Mt	0.3	Gl	85.6	100.0	0.07	0.3	
N72-Cr3-62	1050	46	0.79	5.05	0.8	0.13	-7.31	0.61																
N72-Cr3-63	1050	46	0.83	5.05	0.9	0.75	-7.3	0.61																
N72-Cr3-64	1050	46	0.81	5.05	0.8	0.66	-7.32	0.62																
N72-Cr3-65	1050	46	0.85	5.05	0.8	0.72	-7.31	0.61																
N72-Cr3-66	1050	46	0.74	4.36	0.7	0.72	-7.46	0.63	Ol	1.6	Cpx	2.4			Pl	3.4			Gl	91.7	99.1	0.84	0.4	
N72-Cr3-68	1025	73	0.81	5.25	0.9	0.70	-7.66	0.61	Ol	1.9	Cpx	5.5			Pl	4.3	Mt	1.5	Gl	87.1	100.3	0.29	0.4	
N72-Cr3-69	1025	73	0.81	5.34	0.9	0.69	-7.64	0.61	Ol	0.8	Cpx	3.2			Pl	3.3	Mt	1.2	Gl	91.8	100.3	0.19	0.4	
N72-Cr3-70	1025	73	0.70	3.44	0.5	0.60	-8.1	0.66	Ol	-0.5	Cpx	0.4			Pl	-0.4	Mt	0.3	Gl	100.3	100.2	0.23	0.5	
N72-Cr3-71	1025	73	0.76	3.77	0.6	0.65	-7.97	0.65	Ol	3.3	Cpx	3.4			Pl	17.5	Mt	0.1	Gl	75.8	100.1	0.11	0.4	
N72-Cr3-72	1075	46	1.00	6.65	1.2	1.00	-6.67	0.59																
N72-Cr3-73	1075	46	0.73	4.39	0.8	0.57	-6.94	0.62																
N72-Cr3-74	1075	46	0.80	4.90	0.8	0.67	-6.98	0.62																
N72-Cr3-75	1075	46	0.67	1.37	0.1	0.64	-8.54	0.77	Ol	1.4	Cpx	-3.4			Pl	1.9			Gl	100.5	100.4	0.45	0.4	

Table A-1-4 (continued). Experimental conditions of phase relations experiments

Experiments performed at 100 MPa

N	T, C	Dur (h)	X H ₂ O ini	H ₂ O in glass.	a H ₂ O Burnham	a H ₂ O fluid	lg fO ₂ Burnham	Fe ²⁺ /Fe-tot (K&C)	Ol	Cpx	Opx	Pl	Mt	Gl	Bulk	R ²	Kd Fe ²⁺ -Mg Ol-L
N72-Cr1-81	1050	73	1.00	3.32	1.0	1.000	-6.39	0.49	Ol 6.6			Pl 21.1	Mt 1.6	Gl 70.7	99.9	0.87	0.4
N72-Cr1-82	1050	73	0.70	1.92	0.4	0.659	-7.08	0.56	Ol 5.5	Cpx 7.2		Pl 23.7	Mt 1.7	Gl 62.5	100.6	0.50	0.5
N72-Cr1-83	1050	73	0.86	2.86	0.8	0.821	-6.56	0.51	Ol 5.1	Cpx 5.9		Pl 22.1	Mt 1.4	Gl 65.8	100.3	0.26	0.4
N72-Cr1-84	1050	73	0.83	2.68	0.7	0.765	-6.63	0.52	Ol 3.4	Cpx 1.5		Pl 14.6	Mt 0.6	Gl 80.0	100.1	0.18	0.5
N72-Cr1-85	1050	73	0.00	0.00	0.0	0.319				Cpx 21.5	Opx 10.8	Pl 63.9	Mt 4.3		100.5	0.44	
N72-Cr1-86	1075	72	0.85	2.87	0.8	0.188	-6.18	0.51	Ol 0.9			Pl 4.8	Mt 0.1	Gl 94.6	100.4	0.44	0.5
N72-Cr1-87	1075	72	0.86	3.10	0.9	0.307	-6.08	0.5	Ol 3.7			Pl 13.0	Mt 0.2	Gl 83.2	100.1	0.42	0.4
N72-Cr1-88	1075	72	0.80	2.37	0.6	0.619	-6.43	0.53	Ol 6.2			Pl 18.8	Mt 1.2	Gl 73.7	99.9	0.90	0.4
N72-Cr1-89	1075	72	0.64	1.55	0.3	0.247	-7	0.6	Ol -1.1	Cpx 2.9		Pl 1.3	Mt 1.1	Gl 95.8	100.1	0.11	0.6
N72-Cr1-90	1100	94	0.82	3.03	0.8	0.74	-5.77	0.51				Pl 1.5		Gl 97.9	99.4	0.73	
N72-Cr1-91	1100	94	0.86	3.23	0.9	0.78	-5.69	0.5									
N72-Cr1-92	1100	94	0.82	2.73	0.7	0.71	-5.88	0.52				Pl 8.0		Gl 91.5	99.5	0.92	
N72-Cr1-93	1100	94	0.58	1.55	0.3	0.73	-6.59	0.59	Ol 5.0			Pl 24.3		Gl 71.3	100.6	0.81	0.4
N72-Cr1-94	1025	70.5								Cpx 20.7	Opx 16.0	Pl 59.9	Mt 5.6		102.1	2.58	
N72-Cr1-95	1025	70.5	0.00														
N72-Cr1-96	1025	70.5															
N72-Cr1-97	1025	70.5								Cpx 21.5	Opx 16.7	Pl 59.2	Mt 4.9		102.3	2.91	
N72-Cr1-98	1025	70.5								Cpx 20.5	Opx 17.7	Pl 59.4	Mt 5.1		102.6	3.60	
N72-Cr1-99	1025	70.5		3.00	0.8		-6.93	0.53	Ol 26.8	Cpx 20.5	Opx -38.8	Pl 10.6	Mt 3.5	Gl 77.8	100.3	0.38	
N72-Cr1-100	1050	67	0.00														
N72-Cr1-101	1050	67								Cpx 19.6	Opx 16.7	Pl 60.4	Mt 5.0		101.6	1.95	
N72-Cr1-102	1050	67		2.94	0.8		-6.56	0.51	Ol 4.2	Cpx 14.0		Pl 26.1	Mt 4.0	Gl 51.7	100.0	0.05	0.4
N72-Cr1-103	1050	67		2.09	0.5		-7.02	0.55		Cpx 16.8	Opx 7.8	Pl 37.1	Mt 5.0	Gl 33.4	100.1	0.08	
N72-Cr1-104	1125	48		1.22	0.2		-6.62	0.64	Ol 2.6			Pl 14.1		Gl 82.0	98.6	1.35	0.4
N72-Cr1-105	1125	48		1.53	0.3		-6.3	0.61	Ol 0.4			Pl 9.9		Gl 88.6	98.8	1.06	0.4
N72-Cr1-106	1125	48		1.77	0.4		-6.11	0.59				Pl 5.2		Gl 94.3	99.5	0.77	
N72-Cr1-107	1125	48		2.49	0.6		-5.67	0.54				Pl 0.6		Gl 98.7	99.3	0.94	
N72-Cr1-108	1125	48															
N72-Cr1-114	1075	49	0.00		0.0					Cpx 17.5	Opx 16.2	Pl 66.2			99.8	2.97	
N72-Cr1-115	1075	49							Ol 6.0	Cpx 35.0		Pl 56.8	Mt 4.3		102.2	2.75	
N72-Cr1-116	1075	49															

Table A-1-4. Continued (experiments at 100 MPa)

N	T, C	Dur (h)	X H ₂ O ini	H ₂ O in glass.	a H ₂ O Burnham	a H ₂ O fluid	lg fO ₂ Burnham	Fe ²⁺ /Fe-tot (K&C)	Ol	Cpx	Opx	Pl	Mt	Gl	Bulk	R ²	Kd Fe ²⁺ -Mg Ol-L
N72-Cr1-117	1075	49		2.17	0.5		-6.52	0.55	Ol 4.8			Pl 18.1	Mt 0.9	Gl 76.2	100.0	0.08	0.4
N72-Cr1-118	1175	46		0.75	0.1		-6.74	0.71				Pl 2.0		Gl 97.1	99.0	1.70	
N72-Cr1-119	1175	46		0.92	0.1		-6.42	0.69				Pl -0.2		Gl 99.6	99.3	1.25	
N72-Cr1-120	1175	46		1.30	0.2		-5.89	0.64									
N72-Cr1-121	1175	46		1.56	0.3		-5.65	0.61									
N72-Cr1-122	1200	34		0.91	0.1		-6.14	0.68									
N72-Cr1-123	1200	34		1.06	0.2		-5.9	0.66									
N72-Cr1-124	1200	34		1.32	0.2		-5.57	0.63									
N72-Cr1-125	1200	34		1.60	0.3		-5.29	0.6									
N72-Cr1-126	1000	71	0	0.00	0.0												
N72-Cr1-127	1000	71		1.50						Cpx 16.1	Opx 13.1	Pl 65.2	Mt 5.9		100.3	0.39	
N72-Cr1-128	1000	71		3.00	0.8		-7.36	0.5		Cpx 17.6	Opx 8.6	Pl 38.4	Mt 6.1	Gl 29.4	100.1	0.10	
N72-Cr1-129	1000	71		3.00	0.8		-7.36	0.5		Cpx 16.2	Opx 8.6	Pl 42.4	Mt 6.1	Gl 26.6	99.9	0.07	

Dur (h) – duration of run (hours)

X H₂Oini – initial fraction of H₂O in the capsule

H₂O in glass (wt.%) – H₂O-content in glass determined by FTIR, or by EMPA if no IR determinations was performed.

aH₂O Burnham – activity of H₂O in run determined using H₂O-content in glass with model of Burnham (1979)

aH₂O fluid – activity of H₂O in run determined from fluid composition using and using activity coefficients after Aranovich and Newton (1999) and molar volumes of pure H₂O after Pitzer Pitzer and Sterner (1994);

lg fO₂ (Burnham) – fO₂ calculated using aH₂O determined with model of Burnham (1979);

Fe²⁺/Fe-tot (K&C) by model of Kress and Carmichael (1991) using aH₂O determined by model of Burnham (1979);

$Kd^{Fe^{2+}-Mg}_{Ol-L} = X^{Fe^{2+}}_{Ol} / X^{Mg}_{Ol} * X^{Fe^{2+}}_L / X^{Mg}_L$ (Ol-olivine, L – melt).

Ol – olivine, CPx – clinopyroxene, Opx – orthopyroxene, Pl – plagioclase, Am – amphibole, Mt – magnetite, Gl – glass.

Table A-1-5. Compositions of experimental glasses**Experiments performed at 300 MPa**

Run	T, C	H ₂ O fin	H ₂ O EMA	H ₂ O MIR	H ₂ O NIR	α H ₂ O Burnham	n	SiO ₂	TiO ₂	Al ₂ O ₃	FeO-t	MnO	MgO	CaO	Na ₂ O	K ₂ O	Total
N72-Cr3-6	1000	7.6	7.30		7.67	1.0	5	49.05 (0.4)	0.82 (0.04)	18.55 (0.24)	6.14 (0.28)	0.2 (0.11)	5.32 (0.09)	9.84 (0.34)	2.5 (0.24)	0.27 (0.02)	92.7 (1.14)
N72-Cr3-11	1050	7.2	6.60		7.16	1.0	5	47.5 (0.28)	0.83 (0.05)	16.96 (0.28)	7.85 (0.28)	0.2 (0.1)	6.46 (0.11)	10.99 (0.18)	2.36 (0.26)	0.25 (0.05)	93.4 (0.37)
N72-Cr3-12	1050	5.9	6.27		6.06	1.0	5	48.06 (0.46)	0.87 (0.03)	17.35 (0.14)	7.79 (0.45)	0.17 (0.06)	6.49 (0.3)	10.41 (0.44)	2.38 (0.13)	0.2 (0.02)	93.73 (0.89)
N72-Cr3-13	1050	4.8	3.76		4.73	0.8	8	49.98 (0.67)	0.94 (0.05)	18.03 (0.18)	8.23 (0.24)	0.15 (0.1)	5.96 (0.18)	9.98 (0.29)	2.67 (0.15)	0.29 (0.05)	96.24 (1.05)
N72-Cr3-14	1050	2.2	5.34		2.08	0.3	8	50.93 (3.22)	1.14 (0.06)	16.74 (0.36)	8.4 (0.32)	0.23 (0.09)	4.93 (0.52)	8.66 (0.73)	3.25 (0.18)	0.38 (0.06)	94.66 (4.1)
N72-Cr3-16	1100	6.9	6.57		6.90	1.0	5	47.46 (0.16)	0.87 (0.06)	16.87 (0.24)	8.56 (0.38)	0.17 (0.1)	6.4 (0.15)	10.48 (0.22)	2.42 (0.1)	0.2 (0.03)	93.43 (0.24)
N72-Cr3-17	1100	6.0	6.87		6.20	1.0	5	47.31 (0.41)	0.86 (0.04)	17.01 (0.33)	8.27 (0.5)	0.17 (0.08)	6.32 (0.09)	10.8 (0.38)	2.16 (0.18)	0.23 (0.03)	93.13 (0.6)
N72-Cr3-18	1100	4.6	5.08		4.68	0.8	5	48.29 (0.55)	0.87 (0.03)	17.13 (0.16)	8.66 (0.48)	0.14 (0.11)	6.56 (0.12)	10.74 (0.16)	2.29 (0.21)	0.24 (0.05)	94.92 (0.83)
N72-Cr3-19	1100	3.6	2.46		3.41	0.6	6	49.4 (0.43)	0.89 (0.06)	17.66 (0.27)	9 (0.33)	0.17 (0.1)	6.72 (0.18)	11.03 (0.38)	2.47 (0.22)	0.23 (0.04)	97.56 (0.81)
N72-Cr3-1	1150	6.8	6.06		6.82	1.0	5	47.37 (0.47)	0.86 (0.03)	17.07 (0.28)	8.87 (0.2)	0.19 (0.09)	6.76 (0.11)	10.32 (0.31)	2.29 (0.15)	0.22 (0.03)	93.94 (0.96)
N72-Cr3-2	1150	5.9	6.44		5.91	1.0	5	47.02 (0.31)	0.86 (0.07)	17 (0.24)	8.87 (0.27)	0.27 (0.06)	6.64 (0.2)	10.55 (0.4)	2.09 (0.19)	0.25 (0.01)	93.56 (0.36)
N72-Cr3-3	1150	4.4	4.74		4.43	0.7	5	48.24 (0.34)	0.86 (0.03)	17.3 (0.2)	8.85 (0.45)	0.19 (0.05)	6.75 (0.29)	10.73 (0.12)	2.11 (0.14)	0.23 (0.04)	95.26 (1.2)
N72-Cr3-4	1150	3.3	3.26		3.26	0.5	5	48.81 (0.15)	0.91 (0.04)	17.45 (0.28)	9.16 (0.43)	0.15 (0.05)	6.94 (0.11)	10.75 (0.14)	2.34 (0.15)	0.21 (0.04)	96.74 (0.34)
N72-Cr3-5	1150	0.27	0.27			0.0	7	50.27 (0.49)	1.23 (0.04)	15.17 (0.19)	11.32 (0.59)	0.24 (0.09)	7.59 (0.29)	10.8 (0.26)	2.35 (0.23)	0.28 (0.03)	99.24 (1.08)
N72-Cr3-23	1200	7.1	6.76		7.12	1.0	7	47.02 (0.27)	0.9 (0.05)	16.99 (0.22)	8.57 (0.35)	0.16 (0.14)	6.56 (0.17)	10.62 (0.24)	2.19 (0.15)	0.24 (0.04)	93.24 (0.68)
N72-Cr3-24	1200	5.6	5.91		5.63	1.0	6	47.51 (0.33)	0.92 (0.04)	17.06 (0.13)	8.91 (0.12)	0.19 (0.1)	6.57 (0.25)	10.43 (0.21)	2.28 (0.12)	0.22 (0.04)	94.09 (0.45)
N72-Cr3-25	1200	4.4	4.85		4.42	0.7	6	47.95 (0.49)	0.89 (0.04)	17.03 (0.12)	8.7 (0.16)	0.17 (0.11)	6.79 (0.18)	11 (0.24)	2.4 (0.12)	0.24 (0.04)	95.16 (0.6)
N72-Cr3-26	1200	3.2	3.64		3.25	0.5	7	48.58 (0.45)	0.9 (0.05)	17.4 (0.38)	9.06 (0.51)	0.16 (0.04)	6.85 (0.18)	10.94 (0.26)	2.23 (0.14)	0.23 (0.01)	96.36 (0.81)
N72-Cr3-27	1200	0.90	-0.34	0.89	1.20	0.1	7	50.98 (0.42)	0.93 (0.04)	18.36 (0.33)	8.34 (0.36)	0.16 (0.11)	7.23 (0.17)	11.53 (0.41)	2.57 (0.21)	0.26 (0.03)	100.34 (0.58)
N72-Cr3-28	950	6.48	6.48			1.0	5	57.26 (0.3)	0.66 (0.03)	17.47 (0.26)	4.62 (0.3)	0.21 (0.15)	2.96 (0.22)	7.01 (0.16)	2.9 (0.06)	0.42 (0.04)	93.52 (0.54)
N72-Cr3-30	950	5.75	5.75			0.9	4	59.41 (0.73)	0.68 (0.03)	16.82 (0.28)	4.34 (0.34)	0.21 (0.12)	2.55 (0.06)	6.37 (0.38)	3.37 (0.39)	0.5 (0.05)	94.25 (0.4)
N72-Cr3-33	1150	0.73	1.76	0.73		0.1	5	50.35 (0.29)	1.25 (0.1)	15.85 (0.87)	10.55 (0.48)	0.18 (0.1)	6.41 (0.41)	10.9 (0.3)	2.44 (0.16)	0.31 (0.03)	98.24 (0.72)
N72-Cr3-34	1150	0.76	2.26	0.76		0.1	6	50.43 (0.39)	1.24 (0.04)	15.01 (0.24)	10.56 (0.24)	0.22 (0.12)	6.64 (0.19)	10.94 (0.36)	2.37 (0.3)	0.34 (0.03)	97.74 (0.64)
N72-Cr3-35	1150	1.45	3.61	1.45	2.08	0.2	7	49.18 (0.4)	0.95 (0.04)	16.4 (0.21)	9.08 (0.33)	0.16 (0.09)	7.38 (0.3)	10.63 (0.41)	2.36 (0.14)	0.26 (0.03)	96.39 (0.88)
N72-Cr3-36	1150	1.47	3.22	1.47	2.03	0.2	9	49.37 (0.39)	0.95 (0.05)	16.48 (0.13)	9.32 (0.43)	0.17 (0.08)	7.37 (0.29)	10.59 (0.32)	2.25 (0.18)	0.27 (0.05)	96.78 (0.59)
N72-Cr3-40	1050	0.96	4.51	0.96		0.07	3	50.99 (0.57)	1.17 (0.23)	17.28 (1.84)	8.3 (0.92)	0.23 (0.06)	4.74 (1.23)	9.39 (0.88)	2.95 (0.15)	0.45 (0.05)	95.49 (0.23)
N72-Cr3-42	1100	0.61	3.36	0.61		0.0	1	49.53 (0)	1.79 (0)	15.43 (0)	12.23 (0)	0.21 (0)	5.27 (0)	9.51 (0)	2.24 (0)	0.43 (0)	96.64 (0)
N72-Cr3-43	1100	0.90	3.80	0.89		0.07	1	49.11 (0)	1.97 (0)	14.48 (0)	12.81 (0)	0.31 (0)	5.52 (0)	9.2 (0)	2.28 (0)	0.52 (0)	96.2 (0)
N72-Cr3-44	1100	1.30	2.92	1.30	1.48	0.1	3	50.25 (0.26)	1.23 (0.04)	16.71 (1.19)	10.46 (0.81)	0.17 (0.04)	5.66 (0.33)	9.91 (0.5)	2.42 (0.25)	0.27 (0.06)	97.08 (0.61)
N72-Cr3-45	1100	2.11	2.30	2.11	2.55	0.3	3	50.26 (0.7)	0.98 (0.11)	16.81 (0.25)	9.47 (0.33)	0.25 (0.15)	6.78 (0.18)	10.79 (0.31)	2.13 (0.12)	0.23 (0.03)	97.7 (0.75)
N72-Cr3-47	1125	0.55	0.45	0.55		0.0	5	50.53 (0.55)	1.56 (0.22)	15.01 (1.39)	12.51 (1.15)	0.32 (0.15)	6.62 (1.35)	10.39 (0.65)	2.24 (0.2)	0.37 (0.06)	99.55 (0.93)

Table A-1-5 continued

Run	T, C	H ₂ O fin	H ₂ O EMA	H ₂ O MIR	H ₂ O NIR	aH ₂ O Burnham	n	SiO ₂	TiO ₂	Al ₂ O ₃	FeO-t	MnO	MgO	CaO	Na ₂ O	K ₂ O	Total
							4										
N72-Cr3-48	1125	0.44	1.19	0.44		0.0	5	50.46 (0.52)	1.82 (0.09)	14.33 (0.52)	13.21 (0.41)	0.21 (0.02)	5.99 (0.28)	9.78 (0.25)	2.54 (0.17)	0.46 (0.01)	98.81 (0.8)
N72-Cr3-49	1125	1.24	1.73	1.24		0.1	6	50.15 (0.53)	1.11 (0.04)	16.02 (0.4)	10.72 (0.46)	0.15 (0.09)	6.84 (0.14)	10.45 (0.19)	2.51 (0.11)	0.32 (0.03)	98.27 (0.59)
N72-Cr3-50	1125	1.86	1.16	1.86		0.2	7	49.93 (0.37)	0.97 (0.03)	17.05 (0.16)	9.79 (0.27)	0.2 (0.13)	7.38 (0.24)	10.71 (0.15)	2.53 (0.14)	0.26 (0.04)	98.84 (0.67)
N72-Cr3-51	1125	2.47	2.93	2.47		0.3	7	48.94 (0.43)	0.89 (0.04)	17.71 (0.18)	8.76 (0.29)	0.2 (0.11)	6.76 (0.13)	11.15 (0.23)	2.43 (0.21)	0.23 (0.03)	97.07 (0.79)
N72-Cr3-56	1075	2.29	3.25	2.29	3.11	0.3	5	49.57 (0.27)	0.97 (0.03)	16.94 (0.18)	9.63 (0.26)	0.17 (0.11)	6.17 (0.15)	10.51 (0.19)	2.54 (0.27)	0.26 (0.03)	96.75 (0.69)
N72-Cr3-62	1050	5.05	3.86		5.05	0.8	5	48.49 (0.38)	0.88 (0.04)	17.61 (0.22)	8.79 (0.54)	0.1 (0.06)	6.75 (0.21)	10.64 (0.4)	2.62 (0.35)	0.24 (0.07)	96.14 (0.93)
N72-Cr3-63	1050	5.05	3.61		5.05	0.9	5	48.47 (0.28)	0.83 (0.04)	17.67 (0.22)	8.95 (0.41)	0.13 (0.11)	6.73 (0.1)	10.79 (0.21)	2.61 (0.12)	0.22 (0.03)	96.39 (0.85)
N72-Cr3-64	1050	5.05	3.54		5.05	0.8	5	50.15 (1.49)	1.03 (0.19)	17.45 (0.3)	9 (0.57)	0.17 (0.09)	5.77 (0.89)	9.75 (0.96)	2.87 (0.31)	0.28 (0.07)	96.46 (0.66)
N72-Cr3-65	1050	5.05	4.00		5.05	0.8	5	48.49 (0.14)	0.88 (0.02)	17.63 (0.35)	8.61 (0.44)	0.26 (0.11)	6.56 (0.22)	10.71 (0.17)	2.63 (0.1)	0.22 (0.01)	96 (0.5)
N72-Cr3-66	1050	4.36	3.34		4.36	0.7	5	49.67 (0.33)	0.93 (0.07)	17.81 (0.35)	8.63 (0.41)	0.11 (0.07)	6.24 (0.31)	10.58 (0.43)	2.45 (0.15)	0.26 (0.04)	96.66 (0.73)
N72-Cr3-68	1025	5.25	4.41		5.25	0.9	5	49.19 (0.55)	0.92 (0.04)	17.98 (0.18)	8.19 (0.43)	0.13 (0.05)	5.75 (0.05)	10.36 (0.24)	2.8 (0.22)	0.26 (0.05)	95.59 (0.92)
N72-Cr3-69	1025	5.34	5.62		5.34	0.9	3	48.13 (1.32)	0.89 (0.07)	17.38 (0.59)	8.33 (0.45)	0.2 (0.11)	6.25 (0.43)	10.43 (0.26)	2.54 (0.37)	0.24 (0.03)	94.38 (1.42)
N72-Cr3-70	1025	3.44	3.20		3.44	0.5	5	48.62 (0.04)	0.89 (0.09)	17.75 (0.03)	8.86 (0.33)	0.1 (0.06)	6.89 (0.15)	11.01 (0.32)	2.47 (0.13)	0.21 (0.04)	96.8 (0.28)
N72-Cr3-72	1075	6.65	3.73		6.65	1.0	5	48.4 (0.74)	0.84 (0.04)	17.79 (0.39)	8.86 (0.43)	0.23 (0.11)	6.95 (0.32)	10.67 (0.35)	2.36 (0.21)	0.21 (0.03)	96.27 (1.76)
N72-Cr3-73	1075	4.39	3.20		4.39	0.8	5	48.48 (0.47)	0.85 (0.07)	17.75 (0.15)	8.9 (0.28)	0.15 (0.07)	6.94 (0.09)	10.92 (0.2)	2.52 (0.06)	0.28 (0.06)	96.8 (0.4)
N72-Cr3-74	1075	4.90	3.29		4.90	0.8	5	49.69 (0.71)	0.95 (0.1)	17.69 (0.17)	9.15 (0.2)	0.14 (0.06)	5.97 (0.82)	9.96 (0.81)	2.89 (0.31)	0.26 (0.06)	96.71 (0.8)
N72-Cr3-75	1075	1.37	5.14		1.37	0.13	4	47.86 (1.28)	0.87 (0.04)	16.89 (0.64)	8.77 (0.61)	0.22 (0.14)	6.62 (0.28)	11.14 (0.47)	2.59 (0.28)	0.24 (0.02)	94.86 (2.98)

H₂O [wt%] fin – H₂O-content in glass used for calculations and discussion;

H₂O (wt.%) EMA – H₂O-content in glass determined with „by-difference“ method from EMPA analyses;

H₂O (wt.%) MIR – H₂O-content in glass determined with MIR-spectroscopy;

H₂O (wt.%) NIR - H₂O-content in glass determined with NIR-spectroscopy;

aH₂O Burnham – activity of H₂O in run determined using H₂O-content in glass with model of Burnham (1979);

n – number of analyses;

Numbers in parentheses show standard deviation (1σ) of replicate analyses.

Table A-1-5. Compositions of experimental glasses (continued)

Experiments performed at 100 MPa

Run	T, C	H ₂ O fin	H ₂ O EMA	H ₂ O MIR	H ₂ O NIR	aH ₂ O Burnham	n	SiO ₂	TiO ₂	Al ₂ O ₃	FeO-t	MnO	MgO	CaO	Na ₂ O	K ₂ O	Total
N72-Cr1-81	1050	3.32	2.41		3.32	1.0	5	52.49 (2.01)	1.2 (0.18)	15.91 (0.52)	9.47 (0.45)	0.14 (0.07)	5.36 (0.54)	9.43 (1.13)	3.26 (0.35)	0.35 (0.09)	97.59 (0.84)
N72-Cr1-82	1050	1.92	1.55		1.92	0.4	3	51.94 (0.52)	1.24 (0.04)	16.46 (0.35)	9.61 (0.44)	0.19 (0.07)	5.48 (0.26)	9.79 (0.39)	3.41 (0.14)	0.33 (0.01)	98.45 (0.63)
N72-Cr1-83	1050	2.86	2.04		2.86	0.8	4	51.78 (0.31)	1.17 (0.1)	16.31 (0.43)	9.71 (0.13)	0.28 (0.07)	5.45 (0.2)	9.8 (0.4)	3.12 (0.14)	0.33 (0.02)	97.96 (0.28)
N72-Cr1-84	1050	2.68	2.85		2.68	0.7	3	50.06 (0.42)	1.03 (0.07)	16.41 (0.2)	9.7 (0.34)	0.17 (0.11)	6.37 (0.07)	10.52 (0.2)	2.67 (0.07)	0.28 (0.06)	97.15 (0.87)
N72-Cr1-86	1075	2.87	-0.10		2.87	0.8	5	50.47 (0.24)	0.94 (0.06)	17.79 (1.06)	9.62 (0.3)	0.31 (0.09)	6.99 (0.51)	10.96 (0.44)	2.79 (0.15)	0.25 (0.05)	100.1 (1.86)
N72-Cr1-87	1075	3.10	1.48		3.10	0.9	4	50.78 (0.85)	1.03 (0.06)	16.63 (0.27)	10.11 (0.74)	0.23 (0.09)	6.27 (0.19)	10.34 (0.27)	2.87 (0.25)	0.27 (0.03)	98.52 (1.13)
N72-Cr1-88	1075	2.37	1.75		2.37	0.6	5	51.93 (0.38)	1.19 (0.08)	16.33 (0.42)	9.69 (0.34)	0.23 (0.09)	5.46 (0.23)	9.75 (0.28)	2.99 (0.12)	0.33 (0.02)	98.25 (0.55)
N72-Cr1-89	1075	1.55	1.50	1.22	1.55	0.3	3	49.88 (0.62)	0.89 (0.06)	18.18 (0.43)	8.72 (0.19)	0.1 (0.11)	7.09 (0.11)	10.92 (0.45)	2.44 (0.14)	0.29 (0.04)	98.5 (1.51)
N72-Cr1-90	1100	3.03	1.62		3.03	0.8	5	50.03 (0.52)	0.91 (0.02)	17.77 (0.18)	8.89 (0.28)	0.16 (0.07)	6.87 (0.2)	10.89 (0.23)	2.64 (0.24)	0.21 (0.04)	98.38 (0.97)
N72-Cr1-91	1100	3.23	1.34		3.23	0.9	5	49.68 (0.33)	0.92 (0.1)	18.11 (0.34)	8.88 (0.54)	0.15 (0.05)	7.05 (0.18)	11.04 (0.16)	2.58 (0.14)	0.25 (0.02)	98.66 (0.81)
N72-Cr1-92	1100	2.73	0.66		2.73	0.7	5	50.81 (1.51)	1.11 (0.16)	16.66 (1.28)	9.92 (0.72)	0.17 (0.19)	6.77 (0.34)	10.81 (0.53)	2.79 (0.28)	0.32 (0.06)	99.34 (1.55)
N72-Cr1-93	1100	1.55	-0.73	1.16	1.55	0.3	4	51.83 (0.16)	1.73 (0.34)	14.46 (0.89)	11.34 (1.17)	0.21 (0.09)	6.95 (0.21)	11.21 (0.4)	2.78 (0.25)	0.23 (0.06)	100.73 (0.71)
N72-Cr1-99	1025	2.50	4.57			0.6	3	55.53 (0.24)	1.21 (0.1)	17.98 (0.05)	6.34 (0.09)	0.19 (0.08)	3.96 (0.06)	7.43 (0.34)	2.26 (0.01)	0.52 (0.03)	95.43 (0.44)
N72-Cr1-102	1050	2.94	2.94			0.8	3	55.13 (0.43)	1.22 (0.05)	16.63 (0.78)	7.35 (0.48)	0.15 (0.03)	4.44 (0.24)	8.46 (0.56)	3.22 (0.22)	0.46 (0.04)	97.06 (0.23)
N72-Cr1-103	1050	2.09	2.09			0.5	3	55.43 (0.59)	1.3 (0.06)	17.81 (0.18)	6.8 (0.35)	0.26 (0.08)	3.48 (0.08)	8.72 (0.36)	3.42 (0.53)	0.69 (0.02)	97.91 (0.6)
N72-Cr1-104	1125	1.22	2.39		1.22	0.21	3	50.94 (0.7)	1.07 (0.05)	16.03 (0.07)	9.09 (0.71)	0.24 (0.15)	7 (0.13)	10.53 (0.18)	2.38 (0.33)	0.34 (0.08)	97.61 (0.88)
N72-Cr1-105	1125	1.53	0.99		1.53	0.3	3	51.09 (0.21)	1.04 (0.04)	16.64 (0.39)	9.17 (0.02)	0.14 (0.11)	7.57 (0.31)	10.78 (0.26)	2.32 (0.15)	0.26 (0.02)	99.01 (0.89)
N72-Cr1-106	1125	1.77	1.40		1.77	0.4	5	50.21 (0.4)	0.97 (0.06)	17.23 (0.18)	9.06 (0.43)	0.17 (0.08)	7.59 (0.03)	10.74 (0.21)	2.39 (0.18)	0.25 (0.03)	98.6 (0.87)
N72-Cr1-107	1125	2.49	2.37		2.49	0.6	5	49.65 (0.29)	0.9 (0.04)	17.81 (0.3)	8.45 (0.19)	0.16 (0.11)	7.15 (0.16)	10.88 (0.23)	2.38 (0.19)	0.26 (0.03)	97.63 (0.92)
N72-Cr1-117	1075	2.17	3.06		2.17	0.5	4	50.69 (0.15)	1.11 (0.05)	15.88 (0.14)	9.6 (0.56)	0.12 (0.04)	5.98 (0.08)	10.63 (0.28)	2.61 (0.19)	0.32 (0.05)	96.94 (0.57)
N72-Cr1-118	1175	0.75	-0.46	0.75		0.09	5	51.35 (0.63)	0.93 (0.04)	17.95 (0.25)	8.19 (0.2)	0.17 (0.11)	7.79 (0.11)	11.09 (0.12)	2.72 (0.09)	0.28 (0.02)	100.46 (0.92)
N72-Cr1-119	1175	0.92	-0.20	0.92		0.13	5	50.92 (0.97)	0.93 (0.06)	18.37 (0.08)	8.38 (0.63)	0.17 (0.03)	7.56 (0.2)	11.17 (0.39)	2.46 (0.2)	0.24 (0.05)	100.2 (1.31)
N72-Cr1-120	1175	1.30	-0.78	1.30		0.2	5	50.88 (0.38)	0.88 (0.03)	18.89 (0.4)	8.92 (0.24)	0.27 (0.07)	7.1 (0.29)	11.13 (0.09)	2.48 (0.19)	0.24 (0.02)	100.78 (0.89)
N72-Cr1-121	1175	1.56	0.49	1.56		0.3	5	50.21 (0.41)	0.85 (0.06)	19.11 (0.26)	8.57 (0.22)	0.16 (0.15)	7.09 (0.19)	10.91 (0.12)	2.4 (0.21)	0.21 (0.04)	99.51 (0.38)
N72-Cr1-122	1200	0.91	-0.32	0.91		0.12	5	51.44 (0.81)	0.9 (0.05)	18.85 (0.41)	7.31 (0.31)	0.16 (0.07)	7.3 (0.44)	11.46 (0.11)	2.66 (0.24)	0.24 (0.04)	100.32 (1.16)
N72-Cr1-123	1200	1.06	0.20	1.06		0.16	5	50.84 (0.4)	0.85 (0.02)	18.7 (0.16)	8.15 (0.13)	0.18 (0.06)	7.09 (0.22)	11.18 (0.28)	2.57 (0.16)	0.24 (0.05)	99.8 (0.81)
N72-Cr1-124	1200	1.32	1.14	1.32		0.24	5	50.13 (0.78)	0.86 (0.05)	18.68 (0.16)	8.34 (0.31)	0.11 (0.1)	6.96 (0.19)	11.21 (0.26)	2.34 (0.18)	0.23 (0.04)	98.86 (1.16)
N72-Cr1-125	1200	1.60	0.59	1.60		0.3	5	50.52 (0.5)	0.84 (0.07)	18.52 (0.39)	8.59 (0.36)	0.18 (0.11)	6.84 (0.14)	11.23 (0.51)	2.45 (0.28)	0.23 (0.05)	99.41 (0.76)
N72-Cr1-128	1000	3.00	3.88			0.8	2	57.54 (0.31)	1.22 (0.14)	16.53 (0.17)	5.46 (0.17)	0.31 (0.02)	3.63 (0.02)	6.59 (0.04)	4.17 (0.33)	0.68 (0)	96.12 (0.73)
N72-Cr1-129	1000	3.00	3.53			0.8	3	58.16 (0.42)	1.21 (0.05)	16.62 (0.14)	5.5 (0.2)	0.19 (0.06)	3.65 (0.18)	6.73 (0.26)	3.82 (0.87)	0.59 (0.05)	96.47 (0.65)

Table A-1-6. Compositions of experimental olivines**Experiments performed at 300 MPa**

Run	T, C	n	SiO ₂	TiO ₂	Al ₂ O ₃	FeO-t	MnO	MgO	CaO	Na ₂ O	K ₂ O	Total	Fo	Kd ^{Fe2+-Mg} Ol-L
N72-Cr3-14	1050	3	39.72 (0.15)	0.02 (0.01)	0.42 (0.66)	15.61 (0.5)	0.33 (0.05)	43.45 (0.82)	0.45 (0.35)	0.06 (0.05)	0.01 (0.01)	100.07 (1.14)	83.2 (0.5)	0.31
N72-Cr3-5	1150	3	39.25 (0.13)	0.04 (0.01)	0.06 (0.02)	17.92 (0.14)	0.57 (0.18)	42.67 (0.19)	0.35 (0.06)	-0.01 (0)	0.01 (0.01)	100.86 (0.28)	80.9 (0.2)	
N72-Cr3-33	1150	3	39.43 (0.19)	0.03 (0.02)	0.08 (0.05)	18.35 (0.12)	0.56 (0.09)	42.06 (0.3)	0.38 (0.03)	0.01 (0.02)	0 (0)	100.91 (0.26)	80.3 (0.2)	0.33
N72-Cr3-34	1150	4	39.47 (0.24)	0.06 (0.01)	0.61 (0.76)	17.93 (0.48)	0.6 (0.09)	41.73 (1.01)	0.64 (0.4)	0.07 (0.06)	0 (0)	101.09 (0.41)	80.6 (0.1)	0.33
N72-Cr3-42	1100	3	38.39 (0.11)	0.05 (0.01)	0.12 (0.07)	23.8 (0.15)	0.37 (0.04)	36.49 (0.28)	0.76 (0.5)	0.04 (0.01)	0 (0.01)	100.02 (0.48)	73.2 (0)	0.33
N72-Cr3-43	1100	2	37.89 (0.13)	0.02 (0.04)	0.03 (0.02)	25.69 (0.13)	0.38 (0.02)	35.88 (0.07)	0.29 (0.02)	0.06 (0.04)	0 (0)	100.21 (0.21)	71.3 (0.1)	0.39
N72-Cr3-44	1100	1	40.31 (0)	0.03 (0)	0.32 (0)	19.37 (0)	0.31 (0)	39.87 (0)	0.42 (0)	0.03 (0)	0.01 (0)	100.65 (0)	78.6 (0)	0.35
N72-Cr3-45	1100	2	40.44 (0.09)	0.01 (0.01)	0.07 (0.03)	15.35 (0.75)	0.26 (0.01)	44.49 (0.31)	0.25 (0.01)	0.03 (0.05)	0.01 (0)	100.92 (0.28)	83.8 (0.8)	0.36
N72-Cr3-47	1125	3	38.37 (0.01)	0.04 (0.18)	0.06 (0.01)	22.14 (0.02)	0.39 (0.01)	38.82 (0.01)	0.35 (0.43)	0.01 (0.15)	0 (0.03)	100.2 (0.33)	75.8 (0.4)	0.36
N72-Cr3-48	1125	5	38.4 (0.08)	0.04 (0.65)	0.42 (0.52)	22.3 (0.89)	0.34 (0.01)	37.09 (0.03)	0.88 (0.73)	0.06 (1.06)	0.01 (0.06)	99.53 (0.38)	74.8 (0.2)	0.32
N72-Cr3-49	1125	5	39.62 (0.01)	0.02 (0.19)	0.06 (0.02)	15.87 (0.04)	0.31 (0)	43.97 (0.02)	0.3 (0.18)	0 (0.17)	0.01 (0.03)	100.19 (0.4)	83.2 (0.1)	0.31
N72-Cr3-55	1075	3	39.01 (0)	0.02 (0.16)	0.04 (0.01)	18.52 (0.03)	0.33 (0)	41.19 (0.01)	0.29 (0.08)	0.03 (0.44)	0 (0.05)	99.45 (0.51)	79.8 (0.2)	
N72-Cr3-56	1075	2	40.02 (0.03)	0.02 (0.11)	0.09 (0.03)	14.74 (0)	0.24 (0.01)	44.17 (0.03)	0.33 (0)	0.02 (0.13)	0.01 (0.04)	99.67 (0.23)	84.2 (0)	0.32
N72-Cr3-66	1050	2	40.35 (0.22)	0.03 (0.01)	0.02 (0)	14.98 (0.02)	0.28 (0.03)	45.98 (0.1)	0.29 (0.05)	0 (0.01)	0.01 (0)	101.95 (0.27)	84.5 (0)	0.37
N72-Cr3-68	1025	2	40.38 (0.19)	0.02 (0.01)	0.02 (0)	15.44 (0.17)	0.25 (0.02)	45.44 (0.32)	0.25 (0.01)	0.03 (0.02)	0 (0)	101.85 (0.32)	84 (0.2)	0.39
N72-Cr3-69	1025	2	40.12 (0.23)	0 (0.02)	0.02 (0.01)	15.7 (0.2)	0.27 (0.03)	45.41 (0.11)	0.23 (0.04)	0.01 (0.01)	0 (0)	101.79 (0.05)	83.8 (0.1)	0.43
N72-Cr3-70	1025	2	39.64 (0.23)	0.02 (0.01)	0.02 (0)	17.94 (0.39)	0.36 (0.05)	43.71 (0.02)	0.24 (0.06)	0.01 (0)	0 (0.01)	101.94 (0.76)	81.3 (0.3)	0.48
N72-Cr3-71	1025	2	40.07 (0.16)	0.02 (0)	0.04 (0.01)	17.23 (0.14)	0.32 (0.02)	44.28 (0.14)	0.27 (0.01)	0.02 (0)	0 (0)	102.28 (0.08)	82.1 (0.2)	0.36
N72-Cr3-75	1075	3	39.64 (0.15)	0.01 (0)	0.05 (0.01)	18.22 (0.37)	0.28 (0.04)	43.32 (0.07)	0.33 (0.02)	0.02 (0.01)	0 (0.01)	101.91 (0.28)	80.9 (0.3)	0.41

n – number of analyses;

Numbers in parentheses show standard deviation (1σ) of replicate analyses;

Fo – proportion of Forsteritic component in olivine (mol.%);

$Kd^{Fe^{2+}-Mg}_{Ol-L} = X^{Fe^{2+}}_{Ol} / X^{Mg}_{Ol} * X^{Fe^{2+}}_L / X^{Mg}_L$ (Ol-olivine, L – melt).

Table A-1-6. Compositions of experimental olivines (continued)

Experiments performed at 100 MPa

Run	T, C	n	SiO ₂	TiO ₂	Al ₂ O ₃	FeO-t	MnO	MgO	CaO	Na ₂ O	K ₂ O	Total	Fo	Kd ^{Fe2+-Mg} Ol-L
N72-Cr1-81	1050	3	39.95 (0.49)	0.02 (0.01)	0.04 (0.01)	14.45 (0.07)	0.26 (0.04)	46.34 (0.34)	0.33 (0.01)	0.02 (0.02)	0.01 (0.01)	101.44 (0.75)	85.1 (0)	0.36
N72-Cr1-82	1050	3	39.45 (0.08)	0.02 (0.02)	0.03 (0.02)	19.29 (0.39)	0.39 (0.05)	42.16 (0.26)	0.32 (0.06)	0.03 (0.02)	0 (0)	101.67 (0.53)	79.6 (0.3)	0.47
N72-Cr1-83	1050	3	40.05 (0.1)	0.01 (0.01)	0.06 (0.02)	16.78 (0.14)	0.36 (0.03)	44.58 (0.17)	0.27 (0.02)	0.02 (0.03)	0 (0.01)	102.16 (0.23)	82.6 (0.1)	0.41
N72-Cr1-84	1050	2	39.74 (0.05)	0.03 (0.01)	0.04 (0.02)	17.29 (0.13)	0.35 (0.01)	44.11 (0.17)	0.35 (0.01)	0.02 (0.01)	0.01 (0.01)	101.93 (0.13)	82 (0.2)	0.50
N72-Cr1-86	1075	2	40.12 (0.21)	0.03 (0.02)	0.15 (0.2)	14.51 (0.11)	0.31 (0.03)	45.94 (0.23)	0.29 (0.09)	0.04 (0.03)	0.02 (0.01)	101.42 (0.25)	84.9 (0)	0.45
N72-Cr1-87	1075	2	40.62 (0.24)	0.02 (0.03)	0.04 (0.03)	13.84 (0.16)	0.23 (0.03)	47.07 (0.13)	0.29 (0.01)	0.02 (0)	0 (0)	102.16 (0.21)	85.8 (0.2)	0.36
N72-Cr1-88	1075	2	40.11 (0.17)	0.02 (0)	0.03 (0.01)	15.54 (0.16)	0.29 (0.04)	45.59 (0.12)	0.31 (0.07)	0.03 (0.03)	0 (0)	101.95 (0.1)	83.9 (0.1)	0.36
N72-Cr1-89	1075	3	38.99 (0.23)	0.02 (0.01)	0.06 (0.07)	19.16 (0.6)	0.36 (0.06)	42.11 (0.15)	0.36 (0.03)	0.03 (0.02)	0 (0)	101.08 (0.84)	79.7 (0.5)	0.62
N72-Cr1-93	1100	2	39.75 (0.15)	0.03 (0.02)	0.24 (0.25)	17.03 (0.29)	0.31 (0.08)	43.55 (0.56)	0.4 (0.16)	0.07 (0.02)	0 (0)	101.42 (0.43)	82 (0.1)	0.41
N72-Cr1-99	1025	3	40.14 (0.3)	0.04 (0.01)	0.7 (1.14)	13.57 (0.47)	0.41 (0.03)	45.04 (1.94)	0.64 (0.72)	0.04 (0.04)	0 (0)	100.57 (0.31)	85.5 (0.1)	
N72-Cr1-102	1050	2	40.04 (0.26)	0.02 (0.01)	0.05 (0.02)	13.88 (0.18)	0.39 (0.05)	46.05 (0.1)	0.25 (0.01)	0.01 (0)	0.01 (0)	100.73 (0.06)	85.5 (0.1)	0.36
N72-Cr1-104	1125	3	39.92 (0.16)	0.04 (0.01)	0.18 (0.17)	15.37 (0.17)	0.22 (0.02)	43.84 (0.67)	0.45 (0.13)	0.06 (0.07)	0.02 (0.01)	100.09 (0.67)	83.6 (0.1)	0.42
N72-Cr1-105	1125	3	39.99 (0.44)	0.04 (0.02)	0.16 (0.12)	14.6 (0.34)	0.27 (0.03)	44.85 (0.53)	0.4 (0.09)	0.02 (0.01)	0.01 (0)	100.33 (0.25)	84.6 (0.1)	0.44
N72-Cr1-109	1100	3	39.44 (0.22)	0.02 (0.01)	0.08 (0.05)	16.81 (0.19)	0.33 (0.02)	42.83 (0.22)	0.37 (0.02)	0.03 (0.02)	0.01 (0.01)	99.92 (0.5)	81.9 (0.1)	
N72-Cr1-110	1100	3	40.14 (0.04)	0.02 (0.01)	0.03 (0.01)	14.62 (0.2)	0.28 (0.03)	45.21 (0.06)	0.32 (0.01)	0.01 (0.02)	0.01 (0.01)	100.64 (0.22)	84.6 (0.2)	
N72-Cr1-111	1100	2	40.45 (0.15)	0.02 (0)	0.07 (0.03)	13.4 (0.04)	0.29 (0.01)	45.87 (0.04)	0.32 (0.04)	0.02 (0.01)	0.02 (0.01)	100.46 (0.09)	85.9 (0)	
N72-Cr1-115	1075	1	38.79 (0)	0.05 (0)	0.17 (0)	21.83 (0)	0.33 (0)	37.5 (0)	0.8 (0)		0.01 (0)	99.46 (0)	75.4 (0)	
N72-Cr1-117	1075	2	40.17 (0.31)	0.03 (0.01)	0.04 (0.01)	14.47 (0.08)	0.34 (0.06)	44.51 (0.43)	0.32 (0.06)	0.01 (0)	0 (0)	99.91 (0.99)	84.6 (0.1)	0.37

Table A-1-7. Compositions of experimental plagioclases**Experiments performed at 300 MPa**

Run	T, C	n	SiO ₂	TiO ₂	Al ₂ O ₃	FeO	MnO	MgO	CaO	Na ₂ O	K ₂ O	Total	An
N72-Cr3-7	1000	3	51.06 (1.92)	0.26 (0.3)	28.27 (3.71)	2.11 (1.35)	0.05 (0.08)	0.69 (0.72)	13.54 (2.42)	2.86 (0.15)	0.17 (0.15)	99.01 (1.59)	72 (4.5)
N72-Cr3-8	1000	6	52.14 (0.48)	0.18 (0.08)	28.71 (0.61)	1.63 (0.29)	0.02 (0.01)	0.62 (0.2)	13.05 (0.32)	3.59 (0.26)	0.16 (0.03)	100.09 (0.63)	66.8 (1.8)
N72-Cr3-13	1050	4	46.11 (0.42)	0.05 (0.04)	32.85 (0.62)	1.28 (0.28)	0.04 (0.03)	0.27 (0.27)	17.64 (0.15)	1.51 (0.23)	0.03 (0.02)	99.77 (0.74)	0 (0)
N72-Cr3-14	1050	3	47.01 (0.22)	0.09 (0.03)	32.07 (0.11)	1.38 (0.2)	0.02 (0.02)	0.33 (0.09)	16.81 (0.4)	1.82 (0.13)	0.04 (0.01)	99.57 (0.42)	83.6 (1.3)
N72-Cr3-19	1100	1	48.13	0.59	23.51	5.4	0.1	3.86	13.61	1.98	0.12	97.3	79.1 (79.1)
N72-Cr3-5	1150	7	50.72 (0.37)	0.21 (0.11)	28.23 (1.59)	1.99 (0.85)	0.05 (0.04)	1.18 (0.69)	14.23 (0.5)	3.12 (0.07)	0.1 (0.02)	99.83 (0.56)	71.6 (0.8)
N72-Cr3-28	950	3	45.68 (0.08)	0.03 (0.01)	33.65 (0.01)	1.05 (0.11)	0.05 (0.04)	0.08 (0.04)	18.03 (0.09)	1.35 (0.05)	0.02 (0.01)	99.93 (0.18)	88.1 (0.4)
N72-Cr3-29	950	3	49.76 (0.52)	0.06 (0.01)	30.9 (0.28)	1.08 (0.16)	0.06 (0.04)	0.18 (0.04)	15.03 (0.39)	3.02 (0.23)	0.07 (0.02)	100.13 (0.22)	73.3 (2)
N72-Cr3-30	950	3	47.82 (0.85)	0.04 (0.01)	32.26 (0.32)	1.13 (0.09)	0.03 (0.02)	0.13 (0.02)	16.52 (0.57)	2.2 (0.24)	0.03 (0)	100.15 (0.31)	80.6 (2.2)
N72-Cr3-31	950	5	50.26 (1.05)	0.12 (0.05)	30.52 (1.28)	1.3 (0.25)	0.05 (0.03)	0.27 (0.17)	14.38 (0.91)	2.98 (0.12)	0.09 (0.05)	99.98 (0.88)	72.7 (1.3)
N72-Cr3-33	1150	3	51.46 (0.8)	0.16 (0.08)	29.44 (1.17)	1.21 (0.31)	0.11 (0.07)	0.41 (0.21)	14.24 (0.44)	3.4 (0.23)	0.09 (0.01)	100.49 (0.15)	69.8 (2)
N72-Cr3-34	1150	4	50.77 (0.3)	0.13 (0)	29.41 (0.32)	1.15 (0.23)	0.05 (0.03)	0.47 (0.12)	14.5 (0.05)	3.23 (0.07)	0.07 (0.01)	99.78 (0.33)	71.3 (0.4)
N72-Cr3-35	1150	3	49.06 (0.79)	0.15 (0.08)	30.35 (0.25)	1.13 (0.3)	0.07 (0.05)	0.54 (0.34)	15.51 (0.34)	2.55 (0.29)	0.05 (0.02)	99.41 (0.09)	77.1 (2.4)
N72-Cr3-36	1150	4	48.34 (0.37)	0.05 (0.01)	31.74 (0.35)	0.89 (0.06)	0.04 (0.03)	0.19 (0.05)	16.24 (0.29)	2.27 (0.14)	0.04 (0.01)	99.8 (0.32)	79.8 (1.2)
N72-Cr3-37	1150	4	51.69 (0.2)	0.52 (0.35)	28.37 (1.21)	1.6 (1)	0.11 (0.06)	0.7 (0.35)	13.52 (0.21)	3.58 (0.13)	0.2 (0.03)	100.29 (0.04)	67.6 (0.5)
N72-Cr3-39	1050	3	52.02 (0.15)	0.38 (0.11)	26.64 (0.73)	2.22 (0.26)	0.13 (0.02)	1.56 (0.32)	12.76 (0.16)	3.62 (0.19)	0.22 (0.02)	99.55 (0.49)	66.1 (0.9)
N72-Cr3-40	1050	4	49.89 (0.58)	0.13 (0.03)	30.03 (0.5)	1.39 (0.17)	0.01 (0.04)	0.21 (0.06)	14.63 (0.46)	3.09 (0.26)	0.07 (0.01)	99.44 (0.39)	72.4 (2.3)
N72-Cr3-41	1050	3	51.64 (0.33)	0.95 (0.06)	25.94 (0.05)	3.86 (0.27)	0.21 (0.06)	1.15 (0.03)	12.47 (0.16)	3.36 (0.07)	0.24 (0.01)	99.83 (0.78)	67.3 (0.6)
N72-Cr3-42	1100	2	50.81 (0.17)	0.21 (0.19)	28.84 (1.39)	1.94 (0.77)	0.04 (0.04)	0.64 (0.29)	13.61 (0.56)	3.38 (0.08)	0.13 (0.05)	99.59 (0.71)	69 (1.4)
N72-Cr3-43	1100	1	50.86	0.09	29.62	1.41	0.04	0.29	13.63	3.47	0.1	99.51	68.5 (0)
N72-Cr3-44	1100	1	51.11	0.1	29.72	1.66	0.04	0.46	14.26 (0)	3.18	0.09	100.63	71.2 (0)
N72-Cr3-45	1100	2	49.36 (0.36)	0.05 (0.01)	31.53 (0.11)	1.17 (0.03)	0 (0.05)	0.24 (0.01)	15.89 (0.01)	2.33 (0.11)	0.05	100.64 (0.21)	79 (0.8)
N72-Cr3-46	1100	1	51.5	0.19	28.47	1.53	0.02	0.95	12.85	3.76	0.27	99.54	65.4 (0)
N72-Cr3-47	1125	5	51.37 (0.16)	0.11 (0.31)	28.78 (0.53)	1.63 (0.34)	0.03 (0.01)	0.73 (0.03)	13.67 (0.31)	3.66 (0.18)	0.11 (0.02)	100.11 (0.2)	67.4 (1.5)
N72-Cr3-48	1125	3	50.83 (0.05)	0.27 (0.34)	28.44 (2.21)	2.19 (0.6)	0.05 (0.05)	0.66 (0.28)	13.66 (1.3)	3.56 (0.64)	0.14 (0.05)	99.83 (0.44)	67.9 (1.3)
N72-Cr3-49	1125	4	49.35 (0.16)	0.07 (0.67)	30.17 (1.51)	1.69 (0.55)	0.02 (0.01)	0.76 (0.02)	15.27 (0.55)	2.82 (0.98)	0.06 (0.02)	100.25 (0.16)	74.9 (1.5)
N72-Cr3-50	1125	3	47.82 (0.23)	0.05 (0.82)	31.71 (0.87)	1.46 (0.53)	0.03 (0.02)	0.32 (0.04)	16.58 (0.25)	2.2 (0.14)	0.04 (0.01)	100.22 (0.1)	80.6 (2.2)
N72-Cr3-52	1075	4	52.93 (1.15)	0.19 (2.97)	27.28 (1.25)	1.84 (1.98)	0.02 (0.11)	0.85 (0.04)	12.31 (0.51)	4.29 (0.51)	0.21 (0.04)	99.91 (0.28)	61.4 (10.1)
N72-Cr3-53	1075	2	51.59 (0.02)	0.2 (0.11)	28.36 (0.15)	1.78 (0.01)	0.01 (0.01)	0.68 (0.05)	13.15 (0.12)	3.89 (0.04)	0.19 (0.01)	99.87 (0.09)	65.2 (0.1)
N72-Cr3-54	1075	4	50.16 (0.1)	0.19 (0.13)	29.27 (1.38)	2.12 (0.41)	0.05 (0.02)	0.66 (0.16)	14.41 (0.93)	3.29 (0.53)	0.09 (0.04)	100.24 (0.15)	70.8 (0.5)
N72-Cr3-55	1075	2	49.94 (0.04)	0.61 (1.24)	4.68 (0.74)	8.32 (0.41)	0.2 (0.01)	15.5 (0.16)	20.29 (0.2)	0.39 (0.47)	0 (0.08)	100.04 (0.35)	76.8 (1)
N72-Cr3-56	1075	2	45.92 (0.23)	0.05 (0.61)	33.2 (0.35)	1.28 (0.38)	0.05 (0.01)	0.18 (0.01)	17.98 (0)	1.47 (0.01)		100.15 (0.08)	87.1 (2)

Table A-1-7 300MPa

Run	T, C	n	SiO ₂	TiO ₂	Al ₂ O ₃	FeO	MnO	MgO	CaO	Na ₂ O	K ₂ O	Total	An
N72-Cr3-66	1050	2	46.12 (0.43)	0.03 (0.01)	34.16 (0.17)	1.27 (0.02)		0.14 (0.03)	17.95 (0.25)	1.44 (0.13)	0.02 (0.01)	101.14 (0.7)	87.3 (0.8)
N72-Cr3-68	1025	2	45.66 (0.4)	0.04 (0.01)	34.17 (0.45)	1.13 (0.05)		0.12 (0.07)	18.22 (0.29)	1.17 (0.17)	0.02 (0.01)	100.52 (0.19)	89.6 (1.5)
N72-Cr3-69	1025	3	46.21 (0.81)	0.03 (0.01)	34.05 (0.64)	1.19 (0.06)	0.03 (0.03)	0.11 (0.03)	17.86 (0.89)	1.46 (0.45)	0.02 (0.01)	100.97 (0.36)	87.1 (4)
N72-Cr3-70	1025	3	46.64 (0.44)	0.1 (0.1)	32.6 (1.37)	1.52 (0.52)	0.01 (0.01)	0.38 (0.38)	17.1 (0.92)	1.68 (0.26)	0.04 (0.02)	100.09 (0.97)	84.9 (2.3)
N72-Cr3-71	1025	3	46.52 (0.71)	0.16 (0.21)	32.02 (2.45)	2.27 (1.72)	0.04 (0.02)	0.75 (0.93)	17 (1.32)	1.53 (0.23)	0.05 (0.04)	100.34 (0.1)	85.9 (2.7)
N72-Cr3-75	1075	2	48.59 (0.12)	0.03 (0.02)	32.16 (0.26)	1.08 (0.19)	0.03 (0.01)	0.22 (0.01)	15.93 (0.1)	2.52 (0.09)	0.04 (0.01)	100.63 (0.09)	77.8 (0.7)

Table A-1-7 (continued). Plagioclases in experiments performed at 100 MPa

Run	T, C	n	SiO ₂	TiO ₂	Al ₂ O ₃	FeO	MnO	MgO	CaO	Na ₂ O	K ₂ O	Total	An
N72-Cr1-81	1050	3	46.07 (0.62)	0.04 (0.02)	33.52 (0.17)	1.33 (0.18)	0.01 (0.01)	0.14 (0.01)	18.14 (0.55)	1.32 (0.26)	0.01 (0)	100.57 (0.44)	88.3 (2.4)
N72-Cr1-82	1050	3	48.71 (0.74)	0.07 (0)	31.79 (0.6)	1.29 (0.08)	0.01 (0.02)	0.17 (0.01)	16.13 (0.75)	2.69 (0.41)	0.04 (0.01)	100.91 (0.33)	76.8 (3.6)
N72-Cr1-83	1050	3	47.7 (1.06)	0.11 (0.08)	31.59 (1.57)	1.74 (0.46)	0.02 (0.01)	0.47 (0.32)	16.46 (1.01)	2.17 (0.47)	0.05 (0.02)	100.32 (0.29)	80.7 (4.3)
N72-Cr1-84	1050	2	51.44 (0.46)	0.53 (0.05)	3.43 (0.6)	7.13 (0.15)	0.29 (0.04)	16.62 (0.03)	21.27 (0.07)	0.31 (0)	0.01 (0)	101.08 (0.33)	80.6 (0.4)
N72-Cr1-85	1050	2	52.02 (0.74)	0.29 (0.16)	27.01 (1.74)	2.43 (1.5)	0.08 (0.05)	1.4 (1.03)	12.92 (0.92)	3.63 (0.03)	0.24 (0.08)	100 (0.9)	66.3 (1.8)
N72-Cr1-86	1075	2	46.26 (0.42)	0.03 (0.01)	33.55 (0.24)	1.3 (0.09)	0.03 (0.02)	0.15 (0.02)	17.79 (0.14)	1.63 (0.2)	0.02 (0)	100.76 (0.28)	85.8 (1.6)
N72-Cr1-87	1075	2	45.69 (0.06)	0.02 (0)	33.92 (0.24)	1.31 (0.01)	0.04 (0.04)	0.14 (0.01)	18.25 (0.16)	1.31 (0.12)	0.02 (0.01)	100.72 (0.27)	88.5 (1)
N72-Cr1-88	1075	2	46.8 (0.02)	0.03 (0.01)	33.62 (0.23)	1.41 (0.01)	0 (0)	0.14 (0)	17.41 (0.07)	1.75 (0.02)	0.03 (0)	101.22 (0.25)	84.6 (0.2)
N72-Cr1-89	1075	2	48.97 (0.26)	0.06 (0.01)	31.93 (0.34)	1.46 (0.01)	0.01 (0.01)	0.2 (0.03)	15.94 (0.28)	2.56 (0.08)	0.04 (0)	101.18 (0.8)	77.5 (0.8)
N72-Cr1-90	1100	2	45.7 (0.04)	0.03 (0.03)	34.1 (0.14)	1.13 (0.01)	0.04 (0.02)	0.15 (0.03)	18.47 (0.23)	1.17 (0.03)	0.02 (0)	100.8 (0.39)	89.7 (0.3)
N72-Cr1-92	1100	3	45.99 (0.33)	0.05 (0.04)	33.54 (0.61)	1.21 (0.18)	0.03 (0.02)	0.25 (0.16)	18.33 (0.41)	1.23 (0.17)	0.02 (0)	100.66 (0.18)	89.1 (1.5)
N72-Cr1-93	1100	2	47.78 (0.13)	0.05 (0.02)	32.36 (0.03)	1.13 (0.09)	0.01 (0.01)	0.22 (0.02)	16.84 (0.01)	2.11 (0.15)	0.04 (0.01)	100.57 (0.41)	81.5 (1.1)
N72-Cr1-94	1025	3	51.08 (0.8)	0.35 (0.15)	30.28 (1.54)	2.21 (0.53)	0.02 (0.02)	0.65 (0.36)	13.48 (0.71)	3.09 (0.22)	0.17 (0.06)	101.34 (0.63)	70.7 (0.6)
N72-Cr1-97	1025	3	51.05 (0.39)	0.27 (0.09)	30.96 (1.61)	2.12 (0.46)	0.06 (0.04)	0.56 (0.28)	13.67 (0.61)	3.1 (0.12)	0.17 (0.08)	101.94 (0.84)	70.8 (1.7)
N72-Cr1-98	1025	3	50.27 (0.74)	0.26 (0.22)	31.37 (2.18)	2.38 (0.95)	0.04 (0.03)	0.67 (0.48)	14.11 (1.25)	2.78 (0.07)	0.14 (0.1)	102.02 (0.98)	73.7 (1.6)
N72-Cr1-99	1025	2	48.25 (0.04)	0.1 (0.06)	34.7 (0.83)	1.4 (0.18)	0.01 (0)	0.3 (0.24)	16.29 (0.3)	2.31 (0.05)	0.06 (0.03)	103.42 (0.64)	79.6 (0)
N72-Cr1-101	1050	2	51.81 (0.45)	0.33 (0.27)	30.56 (2.1)	2.41 (0.88)	0.04 (0.06)	0.66 (0.4)	13.18 (0.71)	3.52 (0.15)	0.23 (0.15)	102.79 (0.78)	67.4 (0.2)
N72-Cr1-102	1050	2	48.41 (0.03)	0.17 (0.11)	33.93 (0.82)	2.01 (0.41)	0.02 (0.01)	0.5 (0.38)	15.79 (0.26)	2.31 (0.22)	0.06 (0.03)	103.25 (0.27)	79.1 (1.3)
N72-Cr1-103	1050	2	50.63 (0.69)	0.22 (0.08)	31.27 (0.64)	2.08 (0.51)	0 (0)	0.54 (0.27)	14.2 (0.22)	3.26 (0.04)	0.12 (0.06)	102.32 (0.79)	70.7 (0.6)
N72-Cr1-104	1125	3	48.75 (1.02)	0.07 (0.03)	31.73 (0.39)	1.26 (0.11)	0 (0)	0.46 (0.1)	15.77 (0.74)	2.48 (0.3)	0.07 (0.02)	100.59 (0.28)	77.9 (2.9)
N72-Cr1-105	1125	3	47.69 (0.23)	0.15 (0.14)	31.66 (1.9)	1.75 (1.06)	0.04 (0.02)	0.94 (0.8)	16.2 (0.64)	2.01 (0.22)	0.08 (0.03)	100.48 (0.51)	81.7 (1.3)
N72-Cr1-106	1125	3	46.69 (0.34)	0.04 (0.01)	34.11 (0.24)	1.02 (0.05)	0.03 (0.02)	0.22 (0.07)	17.52 (0.34)	1.52 (0.2)	0.03 (0)	101.16 (0.11)	86.4 (1.8)
N72-Cr1-107	1125	3	45.59 (0.36)	0.04 (0.01)	34.32 (0.63)	1.03 (0.1)	0.03 (0.03)	0.21 (0.06)	17.84 (0.4)	1.33 (0.15)	0.03 (0.01)	100.41 (0.5)	88.1 (1.4)
N72-Cr1-109	1100	2	50.13 (0.09)	0.06 (0.02)	31.18 (0.22)	1.29 (0.18)	0.01 (0)	0.33 (0)	14.94 (0.04)	2.96 (0.11)	0.06 (0.01)	100.96 (0.17)	73.6 (0.7)
N72-Cr1-110	1100	2	48.8 (0.53)	0.18 (0.18)	31.59 (1.25)	1.74 (0.35)	0.04 (0.03)	0.33 (0.04)	15.81 (0.3)	2.25 (0)	0.07 (0.03)	100.77 (0.48)	79.6 (0.3)

Table A-1-7 continued (100 MPa experiments)

Run	T, C	n	SiO ₂	TiO ₂	Al ₂ O ₃	FeO	MnO	MgO	CaO	Na ₂ O	K ₂ O	Total	An
N72-Cr1-111	1100	1	46.83	0.05	33.46 (0)	1.31	0.04	0.18	17.15	1.73	0.03	100.78	84.6 (0)
N72-Cr1-112	1100	2	46.45 (0.1)	0.03 (0.01)	34.04 (0.17)	1.19 (0.01)	0.03 (0.02)	0.18 (0.03)	17.22 (0.24)	1.53 (0.01)	0.03 (0)	100.69 (0.49)	86.1 (0.3)
N72-Cr1-114	1075	1	51.37	0.33	26.64	3.95	0.05	2.27	12.29	3.48	0.13	100.51	70.7 (0)
N72-Cr1-115	1075	1	51.04	0.09	30.7	1.56	0.04	0.21	14.01	3.45	0.1	101.19	69.2 (0)
N72-Cr1-117	1075	2	46.91 (0.37)	0.14 (0.05)	31.89 (0.8)	2.21 (0.21)	0.02 (0.01)	0.68 (0.25)	16.52 (0.27)	1.77 (0.01)	0.05 (0.02)	100.2 (0.19)	83.7 (0.2)
N72-Cr1-118	1175	3	49.46 (0.85)	0.1 (0.04)	30.61 (1.05)	1.05 (0.25)	0 (0.01)	0.89 (0.45)	15.19 (0.37)	2.72 (0.12)	0.06 (0.01)	100.07 (0.93)	75.5 (1.1)
N72-Cr1-119	1175	3	47.71 (0.64)	0.06 (0.03)	32.92 (1.01)	0.82 (0.1)	0 (0)	0.28 (0.17)	16.21 (0.66)	2.13 (0.38)	0.04 (0.02)	100.17 (1.56)	80.8 (3.4)
N72-Cr1-127	1000	3	52.65 (1.18)	0.41 (0.14)	26.13 (1.01)	2.44 (0.26)	0.07 (0.05)	1.11 (0.29)	12.19 (1.07)	3.34 (0.1)	0.33 (0.13)	98.69 (0.51)	66.8 (2.4)
N72-Cr1-128	1000	3	49.49 (0.14)	0.11 (0.09)	31.12 (1.11)	1.49 (0.18)	0.03 (0.01)	0.29 (0.21)	14.84 (0.56)	2.79 (0.09)	0.06 (0.03)	100.21 (1.03)	74.6 (1.3)
N72-Cr1-129	1000	4	49.33 (0.81)	0.24 (0.11)	29.17 (1.46)	2.04 (0.61)	0.01 (0.01)	0.63 (0.31)	13.99 (0.68)	2.79 (0.19)	0.11 (0.05)	98.32 (2.33)	73.5 (1.3)

n – number of analyses;

Numbers in parentheses show standard deviation (1σ) of replicate analyses;

An – proportion of anorthitic component in plagioclase (mol.%).

Table A-1-8. Compositions of experimental clinopyroxenes**Clinopyroxenes in experiments performed at 300 MPa**

Run	T, C	n	SiO ₂	TiO ₂	Al ₂ O ₃	FeO	MnO	MgO	CaO	Na ₂ O	K ₂ O	Total	Mg#	En	Wo	Fs
N72-Cr3-6	1000	4	48.36 (1.74)	0.79 (0.24)	6.28 (1.34)	6.97 (0.58)	0.13 (0.05)	14.64 (0.88)	22.65 (0.23)	0.23 (0.01)	0 (0)	100.05 (0.24)	78.9 (2.4)	42.0	46.7	11.2
N72-Cr3-7	1000	3	48.96 (0.45)	0.87 (0.16)	5.41 (0.47)	8.23 (0.93)	0.3 (0.04)	15.98 (0.5)	19.31 (1.67)	0.35 (0.02)	0 (0.01)	99.41 (0.29)	77.6 (1.4)	46.4	40.2	13.4
N72-Cr3-8	1000	2	50.62 (0.47)	0.71 (0.1)	3.94 (0.08)	8.03 (0.53)	0.34 (0.04)	15.32 (0.07)	20.1 (0.23)	0.39 (0.06)	0.02 (0)	99.48 (0.36)	77.3 (1.1)	44.7	42.2	13.1
N72-Cr3-13	1050	4	48.78 (0.99)	0.57 (0.1)	5.64 (0.79)	7.14 (0.42)	0.17 (0.05)	15.31 (0.66)	21.91 (0.28)	0.26 (0.02)	0.01 (0.01)	99.78 (0.52)	0 (0)	43.7	44.9	11.4
N72-Cr3-14	1050	3	49.16 (0.16)	0.64 (0.04)	5.43 (0.25)	7.46 (0.14)	0.24 (0.03)	15.56 (0.16)	20.53 (0.6)	0.34 (0.02)	0.01 (0)	99.37 (0.19)	78.8 (0.2)	45.1	42.8	12.1
N72-Cr3-28	950	3	50.19 (1.96)	0.59 (0.28)	4.01 (1.46)	6.66 (1.03)	0.25 (0.03)	15.36 (1.04)	22.13 (0.11)	0.26 (0.04)	0.01 (0.01)	99.46 (0.11)	80.4 (3.5)	43.9	45.4	10.7
N72-Cr3-33	1150	4	51.74 (0.84)	0.85 (0.17)	4.05 (0.87)	8.45 (0.77)	0.49 (0.11)	17.74 (1.46)	17.26 (1.9)	0.25 (0.06)	0.01 (0.01)	100.84 (0.19)	78.9 (0.1)	50.8	35.6	13.6
N72-Cr3-34	1150	4	51.98 (0.61)	0.74 (0.14)	3.38 (0.56)	7.69 (0.81)	0.5 (0.28)	17.89 (1.34)	17.81 (1.9)	0.24 (0.03)	0.01 (0.01)	100.22 (0.64)	80.6 (1)	51.1	36.6	12.3
N72-Cr3-37	1150	4	51.64 (0.59)	1.57 (0.56)	3.66 (1.31)	12.73 (1.19)	0.58 (0.06)	16.52 (1.39)	14.12 (2.17)	0.28 (0.24)	0.06 (0.09)	101.15 (0.32)	69.8 (3.3)	48.9	30.0	21.1
N72-Cr3-39	1050	3	50.81 (0.59)	1.51 (0.24)	4.11 (1.19)	12.57 (0.56)	0.75 (0.09)	16.02 (1.46)	15.04 (2.11)	0.36 (0.1)	0.04 (0.04)	101.21 (0.75)	69.4 (1.3)	47.3	31.9	20.8
N72-Cr3-40	1050	3	50.18 (0.32)	1.18 (0.1)	4.63 (0.36)	8.79 (0.33)	0.63 (0.18)	15.97 (0.32)	19.25 (0.55)	0.34 (0.02)	0.01 (0.01)	100.98 (0.47)	76.4 (0.4)	46.0	39.8	14.2
N72-Cr3-41	1050	3	50.56 (0.6)	1.35 (0.16)	4.31 (0.82)	9.7 (0.33)	0.66 (0.26)	15.34 (0.92)	18.35 (0.07)	0.39 (0.11)	0.06 (0.06)	100.71 (0.39)	73.8 (0.6)	45.2	38.8	16.0
N72-Cr3-42	1100	1	50.94 (0)	0.66 (0)	3.95 (0)	11.35 (0)	0.28 (0)	16.66 (0)	15.71 (0)	0.31 (0)	0.02 (0)	99.9 (0)	72.3 (0)	48.5	32.9	18.6
N72-Cr3-43	1100	1	51.62 (0)	0.51 (0)	2.98 (0)	13.7 (0)	0.37 (0)	19.34 (0)	10.96 (0)	0.23 (0)	0.01 (0)	99.72 (0)	71.6 (0)	55.4	22.6	22.0
N72-Cr3-44	1100	1	50.43 (0)	0.56 (0)	4.63 (0)	9.42 (0)	0.22 (0)	17.14 (0)	17.4 (0)	0.27 (0)	0.02 (0)	100.09 (0)	76.4 (0)	49.1	35.8	15.1
N72-Cr3-46	1100	1	50.82 (0)	1.12 (0)	2.45 (0)	16.48 (0)	0.49 (0)	16.14 (0)	11.33 (0)	0.14 (0)	0.01 (0)	98.98 (0)	63.6 (0)	48.1	24.3	27.6
N72-Cr3-47	1125	3	50.8 (0.79)	0.82 (0.57)	6.28 (3.55)	11.37 (1.28)	0.26 (0.16)	15.51 (0.39)	13.86 (0.85)	0.84 (3.37)	0.13 (0.02)	99.95 (0.9)	70.3 (6.3)	48.7	31.3	20.0
N72-Cr3-48	1125	3	51.04 (0.13)	0.63 (1.08)	3.76 (1.05)	12.09 (4.78)	0.31 (0.02)	18.65 (0.22)	13.03 (1.59)	0.3 (3.39)	0.02 (0.03)	99.91 (0.33)	73.2 (0.9)	53.6	26.9	19.5
N72-Cr3-52	1075	4	51.2 (0.15)	0.85 (0.6)	3.07 (0.67)	11.2 (3.11)	0.29 (0.02)	17.04 (0.17)	16.04 (2.06)	0.35 (1.1)	0.02 (0.02)	100.08 (0.58)	73.2 (2.7)	48.9	33.1	18.0
N72-Cr3-53	1075	2	50.85 (0.01)	0.78 (1.25)	4.3 (1.45)	14.13 (0.56)	0.4 (0.01)	17.91 (0.15)	11.79 (0.64)	0.25 (0.37)	0.02 (0.01)	100.47 (0.12)	69.3 (1.4)	52.2	24.7	23.1
N72-Cr3-54	1075	3	50.31 (0.03)	0.66 (0.65)	4.41 (0.82)	9.41 (0.24)	0.3 (0.03)	15.8 (0.08)	18.08 (0.23)	0.32 (0.85)	0.04 (0.07)	99.37 (0.76)	74.9 (1)	46.4	38.1	15.5
N72-Cr3-55	1075	2	49.94 (0.04)	0.61 (1.24)	4.68 (0.74)	8.32 (0.41)	0.2 (0.01)	15.5 (0.16)	20.29 (0.2)	0.39 (0.47)	0 (0.08)	100.04 (0.35)	76.8 (1)	44.6	42.0	13.4
N72-Cr3-56	1075	2	48.44 (0.01)	0.73 (0.15)	6.23 (0.21)	8.13 (0.35)	0.22 (0)	15.57 (0.09)	19.89 (0.4)	0.33 (0.34)	0.02 (0.04)	99.58 (0.66)	77.3 (1.3)	45.2	41.5	13.2
N72-Cr3-66	1050	2	50.05 (0.76)	0.58 (0.21)	5.51 (1.3)	7.8 (0.46)	0.23 (0.08)	16.39 (0.22)	20.22 (0.75)	0.29 (0.03)	0 (0)	101.16 (0.26)	78.9 (1.2)	46.4	41.2	12.4
N72-Cr3-68	1025	2	49.55 (1.06)	0.62 (0.15)	5.59 (0.9)	7.41 (0.47)	0.1 (0.09)	15.23 (0.89)	22.12 (0.07)	0.3 (0.01)	0.01 (0)	100.99 (0.41)	78.5 (2.1)	43.2	45.1	11.8
N72-Cr3-69	1025	2	50.19 (1.75)	0.54 (0.18)	5.08 (1.43)	7.01 (0.54)	0.16 (0.01)	15.74 (1.22)	21.68 (0.17)	0.26 (0.01)	0.01 (0)	100.72 (0.58)	79.9 (2.5)	44.6	44.2	11.2
N72-Cr3-70	1025	2	49.64 (0.15)	0.84 (0.25)	5.31 (0.18)	7.81 (0.63)	0.23 (0.04)	15.45 (0.04)	21.02 (0.21)	0.41 (0.13)	0.01 (0.01)	100.73 (0.89)	77.9 (1.4)	44.2	43.2	12.5
N72-Cr3-71	1025	2	49.81 (0.16)	0.67 (0.02)	5.38 (0.05)	8.08 (0.68)	0.23 (0.1)	16.28 (0.95)	20.21 (2.06)	0.3 (0)	0.02 (0.01)	100.98 (0.43)	78.2 (0.5)	46.1	41.1	12.8
N72-Cr3-75	1075	2	50.74 (0.41)	0.51 (0.01)	4.73 (0.3)	7.94 (0.05)	0.22 (0.04)	16.16 (0.23)	19.68 (0.05)	0.33 (0.02)	0.02 (0.01)	100.79 (0)	78.4 (0.3)	46.5	40.7	12.8

Table A-1-8 (continued). Compositions of experimental clinopyroxenes**Clinopyroxenes in experiments performed at 100 MPa**

Run	T, C	n	SiO ₂	TiO ₂	Al ₂ O ₃	FeO	MnO	MgO	CaO	Na ₂ O	K ₂ O	Total	Mg#	En	Wo	Fs
N72-Cr1-82	1050	3	50.96 (0.41)	0.65 (0.03)	3.87 (0.35)	7.71 (0.16)	0.24 (0.02)	16.53 (0.19)	20.17 (0.26)	0.32 (0.06)	0.02 (0.01)	100.49 (0.25)	79.3 (0.2)	46.8	41.0	12.2
N72-Cr1-83	1050	3	50.27 (0.94)	0.67 (0.15)	4.89 (1.22)	7.85 (0.85)	0.2 (0.05)	16.22 (0.5)	20.65 (1.35)	0.3 (0.04)	0.01 (0)	101.09 (0.31)	78.7 (1.7)	45.7	41.9	12.4
N72-Cr1-84	1050	3	48.14 (1.18)	0.03 (0.01)	32.66 (0.71)	1.46 (0.07)	0.01 (0.01)	0.14 (0.01)	16.78 (0.91)	2.13 (0.56)	0.03 (0.02)	101.38 (0.39)	81.4 (4.8)	46.3	42.6	11.1
N72-Cr1-85	1050	3	51.98 (0.43)	0.79 (0.1)	3.92 (1.47)	12.99 (0.68)	0.33 (0.01)	17.96 (0.93)	12.6 (0.7)	0.39 (0.13)	0.07 (0.06)	101.05 (0.83)	71.1 (0.4)	52.4	26.4	21.3
N72-Cr1-89	1075	2	50.5 (0.43)	0.63 (0.09)	3.98 (0.4)	8.68 (0.91)	0.21 (0.01)	16.81 (0.71)	19.36 (1.75)	0.29 (0.01)	0.02 (0)	100.6 (0.12)	77.6 (1.1)	47.2	39.1	13.7
N72-Cr1-94	1025	3	51.03 (0.55)	0.81 (0.05)	3.65 (0.61)	7.99 (0.47)	0.34 (0.01)	17.45 (0.35)	19.17 (0.23)	0.51 (0.04)	0.01 (0.01)	100.98 (0.67)	79.6 (1)	48.9	38.6	12.6
N72-Cr1-97	1025	3	49.15 (1.76)	1.03 (0.3)	3.88 (0.26)	9.96 (3.46)	0.33 (0.05)	16.79 (0.14)	18.88 (1.11)	0.3 (0.04)	0.01 (0.01)	100.39 (0.93)	75.4 (6.1)	46.7	37.8	15.5
N72-Cr1-98	1025	2	50.06 (0.34)	0.8 (0.15)	4.21 (0.37)	7.74 (0.79)	0.29 (0.06)	16.23 (0.35)	20.8 (0.16)	0.3 (0.1)	0.02 (0.02)	100.49 (0.1)	78.9 (1.3)	45.7	42.1	12.2
N72-Cr1-99	1025	2	50.78 (0.18)	0.74 (0.04)	4.49 (0.5)	7.42 (0.08)	0.27 (0.04)	16.72 (0.16)	20.63 (0.17)	0.29 (0.01)	0.01 (0.01)	101.37 (0.02)	80.1 (0.3)	46.8	41.5	11.7
N72-Cr1-101	1050	2	51.41 (0.2)	0.7 (0.02)	3.16 (0.47)	8.31 (0.38)	0.29 (0.03)	16.53 (0.06)	19.97 (0.79)	0.26 (0)	0.02 (0)	100.67 (0.17)	78 (0.9)	46.5	40.4	13.1
N72-Cr1-102	1050	2	50.17 (0.81)	0.77 (0.13)	4.44 (0.57)	7.58 (0.19)	0.27 (0)	16.81 (0.14)	20.69 (0.33)	0.27 (0.01)	0 (0)	101.05 (0.34)	79.8 (0.5)	46.8	41.4	11.8
N72-Cr1-103	1050	2	51.73 (0.17)	0.52 (0)	2.44 (0.06)	7.78 (0.69)	0.3 (0.03)	18.22 (0.12)	18.29 (0.17)	0.22 (0.05)	0 (0.01)	99.54 (0.96)	80.7 (1.3)	51.0	36.8	12.2
N72-Cr1-110	1100	2	45.26 (1.52)	1.83 (0.17)	8.12 (0.21)	14.5 (0.37)	0.33 (0.12)	11.51 (1.05)	17.53 (2.22)	0.36 (0.04)	0.05 (0.04)	99.5 (0.2)	58.5 (2.8)	35.7	39.1	25.2
N72-Cr1-111	1100	2	44.89 (0.23)	1.6 (0.16)	8.44 (0.07)	12.89 (0)	0.25 (0.02)	12.43 (0.86)	18.54 (0.89)	0.33 (0.05)	0.01 (0.02)	99.37 (0.04)	63.2 (1.6)	37.7	40.4	21.9
N72-Cr1-112	1100	1	46.45	1.33	7.92	12.64	0.25	15.76	14.22	0.32	0.02	98.91	68.9	47.6	30.9	21.5
N72-Cr1-113	1100	2	43.8 (0.23)	1.08 (0.06)	12.44 (0.22)	11.56 (0.34)	0.22 (0.03)	14.33 (1.09)	16.08 (1.55)	0.23 (0.06)	0 (0.01)	99.75 (0.14)	68.8 (1)	44.3	35.7	20.0
N72-Cr1-114	1075	1	50.8	0.85	4.05	11.01	0.38	16.82	15.76	0.31	0.06	100.05	73.1	49.0	33.0	18.0
N72-Cr1-115	1075	1	51.19	0.81	4.37	10.22	0.31	15.36	15.81	0.51	0.1	98.68	72.8	47.3	35.0	17.7
N72-Cr1-127	1000	3	50.96 (0.49)	0.83 (0.08)	3.44 (1.1)	8.14 (0.85)	0.34 (0.03)	16.5 (1.01)	19.14 (0.41)	0.4 (0.08)	0.02 (0.01)	99.77 (0.14)	78.3 (1.6)	47.4	39.5	13.1
N72-Cr1-128	1000	3	51 (0.06)	0.81 (0.02)	4.35 (0.44)	7.02 (0.21)	0.29 (0.05)	16.02 (0.56)	19.84 (0.4)	0.37 (0.13)	0.03 (0.03)	99.74 (0.07)	80.3 (0.8)	46.8	41.7	11.5
N72-Cr1-129	1000	3	50.99 (1.08)	0.78 (0.04)	3.75 (0.47)	6.78 (0.24)	0.26 (0.02)	16.61 (0.48)	20.56 (0.31)	0.31 (0.04)	0.02 (0.01)	100.07 (1.06)	81.3 (0.9)	47.2	42.0	10.8

n – number of analyses;

Numbers in parentheses show standard deviation (1σ) of replicate analyses;

Mg# - magnesian number of cPx $Mg\# = MgO / (MgO + FeO - t)$.

Proportions of minerals in mol. %: En – enstatite, Wo – wollastonite, Fs – ferrosillite.

Table A-1-9. Compositions of experimental orthopyroxenes**Experiments performed at 300 MPa**

Run	T, C	n	SiO ₂	TiO ₂	Al ₂ O ₃	FeO	MnO	MgO	CaO	Na ₂ O	K ₂ O	Total	Mg#	En	Wo	Fs
N72-Cr3-7	1000	3	53.01 (0.12)	0.34 (0.02)	4.08 (0.34)	11.08 (0.43)	0.42 (0.07)	29.45 (0.35)	1.71 (0.23)	0.05 (0.01)	0.01 (0)	100.14 (0.49)	82.6 (0.7)	79.8	3.3	16.8
N72-Cr3-8	1000	4	52.62 (0.53)	0.4 (0.05)	3.19 (0.32)	13.55 (0.11)	0.48 (0.03)	27.09 (1.1)	1.77 (0.19)	0.06 (0.03)	0.01 (0.01)	99.17 (1.14)	78.1 (0.8)	75.3	3.5	21.1
N72-Cr3-29	950	3	53.58 (0.04)	0.29 (0.04)	3.38 (0.29)	11.49 (0.13)	0.48 (0.01)	29.37 (0.24)	1.48 (0.08)	0.05 (0.01)	0.01 (0.01)	100.13 (0.26)	82 (0.3)	79.6	2.9	17.5
N72-Cr3-30	950	4	54.16 (0.97)	0.28 (0.11)	4.76 (3.15)	10.4 (1.32)	0.53 (0.14)	27.14 (5.84)	1.94 (1)	0.12 (0.14)	0.05 (0.1)	99.38 (1.89)	82 (1.8)	79.0	4.1	17.0
N72-Cr3-31	950	4	53.31 (1.32)	0.32 (0.08)	3.47 (1.01)	12.09 (1.24)	0.53 (0.05)	28.8 (1)	1.98 (0.47)	0.09 (0.09)	0.01 (0)	100.6 (0.6)	81 (1.2)	77.8	3.8	18.3
N72-Cr3-40	1050	5	53.1 (0.51)	0.53 (0.03)	4.2 (1.38)	12.56 (0.56)	0.85 (0.08)	27.29 (1.29)	2.28 (0.57)	0.09 (0.09)	0.01 (0.01)	100.9 (0.48)	79.5 (0.6)	75.9	4.6	19.6
N72-Cr3-41	1050	3	52.07 (0.39)	0.71 (0)	3.65 (0.07)	14.89 (0.2)	0.85 (0.1)	26.02 (0.13)	2.1 (0.02)	0.05 (0.01)	0 (0)	100.34 (0.72)	75.7 (0.2)	72.5	4.2	23.3
N72-Cr3-42	1100	2	52.76 (0.14)	0.37 (0.02)	2.87 (0.02)	15.38 (0.02)	0.3 (0.1)	24.77 (0.12)	2.82 (0.06)	0.07 (0.03)	0 (0)	99.34 (0.27)	74.2 (0.1)	69.9	5.7	24.4
N72-Cr3-47	1125	4	52.08 (0.02)	0.36 (0.57)	3.92 (0.17)	14.28 (0.04)	0.3 (0)	25.95 (0.02)	2.37 (0.08)	0.04 (0.3)	0 (0.03)	99.56 (0.48)	76.4 (0.3)	72.8	4.8	22.5
N72-Cr3-52	1075	3	52.09 (0.27)	0.46 (0.07)	4.17 (1.92)	15.53 (1.3)	0.37 (0.02)	23.75 (0.06)	3.04 (1.23)	0.23 (2.02)	0.02 (0.01)	99.68 (0.35)	73.2 (0.3)	68.6	6.3	25.1
N72-Cr3-54	1075	3	52.25 (0.01)	0.34 (0.74)	3.57 (0.83)	13.77 (0.03)	0.35 (0)	26.58 (0.04)	2.09 (0.45)	0.06 (0.41)	0.01 (0.02)	99.04 (0.3)	77.5 (0.8)	74.2	4.2	21.6

Experiments performed at 100 MPa

Run	T, C	n	SiO ₂	TiO ₂	Al ₂ O ₃	FeO	MnO	MgO	CaO	Na ₂ O	K ₂ O	Total	Mg#	En	Wo	Fs
N72-Cr1-85	1050	2	53.79 (0.16)	0.5 (0.14)	2.07 (0.61)	16.21 (0.5)	0.41 (0)	22.55 (0.9)	4.87 (0.15)	0.15 (0.06)	0.08 (0.09)	100.64 (0.47)	71.2 (0.2)	64.2	10.0	25.9
N72-Cr1-94	1025	3	54.17 (0.24)	0.4 (0.05)	4.12 (1.67)	10.87 (0.37)	0.4 (0.07)	28.23 (2.07)	2.62 (0.95)	0.43 (0.51)	0.03 (0.03)	101.31 (1.02)	82.2 (0.7)	77.9	5.2	16.8
N72-Cr1-97	1025	3	53.85 (0.14)	0.4 (0.01)	4.07 (0.99)	10.6 (0.31)	0.42 (0.06)	28.45 (0.29)	2.91 (0.44)	0.12 (0.07)	0.01 (0)	100.79 (0.4)	82.7 (0.5)	78.0	5.7	16.3
N72-Cr1-98	1025	2	53.37 (0.53)	0.41 (0.12)	3.48 (0.77)	11.13 (0.22)	0.42 (0.01)	30.42 (0.34)	1.75 (0.07)	#DIV/0!	0.02 (0)	100.99 (0.28)	83 (0.4)	80.2	3.3	16.5
N72-Cr1-99	1025	3	54.15 (0.86)	0.34 (0.05)	3.04 (0.42)	10.17 (0.87)	0.41 (0.04)	30.65 (0.88)	1.78 (0.18)	0.03 (0.04)	0.01 (0.01)	100.56 (0.19)	84.3 (1.5)	81.5	3.4	15.2
N72-Cr1-101	1050	2	54.78 (0.37)	0.4 (0.1)	2.71 (0.61)	12.73 (0.11)	0.39 (0.04)	27.16 (1.94)	2.26 (0.51)	0.1 (0.08)	0.06 (0.08)	100.61 (0.36)	79.1 (1)	75.6	4.5	19.9
N72-Cr1-103	1050	2	53.79 (0.1)	0.38 (0.01)	2.78 (0.57)	11.92 (0.1)	0.48 (0.12)	29.05 (0.49)	2.01 (0.14)	0.04 (0.02)	0.01 (0.01)	100.47 (0.25)	81.3 (0.4)	78.1	3.9	18.0
N72-Cr1-112	1100	1	49.52	0.64	5.5	12.94	0.21	23.26	5	0.12	0.02	97.23	76.2	68.2	10.5	21.3
N72-Cr1-114	1075	1	44.37	0.27	3.42	16.47	0.43	26.19	8.17	0.33	0.02	99.66	73.9	63.4	14.2	22.4
N72-Cr1-127	1000	3	54.13 (0.13)	0.39 (0.02)	3.53 (1.16)	11.9 (1.27)	0.4 (0.06)	27.19 (1.22)	2.62 (0.51)	0.18 (0.12)	0.01 (0.01)	100.35 (0.61)	80.3 (1.3)	76.1	5.3	18.7
N72-Cr1-128	1000	3	54.44 (0.91)	0.34 (0.05)	2.96 (0.71)	9.98 (0.65)	0.46 (0.05)	30.02 (0.05)	1.95 (0.4)	0.09 (0.07)	0 (0.01)	100.24 (1.36)	84.3 (0.9)	81.1	3.8	15.1
N72-Cr1-129	1000	3	54.25 (0.59)	0.33 (0.02)	2.69 (0.33)	10.13 (0.24)	0.44 (0.07)	30.44 (0.2)	1.8 (0.07)	0.06 (0.02)	0.01 (0)	100.15 (1.04)	84.3 (0.4)	81.4	3.5	15.2

n – number of analyses;

Numbers in parentheses show standard deviation (1σ) of replicate analyses;

Mg# - magnesian number of cPx Mg# = MgO/(MgO+FeO-t).

Proportions of minals in mol.%. En – enstatite, Wo – wollastonite, Fs – ferrosillite.

Table A-1-10. Compositions of experimental amphiboles (300 MPa)

Run	T, C	n	SiO ₂	TiO ₂	Al ₂ O ₃	FeO	MnO	MgO	CaO	Na ₂ O	K ₂ O	Total	Mg#
N72-3-6	1000	4	41.47 (0.2)	1.65 (0.07)	13.94 (0.12)	8.66 (0.14)	0.1 (0.02)	16.44 (0.19)	12.4 (0.12)	2.36 (0.04)	0.15 (0)	97.17 (0.46)	77.2 (0.2)
N72-3-28	950	5	43.27 (0.38)	1.67 (0.08)	11.98 (0.36)	9.42 (0.47)	0.18 (0.04)	16.43 (0.3)	11.94 (0.16)	2.1 (0.05)	0.13 (0.01)	97.14 (0.37)	75.6 (1.2)
N72-3-29	950	3	43.32 (0.22)	2.59 (0.23)	11.54 (0.18)	9.76 (0.19)	0.18 (0.01)	15.86 (0.41)	11.58 (0.15)	2.36 (0.02)	0.17 (0.01)	97.35 (0.42)	74.3 (0.5)
N72-3-30	950	5	43.93 (0.28)	1.9 (0.1)	11.21 (0.14)	9.51 (0.33)	0.18 (0.06)	16.55 (0.12)	11.64 (0.17)	2.19 (0.05)	0.13 (0.01)	97.24 (0.44)	75.6 (0.6)
N72-3-31	950	3	41.97 (1.77)	2.28 (0.63)	12.09 (1.99)	10.37 (0.93)	0.21 (0.09)	15.65 (0.81)	11.62 (0.15)	2.35 (0.04)	0.18 (0.03)	96.73 (0.93)	72.9 (2.8)

n – number of analyses;

Numbers in parentheses show standard deviation (1σ) of replicate analyses;

Mg# - magnesian number of cPx $Mg\# = MgO / (MgO + FeO - t)$.

Table A-1-11. Compositions of experimental magnetites**Experiments performed at 300 MPa**

Run	T, C	n	SiO ₂	TiO ₂	Al ₂ O ₃	FeO	MnO	MgO	CaO	Cr ₂ O ₃	Total	Usp	Sp	Mt	Cr
N72-Cr3-6	1000	4	0.15 (0.05)	2.38 (0.01)	10.42 (0.14)	71.85 (0.31)	0.32 (0.02)	7.99 (0.11)	0.29 (0.02)	0.21 (0.14)	93.64 (0.58)	0.1	0.2	0.7	0.0
N72-Cr3-7	1000	3	0.48 (0.42)	6.4 (0.08)	4.93 (0.06)	76.66 (0.76)	0.33 (0.01)	4.33 (0.12)	0.26 (0.09)	0.67 (0.1)	94.13 (0.97)	0.23	0.07	0.69	0.01
N72-Cr3-8	1000	3	0.4 (0.28)	6.75 (0.09)	4.9 (0.08)	74.76 (1.11)	0.36 (0.06)	4.34 (0.15)	0.41 (0.17)	0.63 (0.77)	92.56 (0.96)	0.25	0.07	0.68	0.01
N72-Cr3-11	1050	3	0.14 (0.04)	1.48 (0.01)	8.13 (0.11)	73.04 (0.53)	0.25 (0.08)	8.23 (0.2)	0.28 (0.02)	1.31 (0.22)	92.88 (0.81)	0.1	0.1	0.8	0.0
N72-Cr3-12	1050	3	0.34 (0.21)	1.63 (0.02)	9.24 (0.03)	71.63 (0.29)	0.17 (0.06)	8.31 (0.05)	0.35 (0.06)	1.56 (0.05)	93.29 (0.07)	0.1	0.2	0.8	0.0
N72-Cr3-13	1050	3	0.18 (0.04)	2.24 (0.03)	10.86 (0.26)	70.79 (0.61)	0.23 (0.02)	7.85 (0.22)	0.29 (0.02)	1.36 (0.14)	93.84 (0.11)	0.09	0.17	0.72	0.01
N72-Cr3-14	1050	3	0.25 (0.08)	3.81 (0.03)	7.97 (0.03)	74.38 (0.26)	0.31 (0.01)	5.98 (0.05)	0.38 (0.02)	0.52 (0.04)	93.62 (0.19)	0.15	0.12	0.72	0.01
N72-Cr3-28	950	3	0.22 (0.18)	2.7 (0.03)	5.31 (0.03)	78.51 (0.21)	0.41 (0.05)	4.65 (0.04)	0.29 (0.04)	0.28 (0.01)	92.37 (0.42)	0.11	0.08	0.80	0.00
N72-Cr3-29	950	4	0.37 (0.26)	5.09 (0.08)	4.52 (0.11)	77.74 (0.52)	0.4 (0.03)	4.17 (0.09)	0.42 (0.13)	0.2 (0.04)	92.94 (0.84)	0.2	0.1	0.7	0.0
N72-Cr3-30	950	3	0.09 (0.03)	3.49 (0.02)	4.95 (0.06)	78.65 (0.2)	0.37 (0.05)	4.32 (0.05)	0.23 (0.03)	0.82 (0.13)	92.93 (0.09)	0.1	0.1	0.8	0.0
N72-Cr3-31	950	6	0.72 (0.58)	5.3 (0.04)	4.37 (0.05)	77.18 (0.83)	0.43 (0.02)	4.3 (0.28)	0.39 (0.18)	0.22 (0.1)	92.92 (0.8)	0.2	0.1	0.7	0.0
N72-Cr3-39	1050	1	0.29 (0)	19.49 (0)	4.85 (0)	72.25 (0)	0.53 (0)	4.03 (0)	0.39 (0)	-	101.85 (0)	0.49	0.05	0.46	0.00
N72-Cr3-40	1050	3	0.22 (0.03)	9.38 (0.07)	7.23 (0.09)	73.85 (0.42)	0.64 (0.13)	5.27 (0.09)	0.29 (0.02)	-	96.89 (0.35)	0.31	0.09	0.60	0.00
N72-Cr3-41	1050	3	0.33 (0.29)	13.09 (0.19)	5.8 (0.13)	73.37 (0.6)	0.68 (0.05)	4.41 (0.02)	0.29 (0.05)	-	98 (0.54)	0.39	0.07	0.54	0.00
N72-Cr3-50	1125	2	3.18 (0.14)	1.2 (1.63)	23.1 (0.23)	46.91 (0.19)	-	12.08 (0.02)	0.93 (1.08)	9 (0.74)	96.62 (1.71)	0.0	0.4	0.5	0.1
N72-Cr3-52	1075	3	2.96 (0.01)	9.02 (4.71)	5.63 (0.48)	68.92 (0.68)	0.36 (0.01)	5.57 (0.64)	0.72 (5.44)	0.45 (0.09)	93.65 (0.77)	0.32	0.08	0.60	0.00
N72-Cr3-53	1075	2	-	10.52 (0.06)	5.91 (0.18)	70.84 (0.17)	0.22 (0)	4.33 (0.69)	0.29 (1.19)	2.54 (2.18)	94.82 (0.26)	0.34	0.07	0.57	0.02
N72-Cr3-54	1075	2	-	5.82 (0.04)	7.5 (0.07)	73.79 (0.06)	-	5.12 (0.01)	0.33 (1.36)	0.73 (0.07)	93.77 (1.55)	0.21	0.11	0.67	0.01
N72-Cr3-56	1075	1	1.43 (0)	2.35 (0)	12.16 (0)	64.36 (0)	0.08 (0)	7.84 (0)	0.61 (0)	4.06 (0)	93.01 (0)	0.10	0.20	0.66	0.04
N72-Cr3-68	1025	1	0.13 (0)	2.71 (0)	10.96 (0)	71.75 (0)	0.2 (0)	7.08 (0)	0.32 (0)	1.86 (0)	95.05 (0)	0.11	0.17	0.71	0.02
N72-Cr3-69	1025	1	0.17 (0)	2.81 (0)	10.81 (0)	71.26 (0)	0.2 (0)	7.02 (0)	0.37 (0)	1.53 (0)	94.19 (0)	0.11	0.17	0.71	0.02
N72-Cr3-70	1025	1	0.12 (0)	4.03 (0)	8.32 (0)	74.81 (0)	0.32 (0)	5.83 (0)	0.22 (0)	1.15 (0)	94.84 (0)	0.15	0.12	0.71	0.01
N72-Cr3-71	1025	1	0.15 (0)	3.52 (0)	9.13 (0)	74.46 (0)	0.22 (0)	6 (0)	0.29 (0)	0.97 (0)	94.74 (0)	0.14	0.14	0.72	0.01

Table A-1-11 (continued). Compositions of experimental magnetites**Experiments performed at 100 MPa**

Run	T, C	n	SiO ₂	TiO ₂	Al ₂ O ₃	FeO	MnO	MgO	CaO	Cr ₂ O ₃	Total	Usp	Sp	Mt	Cr
N72-Cr1-81	1050	1	0.11 (0)	2.61 (0)	7.48 (0)	74.14 (0)	0.25 (0)	6.64 (0)	0.34 (0)	1.76 (0)	93.35 (0)	0.1	0.1	0.8	0.0
N72-Cr1-82	1050	3	0.14 (0.03)	4.93 (0.05)	5.7 (0.1)	76.96 (0.45)	0.32 (0.03)	5.15 (0.06)	0.29 (0.05)	0.65 (0.04)	94.18 (0.26)	0.19	0.08	0.72	0.01
N72-Cr1-83	1050	2	0.11 (0)	3.62 (0.07)	6.37 (0.16)	76.44 (0.15)	0.29 (0.02)	5.88 (0.01)	0.25 (0)	0.88 (0.02)	93.86 (0.09)	0.14	0.10	0.75	0.01
N72-Cr1-84	1050	2	0.15 (0.05)	3.73 (0.02)	6.52 (0.03)	76.51 (0.14)	0.23 (0.07)	5.77 (0.05)	0.28 (0.09)	1.04 (0.07)	94.24 (0.33)	0.15	0.10	0.74	0.01
N72-Cr1-85	1050	1	0.29 (0)	12.03 (0)	4.38 (0)	71.53 (0)	0.39 (0)	4.32 (0)	0.45 (0)	0.58 (0)	93.99 (0)	0.38	0.05	0.56	0.00
N72-Cr1-86	1075	2	2.35 (3.03)	2.22 (0.07)	10.73 (0.62)	65.09 (1.23)	0.05 (0.07)	7.89 (0.15)	0.66 (0.45)	5.99 (0.29)	95.04 (2.49)	0.1	0.2	0.7	0.1
N72-Cr1-87	1075	1	0.82 (0)	2.06 (0)	11.68 (0)	65 (0)	0.11 (0)	8.52 (0)	0.43 (0)	6.52 (0)	95.17 (0)	0.1	0.2	0.7	0.1
N72-Cr1-88	1075	2	5.22 (1.42)	2.38 (0.05)	10.36 (0)	64.03 (1.89)	0.08 (0.05)	7.35 (0.23)	1.26 (0.44)	5.73 (0.25)	96.73 (0.52)	0.1	0.2	0.7	0.1
N72-Cr1-89	1075	1	3.53 (0)	3.97 (0)	8.23 (0)	66.81 (0)	0.05 (0)	6.69 (0)	0.86 (0)	6.14 (0)	96.69 (0)	0.16	0.13	0.65	0.06
N72-Cr1-94	1025	2	0.95 (1.11)	5.5 (0.02)	4.98 (0.36)	76.61 (0.6)	0.45 (0)	5.23 (0.03)	0.45 (0.19)	0.31 (0.03)	94.6 (1.21)	0.21	0.07	0.72	0.00
N72-Cr1-97	1025	2	0.13 (0.01)	5.39 (0.09)	4.8 (0)	76.48 (0.27)	0.41 (0.09)	5.22 (0.13)	0.32 (0.02)	0.76 (0.02)	93.53 (0.33)	0.20	0.07	0.72	0.01
N72-Cr1-98	1025	2	0.23 (0.19)	4.55 (0.05)	5.23 (0.05)	77.24 (0.71)	0.35 (0.02)	5.94 (0.22)	0.31 (0.07)	0.32 (0.12)	94.2 (0.73)	0.18	0.08	0.74	0.00
N72-Cr1-99	1025	2	0.17 (0.02)	4.05 (0.01)	5.46 (0.01)	77.27 (0.47)	0.38 (0.02)	6.04 (0.21)	0.35 (0.01)	0.24 (0.02)	93.97 (0.26)	0.16	0.08	0.76	0.00
N72-Cr1-115	1075	1	0.43 (0)	6.97 (0)	5.24 (0)	74.4 (0)	0.24 (0)	4.96 (0)	0.31 (0)	0.95 (0)	93.52 (0)	0.25	0.07	0.67	0.01
N72-Cr1-117	1075	1	0.86 (0)	2.48 (0)	7.39 (0)	72.58 (0)	0.11 (0)	6.74 (0)	0.47 (0)	2.37 (0)	93.07 (0)	0.1	0.1	0.8	0.0
N72-Cr1-127	1000	2	0.26 (0.05)	6.22 (0.1)	3.69 (0.04)	76.3 (0.55)	0.37 (0.01)	4.91 (0.13)	0.39 (0.05)	0.24 (0.18)	92.4 (0.49)	0.23	0.05	0.71	0.00
N72-Cr1-128	1000	2	0.18 (0.04)	4.41 (0.02)	4.64 (0.18)	76.04 (0.16)	0.34 (0.11)	6.04 (0.14)	0.31 (0.01)	0.31 (0.17)	92.27 (0.38)	0.17	0.07	0.75	0.00
N72-Cr1-129	1000	3	0.22 (0.08)	4.13 (0.04)	4.72 (0.15)	75.94 (0.79)	0.41 (0.02)	6.25 (0.08)	0.24 (0.05)	0.23 (0.02)	92.17 (0.92)	0.16	0.07	0.76	0.00

n – number of analyses;

Numbers in parentheses show standard deviation (1σ) of replicate analyses;

Proportions of magnetite components in mol. %: Usp – ulvöspinel (Ti), Sp – spinel (Al), Mt – magnetite (Fe), Cr – chromite (Cr).

APPENDIX

CHAPTER II.

Table A-2-1. Major-element compositions of experimental glasses (wt.%) determined by electron microprobe

Capsule NN	P (MPa)	SiO₂	TiO₂	Al₂O₃	FeO	MnO	MgO	CaO	Na₂O	K₂O	Total	n
M13	50	47.51 (0.45)	0.9 (0.05)	17.6 (0.26)	9.14 (0.43)	0.15 (0.1)	6.94 (0.23)	10.8 (0.38)	2.3 (0.31)	0.24 (0.03)	95.6 (0.61)	10
M14	50	48.17 (0.42)	0.9 (0.06)	17.45 (0.23)	8.84 (0.38)	0.19 (0.11)	6.66 (0.14)	10.92 (0.36)	2.26 (0.14)	0.23 (0.04)	95.63 (0.58)	10
M15	50	48.31 (0.32)	0.91 (0.06)	17.58 (0.17)	8.69 (0.38)	0.14 (0.08)	6.72 (0.14)	10.74 (0.32)	2.39 (0.19)	0.22 (0.04)	95.69 (0.64)	10
M16	50	48.92 (0.44)	0.92 (0.06)	17.68 (0.25)	8.46 (0.29)	0.11 (0.09)	6.89 (0.16)	11.11 (0.38)	2.34 (0.11)	0.24 (0.04)	96.66 (0.96)	10
M51	50	47.69 (0.28)	0.89 (0.03)	17.39 (0.19)	8.92 (0.31)	0.21 (0.11)	6.70 (0.14)	10.72 (0.19)	2.27 (0.09)	0.25 (0.05)	95.05 (0.59)	10
M50	50	48.07 (0.36)	0.88 (0.03)	17.35 (0.22)	8.65 (0.48)	0.19 (0.12)	6.69 (0.14)	10.77 (0.28)	2.25 (0.19)	0.24 (0.04)	95.09 (0.99)	10
M49	50	48.93 (0.35)	0.92 (0.07)	17.73 (0.20)	8.52 (0.38)	0.14 (0.10)	6.91 (0.21)	10.89 (0.26)	2.46 (0.22)	0.24 (0.03)	96.74 (0.59)	10
M48	50	49.33 (0.38)	0.91 (0.05)	17.85 (0.24)	7.93 (0.36)	0.18 (0.09)	6.86 (0.20)	11.01 (0.33)	2.39 (0.16)	0.24 (0.03)	96.71 (0.77)	10
M47	50	49.65 (0.42)	0.92 (0.04)	18.08 (0.23)	8.16 (0.29)	0.17 (0.10)	6.9 (0.13)	10.91 (0.28)	2.41 (0.16)	0.23 (0.04)	97.45 (0.75)	10
M6	100	47.48 (0.28)	0.88 (0.06)	17.24 (0.10)	8.53 (0.30)	0.23 (0.07)	6.62 (0.23)	10.72 (0.08)	2.41 (0.15)	0.22 (0.05)	94.33 (0.64)	5
M7	100	47.38 (0.21)	0.90 (0.06)	16.93 (0.29)	8.66 (0.37)	0.16 (0.02)	6.47 (0.15)	10.84 (0.44)	2.33 (0.08)	0.23 (0.04)	93.89 (0.81)	5
M8	100	47.93 (0.35)	0.92 (0.03)	17.4 (0.16)	8.91 (0.62)	0.18 (0.11)	6.67 (0.15)	10.91 (0.34)	2.36 (0.16)	0.24 (0.04)	95.53 (0.97)	5
M9	100	49.09 (0.33)	0.95 (0.07)	17.79 (0.15)	7.79 (0.43)	0.17 (0.08)	6.77 (0.12)	10.81 (0.34)	2.31 (0.22)	0.26 (0.03)	95.95 (0.44)	5
M10	100	49.79 (0.46)	0.94 (0.03)	18.07 (0.22)	7.61 (0.21)	0.25 (0.06)	7.20 (0.23)	11.41 (0.20)	2.21 (0.14)	0.23 (0.02)	97.71 (0.36)	5
M11	200	46.44 (0.38)	0.86 (0.02)	16.72 (0.33)	8.19 (0.41)	0.20 (0.11)	6.39 (0.10)	10.46 (0.32)	2.22 (0.16)	0.23 (0.03)	91.70 (1.12)	5
M12	200	46.78 (0.52)	0.88 (0.03)	16.83 (0.25)	8.92 (0.45)	0.20 (0.12)	6.44 (0.19)	10.39 (0.17)	2.10 (0.13)	0.21 (0.04)	92.75 (0.72)	10
M2	200	46.85 (0.37)	0.88 (0.03)	16.87 (0.19)	8.54 (0.15)	0.21 (0.08)	6.52 (0.17)	10.57 (0.19)	2.20 (0.24)	0.24 (0.04)	92.87 (0.45)	5
M3	200	47.44 (0.15)	0.92 (0.04)	17.04 (0.23)	8.96 (0.31)	0.19 (0.08)	6.63 (0.14)	10.71 (0.18)	2.11 (0.22)	0.24 (0.05)	94.26 (0.68)	5
M5	200	49.19 (0.31)	0.89 (0.06)	17.85 (0.10)	7.93 (0.32)	0.27 (0.08)	6.85 (0.25)	11.09 (0.32)	2.38 (0.19)	0.25 (0.05)	96.7 (0.44)	5
M33	300	45.78 (0.24)	0.83 (0.04)	16.53 (0.22)	8.54 (0.44)	0.15 (0.08)	6.38 (0.25)	10.22 (0.30)	2.17 (0.13)	0.20 (0.03)	90.79 (0.72)	10
M34	300	46.00 (0.30)	0.85 (0.05)	16.60 (0.24)	8.67 (0.40)	0.20 (0.08)	6.29 (0.17)	10.15 (0.36)	2.25 (0.12)	0.23 (0.05)	91.25 (0.53)	10
M35	300	45.96 (0.57)	0.84 (0.04)	16.83 (0.26)	8.26 (0.61)	0.16 (0.08)	6.50 (0.18)	10.11 (0.41)	2.28 (0.20)	0.23 (0.03)	91.18 (1.48)	10
M36	300	47.38 (0.41)	0.88 (0.04)	17.34 (0.25)	9.00 (0.34)	0.13 (0.10)	6.51 (0.18)	10.65 (0.34)	2.20 (0.18)	0.23 (0.03)	94.33 (0.70)	10
M37	300	50.04 (0.53)	0.95 (0.03)	18.21 (0.35)	6.66 (0.25)	0.14 (0.07)	7.18 (0.19)	11.31 (0.35)	2.33 (0.15)	0.24 (0.02)	97.05 (1.33)	10
M38	400	45.22 (0.45)	0.84 (0.06)	16.37 (0.23)	8.68 (0.36)	0.14 (0.08)	6.11 (0.25)	10.05 (0.36)	2.24 (0.13)	0.23 (0.02)	89.91 (0.64)	10
M39	400	45.64 (0.26)	0.86 (0.04)	16.59 (0.23)	8.42 (0.32)	0.18 (0.10)	6.22 (0.14)	10.15 (0.20)	2.12 (0.12)	0.24 (0.06)	90.42 (0.65)	11
M30	400	45.86 (0.41)	0.86 (0.04)	16.60 (0.15)	8.59 (0.43)	0.14 (0.09)	6.36 (0.20)	10.37 (0.24)	2.17 (0.15)	0.22 (0.04)	91.16 (0.82)	10
M40	400	47.51 (0.4)	0.92 (0.04)	17.27 (0.22)	8.93 (0.3)	0.17 (0.09)	6.66 (0.21)	10.59 (0.26)	2.24 (0.15)	0.22 (0.04)	94.52 (0.84)	10
M19	500	47.31 (0.31)	0.87 (0.04)	17.08 (0.21)	8.8 (0.37)	0.13 (0.09)	6.63 (0.19)	10.5 (0.38)	2.26 (0.19)	0.23 (0.03)	93.82 (0.49)	10
M20	500	46 (0.4)	0.83 (0.04)	16.65 (0.25)	8.48 (0.35)	0.19 (0.07)	6.38 (0.17)	10.31 (0.25)	2.14 (0.18)	0.25 (0.05)	91.23 (0.94)	10

Table A-2-1 (continued)

Capsule NN	P (MPa)	SiO₂	TiO₂	Al₂O₃	FeO	MnO	MgO	CaO	Na₂O	K₂O	Total	n
M21	500	45.12 (0.35)	0.84 (0.05)	16.32 (0.19)	8.4 (0.28)	0.15 (0.09)	6.26 (0.15)	9.98 (0.21)	2.17 (0.2)	0.21 (0.03)	89.45 (0.69)	15
M22	500	44.85 (0.18)	0.87 (0.03)	16.13 (0.23)	8.35 (0.27)	0.17 (0.12)	6.07 (0.24)	10.13 (0.22)	2.14 (0.24)	0.24 (0.05)	88.93 (0.8)	7
M42	500	48.64 (0.39)	0.9 (0.06)	17.53 (0.24)	8.5 (0.49)	0.15 (0.08)	6.75 (0.21)	10.89 (0.36)	2.36 (0.14)	0.22 (0.02)	95.95 (0.88)	10
M43	500	47.46 (0.4)	0.88 (0.04)	17.21 (0.18)	8.82 (0.28)	0.22 (0.05)	6.65 (0.19)	10.59 (0.39)	2.17 (0.2)	0.23 (0.04)	94.23 (0.73)	10
M44	500	46.75 (0.41)	0.87 (0.05)	16.92 (0.22)	8.64 (0.45)	0.16 (0.05)	6.54 (0.14)	10.6 (0.29)	2.29 (0.19)	0.23 (0.02)	93 (0.62)	10
M46	500	45.69 (0.36)	0.85 (0.03)	16.39 (0.35)	8.45 (0.42)	0.18 (0.07)	6.32 (0.17)	10.12 (0.17)	2.17 (0.21)	0.21 (0.04)	90.37 (1)	10

n - amount of measurements.

Standard deviations for average of n analysis is shown in brackets near values.

n.a. - was not analyzed.

In samples M13 and M33 ratio Fe(II)/Fe-total was not determined, therefore all Fe presented as FeO.

Table A-2-2. Major-element compositions of experimental glasses (wt.%) determined by electron microprobe, recalculated to 100% using Fe²⁺/Fe-total ratio determined by colorimetry.

	SiO ₂	TiO ₂	Al ₂ O ₃	Fe ₂ O ₃	FeO	MnO	MgO	CaO	Na ₂ O	K ₂ O	Total
M13	49.70	0.95	18.41	n.a.	9.56*	0.16	7.26	11.29	2.41	0.25	100.00
M14	50.38	0.94	18.25	3.33	5.92	0.20	6.97	11.42	2.36	0.24	100.00
M15	50.48	0.95	18.37	2.91	6.18	0.14	7.03	11.23	2.49	0.23	100.00
M16	50.61	0.95	18.29	2.36	6.40	0.11	7.12	11.49	2.42	0.24	100.00
M51	50.17	0.94	18.30	3.16	6.23	0.22	7.05	11.28	2.39	0.26	100.00
M50	50.55	0.93	18.25	2.71	6.38	0.20	7.03	11.32	2.37	0.25	100.00
M49	50.58	0.95	18.33	2.19	6.61	0.15	7.14	11.26	2.54	0.24	100.00
M48	51.01	0.94	18.46	1.74	6.46	0.19	7.10	11.38	2.47	0.25	100.00
M47	50.95	0.94	18.55	2.12	6.25	0.18	7.09	11.20	2.48	0.24	100.00
M6	50.34	0.93	18.27	3.22	5.82	0.24	7.02	11.36	2.56	0.23	100.00
M7	50.47	0.96	18.03	3.13	6.10	0.17	6.89	11.54	2.48	0.25	100.00
M8	50.19	0.96	18.22	2.74	6.58	0.19	6.98	11.42	2.48	0.25	100.00
M9	51.16	0.99	18.54	1.33	6.79	0.17	7.05	11.27	2.41	0.27	100.00
M10	50.96	0.96	18.50	0.93	6.86	0.25	7.37	11.67	2.27	0.23	100.00
M11	50.65	0.94	18.24	3.94	4.99	0.22	6.96	11.40	2.42	0.25	100.00
M12	50.44	0.95	18.14	4.16	5.45	0.22	6.94	11.20	2.26	0.23	100.00
M2	50.44	0.94	18.17	1.62	7.57	0.22	7.02	11.38	2.37	0.26	100.00
M3	50.34	0.98	18.08	3.29	6.22	0.20	7.04	11.36	2.24	0.26	100.00
M5	50.87	0.92	18.46	0.98	7.22	0.27	7.09	11.47	2.46	0.26	100.00
M33	50.43	0.91	18.20	n.a.	9.40*	0.17	7.03	11.25	2.39	0.22	100.00
M34	50.41	0.93	18.19	4.09	5.42	0.22	6.89	11.13	2.47	0.26	100.00
M35	50.41	0.92	18.46	3.54	5.51	0.17	7.13	11.09	2.50	0.25	100.00
M36	50.23	0.93	18.38	3.28	6.27	0.14	6.90	11.29	2.33	0.24	100.00
M37	51.56	0.97	18.76	1.42	5.45	0.14	7.40	11.65	2.40	0.25	100.00
M38	50.30	0.93	18.21	4.48	5.17	0.16	6.80	11.18	2.50	0.26	100.00
M39	50.48	0.95	18.35	4.29	5.02	0.19	6.88	11.22	2.35	0.26	100.00
M30	50.31	0.95	18.21	3.87	5.55	0.15	6.97	11.37	2.38	0.24	100.00
M40	50.27	0.98	18.28	3.36	6.09	0.18	7.05	11.21	2.37	0.24	100.00
M19	50.43	0.93	18.20	2.80	6.58	0.14	7.07	11.20	2.41	0.25	100.00
M20	50.43	0.91	18.26	3.64	5.65	0.21	6.99	11.30	2.34	0.27	100.00
M21	50.44	0.93	18.25	4.16	5.23	0.17	7.00	11.16	2.43	0.23	100.00
M22	50.43	0.97	18.14	4.34	5.04	0.19	6.82	11.39	2.40	0.27	100.00
M42	50.69	0.94	18.27	2.19	6.67	0.16	7.03	11.36	2.46	0.23	100.00
M43	50.37	0.93	18.26	3.10	6.26	0.23	7.06	11.24	2.30	0.24	100.00
M44	50.27	0.94	18.19	3.45	5.84	0.18	7.03	11.40	2.46	0.25	100.00
M46	50.57	0.94	18.13	4.00	5.35	0.20	6.99	11.20	2.40	0.23	100.00

CHAPTER III

Table A-3-1. Experimental conditions, results of Karl-Fischer titration, determinations of redox state of Fe and infrared spectroscopy

Sample	NN	P (MPa)	T (C°)	X H ₂ O in	X (H ₂ O) fluid	X H ₂ O gravi-metry	X H ₂ O fluid mass-balance	KFT H ₂ O (wt%)	KFT Error H ₂ O	CO ₂ (ppm)	Error CO ₂ (ppm)	MIR H ₂ O (wt.%)	Error H ₂ O (wt%)	aH ₂ O, fluid	aH ₂ O, Burnham	lgfO ₂ run XH ₂ O fluid	lgfO ₂ run aH ₂ O Burnham	ΔNNO, aH ₂ O fl	ΔNN O aH ₂ O Burnham	Fe ²⁺ /Fe-total (K&C)	Fe ²⁺ /Fe-total (Colorimetry)	Fe-loss (%rel) EMP	
basanite	B2518	1	100	1250	0.95	0.85	0.85	0.93	3.10	0.12	0	0	2.34	0.33	0.86	0.94	-4.68	-4.61	2.47	2.55	0.48	0.54	0.56
basanite	B2518	2	100	1250	1.00	0.99	0.99	1.00	3.38	0.13	0	0	2.39	0.23	0.99	1.05	-4.56	-4.51	2.59	2.64	0.47	0.56	-4.09
basanite	B2518	3	100	1250	0.76	0.56	0.56	0.64	2.29	0.12	284	33	2.09	0.20	0.62	0.61	-4.97	-4.98	2.19	2.17	0.52	0.62	1.65
basanite	B2518	4	100	1250	0.41	0.2*	0.14	0.20	2.21	0.12	648	76	1.31§	0.13	0.18	0.25	-6.04	-5.76	1.11	1.40	0.61	0.70	5.19
basanite	B2518	50	100	1250	0.00	0.11	0.11	0.00	0.85	0.11	518	69	0.93	0.10	0.15	0.12	-6.20	-6.39	0.95	0.76	0.67	0.76	10.08
basanite	B2518	54	100	1250	0.00	0.11	0.11	0.00	0.88	0.11	706	82	0.91	0.10	0.15	0.13	-6.19	-6.32	0.96	0.83	0.67	0.73	6.56
basanite	B2518	9	500	1250	0.64	0.24	0.24	0.35	3.34	0.12	4517	526	2.70	0.26	0.30	0.42	-5.58	-5.31	1.57	1.85	0.72	0.17	-0.16
basanite	A2549	11	100	1250	1.00	1.00	1.00	1.00	3.13	0.14	0	0			1.00	0.99	-4.55	-4.56	2.60	2.59	0.46	0.54	-2.33
basanite	A2549	12	100	1250	0.94	0.91*	0.19	0.91	3.17	0.12	127	15			0.24	1	-5.78	-4.55	1.38	2.60	0.46	0.56	-1.29
basanite	A2549	13	100	1250	0.77	0.76*	0.68	0.76	1.09	0.12	1411	168	0.50§	0.06	0.72	0.05	-4.83	-7.15	2.32	0.00	0.72	0.80	37.47
basanite	A2549	14	100	1250	0.37	0.07*	1.00	0.07	1.29	0.12	1771	209	0.97§	0.10	1.00	0.16	-4.55	-6.14	2.60	1.01	0.63	0.74	5.75
basanite	A2549	51	100	1250	0.00	0.03	0.03	0.00	0.86	0.12	1500	178	0.85	0.10	0.05	0.13	-7.24	-6.32	-0.09	0.83	0.65	0.75	6.52
basanite	A2549	18	500	1250	0.87	0.64	0.64	0.83	5.82	0.12	6716	795			0.69	0.83	-4.87	-4.71	2.28	2.44	0.65	0.55	-1.59
basanite	A2549	19	500	1250	0.62	0.66*	0.97	0.66	0.50	0.12	7654	895	0.49	0.08	0.97	0.02	-4.58	-7.95	2.57	-0.80	0.89	0.86	12.91
basanite	A2549	47	500	1250	0.00	0.00*	0.80	0.00	0.27	0.12	7159	844	0.40	0.10	0.82	0.01	-4.72	-8.55	2.43	-1.40	0.92	0.87	43.76
basanite	A2549	48	500	1250	0.64	0.27	0.27	0.34	3.48	0.13	7368	885			0.33	0.45	-5.50	-5.25	1.65	1.91	0.7	0.05	-0.06
Alkali basalt	B2507	21	100	1250	1.00	0.92	0.92	1.00	3.31	0.13	0	0	2.46	0.24	0.92	1.03	-4.62	-4.53	2.53	2.63	0.48	0.56	0.87
Alkali basalt	B2507	22	100	1250	0.94	0.84	0.84	0.91	3.15	0.12	0	0	2.61	0.25	0.85	0.96	-4.69	-4.59	2.46	2.56	0.49	0.59	0.10
Alkali basalt	B2507	23	100	1250	0.79	0.65	0.65	0.65	2.45	0.13	219	26	2.30	0.23	0.70	0.68	-4.86	-4.89	2.29	2.27	0.52	0.63	1.55
Alkali basalt	B2507	24	100	1250	0.38	0.20	0.20	0.14	1.24	0.11	638	77	1.25	0.13	0.26	0.23	-5.71	-5.83	1.44	1.32	0.62	0.74	3.38
Alkali basalt	B2507	25	100	1250	0.00	0.19	0.19	0.00	0.85	0.12	750	88	0.88	0.11	0.25	0.12	-5.76	-6.39	1.39	0.76	0.68	0.80	10.86
Alkali basalt	B2507	29	500	1250	0.64	0.31	0.31	0.35	3.44	0.12	5440	748	2.86	0.28	0.38	0.43	-5.39	-5.28	1.76	1.87	0.72	0.67	1.18
Alkali basalt	B2507	30	500	1250	0.00	0.00	0.00	0.00	0.65	0.12	5413	809	0.69	0.10	0.00	0.03		-7.60		-0.45	0.88	0.79	3.47
Alkali bas	B2507	52	500	1250	0.00	0.00*	0.27	0.00	0.26	0.12	4852	567	0.29	0.08	0.34	0	-5.49		1.67		0.93	0.87	51.66

Table A-3-1 continued

Sample	NN	P (MPa)	T (C°)	X H ₂ O in	X (H ₂ O) fluid	X H ₂ O gravi-metry	X H ₂ O fluid mass-balance	KFT H ₂ O (wt%)	KFT Error H ₂ O	CO ₂ (ppm)	Error CO ₂ (ppm)	MIR H ₂ O (wt.%)	Error H ₂ O (wt%)	aH ₂ O, fluid	aH ₂ O, Burnham	lgfO ₂ run XH ₂ O fluid	lgfO ₂ run aH ₂ O Burnham	ΔNNO, aH ₂ O fluid	ΔNNO, aH ₂ O Burnham	Fe ²⁺ /Fe-total (K&C)	Fe ²⁺ /Fe-total (Colorimetry)	Fe-loss (%rel) EMP	
nephelinite	E2624	31	100	1250	1.00	0.99	0.99	1.00	3.19	0.13	0	0		0.99	1.05	-4.56	-4.51	2.59	2.64	0.44	0.50	2.13	
nephelinite	E2624	33	100	1250	0.77	0.60	0.60	0.60	2.69	0.12	1090	133	2.32	0.23	0.66	1.06	-4.91	-4.50	2.24	2.65	0.43	0.67	3.38
nephelinite	E2624	35	100	1250	0.00	0.00	0.00	0.00	0.54	0.11	2868	364	0.57	0.07	0.00	0.07	-6.86		0.29	0.67	0.75	16.53	
nephelinite	E2624	38	500	1250	0.87	0.55	0.55	0.75	5.86	0.14	8549	992		0.62	1.1	-4.97	-4.47	2.18	2.68	0.59	n.a.	4.27	
nephelinite	E2624	40	500	1250	0.00	0.00*	0.78	0.00	1.12	0.12	8993	1044	0.96	0.10	0.80	0.11	-4.74	-6.47	2.41	0.68	0.78	0.78	10.53
Ferrobasalt	SC1	B160	500	1200	0.00	0.04	0.04		1.18	0.10	4163	217		0.06			-7.54		0.16				
Ferrobasalt	SC1	B159	500	1200	0.56	0.21	0.21		2.82	0.10	3946	293		0.27			-6.23		1.46				
Ferrobasalt	SC1	B158	500	1200	0.85	0.55	0.55		5.54	0.14	2608	196		0.62			-5.51		2.18				
Ferrobasalt	SC1	B157	500	1200	0.97	0.76	0.76		8.18	0.11	1194	111		0.79			-5.30		2.40				
Ferrobasalt	SC1	B156	500	1200	1.00	0.94	0.94		9.02	0.11	0	0		0.94			-5.14		2.55				
Alkali basalt	OB93	OB93-1	500	1200	0.00	0.02	0.02		1.07	0.10	3130	200		0.02			-8.38		-0.68				
Alkali basalt	OB93	OB93-2	500	1200	0.59	0.21	0.21		3.15	0.10	3233	204		0.27			-6.24		1.45				
Alkali basalt	OB93	OB93-3	500	1200	0.85	0.57	0.57		5.44	0.10	2487	101		0.63			-5.50		2.20				
Alkali basalt	OB93	OB93-4	500	1200	0.97	0.51	0.51		7.45	0.10	1334	124		0.58			-5.57		2.13				
Alkali basalt	OB93	OB93-5	500	1200	0.99	0.86	0.86		7.96	0.10	727	36		0.87			-5.21		2.48				
Alkali basalt	OB93	M148 \$	500	1150	1.00	1	1		9.54	0.48	0	0		1.00			-5.09		2.60				
Alkali basalt	Etna	Etna-11	500	1200	1.00	1.00	1.00		8.78	0.12	0	0		1.00			-5.09		2.60				
Alkali basalt	Etna	Etna-12	500	1200	0.00	0.06	0.06		0.81	0.08	4356	193		0.09			-7.22		0.47				
Alkali basalt	Etna	Etna-13	500	1200	0.63	0.27	0.27		2.22	0.12	4196	176		0.34			-6.03		1.67				
Alkali basalt	Etna	Etna-14	500	1200	0.84	0.50	0.50		4.61	0.11	3337	158		0.57			-5.58		2.11				
Alkali basalt	Etna	Etna-15	500	1200	0.96	0.82	0.82		7.19	0.08	1963	82		0.84			-5.25		2.45				
MORB	169oxi	169oxi-17	500	1200	0.57	0.18	0.18		2.57	0.10	4368	247		0.23			-6.35		1.34				
MORB	169oxi	169oxi-18	500	1200	0.84	0.46	0.46		5.99	0.09	2886	183		0.53			-5.64		2.05				
MORB	169oxi	169oxi-19	500	1200	0.97	0.55	0.55		7.36	0.07	1186	74		0.62			-5.51		2.18				
MORB	169oxi	169oxi-20	500	1200	1.00	1.00	1.00		8.85	0.10	0	0		1.00			-5.09		2.60				

Table A-3-1 (continued). Experimental conditions, results of Karl-Fischer titration, determinations of redox state of Fe and infrared spectroscopy

Sample	NN	P (MPa)	T (C°)	X H ₂ O in	X (H ₂ O) fluid	X H ₂ O gravimetry	X H ₂ O fluid mass-balance	KFT H ₂ O (wt%)	KFT Error H ₂ O	CO ₂ (ppm)	Error CO ₂ (ppm)	MIR H ₂ O (wt%)	Error H ₂ O (wt%)	aH ₂ O fluid	aH ₂ O, Burnham	lgfO ₂ run XH ₂ Ofluid	lgfO ₂ run aH ₂ O Burnham	ΔNN O, aH ₂ O fl	ΔNN O aH ₂ O Burnham	Fe ²⁺ /Fe-total (K&C)	Fe ²⁺ /Fe-total (Colorimetry)	Fe-loss (%rel) EMP	
Tholeiite	N72	M52	700	1250	1.00	1.00*	1.00	1.00	11.21	0.13	0			1.00		-4.55		2.60					
Tholeiite	N72	M55	700	1250	0.83	0.50*	0.49	0.50	6.32	0.14	4233	357		0.56	0.71	-5.03	-4.85	2.12	2.30	0.74	0.63	-1.7	
Tholeiite	N72	M56	700	1250	0.00	0.00*	0.03	0.00	0.79	0.13	4363	363	0.73	0.10	0.04	0.03	-7.29	-7.60	-0.14	-0.45	0.9	0.84	-0.7
Tholeiite	N72	M63	700	1250	0.89	0.67*	0.32	0.67	7.31	0.15	3679	292		0.39	0.83	-5.34	-4.71	1.81	2.44	0.72	0.70	0.9	
Tholeiite	N72	M64	700	1250	0.85	0.52*	0.14	0.52	6.07	0.15	4478	356		0.19	0.67	-5.98	-4.90	1.18	2.25	0.74	0.72	2.8	
Tholeiite	N72	M65	700	1250	0.52	0.06*	0.11	0.06	2.27	0.13	4788	381		0.14	0.19	-6.21	-5.99	0.94	1.16	0.82	0.80	7.6	
Tholeiite	N72	M57	900	1250	1.00	1.00*	1.00	1.00	12.78	0.18	0			1.00		-4.55		2.60					
Tholeiite	N72	M60	900	1250	0.77	0.35*	0.49	0.35	5.89	0.15	5952	487		0.56	0.57	-4.99	-5.04	2.16	2.11	0.78	0.57	-4.7	
Tholeiite	N72	M61	900	1250	0.00	0.00*	0.02	0.00	1.51	0.13	5193	425	0.64	0.07	0.03	0.09	-7.47	-6.64	-0.32	0.51	0.88	0.84	-1.2
Tholeiite	N72	M67	900	1250	0.90	0.61*	0.00	0.61	9.53	0.16	5129	407		0.00	0.98		-4.57		2.58	0.74	0.65	-2.9	
Tholeiite	N72	M68	900	1250	0.90	0.59*	0.36	0.59	8.62	0.15	5252	417		0.44	0.87	-5.20	-4.67	1.95	2.48	0.74	0.68	0.5	
Tholeiite	N72	M69	900	1250	0.85	0.55*	0.27	0.55	7.01	0.14	5976	475		0.33	0.68	-5.43	-4.89	1.72	2.27	0.76	0.70	3.8	
Tholeiite	N72	M70	900	1250	0.56	0.13*	0.08	0.13	2.65	0.13	5943	477		0.11	0.2	-6.37	-5.95	0.78	1.20	0.83	0.82	9.3	
Tholeiite	N72	M71	900	1250	0.00	0.00*	0.04	0.00	1.25	0.12	5320	426	1.18	0.13	0.06	0.06	-6.97	-7.00	0.18	0.16	0.88	0.88	24.9

Notes:

Analytical errors and uncertainties, if not specified in the text, were calculated as described in Shishkina et al. (2010).

* - mole fraction of H₂O in the fluid determined by mass-balance, in all other runs - by gravimetry.

§ for these samples H₂O values determined by MIR were used for constructing of diagrams and calculations, for all other samples KFT determinations of H₂O content were used.

#- minimum CO₂-content that could be estimated from MIR spectra. Correct value was not possible to determine because of saturation of IR detector.

\$ - sample from Botcharnikov et al., 2005

XH₂O ini - initial molar fraction of water (H₂O/(H₂O+CO₂)) in a capsule before an experiment;

XH₂O mass-balance - molar fraction of water in fluid after run determined using data on loaded amounts of volatiles and dissolved in glasses after run.

aH₂Ofl - water activity in a run was calculated from the composition of the fluid phase (XH₂Ofl) using activity coefficients after Aranovich and Newton (1999) and molar volumes of pure H₂O after Pitzer and Sterner (1994).

aH₂O (Burnham) - water activity in a run was determined following the model of Burnham (1979) using the concentrations of dissolved water in experimental glasses;

logfO₂fl - The oxygen fugacity for every single run was calculated as log fO₂capsule = log fO₂intrinsic+2log (aH₂Ofl);

logfO₂ - The oxygen fugacity for every single run was calculated as log fO₂capsule = log fO₂intrinsic+2log (aH₂OBurnham);

ΔNNO - deviation of oxygen fugacity in a run from NNO (nickel-nickel oxide) buffer (from O'Neill 1987) at the same temperature;

Fe²⁺/Fe-total (K&C) - calculated after Kress and Carmichael (1991); Fe²⁺/Fe-total - determined by wet-chemical colorimetric method (Wilson 1960; Schuessler et al. 2008);

Fe-loss (%rel) EMP - loss of total Fe after run determined from electron microprobe analyses of glasses.

Curriculum Vitae / Lebenslauf

Personal information

Family name: **Shishkina**
Name: **Tatiana**
Date of Birth: 12th March 1983
Place of Birth: Kursk, Russia
Nationality: Russian

Education

1989 - 2000 **High school** of Malokurilsk, Sakhalin region, Russia

2000 - 2004 **Bachelor degree (Hons)**
Faculty of Geology, M.V. Lomonosov Moscow State University, Russia
Diploma title: The origin of allivalites in Golovnina volcano (Kurile Islands)
Supervisor: Dr. Pavel Pletchov

2004 - 2006 **Master degree (Hons)**
Faculty of Geology, M.V. Lomonosov Moscow State University, Russia
Diploma title: The origin of olivine-anorthite crystalline inclusions in volcanic rocks of the Kurile-Kamchatka island arc
Supervisor: Dr. Pavel Pletchov

2006 - 2008 **Postgraduate study**
Faculty of Geology, M.V. Lomonosov Moscow State University, Russia
Research direction: Island-arc volcanism. Origin of low-K-tholeiitic volcanic series.
Petrology, mineralogy, geochemistry, melt inclusions in volcanic rocks.

2008 – 2012 **PhD-student**
Institute of Mineralogy, Hannover Leibniz University, Germany

Thesis title: Magma storage conditions and degassing processes of island-arc tholeiitic series: Natural observations and experimental constraints for Mutnovsky volcano, Kamchatka.
Supervisors: Prof. Dr. François Holtz, Dr. Roman Botcharnikov, Dr. Renat Almeev